

THE ORIGIN\$ OF LOAD LOSSES IN ~~SQUIRREL CAGE~~  
INDUCTION MOTORS WITH CAST ALUMINIUM ROTORS

by

Nicos Christofides, B.Sc.(Eng.), A.C.G.I.

Thesis submitted for  
The Degree of Doctor of Philosophy  
in the Faculty of Engineering  
University of London

Imperial College  
London

July 1966

### ACKNOWLEDGMENTS

The work described in this thesis was carried out under the supervision of Dr. B. Adkins, D.Sc., M.A., M.I.E.E., Reader in Electrical Engineering, Imperial College of Science and Technology. The author wishes to express his gratitude to Dr. Adkins for his helpful guidance, constant encouragement and very keen interest.

Appreciation is extended to Dr. D.G.O. Morris, D.Sc., M.I.E.E., formerly of Imperial College and now with Shiraz University, (Iran), for suggesting the back-to-back test for induction motors; to Mr. W. Hill of A.E.I. for many fruitful discussions; and to Mr. R.B. Owen and the workshop staff of Imperial College for invaluable assistance in the preparation of experimental equipment.

Finally sincere appreciation is extended to the A.E.I. company, and in particular to Mr. M. Roberts of that company, for supplying the special experimental rotors, which have made this work possible.

ABSTRACT

The losses in a loaded induction motor are appreciably greater than the segregated losses based on the standard theory, but the precise causes of such losses were not fully understood.

An investigation has been carried out into the nature of these additional losses and a theory is presented which explains their origins in detail. The proposed theory is based on the Fourier analysis of the stator and rotor mmf waveforms into a series of space harmonics. Each harmonic is then considered as if acting on its own; incremental parameters being used when saturation is present.

A full mathematical derivation is given of the losses produced by current flow between two adjacent squirrel cage bars, through the rotor iron, when the squirrel cage is not perfectly insulated from the rotor laminations. The theory also includes a calculation of the eddy-current and hysteresis losses in the stator and rotor teeth, caused by the high frequency harmonic fluxes that penetrate them. It shows how the eddy-currents in the rotor iron surface can reduce the value of the differential harmonic leakage of a bar, thus allowing more harmonic

bar current to flow and hence more  $I^2R$  loss to be produced. It discusses how the effective skew differs from its geometrical value, depending on the width of the rotor bar.

The effect of saturation on the load losses is investigated both theoretically and experimentally and proper saturation factors are derived for this purpose.

Practical tests were carried out on eleven squirrel-cage induction motors and one slip-ring motor in order to verify the theoretical formulae. A new back-to-back testing technique was developed, and by its use direct measurements of the load losses under normal operating conditions were made to a high degree of accuracy and reliability hitherto unobtainable. Other tests included measurements of the torque-slip characteristics both at reduced voltage using a swinging stator dynamometer, and at full voltage using an accelerometer. A special accelerometer, embodying a filter with time varying components to give a very high attenuation at the noise frequencies, was designed for use with this last test.

Comparisons between theoretical calculations and experimental results from all the tests show a good



agreement. Having established the validity of the theoretical formulae, the effect of variations in each machine parameter (skew, bar insulation, slot combination, and air gap length) on the load losses is investigated and ways of reducing these losses suggested.

INDEX

	page
<u>Acknowledgments.</u>	2
<u>Abstract.</u>	3
<u>List of Symbols.</u>	12
<u>CHAPTER 1.    Introduction and definitions.</u>	20
<u>CHAPTER 2.    Description of machines.</u>	28

PART ONETHE MEASUREMENT OF LOAD LOSSES

<u>CHAPTER 3.    Measurement of torque-slip</u>	
<u>characteristics at low currents.</u>	34
3.1   Dynamometer measurements.	34
3.2   Measurement of the fundamental	35
torque.	
<u>CHAPTER 4.    Measurement of torque-slip</u>	
<u>characteristics at high currents.</u>	40
4.1   The accelerometer measurements.	40
4.1.1   The principle of the	
method.	
4.1.2   The design of the	
accelerometer.	
4.2   Measurement of the fundamental	49
torque.	
<u>CHAPTER 5.    Measurement of load losses under</u>	
<u>normal load.</u>	57
5.1   The back-to-back test.	57
5.2   Experimental procedure.	62

PART TWOTHEORETICAL ANALYSIS OF LOAD LOSSES

<u>CHAPTER 6.</u>	<u>Theoretical analysis of load</u>	
	<u>losses.</u>	67
6.1	Analysis of the air gap fields.	67
6.1.1	Air gap fields due to the stator harmonics.	
6.1.2	Air gap fields due to the rotor harmonics.	
6.2	Harmonic losses in rotor bars and harmonic equivalent circuit.	82
6.3	Losses due to imperfect insulation between the squirrel cage bars and the rotor iron.	85
6.3.1	Calculation of losses.	
6.3.2	Choice of interbar resistance.	
6.4	Effects of eddy currents on the rotor iron surface.	100
6.4.1	Calculation of fluxes.	
6.4.2	Calculation of losses.	
6.4.3	The reduction of leakage reactance.	
6.5	Iron losses in the rotor teeth.	113
6.5.1	Damping of the tooth flux.	
6.5.2	Calculation of rotor tooth iron losses.	
6.5.3	Choice of iron permeability.	

6.6	Load losses in the stator due to the rotor mmf harmonics.	120
6.6.1	Harmonic losses in stator windings.	
6.6.2	Losses in the stator iron surface and the stator teeth.	
6.7	Effect of saturation on the load loss formulae.	123
6.7.1	Necessary modifications.	
6.7.1	The saturation factor $k_{s1}$ .	
6.7.2.1	The definition of $k_{s1}$ .	
6.7.2.2	The calculation of flux densities.	
6.7.3.3	The calculation of $k_{s1}$ .	

### PART THREE

## THE DETERMINATION OF PARAMETERS IN THE THEORETICAL FORMULAE.

<u>CHAPTER 7.</u>	<u>The determination of parameters in the theoretical formulae.</u>	137
7.1	The calculation of harmonic resistances and reactances.	137
7.1.1	The magnetising reactance $x_{mv}$ .	
7.1.2	The rotor differential harmonic leakage reactance ( $x_{2dv}$ ) and skew leakage reactance, ( $x_{skv}$ ).	

7.1.3	The rotor slot leakage reactance and bar resistance.	
7.1.4	The total impedance of a rotor bar.	
7.2	Measurement of interbar resistance.	148
7.3	The effective skew.	159

#### PART FOUR

#### COMPARISON OF RESULTS

<u>CHAPTER 8.</u>	<u>Comparison of results.</u>	165
8.1	Torque-speed curves at low currents.	165
8.2	Torque-speed curves at high currents.	185
8.3	The load losses at normal load.	196

#### PART FIVE

#### EFFECT OF MACHINE PARAMETERS ON THE LOAD LOSSES

<u>CHAPTER 9.</u>	<u>The effect of bar insulation on the load losses.</u>	204
9.1	Simplifications to cross current loss formula.	204
9.1.1	Low interbar resistance.	
9.1.2	High interbar resistance.	
9.2	The location of the place of dissipation of the cross current losses.	206

9.3	The modified harmonic equivalent circuit.	210
<u>CHAPTER 10.</u>	<u>The effect of skew on the load losses.</u>	215
10.1	Harmonic bar current load losses.	215
10.2	Cross current load losses.	216
10.3	Iron load losses in the stator and the rotor.	218
10.4	The total load loss.	221
<u>CHAPTER 11.</u>	<u>The effect of slot combination on the load losses.</u>	225
11.1	Harmonic bar current load losses.	225
11.2	Cross current load losses.	229
11.3	Iron load losses in the stator and rotor teeth.	232
11.4	The total load loss.	236
<u>CHAPTER 12.</u>	<u>The effect of air gap length on the load losses.</u>	239
12.1	Harmonic bar current load losses.	239
12.2	Cross current load losses.	239
12.3	Iron load losses in the stator and rotor teeth.	240
12.4	The total load loss.	241

---

<u>CHAPTER 13.</u>	<u>Further verifications of the theory, and "extra" load losses caused by the combined effects of permeance harmonics and saturation.</u>	244
13.1	Measurement and prediction of the stator tooth fluxes.	244
13.2	Load losses caused by the combined effects of permeance harmonic fields and saturation.	254
<u>CHAPTER 14.</u>	<u>Conclusions and suggestions for further work.</u>	262
APPENDIX I	: The distribution of power flow in the back-to-back test.	268
APPENDIX II	: The mmf distribution produced by a three-phase winding.	272
APPENDIX III	: The calculation of the constants A and B in Eqn. 6.38.	277
APPENDIX IV	: The penetration of a travelling magnetic field into a lamination.	279
APPENDIX V	: The reduction of the differential harmonic leakage reactance by the slot openings.	281
<u>REFERENCES.</u>		289

LIST OF SYMBOLS

$a_1, a_2, a_3$	: constants of Section 6.7.
$A$	: area ( $m^2$ ), <u>or</u> constant.
$B$	: flux density ( $Wb/m^2$ ), <u>or</u> constant.
$\overline{B}$	: complex amplitude of flux density.
$b$	: instantaneous value of flux density.
$c$	: integer.
$d$	: integer.
$\overline{D}_v$	: complex damping factor of the $v^{th}$ stator field harmonic due to the induced rotor currents.
$E$	: induced rms voltage (V).
$e$	: induced emf. (instantaneous value) (V).
$E_{ov}$	: induced emf per unit length of rotor bar. (V/m).
$f_o$	: supply frequency. (c/s).
$f_s^r$	: transfer factor from stator phase to rotor bar.
$f_v$	: harmonic frequency induced in the rotor by the $v^{th}$ stator harmonic. (c/s)
$f_\mu$	: harmonic frequency induced in the stator by the $\mu^{th}$ rotor harmonic (c/s)



$f_{1v}, \bar{F}_{1v}$	: stator mmf due to $v^{\text{th}}$ harmonic. (instantaneous and complex amplitude values respectively). (AT)
$f_{2\mu}, \bar{F}_{2\mu}$	: rotor mmf due to $\mu^{\text{th}}$ harmonic. (instantaneous and complex ampli- tude values respectively). (AT)
$g$	: air gap length. (m)
$G_{1v}, G_{2v}, \dots \text{etc.}$	: constants of Chapters 11 and 12.
$h$	: lamination thickness. (m)
$h_s$	: stator tooth body length. (m)
$h_r$	: rotor tooth body length. (m)
$H$	: magnetic field strength. (AT/m)
$I$	: rms current. (A)
$\bar{I}$	: phasor rms current. (A)
$I_1$	: stator phase current. (A)
$I_2$	: rotor current per phase referred to stator. (A)
$I_m \text{ or } I_o$	: magnetising current per phase. (A)
$k_1$	: integer.
$k_{c1}, k_{c2}$	: Carter's coefficients for stator and rotor respectively.
$k_c = k_{c1} \times k_{c2}$	
$k_{skv}$	: skew factor for $v^{\text{th}}$ harmonic.
$k_{dpv}$	: winding factor for $v^{\text{th}}$ harmonic.

$k_{d\ell v}$	:	damping factor for differential leakage.
$k_x$	:	reduction factor for slot leakage.
$k_r$	:	increase factor for bar resistance.
$k''_{tv}$	:	damping factor for rotor tooth flux.
$k_{s1}$	:	saturation factor for main flux.
$k_{s2}$	:	saturation factor for differential leakage flux.
$k_{s3}$	:	saturation factor for slot leakage flux.
$k_2$	:	integer.
$k_3$	:	magnitude of 3 <sup>rd</sup> harmonic component of air gap flux density as a percentage of the fundamental.
$k_v$	:	$1 - w_{20}/\lambda_2$ .
$k_{ov}$	:	reduction factor of differential leakage reactance due to slot openings.
$\ell$	:	length of rotor stack. (m)
$\ell_1$	:	leakage inductance of stator per phase. (h)
$\ell_2$	:	leakage inductance of rotor per phase. (h)
$L (...)$	:	function giving total load loss. (w)

$M$	:	mutual inductance between stator and rotor <u>or</u> slope of saturated part of magnetisation curve.
		(h) <u>or</u> (wb/AT.m)
$n$	:	speed. (rps)
$n_s$	:	synchronous speed. (rps)
$P$	:	power (w)
$P'_{tv}$	:	iron losses in stator teeth (w)
$P''_{tv}$	:	iron losses in rotor teeth. (w)
$P_{2v}$	:	harmonic bar and interbar current losses. (w)
$P'_{ev}$	:	surface eddy current loss in stator iron. (w)
$P''_{ev}$	:	surface eddy current loss in rotor iron. (w)
$p$	:	pairs of poles.
$q$	:	stator slots per pole per phase.
$r$	:	integer.
$R$	:	rotor radius. (m)
$r_1, R_1$	:	resistance of stator winding per phase. ( $\Omega/m$ ) <u>or</u> ( $\Omega$ )
$r_{2v}, R_{2v}$	:	resistance of rotor winding referred to one stator phase. ( $\Omega/m$ ) <u>or</u> ( $\Omega$ )
$r_{bb}$	:	bar-to-bar resistance per unit rotor length. ( $\Omega-m$ )

$r_{bv}, R_{bv}$	: resistance of one rotor bar. ( $\Omega/m$ ) <u>or</u> ( $\Omega$ )
$s$	: fundamental slip.
$s_v$	: slip of rotor with respect to $v^{th}$ harmonic field.
$S_1, S_2$	: number of stator and rotor slots respectively.
$T$	: torque. (N-m)
$t$	: time. (sec)
$V$	: rms voltage (V)
$w_t''$	: rotor tooth body width. (m)
$w_t'$	: stator tooth body width. (m)
$w_{2e}$	: effective rotor bar width. (m)
$w_{2o}$	: rotor slot opening. (m)
$W_t'$	: stator tooth weight. (Kg)
$W_t''$	: rotor tooth weight. (Kg)
$x_1, X_1$	: total stator leakage reactance per phase. ( $\Omega/m$ ) <u>or</u> ( $\Omega$ )
alternatively $x_1$	: stator peripheral coordinate. (m)
$x_2$	: rotor peripheral coordinate. (m)
$x_{2v}, X_{2v}$	: total rotor leakage reactance per phase. ( $\Omega/m$ ) <u>or</u> ( $\Omega$ )
$x_{mv}, X_{mv}$	: magnetising reactance of $v^{th}$ harmonic referred to stator side. ( $\Omega/m$ ) <u>or</u> ( $\Omega$ ).

- $x_{skv}, X_{skv}$  : skew leakage reactance.  
 $(\Omega/m)$  or  $(\Omega)$
- $x_{2sl}, X_{2sl}$  : rotor slot leakage reactance  
referred to stator side.  $(\Omega/m)$   
or  $(\Omega)$
- $x_{2dv}, X_{2dv}$  : differential leakage reactance  
referred to stator side.  $(\Omega/m)$   
or  $(\Omega)$
- $x_{bv}, X_{bv}$  : total reactance of a bar.  $(\Omega/m)$   
or  $(\Omega)$
- $x_{bm}, X_{bm}$  : magnetising reactance of a bar.  
 $(\Omega/m)$  or  $(\Omega)$
- $x_{bd}, X_{bd}$  : differential leakage reactance  
of a bar.  $(\Omega/m)$  or  $(\Omega)$
- $x_{bsl}, X_{bsl}$  : slot leakage reactance of a bar.  
 $(\Omega/m)$  or  $(\Omega)$
- $Z_1$  : stator conductors in series per  
phase.
- $z_{bv}, Z_{bv}$  : total bar impedance.  $(\Omega/m)$   
or  $(\Omega)$
- $\alpha_v$  : angle of skew.  $(rad/m)$
- $\beta_v''$  : half the electrical angle that  
a rotor tooth subtends with  
respect to the  $v^{th}$  harmonic.  
 $(rad)$

$\beta'_\mu$	: half the electrical angle that a stator tooth subtends with respect to the $\mu^{\text{th}}$ harmonic. (rad)
$\theta_v$	: electrical angle that rotor tooth pitch subtends with respect to the $v^{\text{th}}$ harmonic. (rad)
$\gamma'_c$	: amplitude of $c^{\text{th}}$ stator permeance harmonic as a percentage of the mean air gap permeance.
$\gamma''_d$	: amplitude of the $d^{\text{th}}$ stator permeance harmonic as a percentage of the mean air gap permeance.
$\gamma_v$	: propagation constant. ( $\text{m}^{-1}$ )
$\delta$	: depth of penetration. (m)
$\eta_v$	: ratio ( $x_{bsl}/x_{bm v}$ ).
$\lambda_1$	: stator slot pitch. (m)
$\lambda_2$	: rotor slot pitch. (m)
$\lambda_{sk}$	: effective skew. (m)
$\lambda_g$	: geometrical skew. (m)
$\mu$	: order of rotor harmonics <u>or</u> relative permeability.
$\Lambda$	: air gap permeance.
$\Lambda_0$	: mean air gap permeance.
$v$	: order of stator harmonics.

$\xi_v$	:	skew correction factor.
$\rho$	:	resistivity. ( $\Omega$ -m)
$\sigma_h$	:	hysteresis loss constant.
$\sigma_e$	:	eddy current loss constant.
$\tau_{2dv}$	:	factor for differential leakage.
$\phi'_{t\mu}, \phi''_{tv}$	:	flux in stator and rotor tooth bodies due to $\mu^{th}$ and $v^{th}$ harmonics respectively.
$\left[ \phi'_{res} \right]_{slot}, \left[ \phi''_{res} \right]_{slot}$	:	resultant stator and rotor tooth fluxes due to rotor and stator slot harmonics respectively.
$\omega$	:	frequency. (rad/sec)
$\omega_r$	:	rotor speed in mechanical radians/sec.

#### Subscripts and Superscripts.

b	:	bar quantities. (not referred to stator side).
bb	:	referring to the interbar region.
v	:	with respect to $v^{th}$ stator field harmonic.
$\mu$	:	with respect to $\mu^{th}$ rotor field harmonic.
1 or '	:	stator quantities.
2 or ''	:	rotor quantities.

## CHAPTER 1

### INTRODUCTION AND DEFINITIONS

#### 1.1 Practical definition of load losses.

The load losses are defined<sup>1,2</sup> as the difference between the total power loss of a machine on load and the losses determined by the loss segregation method.

The segregated losses are:

(i) The friction and windage loss ( $P_{fw}$ ) and stator core loss ( $P_{fe1}$ ). These losses are measured by a no-load test after correcting for the stator copper loss produced by the no-load current. (This assumes that the stator core loss due to the main flux does not change with load.)

(ii) The stator copper loss ( $P_{c1}$ ) calculated as  $P_{c1} = 3I_1^2 R_1$  where  $I_1$  is the stator phase current and  $R_1$  the stator winding resistance per phase measured at the operating temperature.

(iii) The rotor conductor loss ( $P_{c2}$ ) calculated as  $P_{c2} = s(P_i - 3I_1^2 R_1 - P_{fe1})$ , where  $s$  is the slip at full load and  $P_i$  is the stator input power.

Thus if the total loss of a machine on load is  $P_{t\ell}$  ( $P_{t\ell} = P_i - P_o$ ) the load loss is defined by:

$$P_{\ell\ell} = P_{t\ell} - (P_{fw} + P_{fe1}) - P_{c1} - P_{c2} \quad (1.1)$$



## 1.2 Mathematical formulation and definition of load losses.

The definition of Eqn. 1.1 is based on the way that the load losses manifest themselves during load, and points to a method by which they can be measured. It does not define load losses in terms of their causes nor does it state the place at which they are dissipated. This is done by the theoretical definition given in this Section and is a necessary prerequisite to any theoretical investigation of load losses.

The usual theory of the induction motor is based on the assumption that the radial component of the magnetic field in the air gap of the machine is sinusoidally distributed in space and forms a single wave that rotates round the air gap at its synchronous speed.

This condition would exist, however, only if the surfaces of both stator and rotor were smooth and the windings sinusoidally distributed on them.

In the real machine the windings are placed in slots, and therefore the resulting mmf and flux density distributions are not sinusoidal but contain, apart from the fundamental wave, a series of harmonics which also rotate round the air gap at their own synchronous speeds.<sup>3,4</sup>

Although the amplitudes of these harmonic flux waves are much smaller than the amplitude of the funda-

mental, they induce in both the stator and the rotor high frequency flux pulsations which can produce losses comparable in magnitude with the losses produced by the fundamental flux wave. Since the mmfs producing these fluxes are proportional to the currents flowing in the windings, the losses produced are also dependent on the load currents.

The losses referred to as "load-losses" in this thesis are therefore defined as follows:

If the total loss of a machine on load is  $P_{t\ell}$ , and if the losses in the same machine under the same external loading conditions are  $P'_{t\ell}$  when the machine is excited by a single and purely sinusoidal air gap mmf wave then the load losses are defined as

$$P_{\ell\ell} = P_{t\ell} - P'_{t\ell} \quad (1.2)$$

In a machine where saturation is not present the above definition reduces to:

$$P_{\ell\ell} = \sum_{v \neq 1} P_{tv} + \sum_v \sum_{\mu \neq v} P_{t\mu} \quad (1.3)$$

where  $P_{tv}$  is the total loss produced directly by the  $v^{\text{th}}$  stator mmf harmonic and occurring at the  $v^{\text{th}}$  harmonic frequency, and  $P_{t\mu}$  is the total loss due to the  $\mu^{\text{th}}$  rotor mmf harmonic, (induced by the stator  $v^{\text{th}}$  harmonic) and occurring at the  $\mu^{\text{th}}$  harmonic frequency.

The definition of Eqn. 1.2 is almost exactly the same as the definition of Eqn. 1.1 except that it is stated in terms of the causes of the load losses. The definition of Eqn. 1.2 attributes the existence of the load losses to the harmonic flux waves rotating in the air gap of the machine. The main difference between the two definition is that Eqn. 1.2 includes in the value of load loss the losses that are produced by the stator mmf harmonics on no-load, whereas the definition of Eqn. 1.1 does not. Thus the load losses as defined by Eqn. 1.1 are directly dependent on the value of  $I_2$  whereas as defined by Eqn. 1.2 they are dependent on both  $I_1$  and  $I_2$ . (The losses caused by the stator mmf harmonics depend on  $I_1$  and those caused by the rotor mmf harmonics on  $I_2$ . It will be shown later however that the former are always appreciably greater than the latter so that the load losses as defined by Eqn. 1.2 can be taken to depend only on  $I_1$ .) Since the difference between  $I_1$  and  $I_2$  is small, however, the difference between the theoretical and practical definitions is small. In any case the load losses as obtained by one of the above definitions can easily be converted to the value of the load losses as obtained by the use of the other definition.

Quite apart from the losses produced by the harmonics due to the non-sinusoidal mmf distributions other losses also occur due to the flux harmonics produced by the slotting on either side of the air gap. These harmonics are independent of the currents that flow in the windings, and their amplitudes depend only upon the variations in the air gap permeance and the magnitude of the main flux wave; i.e. upon the slot openings and the terminal voltage. The losses produced by them therefore also occur on no-load in a machine excited by a purely sinusoidal air gap mmf wave, and as such are fundamentally different in nature from the losses produced by the mmf harmonics. Failure to appreciate this fact has led to many misunderstandings and inaccurate terminology in the past.

Although as stated above, the slot openings produce losses which are not included in the load losses, in either of the above definitions, they nevertheless have an indirect effect on the load loss by modifying the losses produced by the mmf slot-harmonics as shown in Section 6.1. Also in a heavily saturated machine the losses produced by the flux pulsations due to the slot openings are not constant but vary with load. The difference between the full-load and no-load values of these losses may therefore be classed as an "extra"

load loss and is treated in greater detail in Chapter 13.

### 1.3 The approach to the problem.

The load losses increase the total loss of a machine and so reduce the efficiency and increase the temperature rise, thus limiting the maximum output power than can be obtained from it. Increases in output power of 10, 20 or sometimes 30 per cent could be made for the same temperature rise, if the load losses could be eliminated.

Whereas as stated above the load losses may be a significant portion of the total loss in an induction motor, they are nevertheless only a small fraction of the output of the machine. Thus to determine these losses directly by measurements of input and output powers, would require tests of very high accuracy indeed which are difficult to perform. Even then only moderate accuracy for the losses could be achieved. In view of this and the lack at the time of any other means of testing which was free from theoretical or practical objections, a less direct but more tangible line of attack was followed.

This consisted of investigating the effects of the load losses on the torque-slip characteristics

of the machine over the entire speed range, (i.e. braking, motoring, and generating regions). Since the load losses increase very rapidly as the speed departs further away from synchronous speed - due to the increase in the load current - the problem of measurement is not as difficult as it is under the normal conditions of operation. It should be noted, however, that this line of attack is not merely a substitute for a test measuring the load losses directly. It is in many ways preferable as it shows more clearly the true nature of load losses over the entire range of harmonic frequencies, and is also important for starting. The torque slip characteristic provides a result which is a much more stringent test for the theoretical formulae than a single value of load losses taken at the normal operating point.

Torque-slip characteristics were taken at both low and high values of current, (Chapters 3 and 4 respectively), and the results give the load losses under conditions of both unsaturated and saturated leakage flux paths. Direct measurements of load losses using a back-to-back test developed later on (Chapter 5) give the load losses under conditions of both saturated and unsaturated main magnetic flux paths. Thus a comprehensive set of experimental

results is obtained under all possible conditions that can exist in a machine.

## CHAPTER 2

### DESCRIPTION OF MACHINES

The experimental work described in the thesis was performed on eleven  $7\frac{1}{2}$  hp squirrel cage induction motors and one 5 hp slip ring motor. For the measurement of the torque-slip characteristics a single stator was used with all squirrel cage rotors but a second identical stator was of course necessary for the back-to-back tests.

Table 1

#### Particulars of stators of squirrel cage machines

Rated voltage	: 400 v
No. of poles	: 4
No. of slots	: 36
Winding pitch	: 77.8%
Turns in series/phase	: 378
Phase connection	: delta
Carter's coefficient	: 1.225
Internal gap diameter	: 13.97 cm
External gap diameter	: 22.21 cm
Lamination thickness	: .636 cm

The slot shape is shown in Fig.1



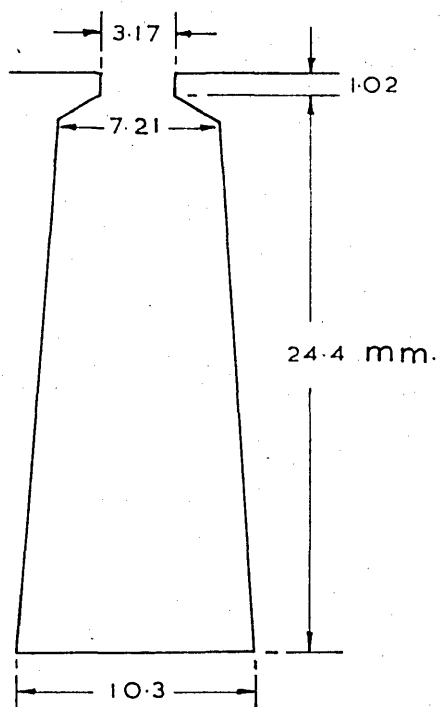


fig1. Stator slot dimensions. (3x full scale)

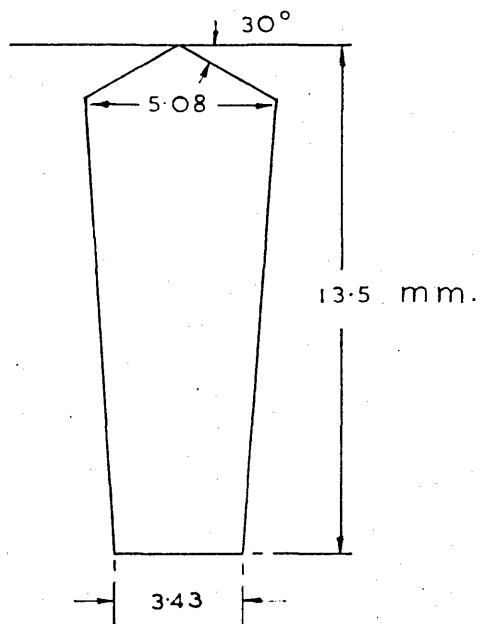


fig2. Rotor slot dimensions. (5 x full scale)  
(rotor N° 1)

Table 2Particulars of squirrel cage rotors

Rotor No.	No. of slots	bar insulation	skew	interlaminar insulation	$r_{bb}$
-	-	-	stator slot pitches	-	$\Omega\text{-m}(x10^{-4})$
1(a)(b)(c)	45	potash treatment	0.705	Fe-scale	6.0
2	45	"	0	" "	5.5
3	45	"	1.101	" "	6.5
4	45	"	0.705	Varnish	6.5
5	50	"	"	Fe-scale	7.0
6	32	"	"	" "	6.0
7	23	"	"	" "	5.0
8	45	slots cleaned before casting	"	" "	1.21
9	"	no treatment	"	" "	2.9
10(a)	"	glass silicate insulation	"	" "	800
10(b)	"	"	"	" "	1200

All rotors had the following in common.

length of stack = 11.44 cm

lamination thickness = .636

resistivity of cast aluminium =  $3.71 \times 10^{-8} \Omega\text{-m}$ .

Unless otherwise stated, the air gap length is .33 mm. For the rotors with differing numbers of slots the bar depth was kept constant thus eliminating any variations due to skin effects between the different rotors. Also in order to maintain the same magnetic flux conditions in the iron teeth and the same current loading conditions in the conductors of the different rotors, the ratio of tooth width to slot pitch was kept constant. Despite difficulties associated with manufacture this constancy was kept to within an accuracy of  $\pm 1\%$ . The cross section of the slots for all rotors was coffin shaped and is shown in Fig.2 for the 45-slot rotor.

Rotors No. 10(a) and 10(b) had the inside walls of the slots blasted with rochite salt powder which provided a very effective insulation of the squirrel cage bars. The thickness of the rochite deposit however reduced the effective bar area by 2% and this must be taken into consideration in the theoretical calculations.

Rotors No. 8 and 9 were not treated in a way that would provide any degree of bar insulation, and

therefore there is an intimate contact between the aluminium bars and the iron. One of these rotors (No.8) had the inside walls of the slots cleaned just before casting and the interbar resistance for this rotor is very low. (Lower than that of rotor No.9 which had no treatment at all.)

Table 3.

Particulars of stator of slip ring motor

Rated voltage	: 240 v
Number of slots	: 36
Turns in series/phase	: 99
Winding pitch	: 77.8%
Number of poles	: 4
Phase connection	: delta
Lamination thickness	: .636 mm

Table 4.

Number of slots	: 24
Skew	: 1 stator slot pitch
Turns in series/phase	: 104
Winding factor	: 66.7%
Phase connection	: star
Geometrical air gap = .33 mm.	

P A R T   O N E

THE MEASUREMENT OF LOAD LOSSES

## CHAPTER 3

### MEASUREMENT OF TORQUE-SLIP CHARACTERISTICS AT LOW CURRENTS.

The torque-slip characteristics of all squirrel cage rotors were taken at both constant voltage and constant current conditions and frequencies of supply of 50,  $33\frac{1}{3}$  and  $16\frac{2}{3}$  c/s. Reduced terminal voltage (25% rated voltage) was used for the constant voltage tests in order to avoid heating problems and also to avoid saturation of the main magnetic flux paths.

#### 3.1 Dynamometer measurements.

If any quantitative comparisons are to be made between the theoretical and experimental results, great precision is required in the measurements. It was found that an accuracy of better than 1% could be achieved in the measurement of torque by the use of a swinging stator dynamometer with weights used to balance the stator. In order to achieve stable operation in what is normally the unstable region of the induction motor, the dynamometer was supplied in a Ward-Leonard connection.<sup>5</sup>.

Corrections to the measured torque were of course made to account for the friction and windage of the

rotating parts. Thus if  $Q_1$  is the measured dynamometer balancing torque with the induction motor excited and  $Q_2$  the balancing torque with no excitation to the motor but with the set running at the same speed, then the electromagnetic torque developed by the induction machine is given by  $Q_1 - Q_2$ .

It should be noted that  $Q_1$  is not exactly the induction motor shaft torque.  $Q_1$  does not include the windage torque of the coupling between the two machines ( $W_{\text{coupl.}}$ ) nor does it include a fraction  $\lambda$  of the dynamometer windage torque ( $W_{\text{dyn.}}$ ). This fraction  $\lambda$  represents the percentage tubes of air flow whose energy is not dissipated by impinging on projecting stator parts. Thus the quantity  $Q_1$  is less than the shaft torque by the amount ( $W_{\text{coupl.}} + \lambda W_{\text{dyn.}}$ ). This amount was determined experimentally as suggested by Emmerling<sup>6</sup> and found to be less than 4% of the total windage loss. In any case the error does not affect the results obtained by the method described above since this small fraction of windage torque is excluded from both  $Q_1$  and  $Q_2$  so that their difference ( $Q_1 - Q_2$ ) is unaffected.

### 3.2 Measurement of the fundamental torque.

The fundamental torque produced by the induction motor was calculated from measurements of the input

power to the stator of the induction machine and of the stator winding resistance.

Since the speeds of rotation of the stator harmonic fields are small compared to the speed of the fundamental wave, the power input to the rotor due to these fields is small and becomes even smaller due to the different direction of rotation of the various harmonics. This is so despite the fact that the harmonic torques produced may be of a very considerable magnitude. It follows therefore that the power input to the rotor, given by:

$$W_T = P_{in} - 3I_1^2 R_1 - P_{fe1} \quad (3.1)$$

is almost entirely due to the fundamental.

In Eqn. 3.1  $P_{in}$  is the measured stator input and  $P_{fe1}$  the stator iron loss at the test voltage. The value of the stator phase resistance  $R_1$  is, of course, taken at the operating temperature which was kept as constant as possible. Readings of  $R_1$  were made before and after each torque measurement and the resistance was not allowed to vary by more than 1.5%. The small variations in input power due to the slot harmonics near their synchronous speeds are apparent in the curves shown in Chapter 3, and particularly so in the curves corresponding to the rotor without skew



for which these harmonics are largest. (Fig.56).

An overall accuracy of better than 0.5% is believed to have been achieved in the measurement of the fundamental torque, and the speed was measured on an electronic digital tachometer to within  $\pm 0.5$  rpm.

The experimental setup is shown in Fig.3 and a typical speed torque curve in Fig.4.

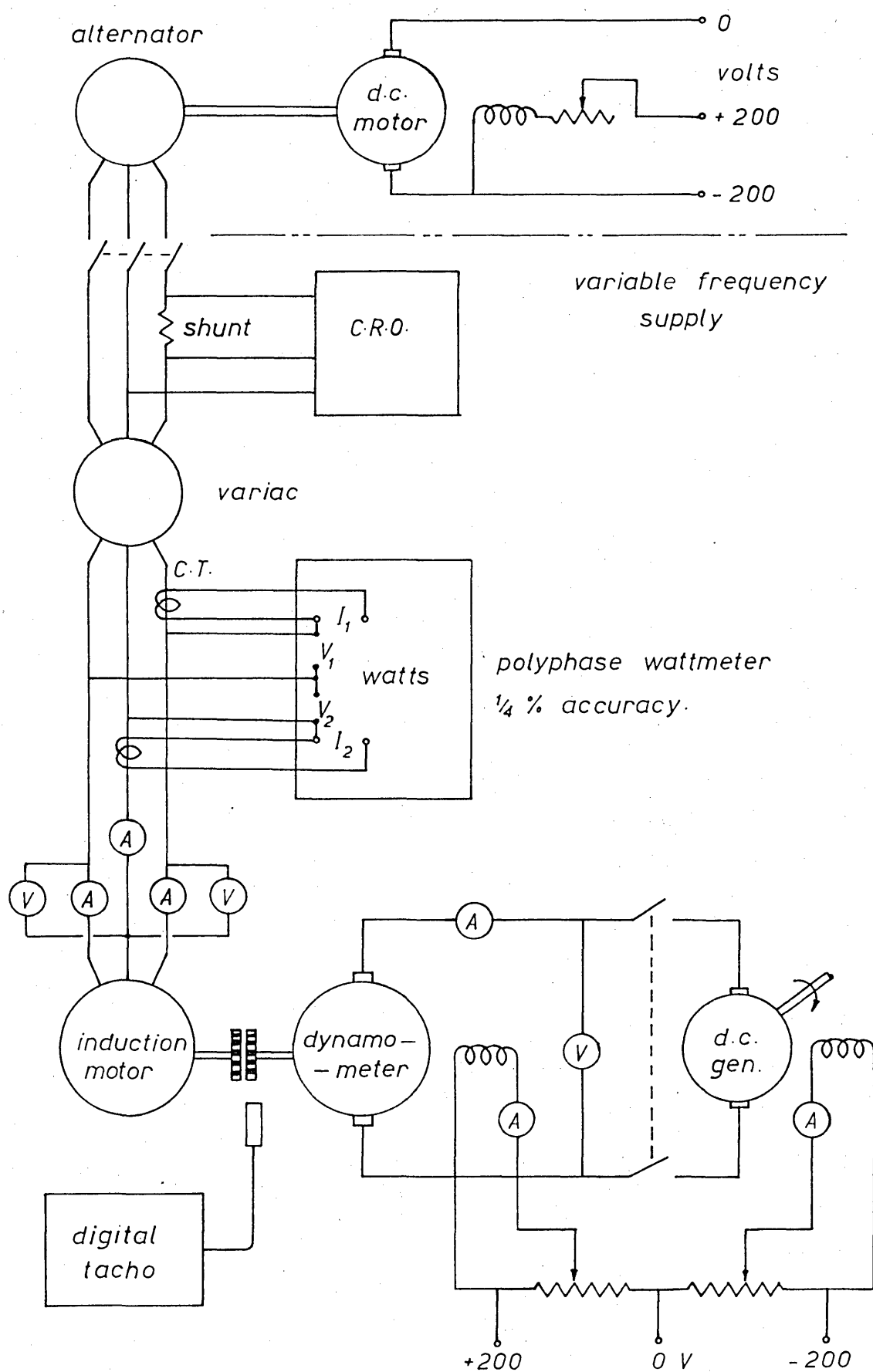


fig.3. General experimental set-up for torque measurement.

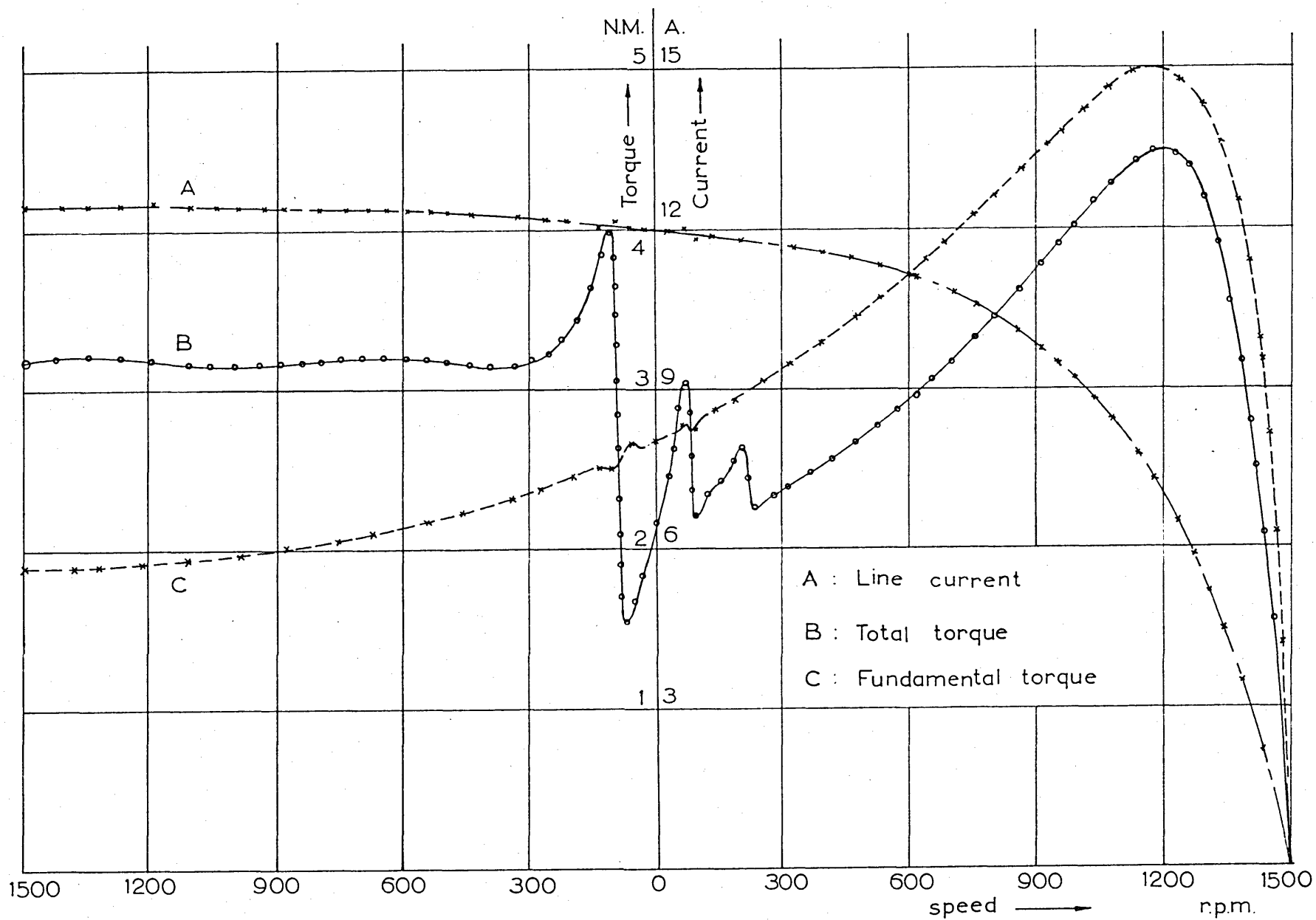


fig. 4. Measured characteristics of rotor N°1 using a dynamometer. (100 V. 50 c/s)

## CHAPTER 4.

### MEASUREMENT OF TORQUE-SLIP CHARACTERISTICS AT HIGH CURRENTS.

Although the measurement of the torque-speed characteristics by the swinging stator dynamometer technique of the last Chapter is perfectly satisfactory when the currents flowing in the machine windings are small; (not much above their full load value), the time taken for each reading is long and therefore the method could not be used when large currents are flowing, because of the excessive heating of the machine that would result. Thus if the torque-speed characteristics are to be measured at the rated voltage over the slip range  $0 < s < 2$  an automatic recording technique must be used which obtains the entire curve in a few seconds.

#### 4.1 The accelerometer measurements.

##### 4.1.1 The principle of the method.

If an induction motor is running on no-load and the phase sequence of the supply is suddenly reversed, the machine will decelerate from a speed of almost  $n_0$  in one direction to standstill and then accelerate to a speed of almost  $n_0$  in the other direction. During the deceleration and acceleration processes

there is an electromagnetic torque acting on the rotor, its value depending on the instantaneous slip of the rotor with respect to the revolving magnetic field.

If the rotor inertia is given by  $J(\text{kg-m}^2)$  and the instantaneous rotor speed is  $\omega_r$  (rad/sec), then the electromagnetic torque  $T_e$  is given by:

$$T_e = J \frac{d\omega_r}{dt} \pm T_{fw} \quad (4.1)$$

where  $T_{fw}$  is the friction and windage torque of the rotating parts and the (-) and (+) signs correspond to the decelerating and accelerating periods respectively.

If  $T_{fw}$  is neglected Eqn. 4.1 shows that the electromagnetic torque is proportional to the acceleration  $\dot{\omega}_r$ . Thus all that is needed is to obtain a speed and an acceleration signal during the speed reversal. When these signals are fed into the X and Y axes respectively of an automatic recorder the resulting curve is - apart from a small correction due to the friction and windage torque - the speed-torque characteristic to a scale of  $J$  N-m/rad/sec.

#### 4.1.2 The design of the accelerometer.

It was found after a short preliminary investigation that with no extra inertia added to the natural

inertia of the induction motor, the time for the speed reversal with rated supply voltage was so short that it was comparable with the period of the supply frequency. The electrical transients following the switching of the phase sequence of the supply existed throughout the decelerating and accelerating periods so that the curves obtained were not the true steady-state torque-speed characteristics. An extra inertia about 30 times the natural inertia of the induction motor was therefore coupled to the machine and the time for the complete speed reversal was then increased to about 2 seconds.

A speed signal can be obtained during the speed reversal of the induction motor from a d.c. tachogenerator coupled to it. This signal can then be electrically differentiated with respect to time to obtain acceleration. Any high frequency noise that may exist on the speed signal before differentiation is greatly magnified by the differentiating process and introduces a "mush" on the acceleration output. Thus in order to eliminate this mush and obtain accurate speed-torque characteristics a low noise (2% maximum ripple) tachogenerator was used and an elaborate filtering system developed to eliminate the remaining noise which is primarily introduced by

the commutator segments.

The frequency of the commutator ripple noise is given by:  $\omega_n = n_c \cdot \omega_r$  where  $n_c$  is the number of commutator segments. Thus the noise frequency varies linearly with machine speed as shown in Fig.5.

It was noticed from the swinging stator dynamometer tests (e.g. Fig.4) that the harmonic torques near their synchronous speeds are quite sharp and therefore as the induction motor passes through these speeds during the reversal, large amplitude and quite high frequency acceleration signals result. Since these signals must be recorded without appreciable attenuation, an ordinary low pass filter cannot be used effectively to reduce the commutator ripple noise. A filter is required which will discriminate between noise and signal even though their frequencies are (at low speeds) comparable in magnitude.

The circuit of Fig.6 has a transfer characteristic as shown in Fig.7 and is seen to present an infinite impedance when in resonance. The resonant frequency  $\omega_c$  is given by  $1/\sqrt{LC}$ . If the value of either L or C could be varied continuously  $\omega_c$  could be made to coincide with  $\omega_n$  at all rotor speeds and the commutator ripple would be continuously eliminated. Of the two elements in Fig.6 the capacitor is the easiest to vary but even then an air-cored continuously variable capacitor

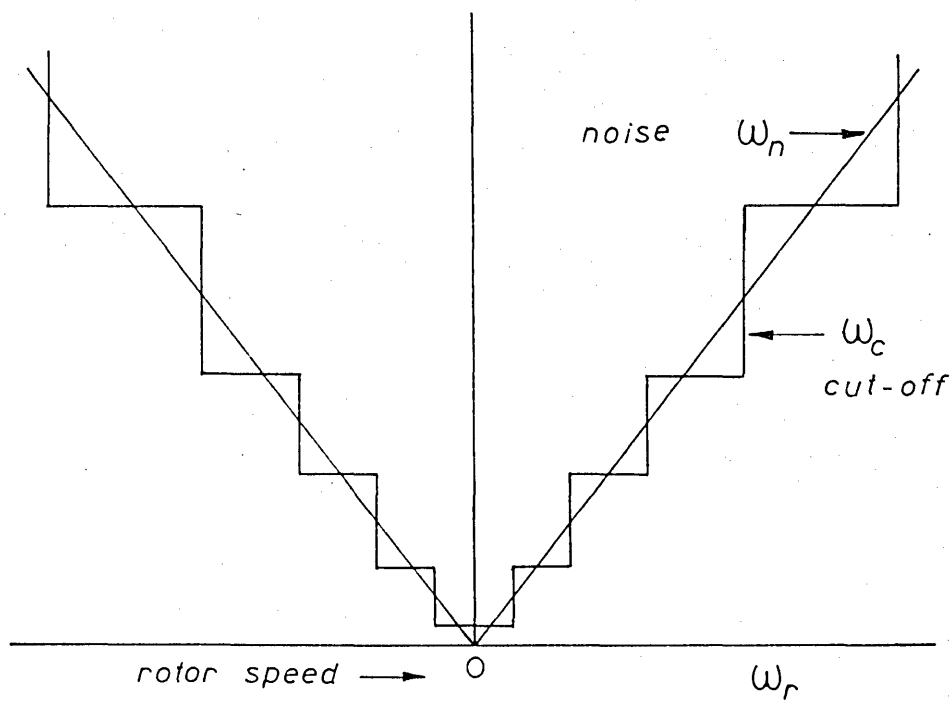


fig. 5. Switching characteristic of filter.

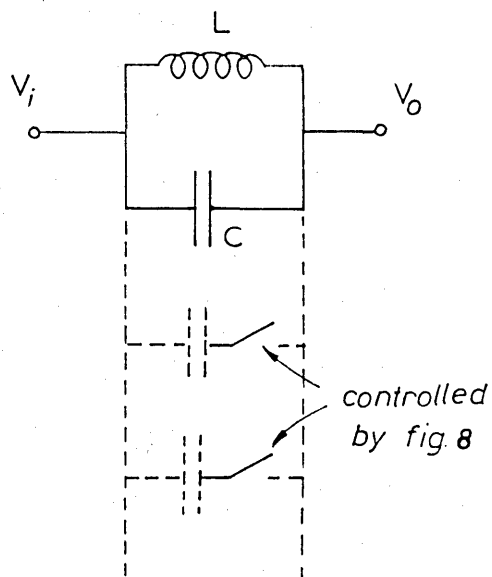


fig. 6. Variable parameter filter.

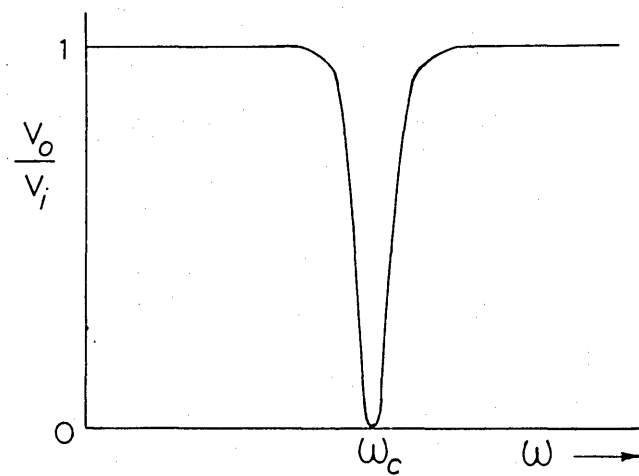


fig. 7. Frequency response of fig. 6 with constant C.



of large enough value is impracticable. The capacitor was therefore varied in steps by connecting other capacitors in parallel with it, (as shown dotted in Fig.6) in such a way so that  $\omega_c$  approximately follows the noise frequency  $\omega_n$  as the machine speed varies. The variation of  $\omega_c$  with speed is shown by the stepped curve in Fig.5.

The control of the switching in and out of the capacitors is performed by a single transistor, level-sensing circuit fed by a speed signal as shown in Fig.8. There is one such circuit corresponding to each capacitor switch.

A speed signal is obtained from an auxiliary and not necessarily ripple-free tachogenerator coupled to the induction motor. The rectifier shown converts the tacho output to a unidirectional signal independent of the direction of rotation of the induction machine. When  $V_s$  is large enough for the voltage  $V_b$  at the base of the transistor to just become positive the transistor conducts and the relay switches the corresponding capacitor in the filter circuit. The critical value of  $V_s$  at which the switching occurs is determined by the ratio  $R_1 : R_2$  and can be varied by varying  $R_1$ . Thus the values of  $R_1$  in the circuits controlling different capacitors are adjusted so that the switching occurs at the required instant.

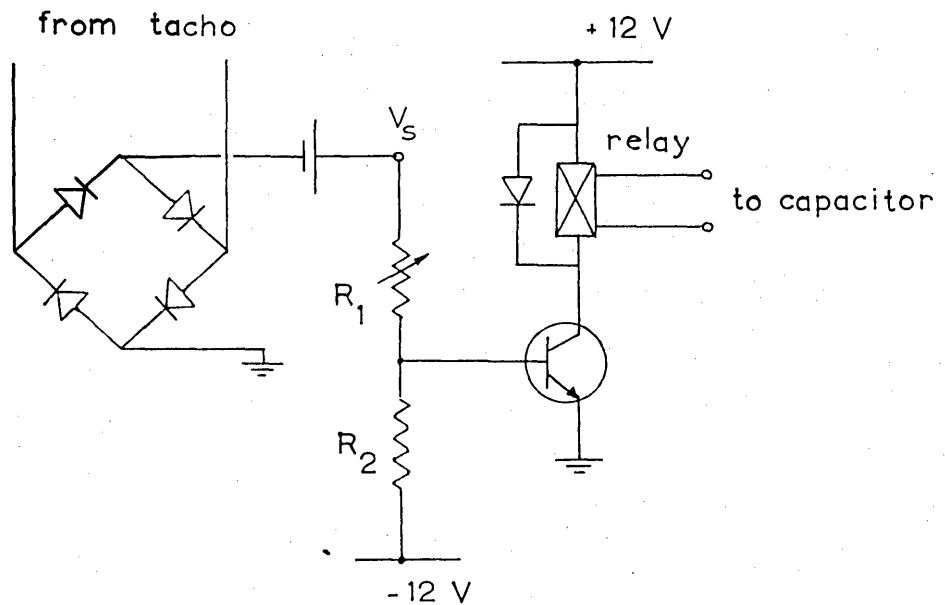


fig. 8. Circuit for control of the switching of capacitors in fig. 6.

There is one circuit for each capacitor and  $R_1$  is varied to give switching at the right instant.

It should be noted that when the signal  $V_s$  falls below its critical value the relay will switch the capacitor off again so that the circuits operate correctly during both the decelerating and accelerating periods of the speed reversal of the induction motor.

In the experimental equipment the capacitance was varied in 10 steps. With every switching of a capacitor a transient is associated which introduces a very sharp spike in the signal being filtered. When a capacitor is being switched out the spike is practically non-existent, but it becomes appreciable when a capacitor is being switched in. However these spikes are of very high frequencies and can easily be completely eliminated by an ordinary low-pass filter that follows the variable capacitance filter. The low-pass filter is shown in Fig.9 and its transfer function in Fig.10. It is seen from this last figure that the cut off frequency of the filter is high (about 100 c/s) and therefore it does not appreciably attenuate the signal the highest frequency of which is about 25 c/s - corresponding to a time of speed reversal of 2 seconds.

Once the signal from the tachogenerator has been filtered it can be differentiated quite easily by an ordinary differentiating circuit as shown in Fig.11 and then fed into the Y-axis of a recorder.

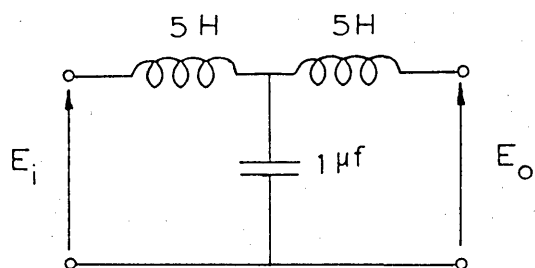


fig.9. Low-pass filter section

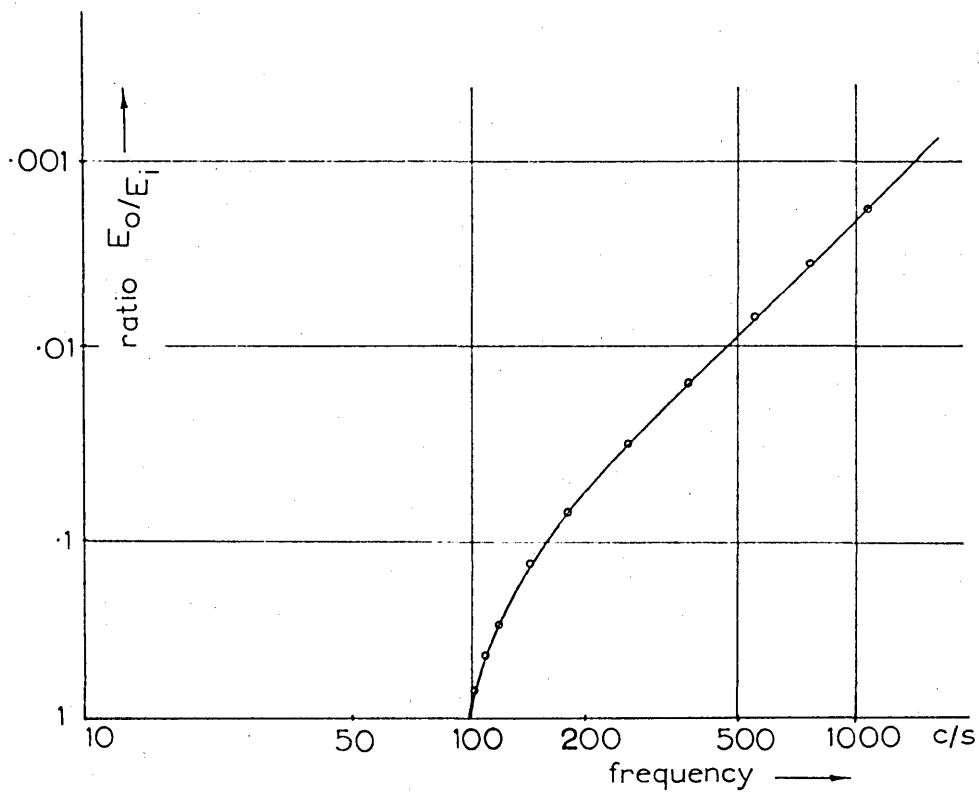


fig.10. Frequency response of filter in fig.9

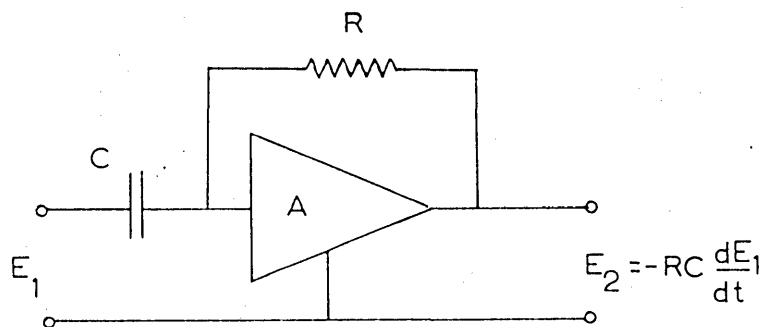


fig.11. Differentiating circuit

The complete circuit is shown in the block-diagram of Fig.12, and a typical plotter trace shown in Fig.13.

In order to establish the accuracy of the accelerometer, measurements made with a supply voltage of  $1/4$  rated voltage (100 v.), were compared with similar measurements taken by the swinging stator dynamometer (see Chapter 3). The torque-speed characteristic obtained by the accelerometer, after correcting for friction and windage, is shown in Fig.14, together with corresponding points measured by the dynamometer. Thus the accelerometer results are seen to be correct to  $\pm 2\%$ , an accuracy appreciably better than is usually associated with this method.

#### 4.2 Measurement of the fundamental torque.

In order to measure the effect of the load losses on the output torque, both measurements of the total and fundamental torques are necessary. The fundamental torque can be deduced from measurements of input power as explained in Section 3.2. Electronic multiplying and summing units were employed in order to obtain the instantaneous power flow to the induction machine during the speed reversal. From this power input the stator  $I^2R$  and iron losses were subtracted to give the air-gap power. This power plotted against speed is the fundamental speed-torque curve to a scale of  $1/\omega_s$  N-m/W.

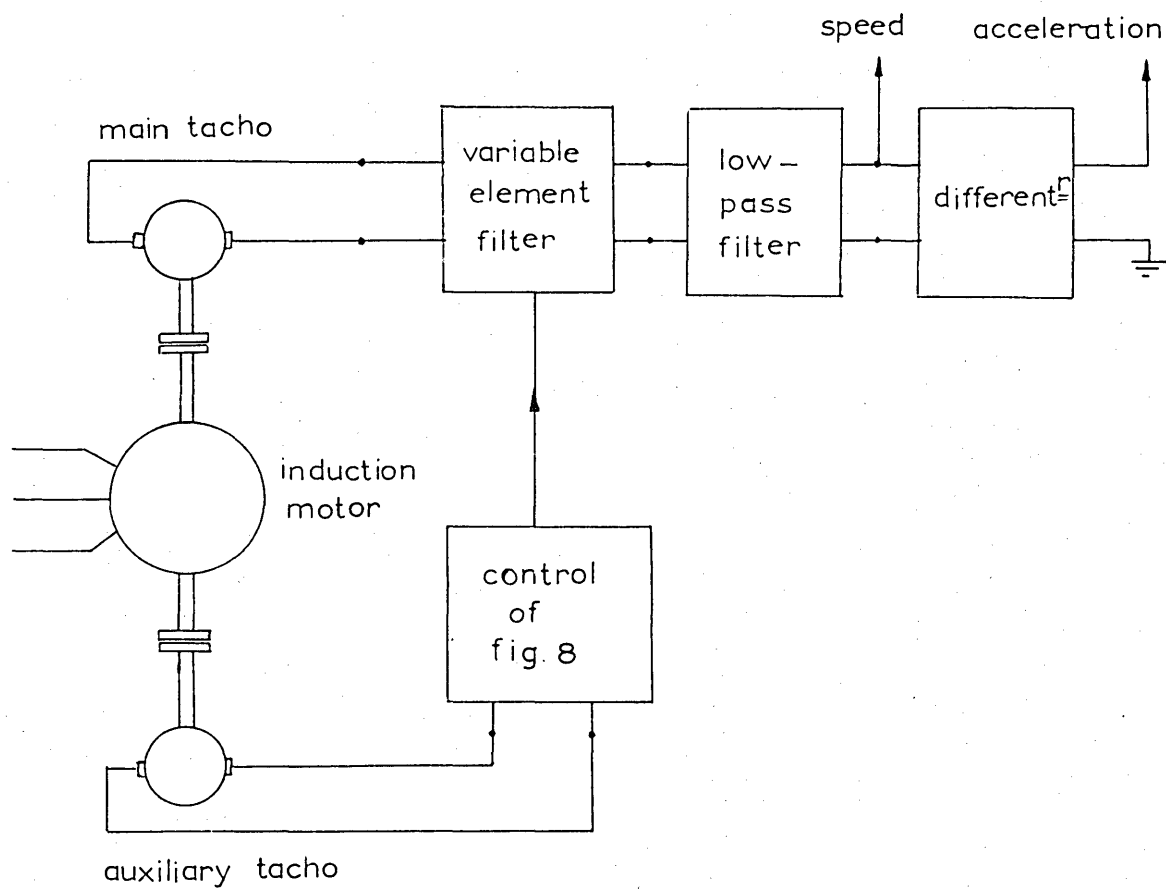
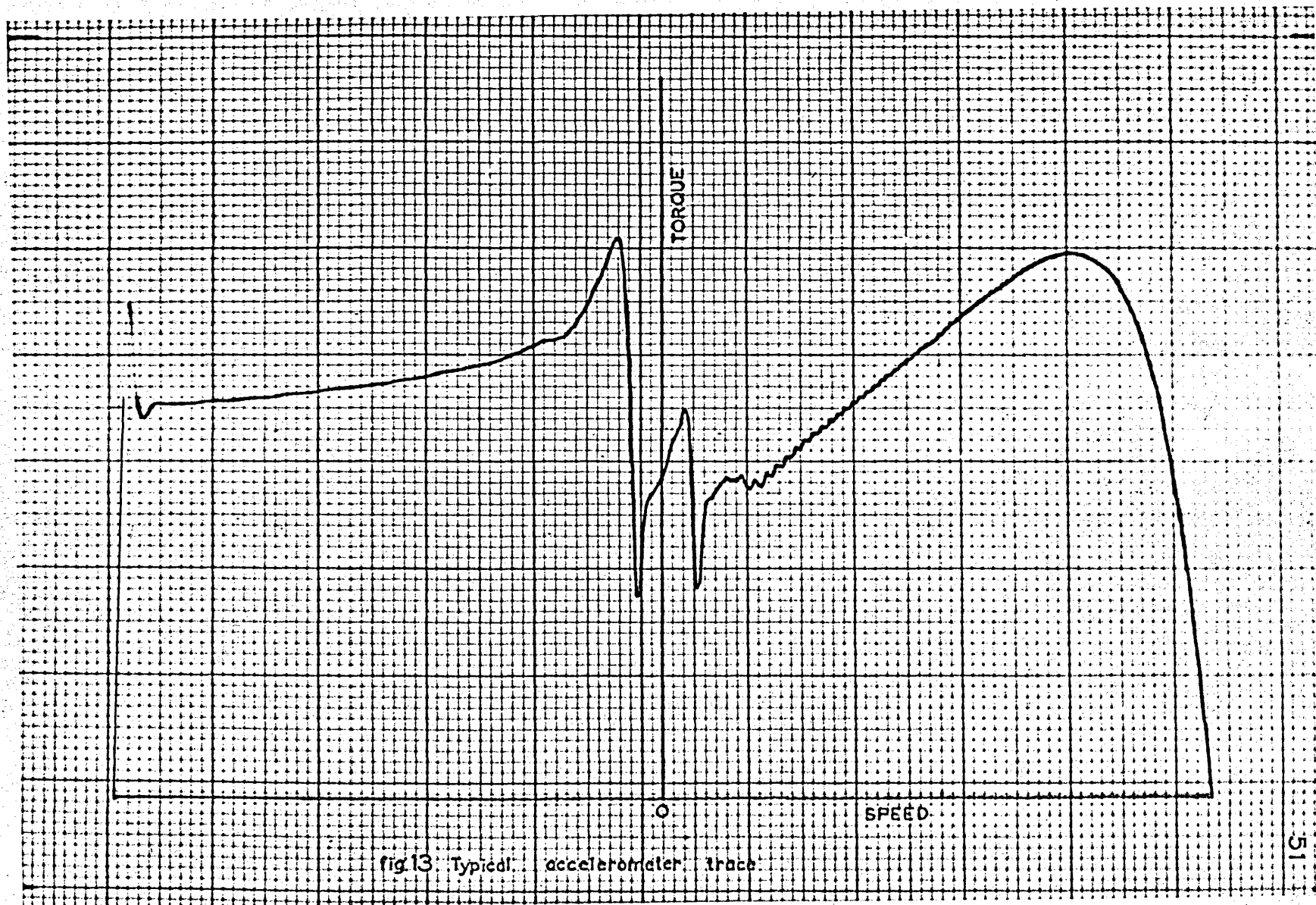


fig.12. Block diagram of accelerometer connections



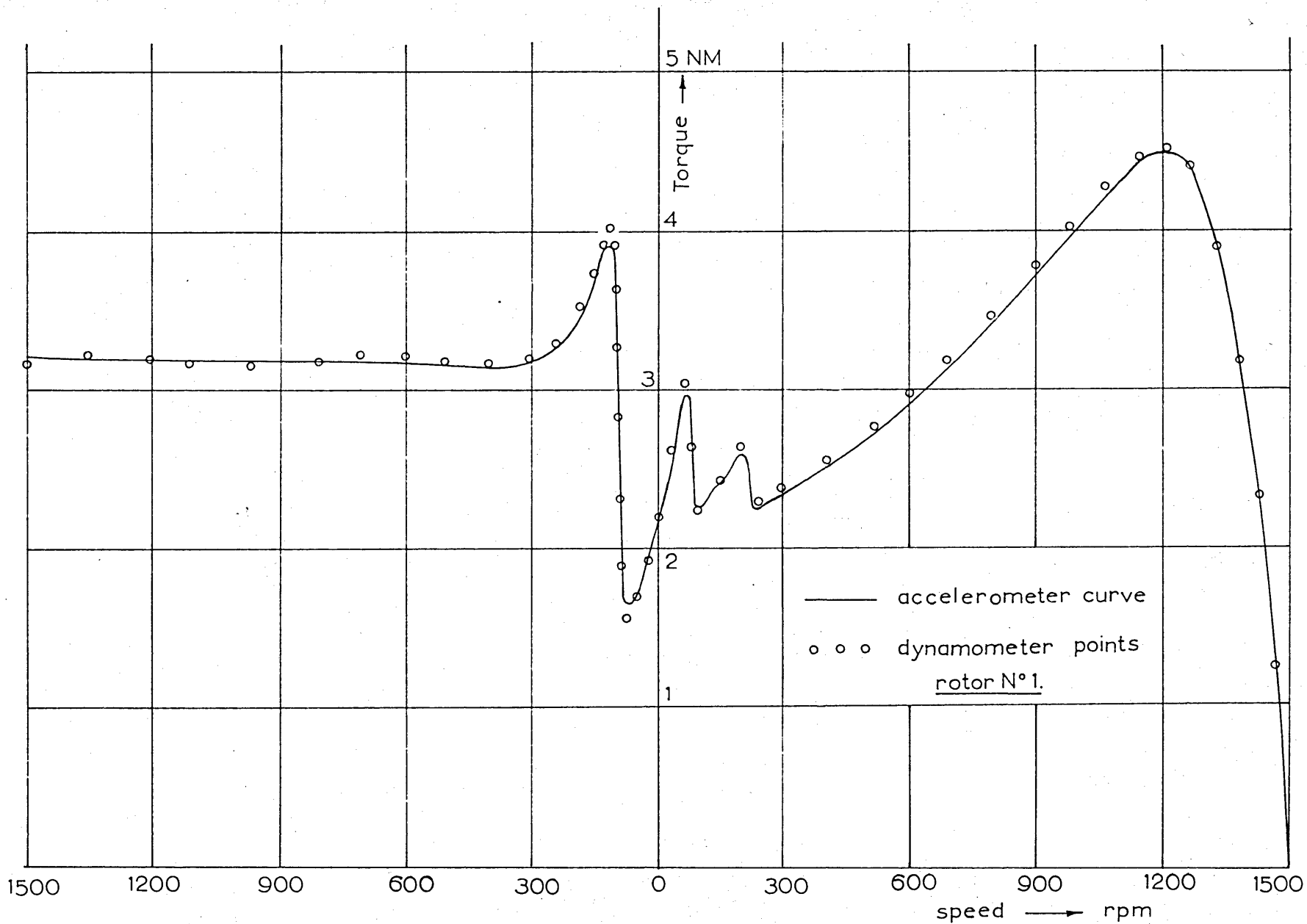


fig.14. Comparison of methods of torque measurement at 100v 50 c/s.



The arrangement of the apparatus is shown in Fig. 15. The stator core loss depends on the voltage  $(V - I_1 R_1)$  where  $V$  is the terminal voltage and  $I_1 R_1$  the voltage drop across the primary resistance. Thus as the machine reverses in speed,  $I_1$  is large and the voltage  $(V - I_1 R_1)$  is appreciably less than  $V$  with the result that the stator core loss is reduced below the value calculated by neglecting the  $I_1 R_1$  voltage drop. Although this reduction in the stator core loss can be properly simulated it requires more summing units, and the loss was therefore simulated by a properly proportioned constant quantity as shown in Fig. 15. This constant quantity is based on the mean voltage  $(V - \overline{I_1 R_1})$  where  $\overline{I_1 R_1}$  is the mean value of the stator resistance drop during the reversal. The error in the resultant fundamental speed-torque curve due to this approximation is small and the saving of electronic equipment considerable.

A typical plotter trace is shown in Fig. 16.

Again in order to establish the accuracy of the method, a comparison was made, at a reduced supply voltage, (100 v.), between power input measurements using wattmeters and the above method. The results are shown in Fig. 17 from which the accuracy over most of the speed range is seen to be within  $\pm 2.5\%$ .

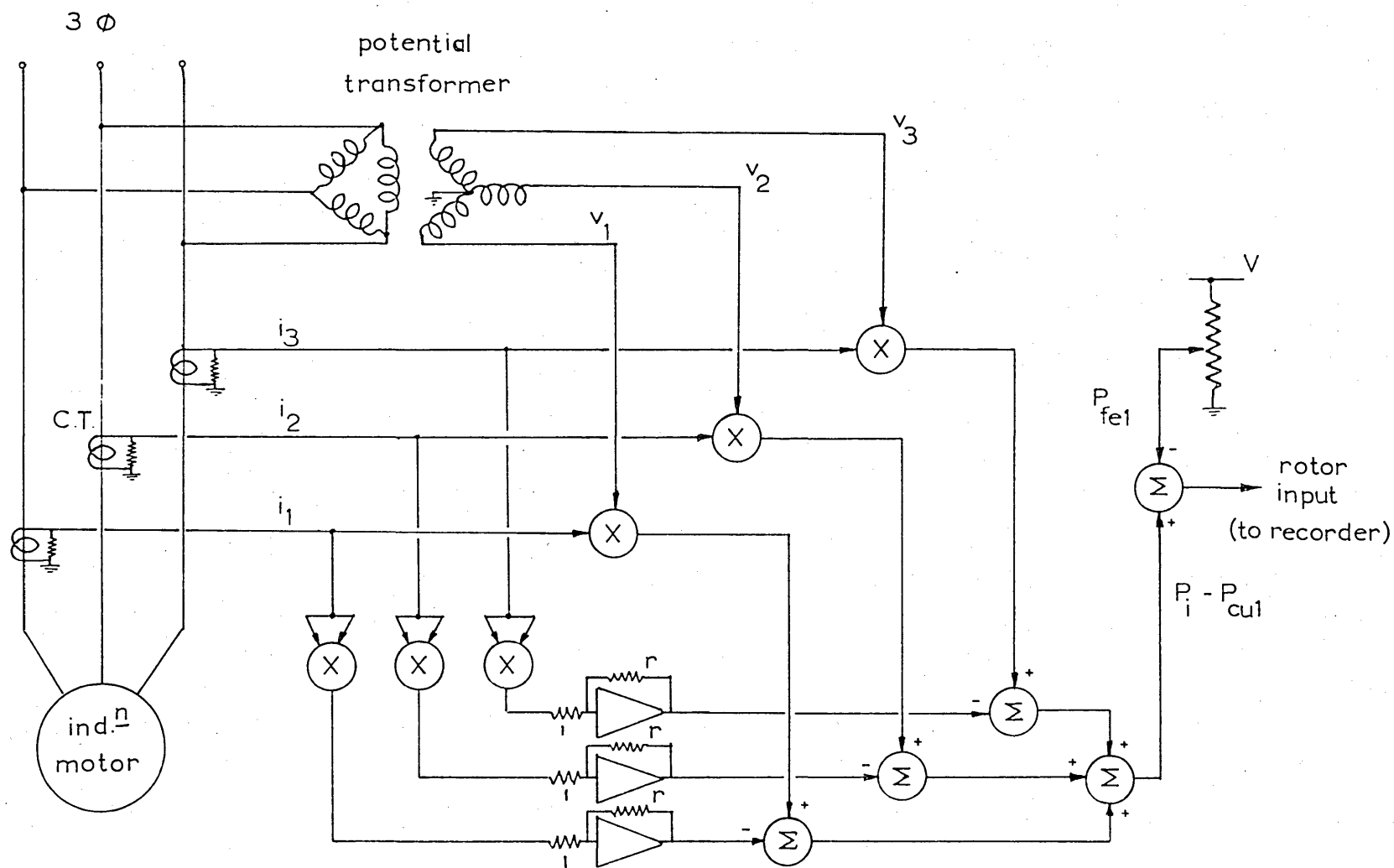


fig.15 Measurement of fundamental torque.

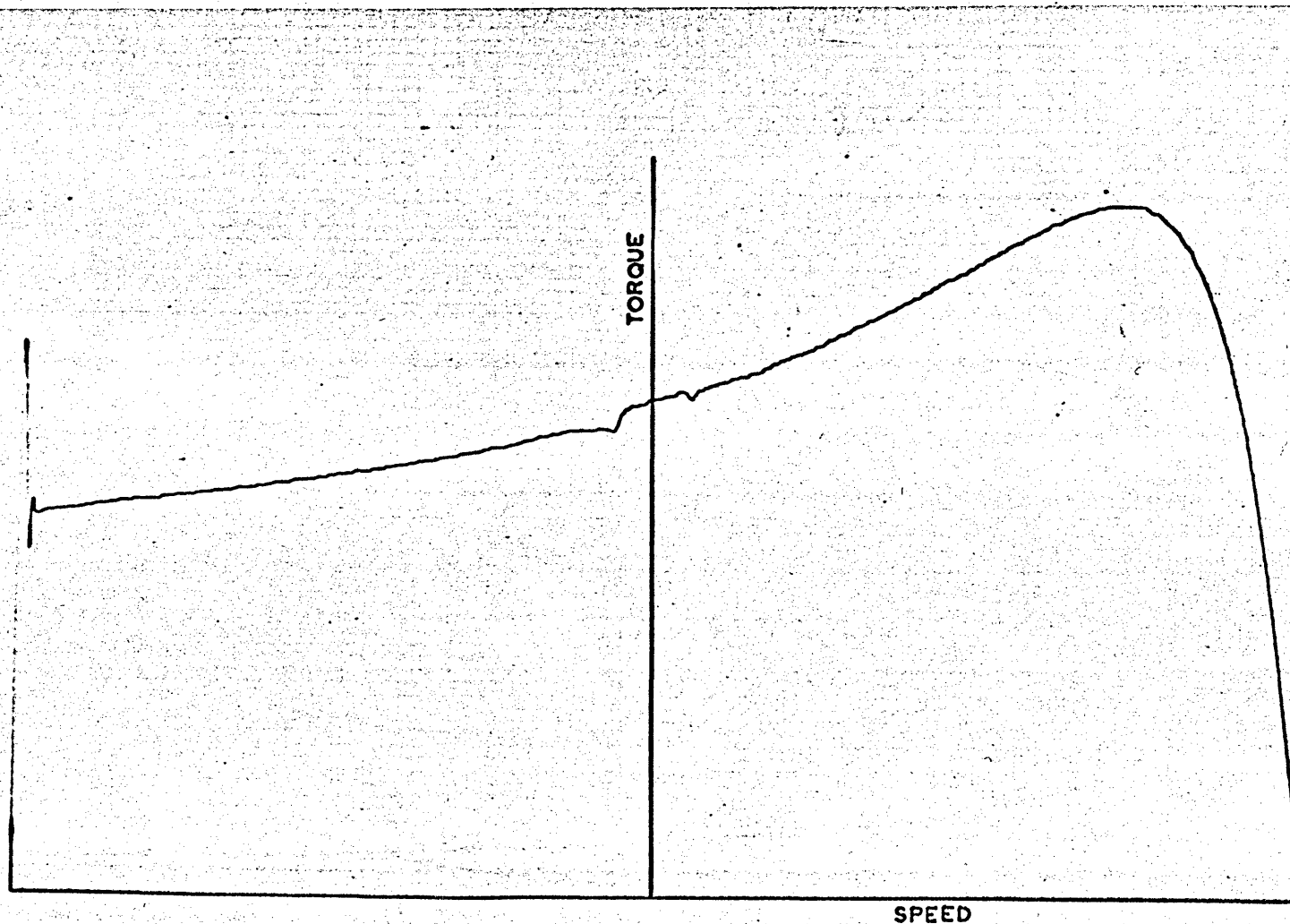


fig. 16 Typical input power trace

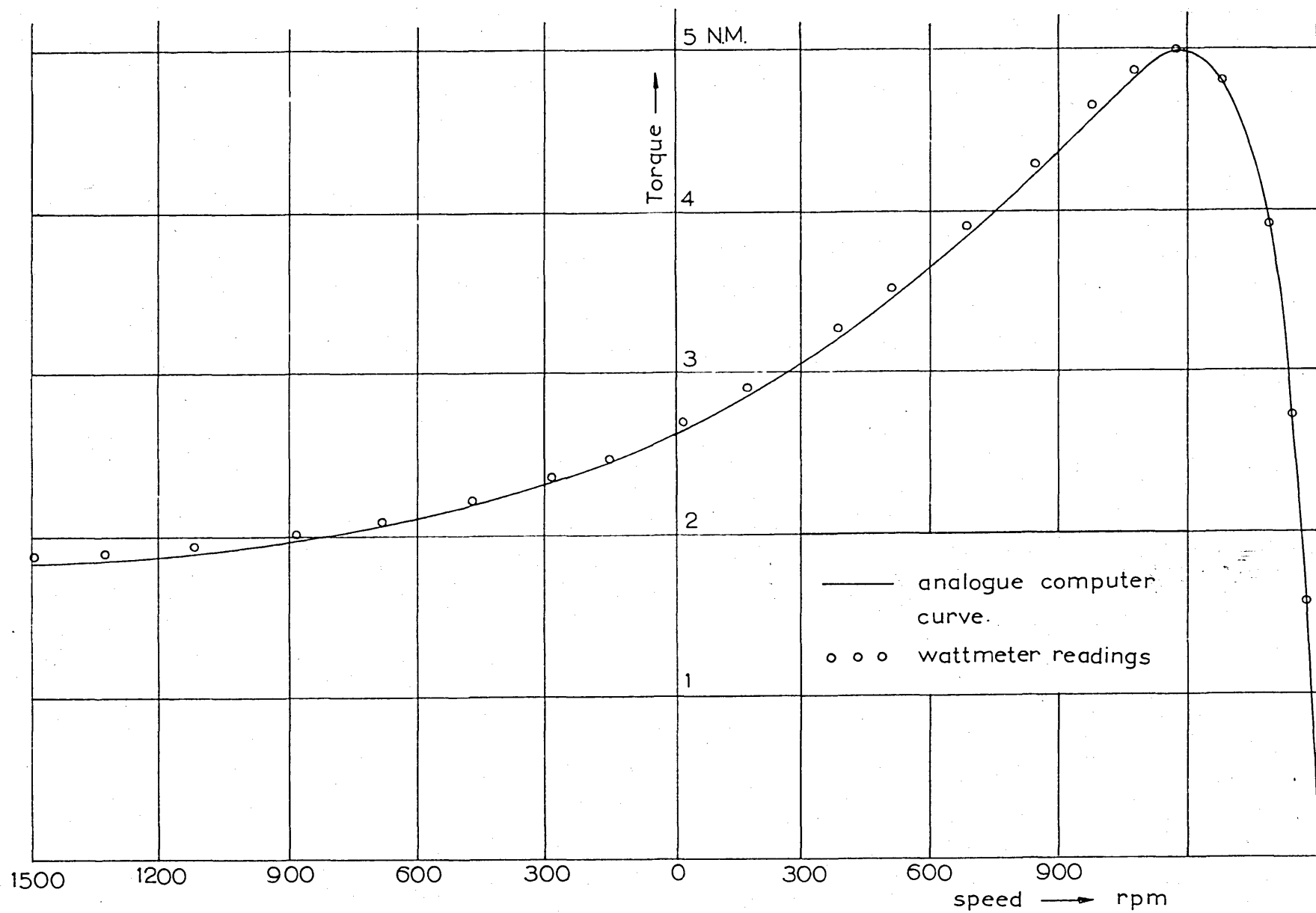


fig.17. Measurements of fundamental torque of rotor N°1 at 100v.50c/s. (Calibration of analogue computer)

## CHAPTER 5.

### MEASUREMENT OF LOAD LOSSES UNDER NORMAL LOAD.

The last two Chapters dealt with the measurement of the torque-slip characteristics of induction motors at any value of supply voltage. From the torque-speed curves the load losses can be measured as the difference between the fundamental and actual torques. This difference is appreciable at large values of fundamental slip, (due to the high currents that flow in the machine in these regions), but becomes very small and difficult to measure under the normal operating conditions. The back-to-back test described below (originally suggested by Dr. D.G.C.Morris) was developed to measure the load losses under the usual conditions of operation.

#### 5.1 The back-to-back test.

Direct current or synchronous machines can operate either as motors or as generators at exactly the same rotor speed. Two similar machines, belonging to one of the above two groups, can therefore have their shafts directly connected and be operated in a back-to-back arrangement where one machine is acting as a motor and the other as a generator. The net energy input to the system would then be the total loss in both machines, and can be measured directly and accurately.

Induction machines on the other hand must - if operated from a constant frequency supply - run at different speeds when generating than when motoring. Thus direct shaft connection between the machines is not possible.

Attempts have been made in the past to remove this restriction and the following methods of testing evolved.

(i) The supply to one induction machine is at a lower frequency than the second supply in which case the two machine shafts can be coupled directly.<sup>7</sup>

(ii) The two machines are supplied at the same frequency and the rotors are belted together using pulleys of different diameters.<sup>8,11</sup>

(iii) With the same supply to the two machines their shafts are connected together through a differential gear-box.<sup>9</sup>

(iv) The two induction motors are coupled to two d.c. machines and the load back is affected through these two machines. This test is associated with a separate back-to-back test of the d.c. machines.<sup>10</sup>

All the above tests introduce losses in auxiliary apparatus which cannot be accurately measured. The test described below introduces no such extraneous losses and provides for the first time an accurate method of determining induction motor losses.

In this test the two induction machines are coupled to two dynamometers that are loaded in a back-to-back arrangement as shown in Fig.18. The dynamometers are fixed on a stationary bedplate whilst the stators of the two induction motors are strapped together and are free to rotate on their own bearings. The mechanical arrangement of the test is shown in Fig.19.

One machine is driven at a speed of  $n_g$  rps, and the other runs at a speed of  $n_m$ ; where  $n_m < n_o < n_g$ . The first machine is then operating as a generator and the second one as a motor. The speeds  $n_m$  and  $n_g$  are adjusted (by varying the field supplies to the dynamometers) until the two stator frames have no tendency to rotate, which means that the torques in the two couplings are equal. If at this point of balance the electrical input to the two induction machines is  $P_{ac}$  then the total electrical loss of both machines is given by:

$$P_{t\ell} = P_{ac} + T \cdot 2\pi (n_g - n_m) \quad (5.1)$$

In Appendix I it is shown that the power input  $P_{ac}$  supplies the stator losses plus very nearly the whole of the load losses. The mechanical power input  $T \cdot 2\pi (n_g - n_m)$  supplies the fundamental rotor  $I^2R$  losses and a negligible part of the load loss. Thus the load

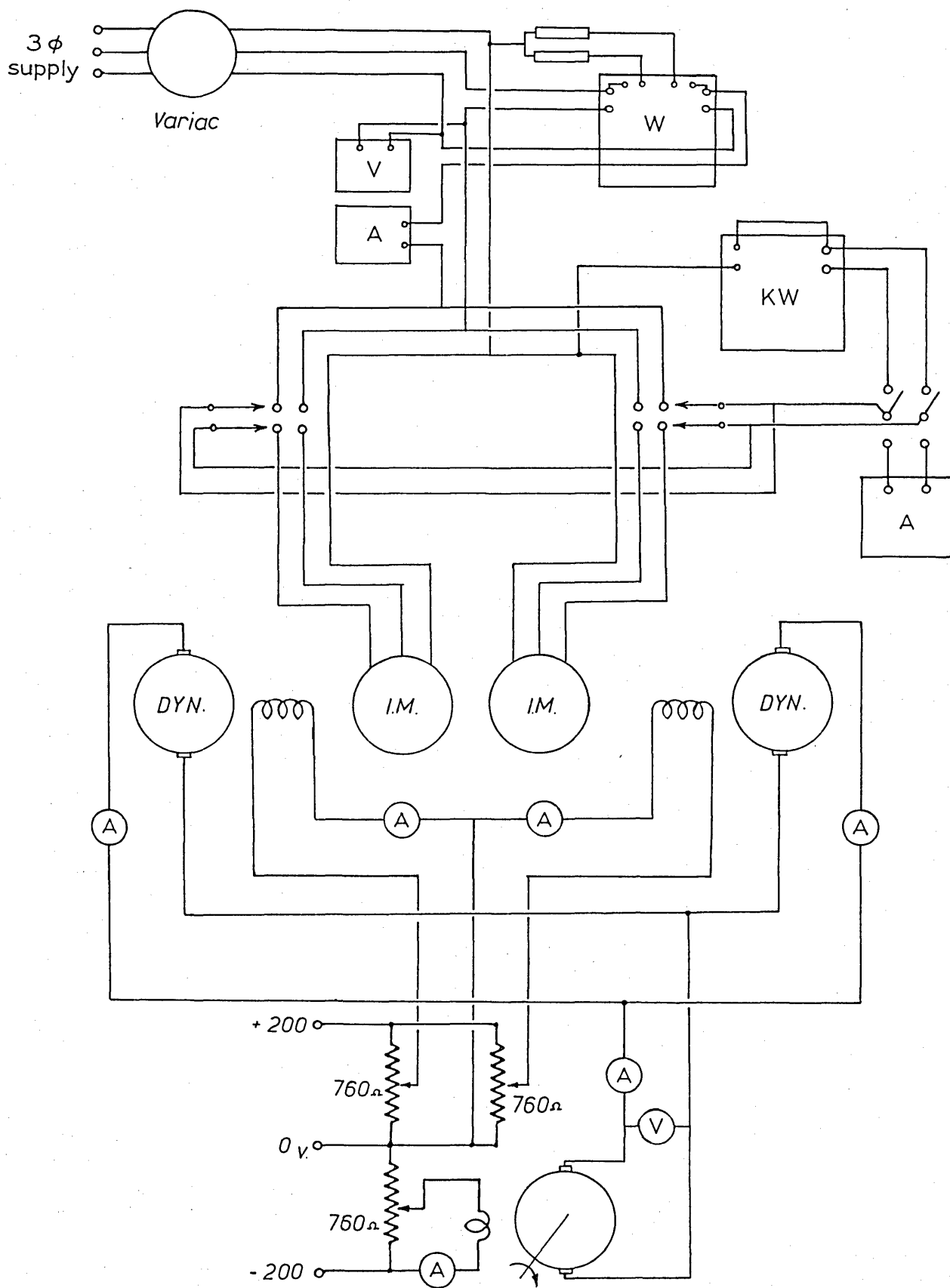


fig.18. Electrical connections of back-to-back test.



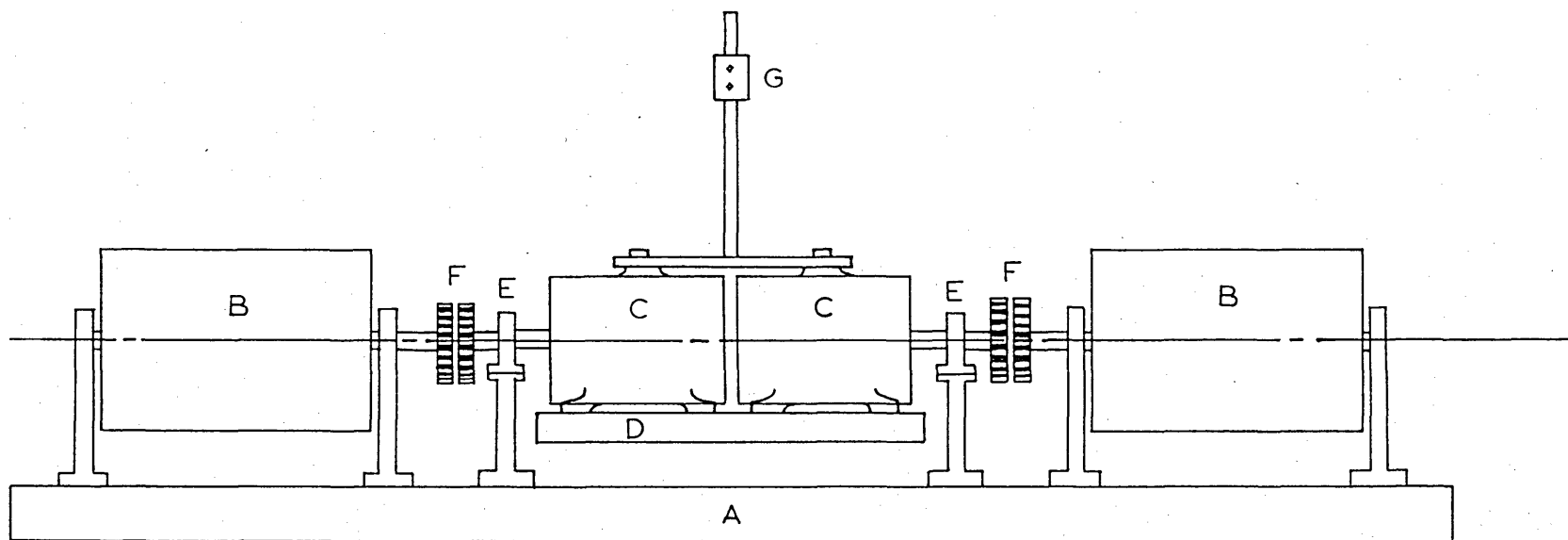


fig.19. Mechanical arrangement of back-to-back test.

- A fixed bedplate.
- B dynamometers.
- C induction machines.
- D floating bedplate.
- E extra support bearings.
- F couplings with lines for digital speed measurement.
- G counter-weight.

losses can be determined to a sufficiently high degree of accuracy as:

$$P_{ll} = P_{ac} - (P_{fe1} + 3I_1^2 R_1) \quad (5.2)$$

The measurement of the rotor  $I^2R$  loss is usually the least reliable and most inaccurate of the "conventional" loss measurements. It is therefore an important advantage of this test that the rotor fundamental loss does not enter into the determination of the load losses as calculated from Eqn. (5.2).

## 5.2 Experimental procedure.

The value of the load losses measured in the back-to-back test is the sum of the load losses of the two machines. If the two machines are identical their load losses under the same loading conditions can be assumed to be the same. Rotors Nos. 1(a), 1(b), and 1(c) in Table 2 (Chapter 2) are nominally identical. Their true identity was established by measuring their torque-slip characteristics by the methods of Chapters 3 and 4. The identity of two machines can also be checked - to some extent - by the back-to-back test itself, by reversing their operation so that the motor becomes a generator and vice versa; if the machines are the same, the power flow should remain unchanged.

Having established the identity between these rotors the total load loss measured in the back-to-back test, can be split up into the individual loss losses in the ratio:

$$\frac{P_{llm}}{P_{llg}} = \left[ \frac{I_m}{I_g} \right]^2 \cdot \left[ \frac{N_m}{N_g} \right]^{1.6} \quad 5.3(a)$$

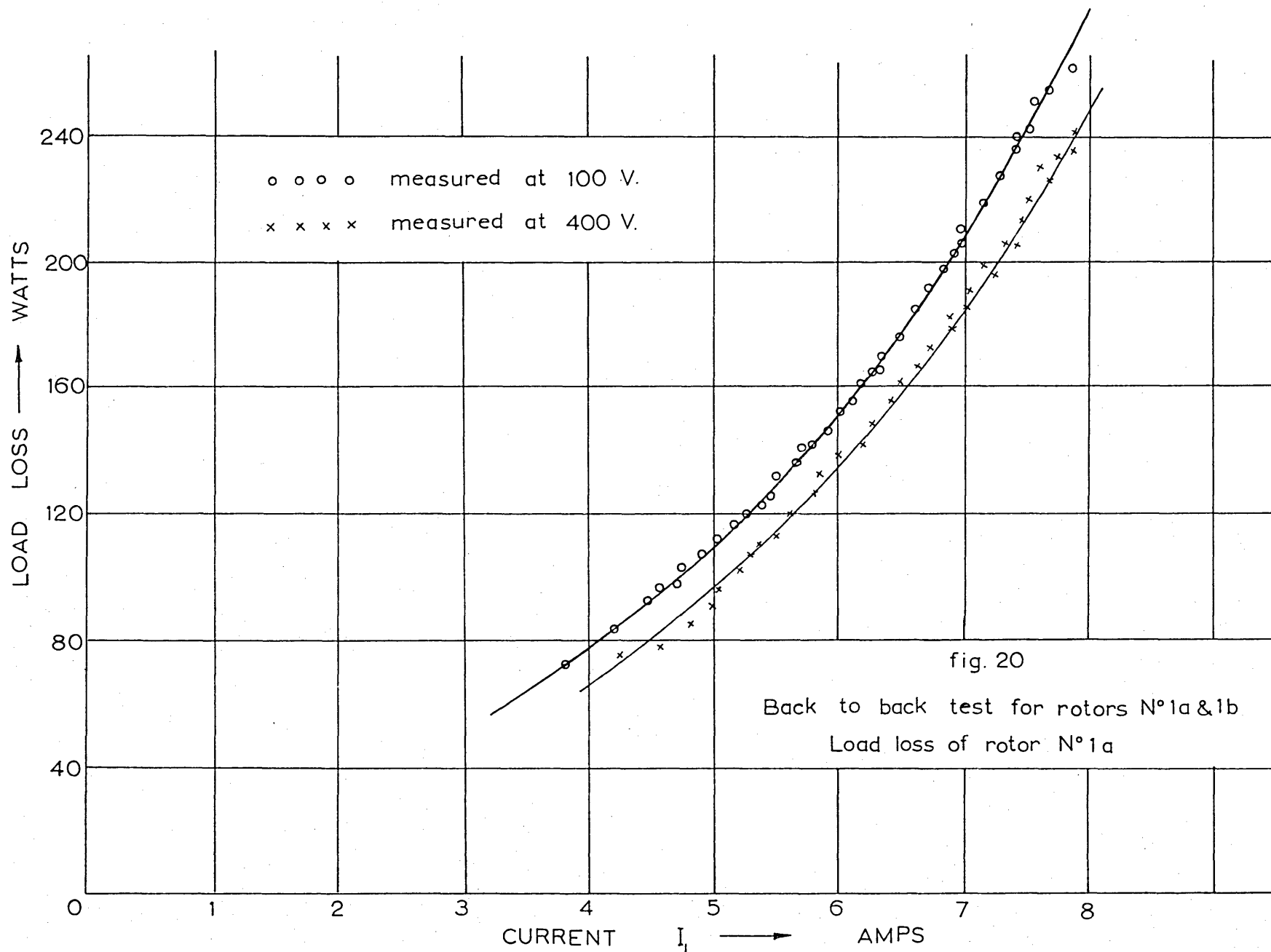
$$= \left[ \frac{I_m}{I_g} \right]^2 \cdot \left[ \frac{1-s_m}{1+s_g} \right]^{1.6} \quad 5.3(b)$$

It is explained in the Introduction that the load losses depend both on the value of  $I_1$  and  $I_2$ . It is shown in the next Chapter however that the dependence on  $I_1$  is much larger than that on  $I_2$  and hence the currents  $I_m$  and  $I_g$  in Eqn. 5.3(a) can be taken to be the stator currents in the motor and generator respectively. The quadratic variation of load losses with current is derived theoretically in the next Chapter. It is also shown in that Chapter that the variation with speed is extremely complex but numerical computations show that it can be satisfactorily approximated by a 1.6 power law.<sup>12</sup> Other investigators<sup>13,9</sup> have also found experimentally that the index of variation of load losses with frequency lies between 1.5 and 2. In any case since the slips  $s_m$  and  $s_g$  are both small compared with unity the ratio  $(1 - s_m)/(1 + s_g)$  in Eqn. 5.3 (b)

is near unity and a small error in the 1.6 power index only causes a very small error in the division of the load losses between the two machines.

By testing rotors Nos. 1(a) and 1(b) against each other in the back-to-back arrangement the load losses of these rotors were precisely measured at all conditions of current, voltage, and speed loading. Rotor No.1(a) was then used as a standard against which all other rotors were tested.

Fig.20 shows the variation of load losses with current  $I_1$  for rotor No. 1(a). The results obtained for this and all other rotors are compared with each other and with the theoretical predictions of load losses in Chapter 8.



P A R T   T W O

THEORETICAL ANALYSIS OF LOAD LOSSES

## CHAPTER 6.

### THEORETICAL ANALYSIS OF LOAD LOSSES

#### 6.1 Analysis of the air gap fields.

This Section deals with the general nature of the fields that exist in the air gap of an induction machine. It considers both the harmonic flux density fields of the stator and the harmonic and subharmonic fields of the rotor, as produced by the interaction of the mmf and permeance harmonics. It gives a physical picture of the mechanism by which torques, (both synchronous and asynchronous), are produced and is an essential preliminary to a better understanding of the more specific analyses that follow in later Sections.

##### 6.1.1 Air gap fields due to the stator harmonics.

It is shown in Appendix II that the stepped mmf distribution (Fig.21) produced by a three phase double-layer lap winding can be analysed by Fourier series into a series of rotating harmonic waves, the  $v^{\text{th}}$  one being given by:

$$f_{1v} = \bar{F}_{1v} \cos \left( \omega t - \frac{v\pi x_1}{Y} + \theta_v \right) \quad (6.1)$$

where  $\bar{F}_{1v}$  is its complex amplitude given as:<sup>3</sup>

$$\bar{F}_{1v} = \frac{3\sqrt{2}}{\pi} \frac{E_1}{2p} \cdot \left( \frac{k_{dpv}}{v} \right) \cdot \bar{I}_1 \cdot \bar{D}_v \quad (6.2)$$

and  $\theta_v$  is given by Ecn. II.8 in Appendix II.

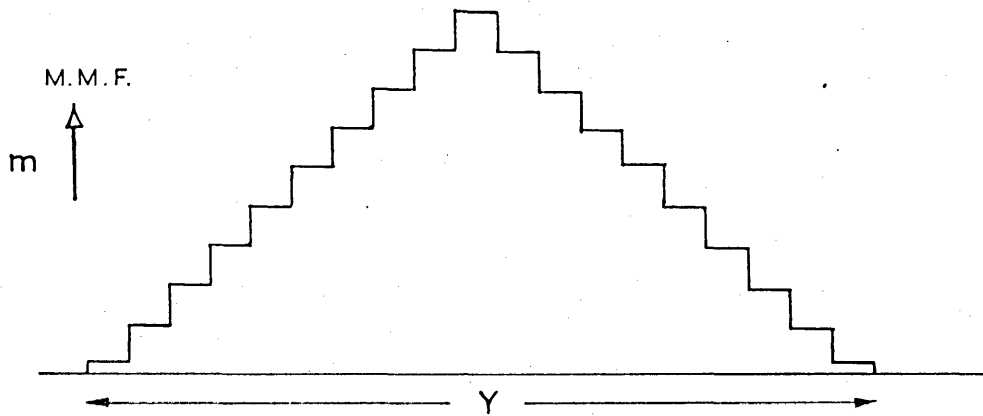


fig.21. Stepped mmf. distribution due to currents in a three phase winding.

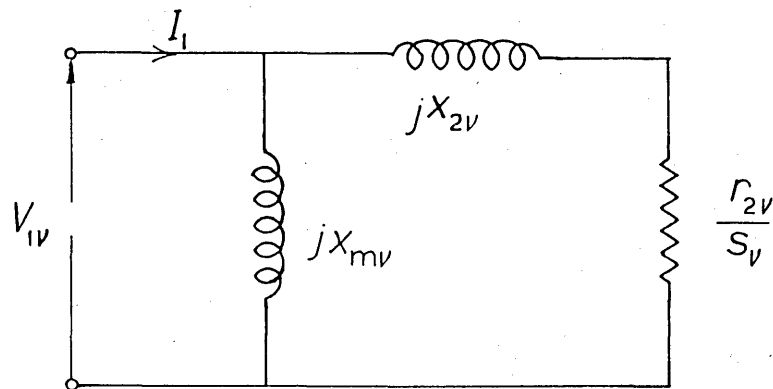


fig.22. Equivalent circuit of  $\nu^{\text{th}}$  stator field harmonic.



The origin is taken to be the centre of a stator slot.

If the actual air gap length is  $g$  then the air gap permeance can be written as:

$$\Lambda = \Lambda_o \left\{ 1 - \gamma_1' \cos \frac{\pi S_1}{pY} x_1 - \gamma_2' \cos \frac{2\pi S_1}{pY} x_1 - \dots \right\} \times$$

$$\times \left[ 1 - \gamma_1'' \cos \frac{\pi S_2}{pY} x_2 - \gamma_2'' \cos \frac{2\pi S_2}{pY} x_2 - \dots \right] \quad (6.3)$$

where the stator and rotor coordinates  $x_1$  and  $x_2$  are shown in Fig.23.

The average permeance  $\Lambda_o$  is equal to  $(\mu_o / g k_{c1} k_{c2})$ . The pulsations  $\gamma_1'$ ,  $\gamma_2'$  etc., in the curly brackets, are due to the stator slot openings; and the pulsations  $\gamma_1''$ ,  $\gamma_2''$  etc., in the square brackets are due to the rotor slot openings. These coefficients are given by Freeman.<sup>15</sup>

Transforming the rotor coordinate  $x_2$  to the stator side, Eqn. 6.3 can be re-written as:

$$\Lambda = \Lambda_o \left[ 1 - \sum_{c=1,2,\dots} \gamma_c' \cos \frac{c\pi S_1}{pY} x_1 - \sum_{d=1,2,\dots} \gamma_d'' \cos \frac{d\pi S_2}{pY} (x_1 - \omega_r R t) \right.$$

$$\left. + \sum_{c=1,2,\dots} \sum_{d=1,2,\dots} \gamma_c' \cdot \gamma_d'' \cos \left( \frac{c\pi S_1}{pY} x_1 \right) \cos \frac{d\pi S_2}{pY} (x_1 - \omega_r R t) \right] \quad (6.4)$$

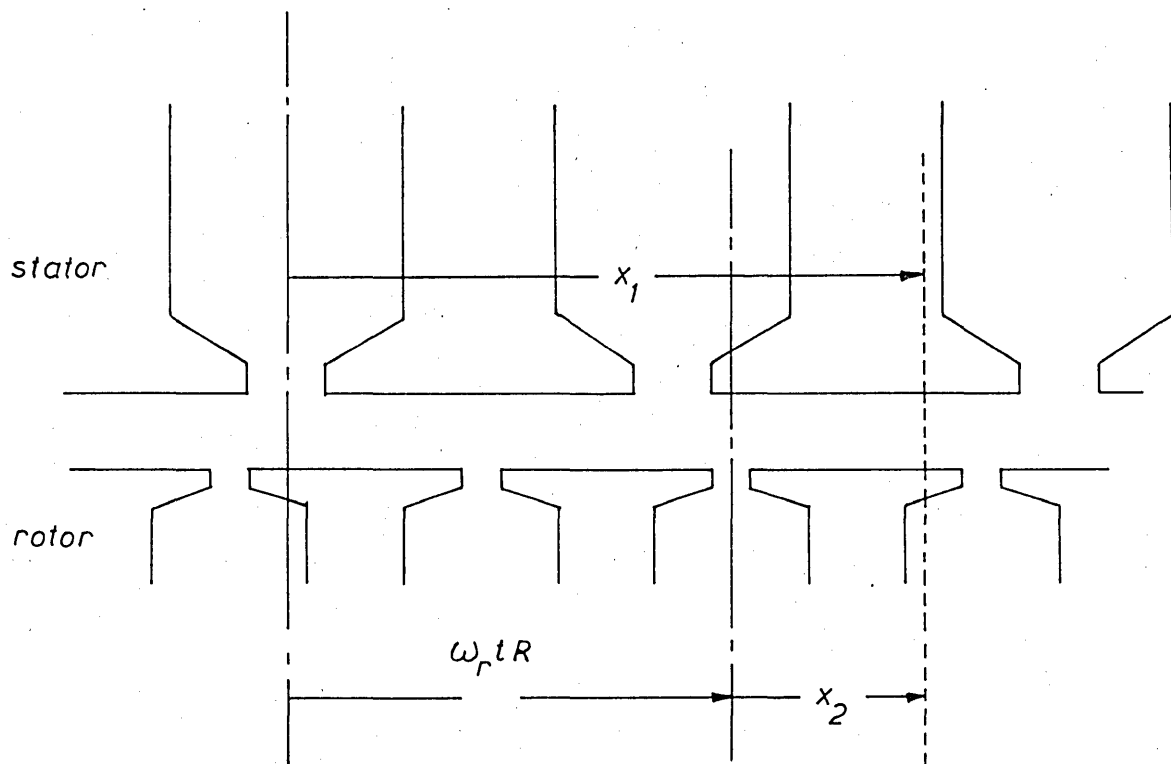


fig.23. Stator and rotor coordinates.

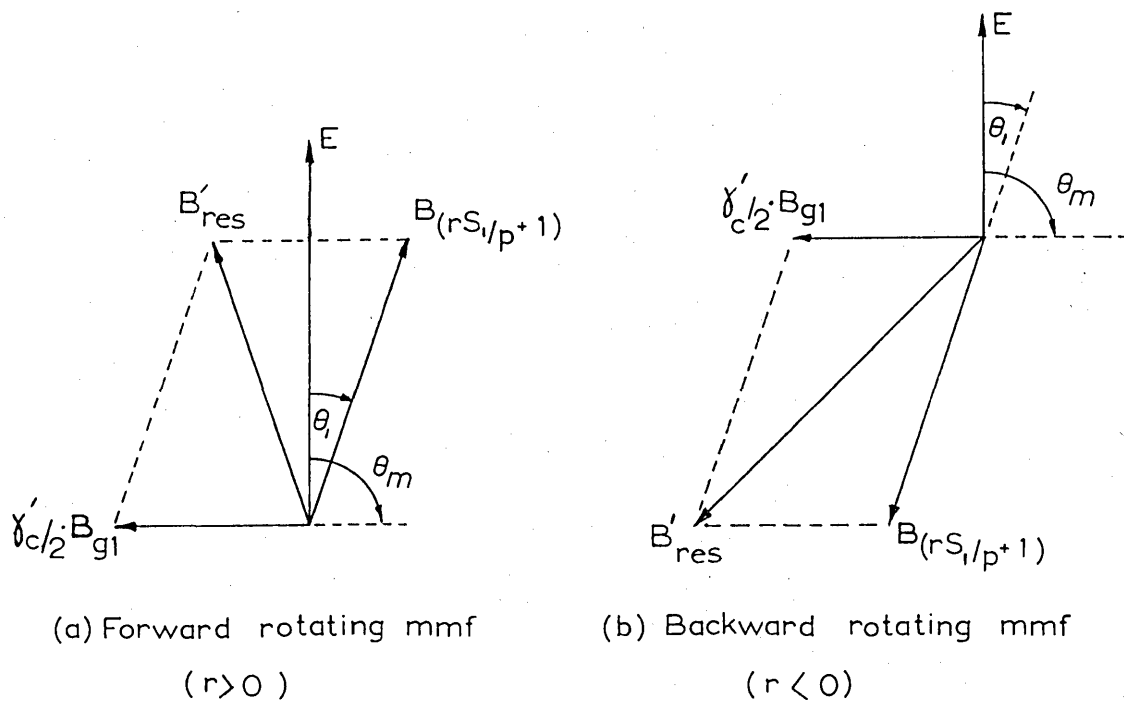


fig.24. Addition of slot harmonic fields due to permeance and mmf.

The last term of Eqn. 6.4 can be neglected as it involves the products  $\gamma_c' \gamma_d''$  which are very small second order quantities.

The air gap flux density fields due to the stator  $v^{\text{th}}$  harmonic is therefore given by multiplying together Eqns. 6.1 and 6.4 as:

$$b_{1v} = f_{1v} \cdot A \quad (6.5)$$

It can be shown<sup>3</sup>, by considering the symmetry of the winding distribution, that  $v$  cannot take any value but is limited to the values given by:

$$v = 6k_1 + 1 \quad (6.6)$$

where  $k_1$  is a positive or negative integer including zero. A negative value of  $v$  indicates that the harmonic rotates in a direction opposite to that of the fundamental.

Considering the fundamental mmf wave ( $v=1$ ) Eqn. 6.5 gives the corresponding flux density field as:

$$\begin{aligned} b_1 = & \bar{B}_{g1} \left[ \cos \left( \omega t - \frac{\pi x_1}{Y} + \theta_1 \right) - \right. \\ & - \sum_{c=\pm 1, \pm 2, \dots} \frac{\gamma_c'}{2} \cos \left\{ \omega t - \frac{\pi x_1}{Y} \left( \frac{cS_1}{p} + 1 \right) + \theta_1 \right\} \\ & - \sum_{d=\pm 1, \pm 2, \dots} \frac{\gamma_d''}{2} \cos \left\{ \left[ 1 + (1-s) \frac{dS_2}{p} \right] \omega t \right. \\ & \left. \left. - \frac{\pi x_1}{Y} \left( \frac{dS_2}{p} + 1 \right) + \theta_1 \right\} \right] \quad (6.7) \end{aligned}$$

where  $\bar{B}_{g1}$  is given by:

$$\bar{B}_{g1} = \frac{3\mu_0\sqrt{2} Z_1 k_{dp1}}{2\pi g k_{c1} k_{c2p}} \cdot \bar{I}_1 \cdot \bar{D}_1 \quad (6.8)$$

In the following Sections it is shown that by far the most important stator mmf harmonics are the slot harmonics of order  $v = r \frac{S_1}{p} + 1$ , where  $r$  is any positive or negative integer. It is also shown in Appendix II that for these slot harmonics the angle

$$\theta_v = \theta_{\left(r \frac{S_1}{p} + 1\right)} = \theta_1 + 2n\pi \quad \text{where } n \text{ is any integer.}$$

Thus from Eqns. 6.1, 6.4 and 6.5 the flux density fields corresponding to the stator slot harmonic mmf waves are given by:

$$\begin{aligned} b_{\left(r \frac{S_1}{p} + 1\right)} &= \bar{B}_{\left(r \frac{S_1}{p} + 1\right)} \cdot \left[ \cos \left\{ \omega t - \left( r \frac{S_1}{p} + 1 \right) \frac{\pi x_1}{Y} + \theta_1 \right\} \right. \\ &\quad - \sum_{c=+1, -2, \dots} \frac{Y'_c}{2} \cos \left\{ \omega t - \left[ (r-c) \frac{S_1}{p} + 1 \right] \frac{\pi x_1}{Y} + \theta_1 \right\} \\ &\quad \left. - \sum_{d=1, 2, \dots} \gamma_d'' \cos \left\{ \omega t - \left( r \frac{S_1}{p} + 1 \right) \frac{\pi x_1}{Y} + \theta_1 \right\} \cdot \cos \frac{d\pi S_2}{pY} (x_1 - \omega_r R t) \right] \end{aligned} \quad (6.9)$$

where  $\bar{B}_{\left(r \frac{S_1}{p} + 1\right)}$  is given by:

$$\bar{B}_{\left(\frac{S_1}{p}+1\right)} = \frac{3\mu_0\sqrt{2} Z_1 k_{dp1}}{2\pi g k_{c1} k_{c2} \left(\frac{S_1}{p}+1\right)} \cdot \bar{I}_1 \bar{D}_{\left(\frac{S_1}{p}+1\right)} \quad (6.10)$$

Comparing Eqns. 6.7 and 6.9 it is seen that when the values of  $c$  and  $r$  coincide, the second term of Eqn. 6.7 and the first term of Eqn. 6.9 represent waves which are of the same order, rotate at the same speed, and are therefore stationary with respect to each other. These two waves should therefore be considered together as one resultant field having the complex amplitude:

$$\left[ \bar{B}'_{res} \right]_{slot} = \bar{B}_{\left(\frac{S_1}{p}+1\right)} - \bar{B}_{g1} \cdot \frac{\gamma'_c}{2} \quad (6.11)$$

The factor  $\bar{D}_1$  in Eqn. 6.8 represents the damping of the stator fundamental mmf due to the rotor currents and is therefore given by:<sup>3</sup>

$$\bar{D}_1 = \frac{\bar{I}_m}{\bar{I}_1} \quad (6.12)$$

The damping factor  $\bar{D}_{\left(\frac{S_1}{p}+1\right)}$  by which the stator  $\left(\frac{S_1}{p}+1\right)^{st}$  mmf harmonic is reduced by the corresponding frequency rotor currents is similarly given by:

$$\bar{D}_{\left(\frac{S_1}{p}+1\right)} = \frac{\bar{I}_m \left(\frac{S_1}{p}+1\right)}{\bar{I}_1} \quad (6.13)$$

Since for the slot harmonics the harmonic leakage reactance is much larger than the harmonic magnetising reactance, (see Chapter 7 ), the harmonic magnetizing current is very nearly the same as the total current  $I_1$  and hence:

$$\bar{D}_{\left(\frac{S_1}{p}+1\right)} \approx 1 \quad (6.14)$$

Introducing the damping factors from Eqns. (6.12) and (6.14) into Eqns. (6.8), (6.10) and (6.11) (taking the fundamental air gap voltage  $\bar{E}$  as the reference phasor), this last equation may be re-written as:

$$\left[ \bar{B}'_{res} \right]_{slot} = B_{\left(\frac{S_1}{p}+1\right)} \cdot e^{j\theta_1} \cdot B_{g1} \cdot \frac{\gamma'_c}{2} \cdot e^{j\theta_m} \quad (6.15)$$

where  $\theta_1$  and  $\theta_m$  are the phase angles of  $I_1$  and  $I_m$  and  $B_{\left(\frac{S_1}{p}+1\right)}$  and  $B_{g1}$  are the magnitudes of the corresponding space phasors.

Figs. 24(a) and 24(b) show the geometrical representation of Eqn. 6.15. It is seen that the backward rotating mmf slot harmonics ( $r$  negative) add with the permeance slot harmonics to give a resultant:

$$\left[ B'_{res} \right]_{slot} = \sqrt{B_{g1}^2 \frac{S_1}{(r_p+1)} + \left( B_{g1} \frac{\gamma'_c}{2} \right)^2} \cdot \sqrt{1 + \frac{2\sin\theta_1}{\alpha' + 1/\alpha'}} \quad (6.16)$$

where  $\alpha'$  is the ratio

$$\frac{B_{g1} \frac{S_1}{(r_p+1)}}{B_{g1} \frac{\gamma'_c}{2}} = \frac{2}{\gamma'_c \frac{S_1}{(r_p+1)}} \cdot \frac{I_1}{I_m} \quad (6.16)(a)$$

Thus the losses caused by the resultant field and which are shown in the later Sections to depend on  $B_{res}^2$  are greater than the sum of the individual losses of the mmf and permeance slot harmonics by the factor:

$$\zeta(r < 0) = 1 + \frac{2\sin\theta_1}{\alpha' + 1/\alpha'} \quad (6.17)$$

Similarly (Fig.24 (a)) the forward rotating mmf slot harmonics ( $r$  positive) add with the permeance slot harmonics to give a resultant field whose losses are less than the sum of the individual losses of the harmonics by the factor:

$$\zeta(r > 0) = 1 - \frac{2\sin\theta_1}{\alpha' + 1/\alpha'} \quad (6.18)$$

It is seen therefore that the presence of the slot openings increases the losses due to the backward rota-

ting fields (by the factor  $\zeta_{(r < 0)}$ ) and decreases the losses due to the forward rotating fields (by the factor  $\zeta_{(r > 0)}$ ). However, since the backward rotating fields are always more important than the forward rotating ones, (see later Sections) the overall effect of the addition of the harmonic fields caused by the slot openings to those caused by the mmf harmonics, is an increase in the overall loss above the sum of the losses of the individual component fields. To apply the exact corrections given by Eqs. 6.17 and 6.18 to every slot harmonic is a very laborious process, since both  $\zeta_{(r < 0)}$  and  $\zeta_{(r > 0)}$  vary with load as  $\theta_1$  and  $\alpha'$  changes. This increase in the overall loss was therefore taken into consideration by increasing the amplitude of all the fields due to the mmf slot harmonics by a constant mean factor  $= (1 + \frac{\Lambda_s}{2\Lambda_0})$ , as suggested by Alger;<sup>4</sup> where  $\Lambda_s$  is the half amplitude of the permeance pulsation due to the stator slot openings. Once this correction is applied, the two components of the resultant slot harmonic fields, (i.e. that due to the stator mmf harmonics, and that due to the stator slot openings), are considered separately. The losses produced by the former are then included in the load losses whilst those of the latter harmonics are considered as no-load losses in accordance with the definition given in the Introduction.



### 6.1.2 Air gap fields due to the rotor harmonics.

Each one of the stator field harmonics induces currents in the rotor ~~squirrel~~ cage bars whose frequency depends on the relative motion of the rotor with respect to the harmonic in question. These currents produce a rotor mmf which contains apart from a wave of order  $\nu$  a series of subharmonics of different number of poles from the inducing field. Liwschitz<sup>3</sup> has shown that the  $\mu^{\text{th}}$  of these subharmonics induced by the  $\nu^{\text{th}}$  stator harmonic has the order:

$$\mu = \nu + k_2 \left( \frac{S_2}{p} \right) \quad (6.19)$$

where  $k_2$  is any positive negative or zero integer.

As an example Table 5 shows the rotor harmonics that are produced by the various stator harmonics in a 4-pole machine with 36 stator and 45 rotor slots.

The harmonics in the induction motor produce asynchronous as well as synchronous torques.

An asynchronous torque occurs when a travelling harmonic wave due to either the rotor or the stator induces currents or losses in the opposing member of the machine which are of the same frequency as the inducing field. A synchronous torque occurs when a stator harmonic  $\nu_a$  produces a rotor harmonic  $\mu_a$  which has the same rotational frequency and order as another stator

harmonic  $v_b$  at a single rotor speed. In such a case  $v_a$  is the source of excitation for the rotor, and  $v_b$  the source of power of the stator. It can be easily shown<sup>3</sup> that the synchronous torque is produced at a speed of:

$$n = - \frac{2f_o}{k_2 S_2} \text{ rps} \quad (6.20)$$

where  $k_2$  is the value in Eqn. 6.19 that gives the value of  $\mu_a$  in question.

From Table 5 it is seen that there exists no value of rotor harmonic ( $\mu_a$ ) that coincides with a stator harmonic ( $v_b$ ) and is not caused by it. Therefore no synchronous torques exist in a machine with 36 stator and 45 rotor slots to which Table 5 applies.

Table 5

Stator and rotor harmonic fields.

Stator harmonics

Rotor harmonics

( $v$ ) pole-pairs

( $\mu$ ) pole-pairs

-	$k_2=0$	$k_2=1$	$k_2=-1$	.
+2	+2	+47	-43	..
-10	-10	+35	-55	..
+14	+14	+59	-31	..
-22	-22	+23	-67	..
+26	+26	+71	-19	..
-34	-34	+11	-79	..
+38	+38	+83	-7	..
.	.	.	.	..

The rotor subharmonic fields, given by Eqn. 6.19 with  $k_2 \neq 0$ , react back on the stator and cause losses which also appear as harmonic torques.<sup>16</sup>

The harmonic currents that flow in the bars of a squirrel cage winding are small due to the fact that the harmonic leakage reactance is appreciably larger than the harmonic magnetising reactance. Thus the rotor subharmonic fields produced by the  $v^{\text{th}}$  stator harmonic field (where  $v \neq 1$ ) are small and their reaction back on the stator can be neglected. These subharmonic fields can, therefore, be considered to contribute only to the differential leakage reactance of the  $v^{\text{th}}$  stator harmonic.

The rotor subharmonic fields produced by the stator fundamental field, however, may be appreciable and their reaction back on the stator is considered. These rotor subharmonic fields (rotor slot harmonics) are shown in square boxes in Table 5. The stator slot harmonics are shown encircled.

It can be shown<sup>3</sup> that the rotor slot harmonic mmfs produced by the stator fundamental field can be written as:

$$f_{2\mu} = \bar{F}_{2\mu} \cdot \cos \left[ \left[ 1 + (1-s) \frac{k_2 S_2}{p} \right] \omega t - \frac{\pi x_1}{Y} \left( \frac{k_2 S_2}{p} + 1 \right) + \theta_\mu \right]$$

(6.21)

where  $\bar{F}_{2\mu}$  is its complex amplitude given as:

$$\bar{F}_{2\mu} = \frac{3\sqrt{2}}{\pi} \frac{Z_1}{2p} \cdot \frac{k_{dp1}}{k_{sk1}} \cdot \frac{\bar{I}_2}{(1 + \frac{k_{2S2}}{p})} \quad (6.22)$$

The damping of the rotor slot harmonics by any currents that these harmonics may induce in the stator winding is neglected since the induced stator harmonic currents are extremely small. More is said of these matters in Section 6.6.

The rotor mmf given by Eqn. 6.21 acts on the air-gap permeance of Eqn. 6.4 to produce the flux density waves given by Eqn. 6.23

$$\begin{aligned} b_{\left(\frac{k_{2S2}}{p} + 1\right)} &= \bar{B}_{\left(\frac{k_{2S2}}{p} + 1\right)} \cdot \left[ \cos \left\{ \left[ 1 + (1-s) \frac{k_{2S2}}{p} \right] \omega t - \frac{\pi x_1}{Y} \left( \frac{k_{2S2}}{p} + 1 \right) + \theta_\mu \right\} \right. \\ &\quad - \sum_{c=1,2,\dots} \gamma_c' \cos \frac{c\pi S_1}{pY} x_1 \cdot \cos \left\{ \left[ 1 + (1-s) \frac{k_{2S2}}{p} \right] \omega t - \frac{\pi x_1}{Y} \left( \frac{k_{2S2}}{p} + 1 \right) + \theta_\mu \right\} \\ &\quad \left. - \sum_{d=-2,+2} \frac{\gamma_d''}{2} \cos \left\{ \left[ 1 + (1-s) (k_2 - d) \frac{S_2}{p} \right] \omega t - \frac{\pi x_1}{Y} \left[ \frac{S_2}{p} (k_2 - d) + 1 \right] + \theta_\mu \right\} \right] \end{aligned} \quad (6.23)$$

Again comparing Eqn. 6.23 with Eqn. 6.7 giving the fundamental flux density it is seen that the first term of Eqn. 6.23 and the last term of Eqn. 6.7 represent waves which are stationary with respect to each other.

It can be shown by an analysis identical to that given in Appendix II but applied to the rotor, that for the rotor slot harmonics  $\theta_\mu = \theta_1$ . Hence by a direct analogy to Eqn.6.16 the resultant rotor slot harmonic field; caused by both the rotor mmf and the rotor slot openings; can be written as:

$$\left[ B''_{\text{res}} \right]_{\text{slot}} = \sqrt{B_{\frac{k_2 S_2}{p} + 1}^2 + \left( B_{g1} \frac{\gamma_d''}{2} \right)^2} \cdot \sqrt{1 \pm \frac{2 \sin \theta_2}{\alpha''_{+1}/\alpha''}} \quad (6.24)$$

$$\text{where } B_{\frac{k_2 S_2}{p} + 1} = \frac{3\mu_0 \sqrt{2} Z_1 k_{dp1} I_2}{2\pi p g k_{c1} k_{c2} k_{sk1} \left(1 + \frac{k_2 S_2}{p}\right)} \quad (6.25)$$

$$\alpha'' = \frac{B_{\frac{k_2 S_2}{p} + 1}}{B_{g1} \frac{\gamma_d''}{2}} = \left[ \frac{2}{\gamma_d'' \left( \frac{k_2 S_2}{p} + 1 \right)} \right] \cdot \frac{I_2}{I_m} \quad (6.25)(a)$$

and  $\theta_2$  is the angle between  $\bar{I}_2$  and the reference phasor  $\bar{E}$ . Again the positive sign in Eqn.6.24 applies to the backward rotating harmonics and the negative sign to the forward rotating ones.

When the rotor slot openings are small, (as is the case for practically all cast aluminium rotors),  $\gamma_d''$  becomes very small and  $\alpha''$  very large. The correction factor given by the second square root in Eqn.6.24 therefore becomes unity and the total loss caused by the rotor slot harmonic fields in the stator can be

taken to be the sum of the individual losses caused by the fields due to the rotor mmf and slot openings.

## 6.2 Harmonic losses in rotor bars and harmonic equivalent circuit.

If saturation in the magnetic circuit of the machine is neglected then superposition can be used to calculate the total shaft torque of the induction motor by treating each harmonic field wave separately and adding their individual torques. This corresponds to having a different "motor" for each harmonic, the motors being connected in series mechanically. The conventional equivalent circuit of the induction motor is then modified as shown in Fig.25. In this figure the harmonic circuits excited by the current  $I_1$  and having  $v$  as a suffix are those due to the stator mmf harmonics. The harmonic circuits excited by a current  $I_2$  and having a suffix  $\mu$  are due to the rotor mmf harmonics; and the harmonic circuits excited by a current  $I_0$  and having a suffix  $\lambda'$  or  $\lambda''$  are due to the combination of the fundamental flux density and the stator and rotor slot openings respectively.

The circuit of Fig.25 applies only to the calculation of the losses and torques produced by the harmonic currents that flow in the rotor or stator windings.

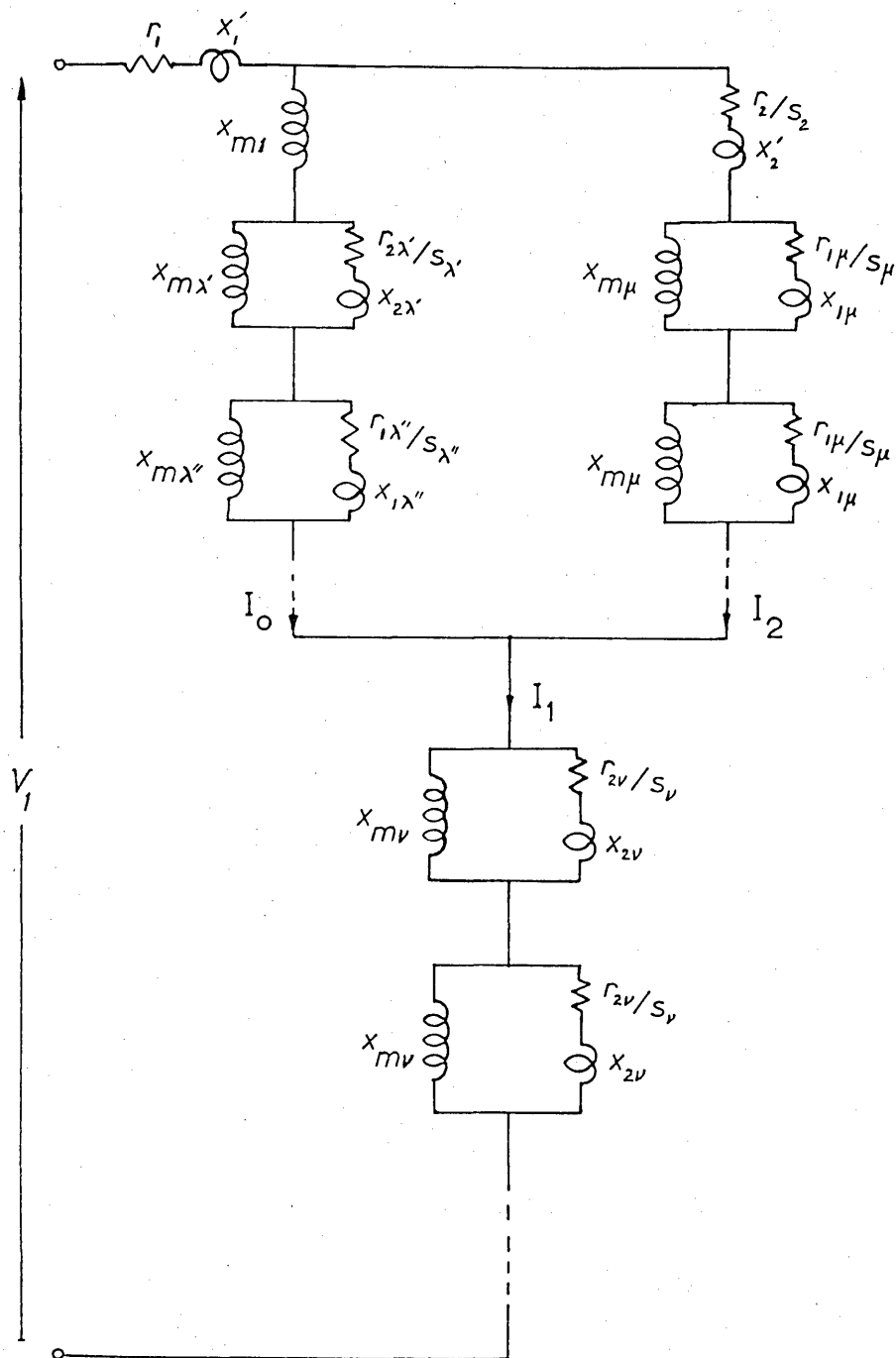


fig.25. "Complete" equivalent circuit of an induction motor.

suffix :  $\nu$  indicates a harmonic due to the stator mmf  
 "  $\mu$  " " " " " rotor "  
 "  $\lambda'$  " " " " " stator slot openings  
 "  $\lambda''$  " " " " " rotor " "

In Section 6.6 it is shown that the branches that are shunting the reactances  $x_{mu}$  are very large thus allowing only very small harmonic currents to flow in the stator windings. The most important harmonics contributing to the load losses dissipated in the machine windings are therefore the stator mmf harmonics.

The equivalent circuit of a single stator harmonic is shown in Fig.22, and since this is essentially the same as the equivalent circuit of the fundamental, it produces a torque-slip characteristic of the same shape as the main torque-curve, but with a synchronous speed at  $n_{ov} = \frac{n_o}{v}$  instead of at  $n_o$ .

Due to the fact that the harmonic magnetising reactance is very much smaller than the main magnetising reactance (see Chapter 7), the harmonic terminal voltage  $V_{1v}$  in Fig.22 is small in comparison with the terminal voltage  $V_1$ . The voltage  $V_{1v}$  therefore does not appreciably affect the current  $I_1$  which is primarily determined by the fundamental. Hence the equivalent circuit of Fig.22 can be considered as being excited by a current source of magnitude  $I_1$  rather than by a voltage source. This is rather important since it shows that the fundamental subdivision is in the current distribution.



Once all the parameters in the harmonic equivalent circuit of Fig.22 are determined (see Chapter 7) one can use the equivalent circuit of Fig.25 with as many harmonic branches as necessary to calculate the total losses dissipated in the machine windings, or to calculate the torque-slip characteristic. This has been done for rotor No.1(a) (see Table 2, Chapter 2) and the result is shown by curve "B" in Fig.26. Curve "C" of the same figure shows the measured torque-slip characteristic of the machine with the same rotor, and curve "A" the fundamental torque, (both calculated and measured).

From this figure it is obvious that the difference between the fundamental and the actual torque; a difference due to the load losses; cannot be explained quantitatively by the equivalent circuit of Fig.25 and at least part of this difference must be attributed to other causes. The effects of the cross-current losses and of the stator and rotor iron losses on the torque-slip characteristics and the load losses are therefore investigated in the following Sections.

### 6.3 Losses due to imperfect insulation between the squirrel cage bars and the rotor iron.

If the bars of a squirrel cage winding are skewed

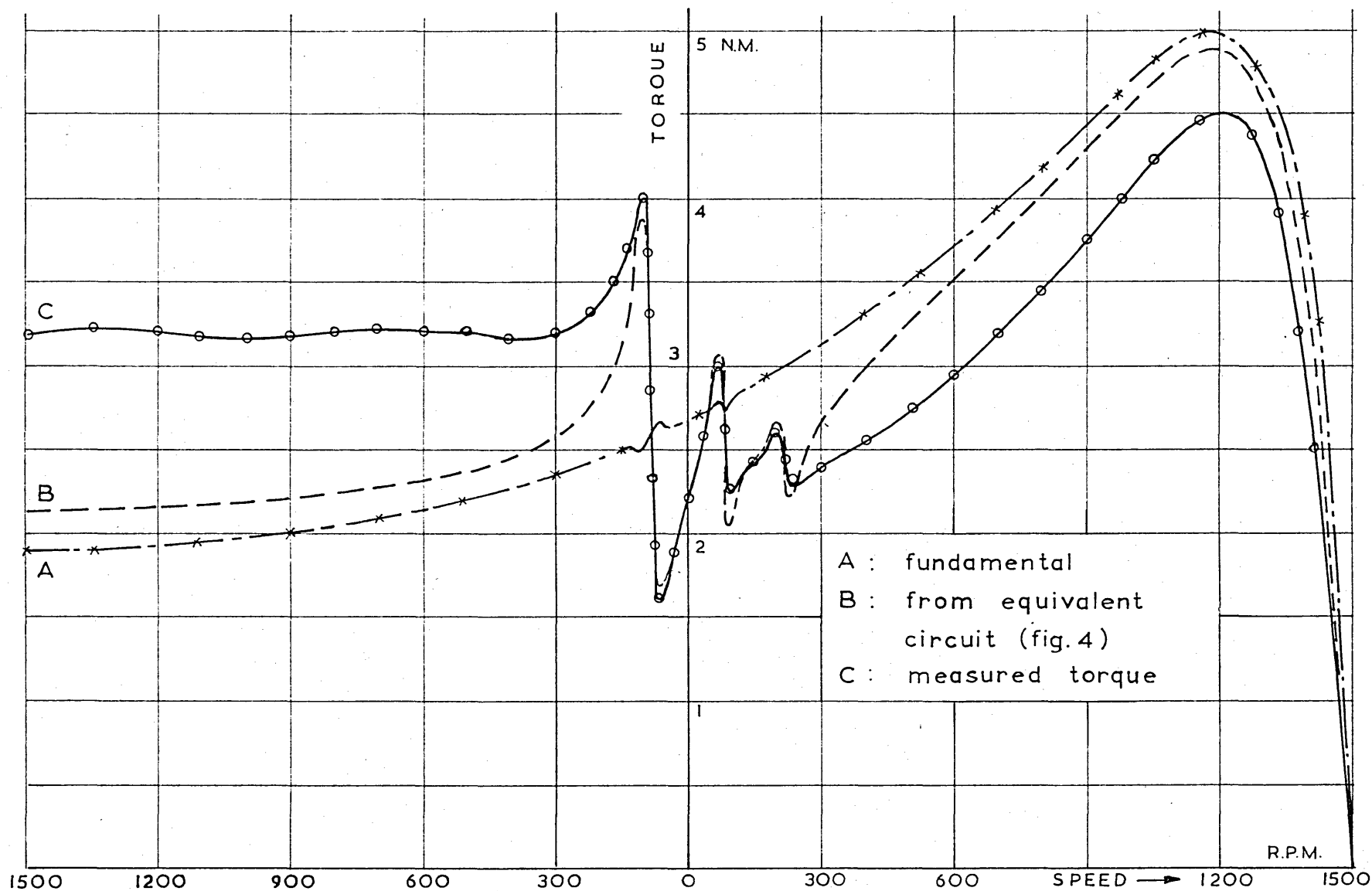


fig.26. Torque - slip curves of rotor N°1. (100 V 50 c/s)

but not completely insulated from the rotor laminations, the difference in the voltage induced between adjacent bars will circulate currents in the circumferential direction. These currents flowing from bar to bar via the rotor iron produce losses in the rotor which result in a corresponding loss of accelerating torque. The theoretical analysis of the load losses due to this mode of current flow has been investigated by Rossmailer,<sup>17</sup> and Odok<sup>18</sup> both of which derived expressions for the cross-current load loss. The analysis of Section 6.3.1 is similar to the analyses of the above mentioned investigators. It was found, however, that the interbar resistance  $r_{bb}$  in the equations is highly non-linear and so in order to choose the right value of  $r_{bb}$  it is also necessary to investigate the spacial distribution of interbar voltage and current. This is done in Section 6.3.3.

#### 6.3.1 Calculation of losses.

The analysis of load losses carried out in this section is based on the following assumptions:

- (i) The interbar impedance (impedance between two neighbouring bars) is assumed purely resistive. The value of this resistance ( $r_{bb}$ ) is assumed to be constant independent of the magnitude or

frequency of the interface current that flows.

It is left until later on (Chapter 7) to determine the "best" constant value to be used in actual calculations.

- (ii) The impedance of the end-rings is neglected in comparison with the bar impedance. With no end-ring impedance and no skew, no interbar voltage exists. The end-ring impedance would introduce a loss even with no skew and it causes an error in the calculation when skew is present. An approximate check showed the effect was negligible.
- (iii) The width of the bars is neglected. The effect of the bar width on the differential harmonic leakage and the effective skew is considered separately in Section 6.7 and in Chapter 7.

Fig.27 shows two consecutive bars of the squirrel cage. The electrical angle between the bars with respect to the  $v^{\text{th}}$  stator field harmonic is  $\theta_v$ , the effective length of the rotor stack is  $\ell$ , and the effective skew is  $\alpha_v$  radians per unit length of stack. Subscript "b" refers to the bar quantities and subscript "bb" to the interbar region.

In the following analysis the capital letters for voltages and currents are phasor quantities, (unless

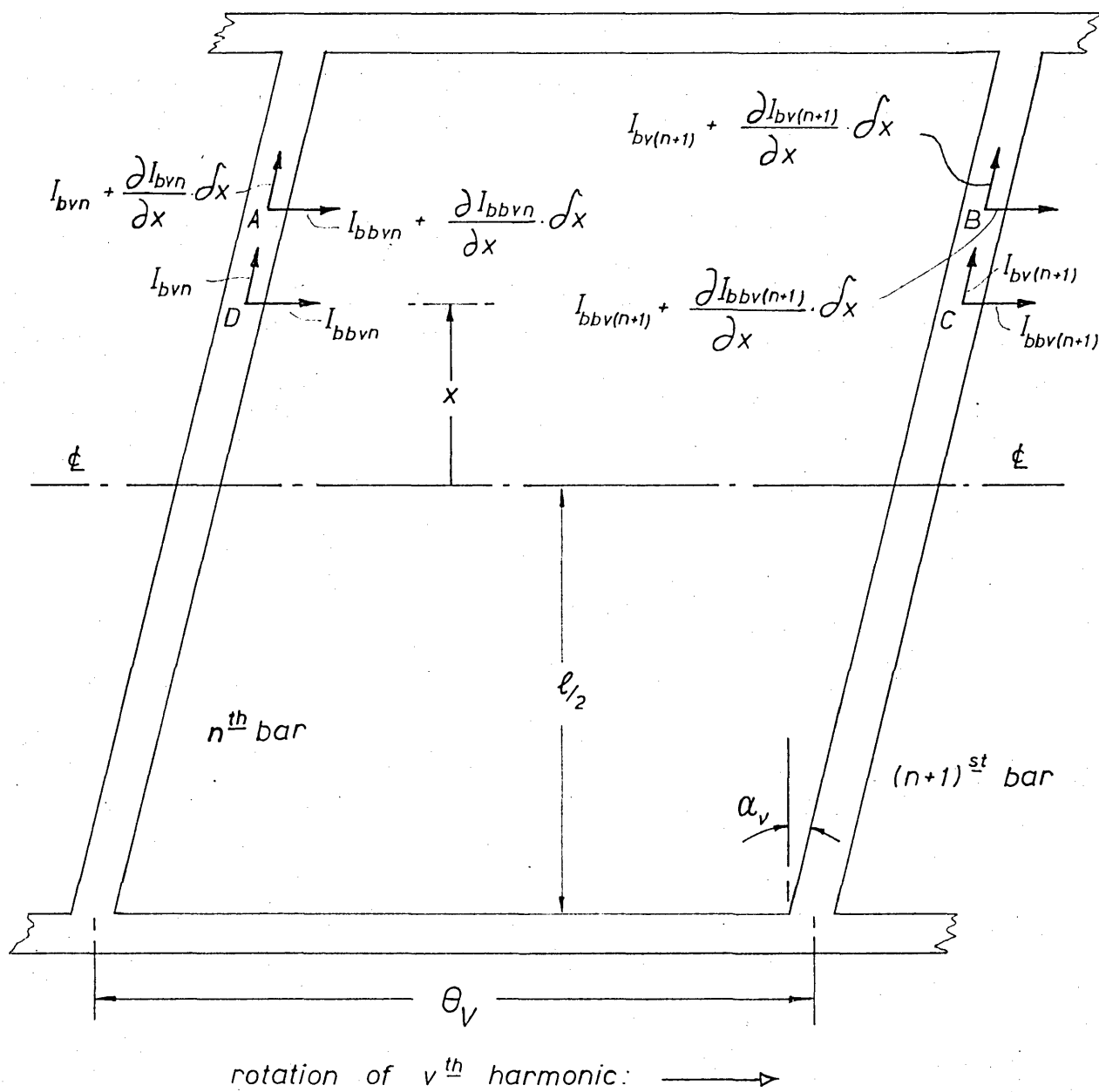


fig.27 Section of the squirrel cage.

otherwise stated), representing harmonic components. Capital letters for reactances and resistances refer to total values, whereas small letters refer to the values for a unit length of rotor stack. The meaning of all symbols can be found in the Nomenclature.

Kirchhoff's first law applied to element  $\delta x$  of the  $n^{\text{th}}$  bar gives:

$$I_{bv_n} + I_{bbv(n-1)} \cdot \delta x = I_{bv_n} + \frac{\partial I_{bv_n}}{\partial x} \cdot \delta x + I_{bbv_n} \cdot \delta x$$

$$\therefore \frac{\partial I_{bv_n}}{\partial x} = I_{bbv(n-1)} - I_{bbv_n} \quad (6.26)$$

where  $I_{bbv}$  is the circumferential current per unit length.

Since sinusoidal conditions are considered the following relations apply to the bar and interbar currents:

$$I_{bv(n-1)} = I_{bv_n} \cdot e^{j\theta_v} \quad (6.27)(a)$$

and 
$$I_{bbv(n-1)} = I_{bbv_n} \cdot e^{j\theta_v} \quad (6.27)(b)$$

Substituting Eqn. 6.27(b) into Eqn. 6.26 gives:

$$-\frac{\partial I_{bv_n}}{\partial x} = I_{bbv_n}(1 - e^{j\theta_v}) \quad (6.28)$$

Kirchhoff's second law applied to path ABCD gives:

$$\begin{aligned}
E_{DA} - E_{CB} = I_{bv n} \cdot z_{bv} \cdot \delta x + (I_{bbvn} + \frac{\partial I_{bbvn}}{\partial x} \cdot \delta x) \cdot r_{bb} \\
- I_{bv(n+1)} \cdot z_{bv} \cdot \delta x - I_{bbvn} \cdot r_{bb} \quad (6.29)
\end{aligned}$$

where  $E_{DA}$  and  $E_{CB}$  are the voltages induced in bar sections DA and CB respectively by the  $v^{th}$  stator field harmonic;  $z_{bv}$  is the total bar impedance per unit length of stack with respect to the  $v^{th}$  harmonic and  $r_{bb}$  is the bar-to-bar resistance per unit length.

Since  $E_{CB} = E_{DA} \cdot e^{-j\theta_v}$  substitution into Eqn. 6.29 gives after some simplification.

$$E_{DA} = I_{bv n} \cdot z_{bv} \cdot \delta x - \frac{\partial^2 I_{bv n}}{\partial x^2} \cdot \frac{r_{bb}}{4 \sin^2 \frac{\theta_v}{2}} \cdot \delta x \quad (6.30)$$

The elemental voltage  $E_{DA}$  is given by the flux cutting rule as:

$$E_{DA} = B_{1v} \cdot \delta x \cdot u_v \cdot e^{j\alpha_v x} \quad (6.31)$$

where  $B_{1v}$  is the rms flux density due to the stator current only, and  $u_v$  is the linear speed of the rotor bars with respect to the  $v^{th}$  stator field harmonic.

The factor  $e^{j\alpha_v x}$  is introduced to account for the phase shift in the voltage induced at different parts of the bar due to skew. The voltage induced at the center of the bar is taken as the reference phasor. The total

voltage induced in bar section DA is, of course, the sum of the voltage induced by the stator  $v^{\text{th}}$  harmonic and the voltage induced by the revolving field of the rotor produced by all the bar currents due to the  $v^{\text{th}}$  harmonic. This second part of the induced voltage, however, is taken into consideration by using the total bar impedance  $z_{bv}$  which includes the bar magnetising reactance  $x_{bm v}$ , the differential leakage reactance  $x_{bdv}$ , and the slot leakage reactance  $x_{b.s\ell}$ . In this way  $E_{DA}$  is the voltage induced by the stator field acting alone, and is thus given by Eqn. 6.31 despite the fact that the total air-gap flux density  $B_{gt}$  can have radial as well as axial components due to the redistribution of currents in the rotor.

The flux density  $B_{1v}$  in Eqn. 6.31 is given by:<sup>3</sup>

$$B_{1v} = \frac{3\mu_o I_1 Z_1 k_{dpv}}{2\pi g k_c p v} \quad (6.32)$$

and the speed  $u_v$  is given by:  $u_v = \frac{2Yf_{2v}}{v}$ .

Substituting the above two equations into Eqn. 6.31 gives:

$$E_{DA} = \frac{3\mu_o I_1 Z_1 k_{dpv} \cdot Y \cdot f_{2v} \cdot e^{j\alpha_v x}}{\pi g k_c p v^2} \cdot \delta x \cdot e \quad (6.33)$$

Eliminating  $E_{DA}$  between Eqns. 6.30 and 6.33 the following equation results:

$$r'_{bbv} \frac{\partial^2 I_{bv}}{\partial x^2} = I_{bv} \cdot z_{bv} - E_{ov} e^{j\alpha_v x} \quad (6.34)$$



where the subscript "n" for the bar current has been dropped since all the bars are identical.

In Eqn. 6.34 above  $E_{ov}$  is the magnitude of the voltage induced in a unit length of bar and is given by:

$$E_{ov} = \frac{3\mu_o I_1 Z_1 k_{dpv} Y_{f2v}}{\pi g k_{cpv}^2} \quad (6.35)$$

$$\text{or } E_{ov} = x_{bm v} \cdot I_1 \cdot (3Z_1 k_{dpv} / S_2) \quad 6.36(a)$$

$$\text{or } E_{ov} = X_{mv} \cdot I_1 / (\ell Z_1 k_{dpv}) \quad 6.36(b)$$

where  $x_{bm v}$  is the magnetising reactance of a single bar per unit length of stack, and  $X_{mv}$  is the total magnetising reactance of the  $v^{\text{th}}$  harmonic in the equivalent circuit referred to the stator side.

The quantity

$$r'_{bbv} = \frac{r_{bb}}{4 \sin^2 \frac{\theta_v}{2}} \quad (6.37)$$

has been introduced to simplify the expressions.

Eqn. 6.34 is a differential equation giving the bar current at a distance  $x$  from the centre of the rotor stack. Its solution is given by:<sup>19</sup>

$$I_{bv} = A \cosh \gamma_v x + B \sinh \gamma_v x + \frac{E_{ov} e^{j\alpha_v x}}{E_{bv} + \alpha_v^2 r'_{bbv}} \quad (6.38)$$

where A and B are constants to be evaluated from the boundary conditions, and  $\gamma_v = \sqrt{\frac{z_{bv}}{r_{bbv}}}$  is the propagation constant-by analogy to transmission line theory.

The voltage between adjacent bars at the point x is:

$$V_{bbv} = I_{bbv} \cdot r_{bb} = -\left(\frac{1}{1-e^{j\theta_v}}\right) \cdot \frac{\partial I_{bv}}{\partial x} \cdot r_{bb} \quad (6.39)$$

and since the impedance of the end-rings is neglected  $V_{bbv}$  is zero at  $x = \pm \ell/2$ .

$$\text{i.e.} \left[ \frac{\partial I_{bv}}{\partial x} \right]_{\text{at } x=\pm \ell/2} = 0 \quad (6.40)$$

The above two conditions can be used to calculate the constants A and B of Eqn. 6.38 as shown in Appendix III.

The losses in the rotor due to the  $v^{\text{th}}$  stator harmonic are given by:

$$P_{2v} = S_2 \text{Re} \int_{-\ell/2}^{+\ell/2} I_{bv} \cdot E_{bv}^* dx$$

where  $E_{bv}^*$  is the conjugate of the voltage  $E_{bv}$  induced in the bar at point x, and is therefore given by:

$$E_{bv}^* = E_{0v} \cdot e^{-j\alpha_v x}$$

Hence the rotor power loss becomes:

$$P_{2v} = S_2 \operatorname{Re} \int_{-\ell/2}^{+\ell/2} I_{bv} \cdot E_{ov} \cdot e^{-j\alpha_v x} dx \quad (6.41)$$

Eqn. 6.41 includes the losses due to both bar and inter-bar currents.

Substituting the value of  $I_{bv}$  from Eqn. 6.38 into Eqn. 6.41 and performing the integration<sup>12</sup> gives:

$$P_{2v} = \frac{E_{ov}^2 S_2}{r_{bbv}'} \cdot \operatorname{Re} \left[ \frac{\ell}{\alpha_v^2 + \gamma_v^2} + \frac{2\alpha_v^2 \left( \tanh \frac{\gamma_v \ell}{2} \cos^2 \frac{\alpha_v \ell}{2} + \coth \frac{\gamma_v \ell}{2} \sin^2 \frac{\alpha_v \ell}{2} \right)}{\gamma_v (\alpha_v^2 + \gamma_v^2)^2} \right] \quad (6.42)$$

or:

$$P_{2v} = \frac{E_{ov}^2 S_2}{r_{bbv}'} \cdot \operatorname{Re} \left[ \frac{\ell}{\alpha_v^2 + \gamma_v^2} + \frac{2\alpha_v^2}{(\alpha_v^2 + \gamma_v^2)^2} \cdot \frac{\cosh \gamma_v \ell - \cos \alpha_v \ell}{\gamma_v \sinh \gamma_v \ell} \right] \quad (6.43)$$

Once the losses due to the  $v^{\text{th}}$  stator harmonic are determined the asynchronous torque produced by this harmonic can be calculated from the equation:

$$T_{2v} = \frac{P_{2v}}{\omega_{ov} \cdot s_v} \quad (6.44)$$

where  $\omega_{ov}$  is the harmonic synchronous speed and  $s_v$  the slip of the rotor with respect to the  $v^{\text{th}}$  harmonic field.

The loss expression of Eqn. 6.42 is the most convenient one for numerical computations, whereas the expression of Eqn. 6.43 is more suitable if any theore-

tical deductions are to be made (e.g. see Chapter 9).

### 6.3.2 Choice of interbar resistance.

It has already been stated that the interbar resistance  $r_{bb}$  is not constant but varies as shown in Fig.28. (See Chapter 7 for the exact form of the curves.)

Thus to determine the best possible constant value of  $r_{bb}$  that must be used, one must have some idea of the value of interbar current that is flowing. From Eqns. 6.38 and 6.28 the harmonic interbar current can be calculated as:

$$I_{bbv} = \left( \frac{-1}{1 - e^{j\theta_v}} \right) \cdot \left[ A\gamma_v \sinh\gamma_v x + B\gamma_v \cosh\gamma_v x + \frac{j\alpha_v E_o e^{j\alpha_v x}}{r'_{bbv} (\alpha_v^2 + \gamma_v^2)} \right] \quad (6.45)(a)$$

and hence the total interbar current is:

$$I_{bb} = \sum_{v=1}^{\infty} I_{bbv} \quad (6.45)(b)$$

The values of the constants A and B are given in Appendix III.

This distribution of cross-current flow along the bar is shown in Fig.29. From this figure it is seen that the maximum value of the cross-current  $I_{bb}$  occurs near the centre of the rotor stack. If this value of  $I_{bb}$  is assumed to determine the value of  $r_{bb}$ , then

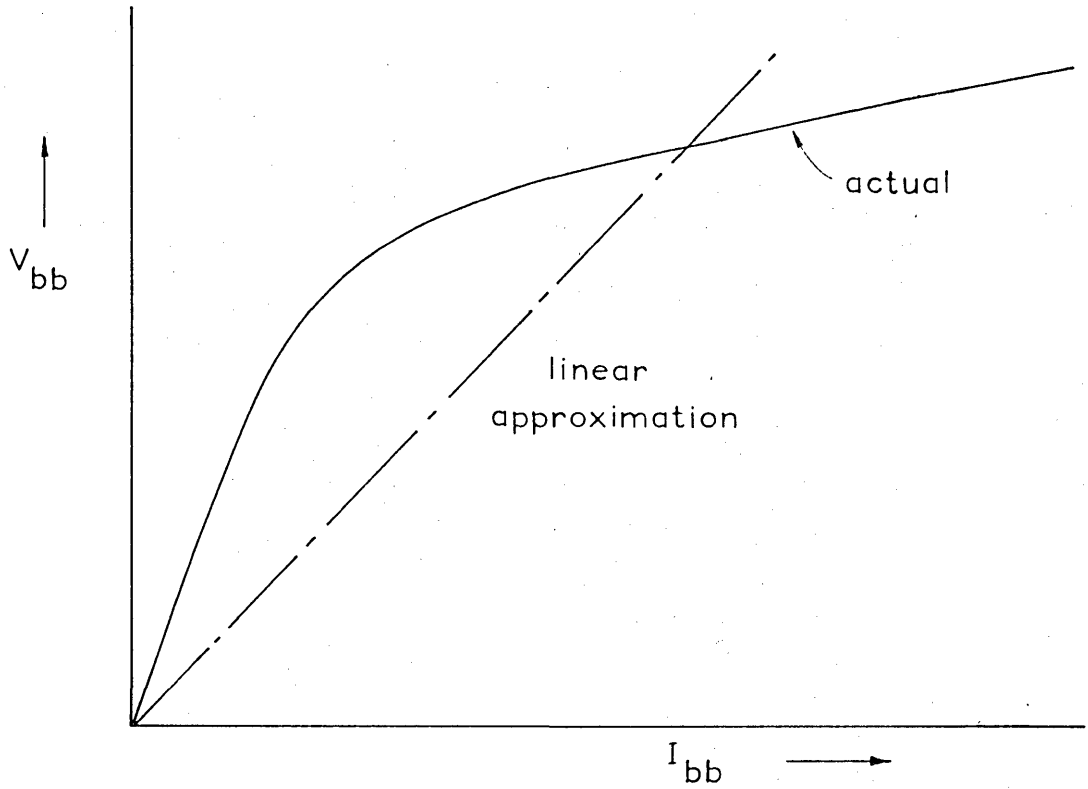


fig.28. Typical variation of interbar resistance  $r_{bb}$ .

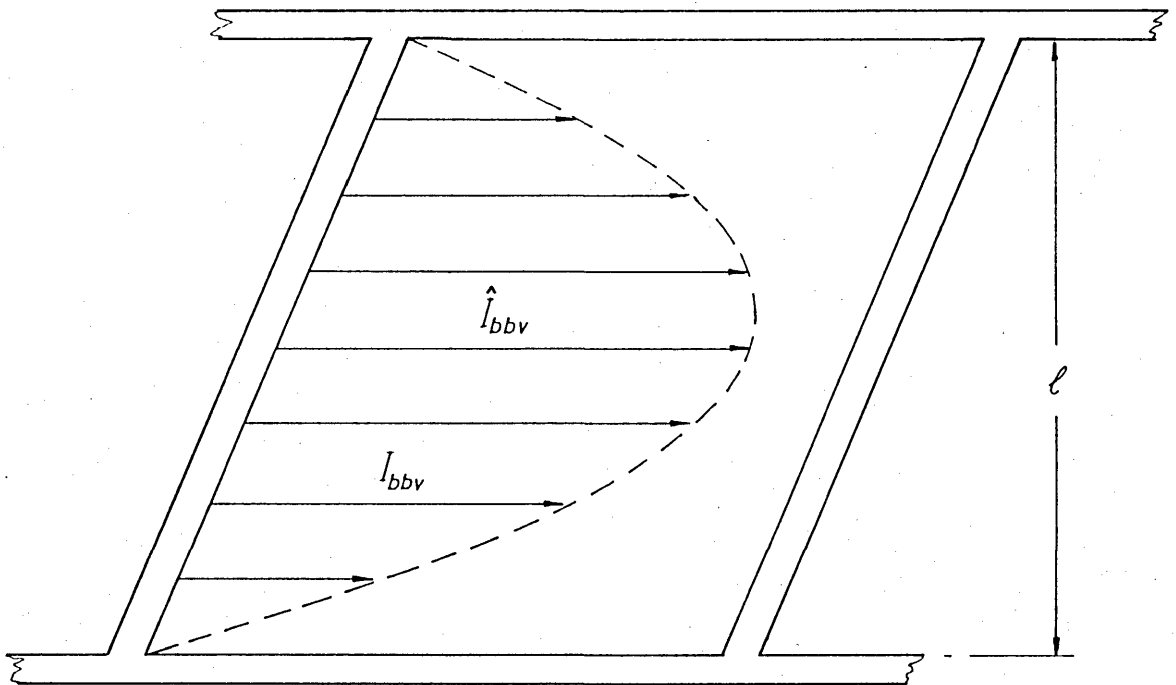


fig.29. Distribution of cross - currents.

assuming a value for  $r_{bb}$  the current  $I_{bb}$  can be calculated from Eqn. 6.45(b). Using this value of  $I_{bb}$  and Fig.29 another value of  $r_{bb}$  can be obtained which again could be used to calculate  $I_{bb}$  and so on until an accurate value of  $r_{bb}$  is obtained. This iteration process although possible is very difficult indeed to perform in practice and consumes a very great deal of computer time. Moreover, the value of  $r_{bb}$  that would be obtained is strictly applicable only to the central region of the rotor stack. Near the ends of the stack the cross-current  $I_{bb}$  is much less than  $I_{bb}$  and so in these regions  $r_{bb}$  should be calculated from the initial slope of the curve in Fig.28. In view of these uncertainties, the complexity of the above iteration process was not thought to be justified and another method of choosing  $r_{bb}$  was therefore used.

Although the cross-current  $I_{bbv}$  depends very much on the interbar resistance, the bar-to-bar voltage is not affected a great deal. Thus putting  $r'_{bb} \rightarrow \infty$  and using the relation  $V_{bbv} = I_{bbv} \cdot r_{bb}$  the interbar voltage can be calculated as:

$$V_{bbv} = \frac{jE_{ov} \cdot 4 \sin^2 \frac{\theta_v}{2}}{\alpha_v (1 - e^{j\theta_v})} \cdot \left[ \cos \frac{\alpha_v \ell}{2} + 2j \frac{x}{\ell} \sin \frac{\alpha_v \ell}{2} - e^{j\alpha_v x} \right] \quad (6.46)$$

and the maximum value (given by putting  $x=0$ ) finally simplifies to:

$$\hat{V}_{bbv} = \frac{E_{ov}}{\alpha_v} \cdot 4 \sin^2 \frac{\alpha_v \ell}{4} \cdot \sin \frac{\theta_v}{2} \cdot e^{-j \frac{\theta_v}{2}} \quad (6.47)$$

The above expression gives the interbar voltage of one particular frequency produced by the  $v^{\text{th}}$  stator field harmonic only. Other harmonics produce interbar voltages of different frequencies and phase angles. Thus the total voltage, (which is the sum of all these different voltages), is non-sinusoidal and non-periodic. The maximum value that it can reach, however, is the sum of the amplitudes of its harmonic components which is given by:

$$\left[ \hat{V}_{bb} \right]_{\text{total}} = 4 \sqrt{2} \sum_{v=1}^{\infty} \left( \frac{E_{ov}}{\alpha_v} \cdot \sin^2 \frac{\alpha_v \ell}{4} \cdot \sin \frac{\theta_v}{2} \right) \quad (6.48)$$

The value calculated from Eqn. 6.48 could be used in conjunction with Fig. 28 to determine what value of  $r_{bb}$  should be used in the computations. (See Chapter 7).

A comparison of the cross-current losses calculated by the use of the previously described iteration process of choosing  $r_{bb}$ , with the results obtained by the use of Eqn. 6.48 was made for one case only and the agreement was found to be quite good.<sup>53</sup>

## 6.4 Effects of eddy currents on the rotor iron surface.

### 6.4.1 Calculation of fluxes.<sup>20</sup>

As the magnetic fields rotate past the rotor surface, eddy currents are induced in the rotor laminations which cause surface  $I^2R$  losses and also oppose the penetration of flux into the rotor body in accordance with Lenz's law.

Considering the  $v^{\text{th}}$  stator field harmonic by itself: the magnetic flux density wave is given by:

$$b_v = B_{1v} \cos \left( \frac{v\pi x_1}{Y} + \omega t \right)$$

which in terms of the rotor coordinate  $x_2$  (Fig.23)

becomes:

$$b_v = B_{1v} \cos \left( \frac{v\pi x_2}{Y} + s_v \omega t \right) \quad (6.49)$$

where  $s_v$  is the slip of the rotor with respect to the  $v^{\text{th}}$  stator harmonic given by  $s_v = v(1-s + 1/v)$ .

Eqn. 6.49 can be expanded to give:

$$b_v = B_{1v} \cos \frac{v\pi x_2}{Y} \cos s_v \omega t - B_{1v} \sin \frac{v\pi x_2}{Y} \sin s_v \omega t \quad (6.50)$$

The terms of Eqn. 6.50 represent two pulsating fields which are out of phase by  $90^\circ$  both in space and in time. Figs. 30 and 31 show these two flux density distributions in relation to a rotor tooth. The net



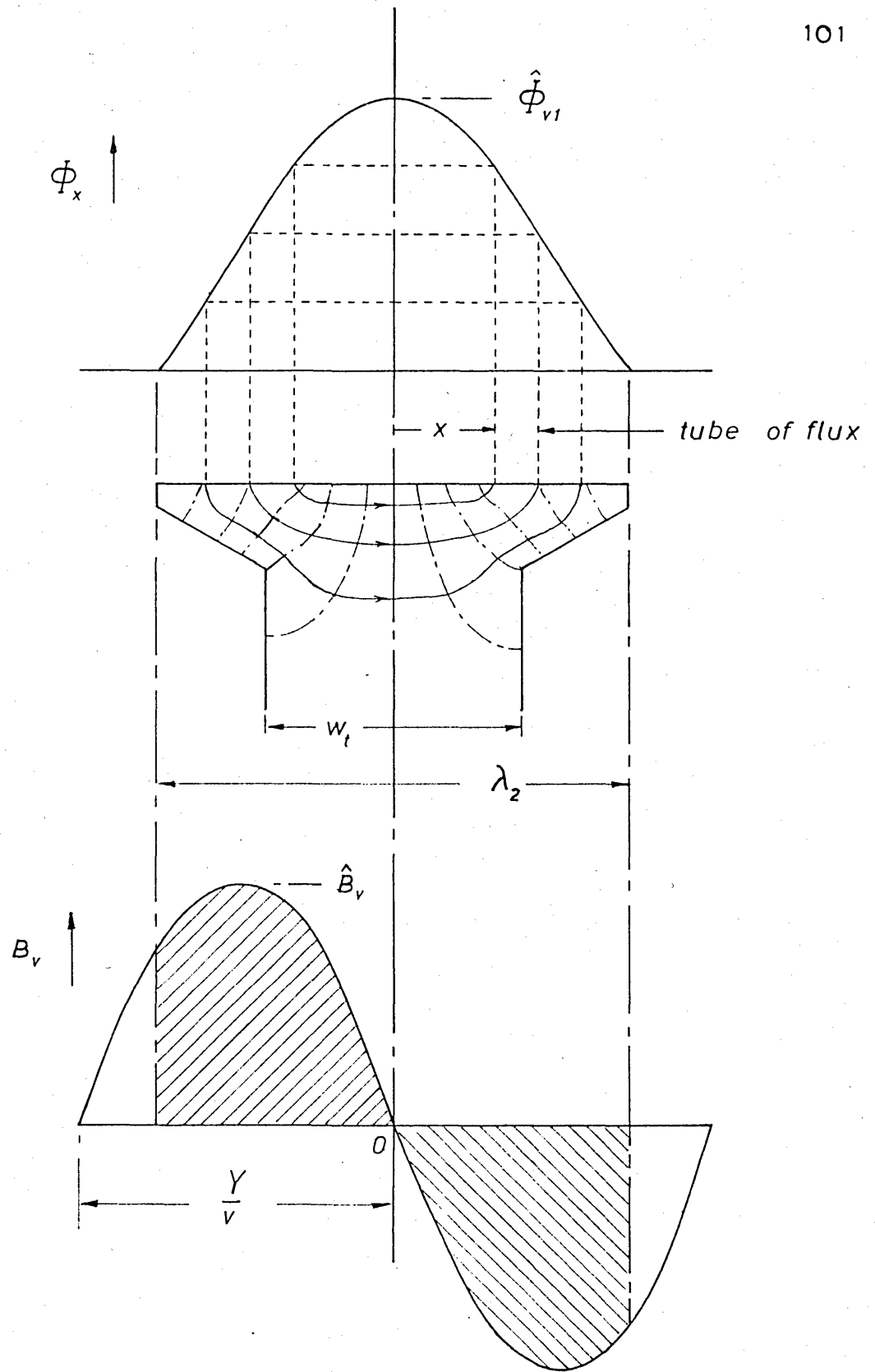


fig.30. Tooth fluxes.

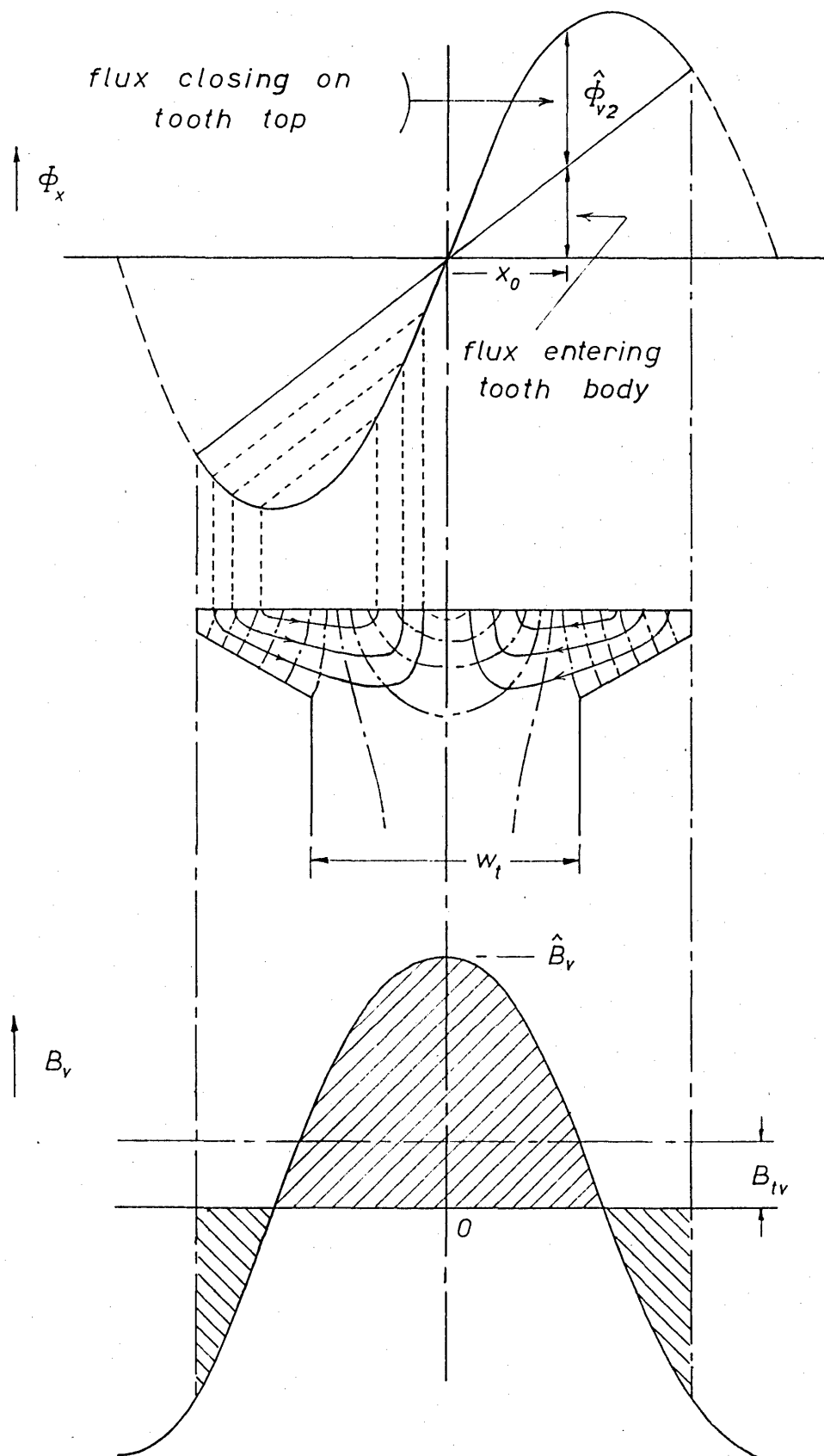


fig. 31. Tooth fluxes.

flux entering the rotor tooth body is given by the integration of the flux density distribution over the rotor tooth width  $\lambda_2$ . Thus it is seen that for the sine component (Fig.30) no flux enters the tooth and all the flux lines must therefore close themselves in the tooth top. For the cosine component on the other hand, there is some flux  $\Phi_{tv0}''$  that enters the tooth body, given by the difference between the two shaded areas in Fig.31.

$$\begin{aligned} \text{Hence: } \Phi_{tv0}'' &= \ell \cdot \int_{-\lambda_2/2}^{+\lambda_2/2} B_{1v} \cos \frac{v\pi x}{Y} dx \\ &= B_{1v} \cdot \lambda_2 \ell \cdot \left( \frac{\sin \beta_v''}{\beta_v''} \right) \end{aligned} \quad (6.51)$$

where  $\beta_v'' = \left( \frac{v\pi\lambda_2}{2Y} \right)$ , is half the electrical angle that a rotor tooth subtends with respect to the  $v^{\text{th}}$  stator field harmonic.

If the amount of flux given by Eqn. 6.51 is subtracted from the flux entering the tooth top, the remaining flux lines must close themselves on the tooth surface.

Referring to Fig.30 the total flux entering the tooth top between the tooth tip and point  $x$  is  $\Phi_{vx1}''$  where:

$$\begin{aligned}
 \Phi_{v x1}'' &= \int_{-\lambda_2/2}^x B_{1v} \sin \frac{v \pi x}{Y} dx \\
 &= B_{1v} \left( \frac{Y}{v \pi} \right) \left( \cos \frac{v \pi x}{Y} - \cos \beta_v'' \right) \quad (6.52)
 \end{aligned}$$

per unit axial length of tooth.

The flux entering the left hand portion of the tooth surface is therefore: (putting  $x=0$ )

$$\hat{\Phi}_{v1}'' = B_{1v} \left( \frac{Y}{v \pi} \right) (1 - \cos \beta_v'') \quad (6.53)$$

Similarly for the cosine component (Fig.31) one gets:

$$\begin{aligned}
 \Phi_{v x2}'' &= \int_0^x \left( B_{1v} \cos \frac{v \pi x}{Y} - B_{1v} \left( \frac{\sin \beta_v''}{\beta_v''} \right) \right) dx \\
 &= B_{1v} \cdot x \cdot \left[ \frac{\sin \left( \frac{v \pi x}{Y} \right)}{\left( \frac{v \pi x}{Y} \right)} - \frac{\sin \beta_v''}{\beta_v''} \right] \quad (6.54)
 \end{aligned}$$

The maximum flux occurs at a value of  $x$  given by:

$$x_o = \left( \frac{Y}{v \pi} \right) \cdot \arccos \left( \frac{\sin \beta_v''}{\beta_v''} \right)$$

as can easily be shown by differentiating Eqn. (6.54).

Hence:

$$\hat{\Phi}_{v2}'' = B_{1v} x_o \left[ \frac{\sin \frac{v \pi x_o}{Y}}{\frac{v \pi x_o}{Y}} - \frac{\sin \beta_v''}{\beta_v''} \right] \quad (6.55)$$

Once the flux distribution is known the flux lines in the rotor tooth can be drawn in by projection from the flux curves and using free-hand flux plotting as shown by the full lines in Figs. 30 and 31.

#### 6.4.2 Calculation of losses.

If in the flux plots derived in the above Section there are  $n$  tubes of flux, the elemental flux in each tube will be:

$$\Delta\Phi = \left(\frac{\hat{\Phi}}{n}\right) \text{ per unit axial length of tooth.}$$

The flux density is therefore:

$$B = \frac{\Delta\Phi}{\delta b} = \frac{\hat{\Phi}}{n(\delta b)}$$

where  $\delta b$  is the breadth of a curvilinear square, (Fig.32).

Carter<sup>22</sup> has shown that if flux pulsates through a lamination of thickness  $h$  with a maximum flux density  $B$  and angular frequency  $\omega$ , and if the reaction of the eddy currents on the forcing flux is neglected, the eddy current loss is given by:

$$P_e = \left(\frac{h}{2}\right)^3 \cdot \frac{B^2 \omega^2}{3\rho} \quad \text{Wb/m}^2$$

The eddy current loss for each curvilinear square is therefore:

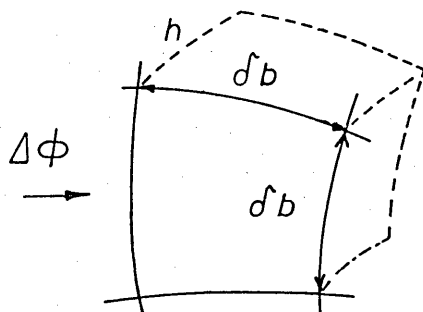


fig. 32

Curvilinear square.

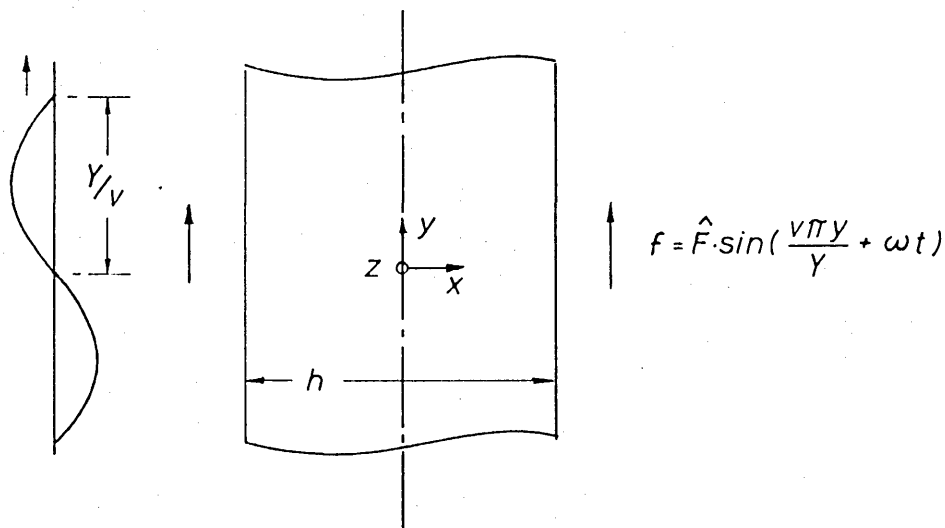


fig.33. Penetration of a rotating flux wave into a lamination.

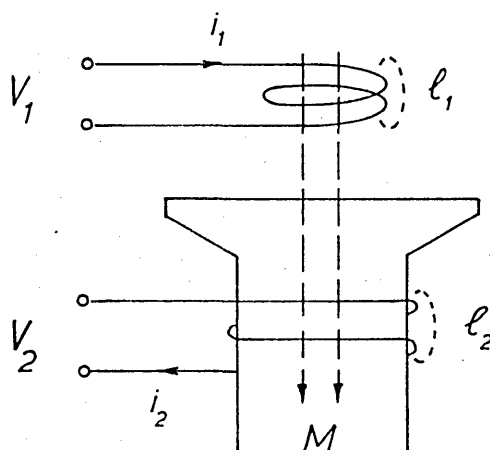


fig.34. Penetration of flux into a tooth.

$$\begin{aligned}
 P_e'' &= \frac{h^3 B^2 \omega^2}{2^4 \rho} (\delta b)^2 \\
 &= \frac{h^3 \hat{\Phi}^2 \omega^2}{2^4 \rho n^2}
 \end{aligned}$$

If there is a total of  $N$  curvilinear squares in the flux plot, and the number of rotor slots is  $S_2$ , then the total surface eddy current loss becomes:

$$P_e'' = S_2 \cdot \frac{N\ell}{n^2 \cdot 2^4 \rho} (\hat{\Phi} \omega h)^2 \quad (6.56)$$

Substituting for the values of  $\hat{\Phi}$  given by Eqns. 6.53 and 6.55 for the sine and cosine components of the flux respectively, one finally gets:

$$\begin{aligned}
 P_{ev}'' &= \frac{S_2 \ell}{2^4 \rho} \cdot \left( \frac{B_{1v} \cdot Y \omega s_v h}{v \pi} \right)^2 \cdot \left[ \frac{N_1}{n_1^2} (1 - \cos \beta_v')^2 + \right. \\
 &\quad \left. + \frac{N_2}{n_2^2} \left( \frac{v \pi x_o}{Y} \right)^2 \cdot \left( \frac{\sin \frac{v \pi x_o}{Y}}{\frac{v \pi x_o}{Y}} - \frac{\sin \beta_v''}{\beta_v''} \right)^2 \right] \quad (6.57)
 \end{aligned}$$

where subscript "1" refers to the sine flux plot and subscript "2" to the cosine one.

Using Eqn. 6.57 the surface loss in the rotor, produced by the  $v^{\text{th}}$  stator harmonic can be calculated, and the sum of the losses produced by all the harmonics will give the total rotor surface loss.

It should be noted that skin effects have been completely neglected and so the value of the surface

loss calculated from Eqn. 6.57 will give a value on the high side since the volume of the material excited by the harmonic flux is in fact reduced by the reaction of the eddy currents.

Carter<sup>21</sup> considered the problem of a wave travelling on top of a smooth laminated surface and obtained expressions for the surface loss which take into consideration the damping of the flux by the eddy currents as well as the boundary conditions imposed by the edges of the laminations.

The surface losses calculated by the present semi-analytical method applied to rotor No.1, gave values about twice as high as those calculated by Carter's method. This is partly due to the neglected eddy current reaction effect but also due to the fact that the surface losses are increased by the slotting of the rotor surface as shown by Dreyfus.<sup>20</sup> This last effect was not included in Carter's analysis.

In the actual calculation a value half way between that given by Eqn. 6.57 and that given by Carter's method was used. The numerical results have shown that the surface losses in the rotor were not a very large part of the total load loss and hence the small errors introduced by the compromising method of calculation mentioned above were not very important.



### 6.4.3 The reduction of leakage reactance.

The eddy currents that are induced on the rotor surface not only cause losses in the surface itself, but by damping the differential harmonic leakage flux of the squirrel cage, cause more harmonic currents to flow in the bars and hence also increase the bar  $I^2R$  losses. This increase of the bar  $I^2R$  loss is by no means secondary in importance to the rotor iron surface losses. This is particularly so when skin effects are pronounced, (i.e. at high harmonic frequencies), in which case the extra bar losses can be several times the value of the surface loss.

To account for this effect the factor  $k_{d\ell}$  by which the undamped value of the differential leakage reactance must be multiplied will now be calculated.

Consider an mmf wave given by  $f_y = F_y \sin(\frac{v\pi y}{\tau} + \omega_y t)$  to travel on the two sides of a lamination of thickness  $h$  as shown in Fig.33. If the displacement current in the iron is neglected in comparison with the conduction current, it is shown in Appendix IV that the  $y$ -component of the phasor flux density inside the lamination satisfies the equation:

$$\frac{\partial^2 B_{yv}}{\partial x^2} - k^2 B_{yv} = 0 \quad (6.58)$$

$$\text{where } k^2 = \frac{j \omega \mu \mu_o}{\rho} + \left(\frac{v\pi}{Y}\right)^2 \quad (6.59)$$

The solution for  $B_{yv}$  therefore has the form:

$$B_{yv} = C_1 e^{kx} + C_2 e^{-kx} \quad (6.60)$$

where  $C_1$  and  $C_2$  are constants that can be evaluated from the fact that on the surface of the lamination, ( $x = \pm h/2$ ), the flux density becomes  $B_{ov} = \mu_o F_{ov}$ .

The constants are then calculated as:

$$C_1 = C_2 = \frac{B_{ov}}{e^{hk/2} + e^{-hk/2}}$$

and the flux density at any point inside the lamination is therefore given by:

$$B_{yv} = B_{ov} \cdot \frac{\cosh kx}{\cosh \frac{kh}{2}}$$

The total flux carried by the lamination per unit length in the  $z$ -direction is:

$$\begin{aligned} \Phi_v &= \int_{-h/2}^{+h/2} B_{yv} dy \\ &= B_{ov} \cdot \frac{2}{k} \tanh \frac{hk}{2} \end{aligned}$$

If no eddy currents were present and the flux penetration was unopposed the lamination would carry a flux  $\Phi_{ov}$  given by:

$$\Phi_{ov} = B_{ov} \cdot h$$

$$\text{Hence: } \frac{\Phi_v}{\Phi_o} = \frac{\tanh \frac{kh}{2}}{\frac{kh}{2}} \quad (6.61)$$

If the forcing mmf on the surfaces of the lamination was pulsating instead of a travelling wave the flux attenuation would still be given by an expression of the form shown by Eqn. 6.61 but  $k^2$  would have the value:  $j\omega_v\mu\mu_o/\rho = 1/\delta^2$  where  $\delta$  is the classical depth of penetration.

It is seen from Eqn. 6.59 that the effective penetration of the flux into the lamination is slightly worse for a travelling rather than a pulsating magnetic field. However, at the values of frequency ( $\omega_v$ ) and wavelengths ( $2Y/v$ ) in question this change is totally negligible as can be seen by comparing the two terms of Eqn. 6.59. The second term is less than 1% of the first term and hence to a good approximation:

$$k^2 = \frac{j\omega_v\mu\mu_o}{\rho} = \frac{1}{\delta^2}$$

in which case Eqn. 6.61 reduces to:

$$k_{d\ell v} \equiv \frac{\Phi_v}{\Phi_{ov}} = \frac{\tanh \frac{h}{2\delta}}{h/2\delta} \quad (6.62)$$

The damping factor  $k_{d\ell v}$  is shown plotted in Fig. 35 against frequency and with the permeability  $\mu$  as a parameter. The figure applies to laminations of thick-

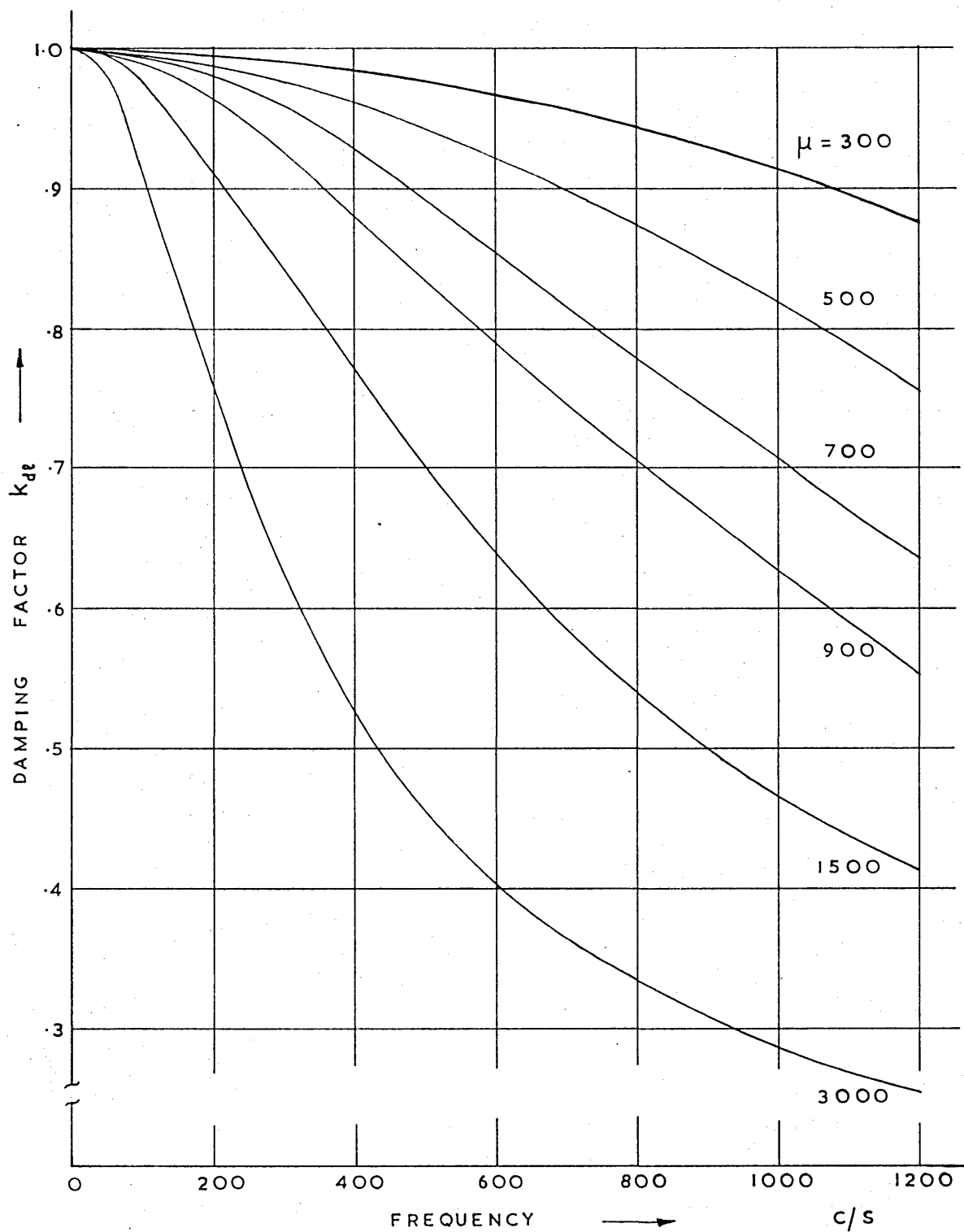


fig.35. Variation of  $k_d$  with frequency.

ness .635 mm which are used in all the experimental rotors. A value of  $\mu$  of 900 was used in the calculations and this choice is explained in the next Section.

## 6.5 Iron losses in the rotor teeth.

### 6.5.1 Damping of the tooth flux.

It was calculated in Section 6.41 that an amount of flux  $\Phi_{tvo}$  given by Eqn. 6.51 penetrates the whole of the rotor tooth and not merely the surface.

The flux density in the tooth body is therefore given by:

$$B''_{tvo} = B_{1v} \cdot \left( \frac{\lambda_2 \ell}{w''_t} \right) \cdot \left( \frac{\sin \beta''_v}{\beta''_v} \right) \quad (6.63)$$

where  $w''_t$  is the width of the rotor tooth body.

In a squirrel cage, however, each rotor tooth has a low impedance loop surrounding it and therefore circulating currents can be induced in this loop to oppose the flux penetration into the tooth.

Consider for example the analogous system shown in Fig.34.  $M$  is the mutual inductance between the two coils and  $\ell_1$  and  $\ell_2$  their leakage inductances.

It can be easily shown that for this system the damping of the tooth flux by the currents circulating round the tooth is given by the factor,

$$k''_{tv} \equiv \frac{\Psi_m}{\Psi_{m0}} = 1 - \frac{M}{M + \ell_2} \quad (6.64)$$

The value of  $M$  in Eqn. 6.64 includes not only the magnetising field reactance  $x_{mv}$  but also the differential harmonic reactance  $x_{2dv}$ .

$$\text{Thus } M = x_{mv} + x_{2dv} \quad (6.65)$$

Although normally  $x_{2dv}$  is considered as a leakage reactance for calculations of torque from the equivalent circuit; in the context of the present discussion it cannot be considered as such since it is directly the result of the harmonic currents induced in the squirrel cage bars by the air gap harmonic fields. It should be noted here that the difference between the actual stepped air gap field and the fundamental sinusoid is not a true leakage flux. For example the stator and rotor field waveforms may be stepped, but if they are identical the true leakage is zero, despite the fact that neither waveforms are sinusoidal.

The subharmonic fields produced by the stepped mmf waveform may or may not produce torques - depending on the stator and rotor circuits - but they always contribute to the damping of the tooth fluxes.

The leakage reactance  $\ell_2$  is the sum of the slot and skew leakage, i.e.

$$\begin{aligned} \ell_2 &= x_{2sl} + x_{skv} \\ &= x_{2sl} + x_{mv} \left[ \frac{1 - k_{skv}^2}{k_{skv}^2} \right] \end{aligned} \quad (6.66)$$

where  $x_{2sl}$  includes the small end-ring leakage to the actual slot leakage.<sup>3</sup>

Substituting Eqns. 6.65 and 6.66 into Eqn. 6.64 gives:

$$k''_{tv} = 1 - \frac{x_{mv} + x_{2dv}}{\frac{x_{mv}^2}{k_{skv}^2} + x_{2dv} + x_{2sl}} \quad (6.67)$$

The flux density penetrating the rotor tooth bodies is therefore modified by this factor and is given by:

$$\begin{aligned} B''_{tv} &= B''_{tvo} \cdot k''_{tv} \\ &= k''_{tv} \cdot B_{1v} \left( \frac{\lambda_2}{w_t''} \right) \cdot \left( \frac{\sin \beta_v''}{\beta_v''} \right) \end{aligned} \quad (6.68)$$

### 6.5.2 Calculation of rotor tooth iron losses.

The flux density  $B''_{tv}$  given by Eqn. 6.68 causes both eddy current and hysteresis losses in the tooth iron. The hysteresis losses, however, are very difficult to calculate exactly, due to the unsymmetrical magnetisation of the iron.<sup>23,24,25</sup>

Since the magnetising mmf consists of a main field and a series of harmonics, (particularly the slot-harmonics), the hysteresis loop traversed will have several minor loops quite apart from the main loop. If only one harmonic mmf is considered together with the

fundamental then the hysteresis loop is as shown in Fig.36. The total hysteresis loss per fundamental cycle in this case is given by:

$$\text{Loss/cycle} = A_0 + \sum_{n=1}^v A_{nv}$$

where  $A_0$  is the area of the main loop due to the fundamental and  $A_{nv}$  is the area of the  $n^{\text{th}}$  minor loop due to the  $v^{\text{th}}$  stator harmonic.

The total hysteresis loss per cycle considering all the harmonic mmfs superimposed on the main field, but neglecting the interaction between the harmonics themselves, is therefore:

$$\text{Total loss/cycle} = A_0 + \sum_{v \neq 1}^{\infty} \sum_{n=1}^v A_{nv} \quad (6.69)$$

Obviously one cannot use Eqn. 6.69 for any practical calculations without doing a great deal of experimental work on the magnetic material itself.

In view of this difficulty the iron losses in the teeth - both eddy current and hysteresis - were calculated by Eqn. (6.70) which was suggested by Richter.<sup>26</sup>

$$P_{tv}'' = (B_{tv}'')^2 \cdot [\sigma_h f_v + \sigma_e f_v^2] \cdot W_t'' \cdot S_2 \quad (6.70)$$

where  $\sigma_h$  and  $\sigma_e$  are experimentally determined material constants<sup>25,27,28,29</sup> and  $f_v$  is the frequency of the rotor tooth flux pulsation due to the  $v^{\text{th}}$  stator field



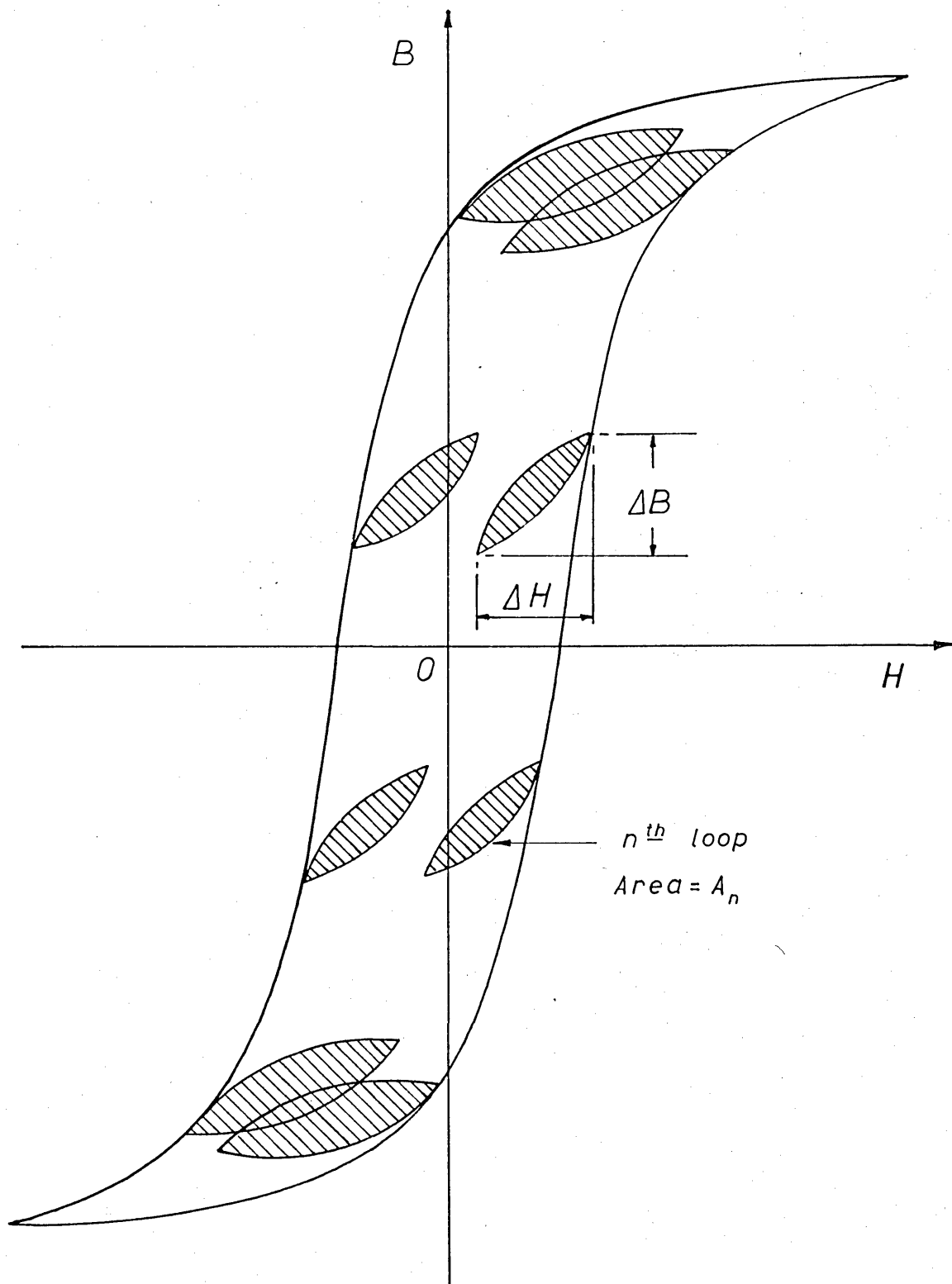


fig.36. Unsymmetrical hysteresis loop.

(Fundamental plus one harmonic pulsation.)

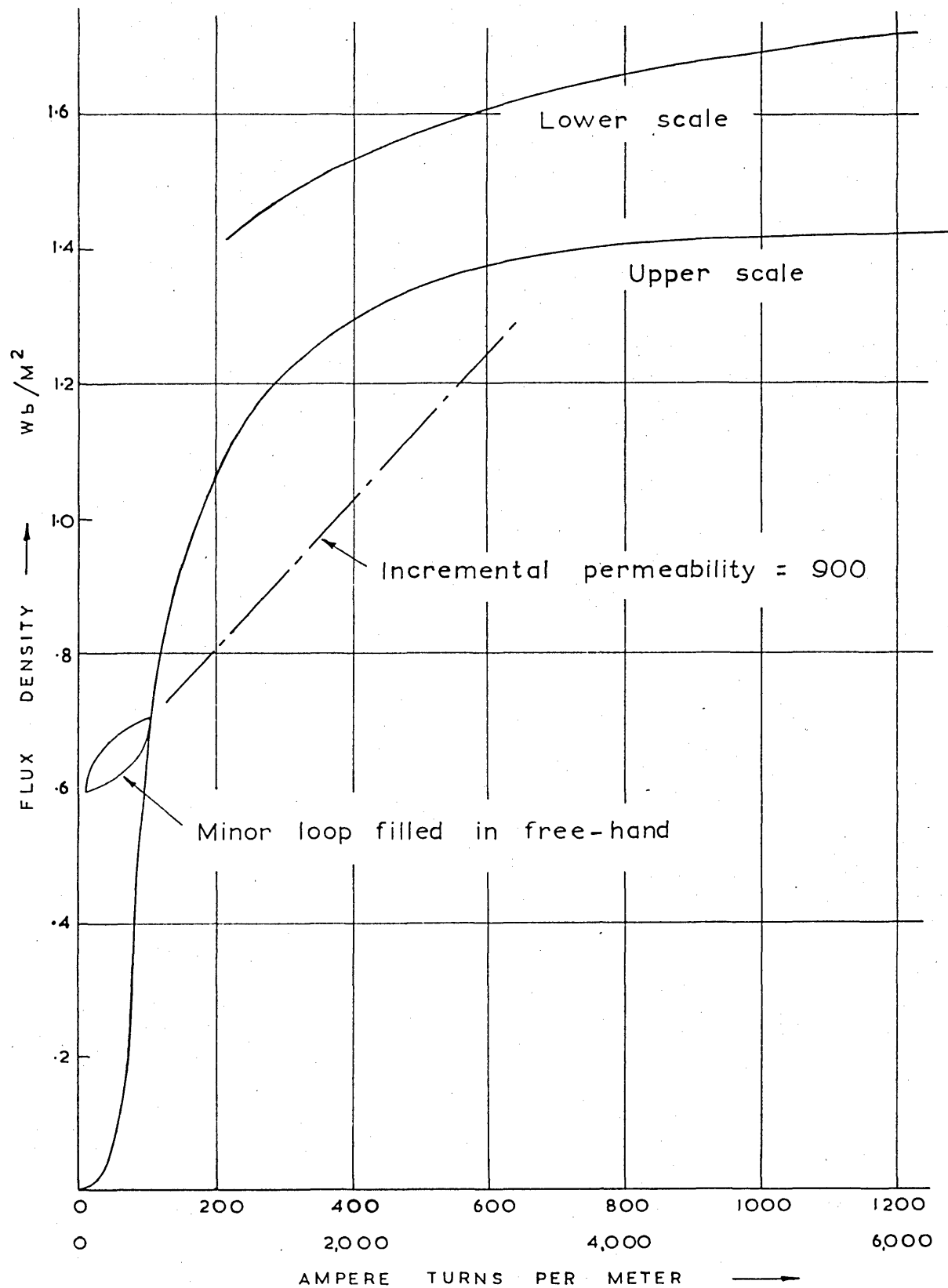


fig.37. Magnetization curve of rotor iron.

harmonic.  $W_t''$  is the weight of the rotor tooth body, including a correction due to the iron in the rotor core between two consecutive teeth, which is also excited by the harmonic tooth flux.<sup>20</sup>

### 6.5.3 Choice of iron permeability.

In view of what has already been said about the nature of magnetisation in the teeth, the magnetic permeability that should be used in connection with the field harmonics, (e.g. in calculating the damping factor  $k_{d\ell v}$  in Section 6.4.3), should be the incremental permeability given by:

$$\mu = \frac{\Delta B}{\Delta H} \quad (\text{see Figs. 37 \& 36}) \quad (6.71)$$

This value of permeability varies between the different minor loops, depending on the value that the fundamental flux density has at the instant of the pulsation. However, an overall mean value can be estimated and a value of incremental  $\mu$  of 900 was chosen for the numerical computations, based partly on the results of Spooner<sup>30</sup>, Ball<sup>23</sup> and reference 29 and partly on the results of Smith<sup>31</sup> who showed that the value of incremental  $\mu$  can be appreciably reduced when the pulsations occur at high frequencies, (like the present case).

## 6.6 Load losses in the stator due to the rotor mmf harmonics.

The last three Sections, have dealt with the losses that are produced in the rotor by the stator field harmonics. This Section will consider the losses produced in the stator due to the rotor field harmonics which result from the rotor stepped mmf distribution. In many ways the losses in the stator can be deduced from the formulae giving the losses in the rotor by interchanging stator and rotor quantities as explained below.

### 6.6.1 Harmonic losses in stator winding.

The rotor harmonic fields will induce harmonic currents in the stator winding if closed paths exist for them to flow in.<sup>16</sup> The magnitude of the induced currents will depend on the magnetic interlinkage between the stator and rotor windings with respect to the harmonic in question. Thus the  $\mu^{\text{th}}$  rotor harmonic given by Eqn. 6.21 induces currents in the stator whose magnitude is reduced by the factors:

$$k_{dp\mu} = \left( \frac{\sin \frac{\mu\pi}{2q}}{n \sin \frac{\mu\pi}{2nq}} \right) \cdot \sin \frac{\mu\pi Y}{2Y} \quad (6.72)$$

$$\text{and } k_{sk\mu} = \left( \frac{\sin \alpha_{\mu} \ell/2}{\alpha_{\mu} \ell/2} \right) \quad (6.73)$$

The factor of Eqn. 6.72 is the stator winding factor with respect to the  $\mu^{\text{th}}$  rotor harmonic and the factor of Eqn. 6.73 the skew factor also with respect to the same harmonic.

For the stator slot harmonics  $k_{dp\nu}$  is always equal to  $k_{dp1}$  and is very nearly equal to unity; whereas for the rotor slot harmonics  $k_{dp\mu} < k_{dp1}$  in all cases. Thus the stator slot harmonics are reduced only by skewing whereas the rotor slot harmonics are reduced by skewing as well as by the stator pitching.

The factor  $k_{dp\mu}$  is small for the usual stator pitching and slot combinations, and the losses produced by the harmonic currents induced in the stator winding are negligible as they are proportional to  $k_{dp\mu}^2$ . Hence in most practical cases the stator winding can be assumed to present an open-circuit to the rotor slot harmonics.<sup>4</sup>

In special cases where  $k_{dp\mu}^2$  is not small the extra losses in the stator can be calculated quite easily by conventional theory applied to each rotor harmonic. Alternatively the losses can even be deduced from Eqn. 6.43 by multiplying it by  $k_{dp\mu}^2$ , setting  $r_{bb} = \infty$ , and interchanging rotor bar quantities with stator quantities referred to a single stator slot.

### 6.6.2 Losses in the stator iron surface and the stator teeth.

The pattern of flux penetration into the stator teeth can be deduced in an exactly analogous way to that used for the calculation of flux densities in the rotor teeth. (Sections 6.4 and 6.5). The harmonic flux density in the stator tooth body can therefore be calculated to be:

$$B'_{t\mu 0} = B_{2\mu} \cdot \left( \frac{\lambda_1 \ell}{w'_t} \right) \cdot \left( \frac{\sin \beta'_{\mu}}{\beta'_{\mu}} \right) \quad (6.74)$$

and since only the rotor slot harmonics induced by the stator fundamental field need be considered; (see Section 6.1.2)  $B_{2\mu}$  becomes  $B \frac{k_2 S_2}{(\frac{2}{p} + 1)}$  which is given by Eqn. 6.25. The angle  $\beta'_{\mu}$  in Eqn. 6.74 is half the electrical angle that a stator tooth subtends with respect to the  $\mu^{\text{th}}$  rotor field harmonic. ( $\beta'_{\mu} = \frac{\mu \pi \lambda_1}{2Y}$ ).

Since the flux given by Eqn. 6.74 can penetrate a stator tooth unopposed, it causes an iron loss in the teeth - both due to eddy currents and hysteresis - whose total value is:

$$P'_{t\mu} = (B'_{t\mu 0})^2 \cdot [\sigma_h f_{\mu} + \sigma_e f_{\mu}^2] \cdot w'_t \cdot S_1 \quad (6.75)$$

Again  $W_t'$  is the weight of one stator tooth body increased by the weight of some of the iron in the stator core, between two consecutive teeth, which is also excited by the harmonic tooth flux.<sup>20</sup>.

## 6.7 Effect of saturation on the load loss formulae.

### 6.7.1 Necessary modifications.

In the foregoing theory it has been assumed that the stator and rotor mmf waveforms can be analysed into series of harmonics, and that each harmonic can be considered in isolation from the rest. Under the non-linear conditions resulting from saturation, it is strictly not possible to consider each harmonic field separately and calculate the total load loss by adding the individual harmonic losses. This restriction, however, must be relaxed by necessity since it is simply not feasible to consider the losses and torques produced by a stepped stator applied mmf without first analysing the mmf waveform into harmonics. A further justification for considering the mmf waveform as a series of harmonic fields, even under saturated conditions, comes from the fact that the harmonics are small compared with the fundamental and therefore non-linear interactions between themselves can be neglected. Thus each harmonic can be considered by itself together with

the fundamental provided that incremental quantities are used for the harmonic parameters.

The effect of saturation of the main magnetic flux paths on the load losses is therefore assumed to be fully taken into account by:

(i) Increasing the effective value of the air gap in the formulae of Sections 6.1 to 6.6, by a factor  $k_{s1}$  (to be calculated).

(ii) Reducing the effective value of the incremental permeability of the rotor iron in Section 6.5.

The effect of saturation of the leakage magnetic flux paths on the load losses is included by applying a saturation factor  $k_{s2}$  to the harmonic magnetising reactance  $x_{mv}$  and differential leakage reactance  $x_{2dv}$  in the load loss formulae. This factor  $k_{s2}$  is calculated in exactly the same way as the saturation factor for the zig-zag leakage is calculated by Angst,<sup>32</sup> (see also Chapter 7).

All that is left therefore is to calculate the factor  $k_{s1}$  due to the saturation of the main magnetic flux paths. The incremental permeability under saturated conditions can be chosen by the empirical laws given by Spooner.<sup>30</sup>



## 6.7.2 The saturation factor $k_{s1}$ .

### 6.7.2.1 The definition of $k_{s1}$ .

Numerical computations using the formulae developed in the last five Sections indicate that the slot harmonics (of both the stator and the rotor) are the main contributors to the total load losses. These harmonics follow the flux-paths shown dotted in Fig.38.

If at any instant of time, slot A is displaced by an electrical angle  $\theta$  from the centre of the phase band carrying maximum current, then, neglecting the variations of the main flux density over a single slot pitch, the flux density in the teeth on either side of slot A is approximately given by, say,  $b_{ms}(\theta)$  and that in the teeth on either side of the rotor slot B approximately given by, say,  $b_{mr}(\theta)$ . These flux densities cause mmf drops of  $F_s(\theta)$  in one stator tooth and  $F_r(\theta)$  in one rotor tooth. The mmf drops in the cores over the distance  $\lambda_1$  and  $\lambda_2$  are small and are neglected.

Thus if the mmf drops across the air gap at the point  $\theta$  is  $F_g(\theta)$ , then the total mmf consumed in one half of the slot harmonic flux path shown dotted is  $F_g(\theta) + F_s(\theta) + F_r(\theta)$  and this is equivalent to increasing the value of the air gap by the factor:

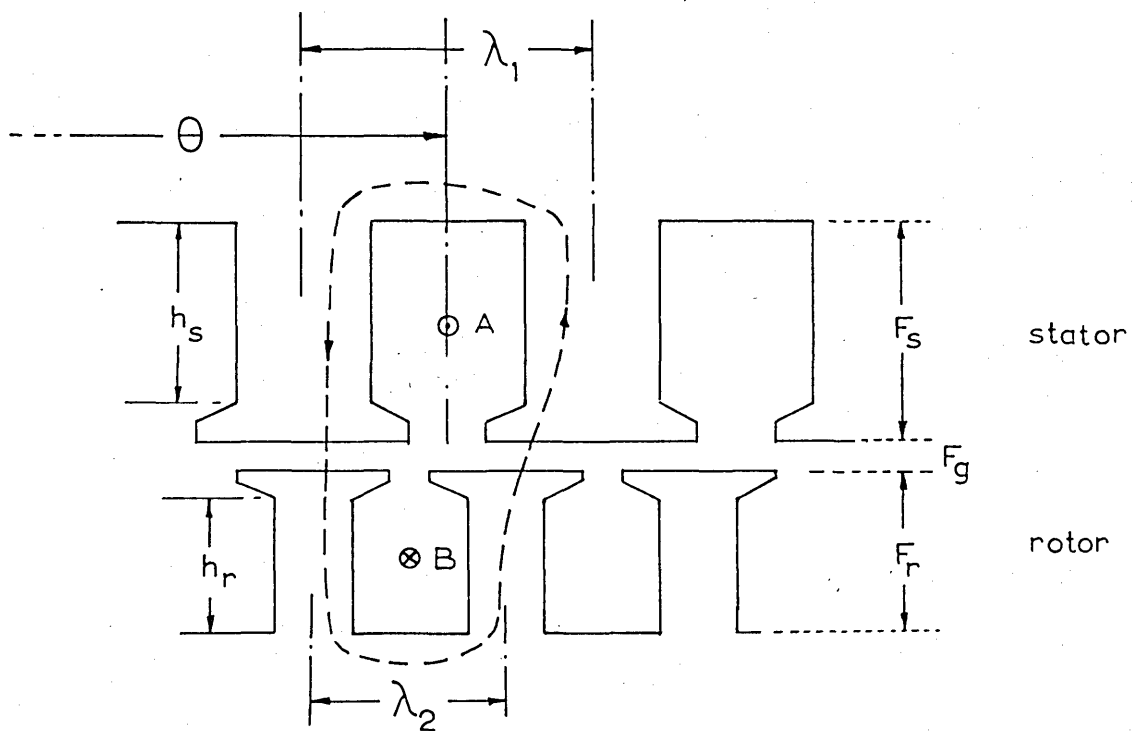


fig.38. Slot harmonic flux paths.

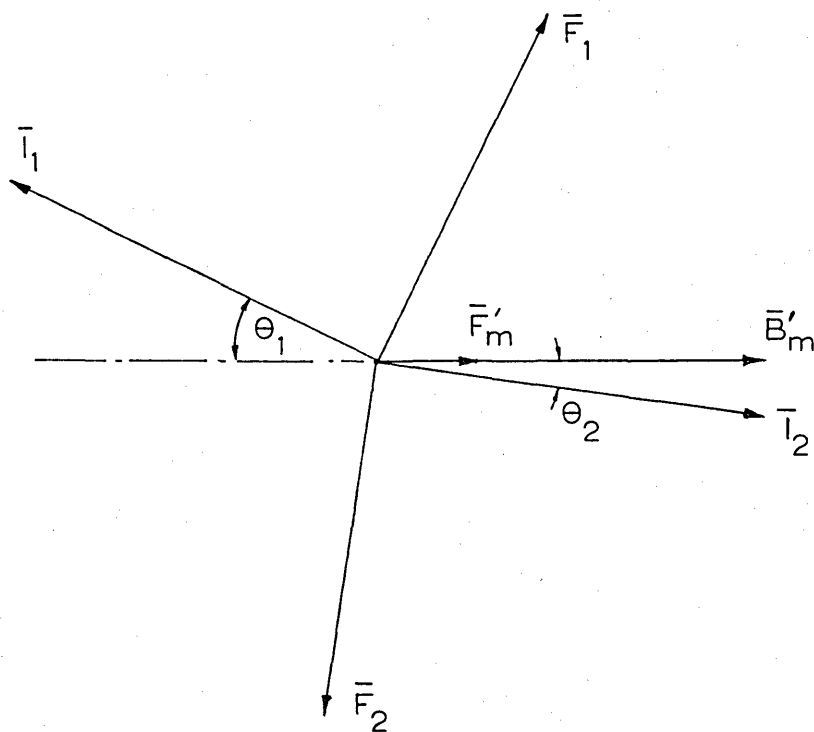


fig.39. Induction motor phasor diagram.

$$k_s(\theta) = 1 + \frac{F_s(\theta) + F_r(\theta)}{F_g(\theta)} \quad (6.76)$$

It is explained in Chapter 5 that the load losses can be taken to vary as  $i_1^2$  and since  $i_1 = I_1 \cos \theta$ , the importance that the saturation of a tooth has on the load losses is determined by the "weight" factor  $\cos^2 \theta_A$  where  $\theta_A$  is the distance of the tooth from the maximum current density position. The total weight is given by:

$$w = \int_{-\pi/2}^{\pi/2} \cos^2 \theta \, d\theta = \pi/2$$

and hence the value of the saturation factor properly averaged over a pole pitch is given by:

$$k_{s1} = \frac{2}{\pi} \int_{-\pi/2}^{\pi/2} k_s(\theta) \cos^2 \theta \, d\theta \quad (6.77)$$

#### 6.7.2.2 The calculation of flux densities.

The phasor diagram of the induction motor is shown in Fig.39. The space phasors  $\bar{I}_1$  and  $\bar{I}_2$  represent the stator and rotor currents and are in line with the position where the currents are maximum.

The mmf phasors  $\bar{F}_1$  and  $\bar{F}_2$  represent the magnetic axes of  $\bar{I}_1$  and  $\bar{I}_2$  and are therefore at right angles to the currents.

Fig.40 shows the current density and flux density waves in the air gap of a developed machine.

The curve  $b'_{mg}$  corresponds to the phasor  $\bar{B}'_m$  and  $i_1$  to the phasor  $\bar{I}_1$  in Fig.39. The actual flux density distribution, however, has a flattened top due to the iron saturation as shown by the curve  $b_{mg}$ . This curve can be analysed into a fundamental sinusoidal flux distribution of the same pole pitch as  $b'_{mg}$  and a series of harmonics, by far the most important of which is the third.<sup>33,34</sup>

Thus to a good approximation.

$$b_{mg} = B''_{mg} \cos(\theta + \theta_1) - k_3 B''_{mg} \cos(3(\theta + \theta_1)) \quad (6.78)$$

where  $B''_{mg}$  is the amplitude of the fundamental component of  $b_{mg}$ .

If the total flux per pole is  $\Phi$  then:

$$\Phi = \frac{\ell Y}{\pi} \int_{\pi/2 - \theta_1}^{\pi/2 + \theta_1} b_{mg} d\theta$$

which gives  $B''_{mg} = \frac{\pi \Phi}{2 \ell Y (1 + \frac{1}{3} k_3)} \quad (6.79)$

The flux densities in the stator and rotor teeth are  $b_{ms} = b_{mg} \cdot \lambda_1 / w'_t$  and  $b_{mr} = b_{mg} \cdot \lambda_2 / w''_t$  where  $\lambda_1$  and  $\lambda_2$  are the slot pitches and  $w'_t$  and  $w''_t$  the tooth body widths of the stator and the rotor respectively.

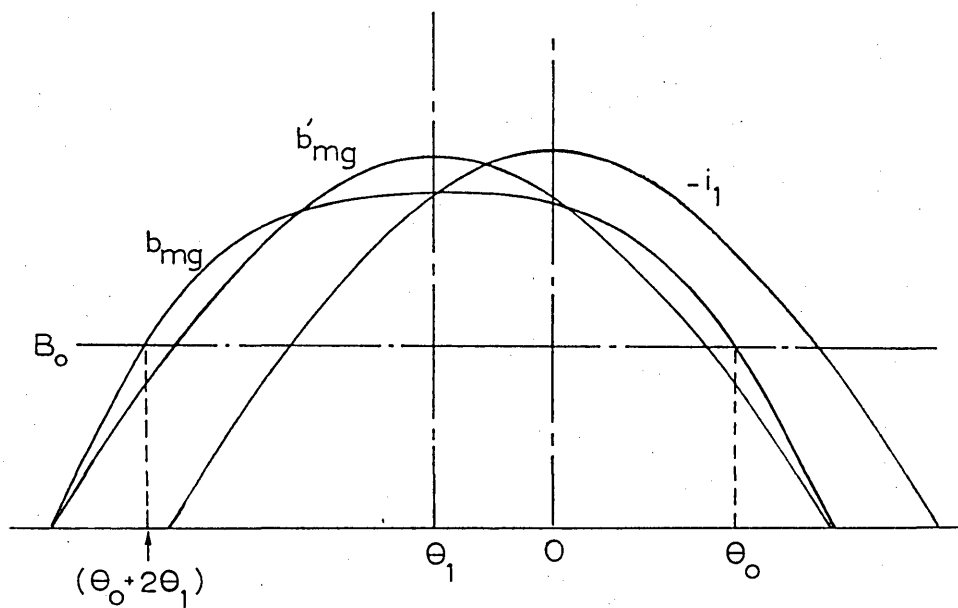


fig.40. Current and flux density distributions.

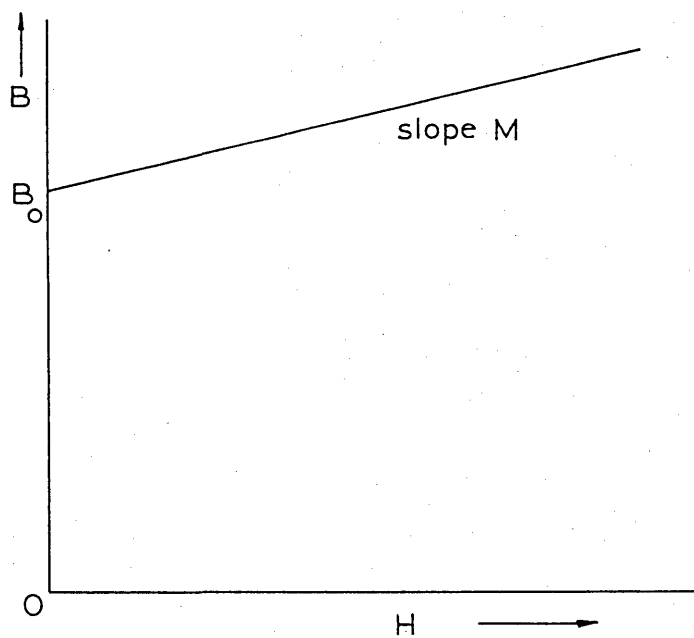


fig.41. Idealised saturation curve.

The amplitudes of the fundamentals of  $b_{ms}$  and  $b_{mr}$  are therefore given by:

$$B_{ms}'' = \frac{\pi p \Phi}{\ell_w' S_1 (1 + \frac{1}{3} k_3)} \quad 6.80(a)$$

$$\text{and } B_{mr}'' = \frac{\pi p \Phi}{\ell_w'' S_2 (1 + \frac{1}{3} k_3)} \quad 6.80(b)$$

respectively.

The flux  $\Phi$  is given by:  $\Phi = V_1 \sqrt{2/(\pi f Z_1 k_{dp1})}$

#### 6.7.2.3 The calculation of $k_{s1}$

Let the magnetisation curve of the iron be approximated by a straight line intersecting the flux density axis at  $B_o$  as shown in Fig. 41. When the tooth flux densities are less than  $B_o$ , no ampere turns are consumed in the teeth and the factor  $k_s(\theta)$  in Eqn. 6.76 is unity.

Let the stator tooth flux density  $b_{ms}$  reach the value  $B_o$  at an angle  $\theta_o$ , then from Eqns. 6.78, 6.79 and 6.80(a)

$$B_{ms}'' \cos(\theta_o + \theta_1) - k_s B_{ms}'' \cos 3(\theta_o + \theta_1) = B_o$$

$$\text{or: } \cos^3(\theta_o + \theta_1) - \left( \frac{1+3k_3}{4k_3} \right) \cos(\theta_o + \theta_1) + \frac{1}{4k_3} \cdot \left( \frac{B_o}{B_{ms}''} \right) = 0$$

(6.81)

Eqn. 6.81 is a cubic in  $\cos(\theta_o + \theta_1)$  and can be solved to yield  $\theta_o$ . The rotor tooth flux density  $b_{mr}$  reaches the value  $B_o$  at a different angle  $\theta'_o$ . In practice, however, the angles  $\theta_o$  and  $\theta'_o$  are very near each other, due to the fact that  $B''_{ms}$  and  $B''_{mr}$  are only slightly different.

When the total flux densities are greater than  $B_o$ , the magnetic field intensity is given by:

$$H = \frac{B}{M} - \frac{B_o}{M} \quad (6.82)$$

Thus the ampere turns consumed in a stator tooth is:

$$F_s(\theta) = \frac{B''_{ms}}{M} \cdot h_s [\cos(\theta + \theta_1) - k_3 \cos 3(\theta + \theta_1)] - \frac{B_o}{M} \cdot h_s \quad (6.83)$$

and those in a rotor tooth:

$$F_r(\theta) = \frac{B''_{mr}}{M} \cdot h_r [\cos(\theta + \theta_1) - k_3 \cos 3(\theta + \theta_1)] - \frac{B_o}{M} \cdot h_r \quad (6.84)$$

The ampere turns consumed in the air gap is:

$$F_g(\theta) = \frac{B''_{mg}}{\mu_o} \cdot g \cdot [\cos(\theta + \theta_1) - k_3 \cos 3(\theta + \theta_1)] \quad (6.85)$$

Substituting Eqns. 6.83, 6.84 and 6.85 into Eqn. 6.76 gives:

$$k_s(\theta) = a_1 - a_2 \cdot \frac{1}{\cos(\theta + \theta_1) - k_3 \cos 3(\theta + \theta_1)} \quad (6.86)$$

$$\text{where: } a_1 = 1 + \frac{\mu_o (B''_{ms} \cdot h_s + B''_{mr} \cdot h_r)}{M \cdot g \cdot B''_{mg}} \quad (6.87)$$

$$\text{and } a_2 = \frac{\mu_o B_o (h_r + h_s)}{MgB''_{mg}} \quad (6.88)$$

Two cases will now be discussed:

(i) when  $\theta_1 > \frac{\pi}{4} - \frac{\theta_o}{2}$  as shown in Fig.42(a)

and (ii) when  $\theta_1 < \frac{\pi}{4} - \frac{\theta_o}{2}$  as shown in Fig.42(b).

Case (i). The value of  $k_s(\theta)$  is given by Eqn. 6.86 in the ranges  $-\pi/2 < \theta < \theta_o$  and  $\pi - \theta_o - 2\theta_1 < \theta < \pi/2$ , and is equal to unity in the range  $\theta_o < \theta < \pi - \theta_o - 2\theta_1$ . Thus from Eqn. 6.77 the saturation factor is given by:

$$\begin{aligned} k_{s1} = & \frac{2}{\pi} \int_{-\pi/2}^{\theta_o} \left[ a_1 \cos^2 \theta - \frac{a_2 \cos^2 \theta}{\cos(\theta + \theta_1) - k_3 \cos 3(\theta + \theta_1)} \right] d\theta \\ & + \frac{2}{\pi} \int_{\pi - \theta_o - 2\theta_1}^{\pi/2} \left[ a_1 \cos^2 \theta - \frac{a_2 \cos^2 \theta}{\cos(\theta + \theta_1) - k_3 \cos 3(\theta + \theta_1)} \right] d\theta \\ & + \frac{2}{\pi} \int_{\theta_o}^{\pi - \theta_o - 2\theta_1} \cos^2 \theta d\theta \end{aligned} \quad (6.89)$$

After integration the above expression reduces to:



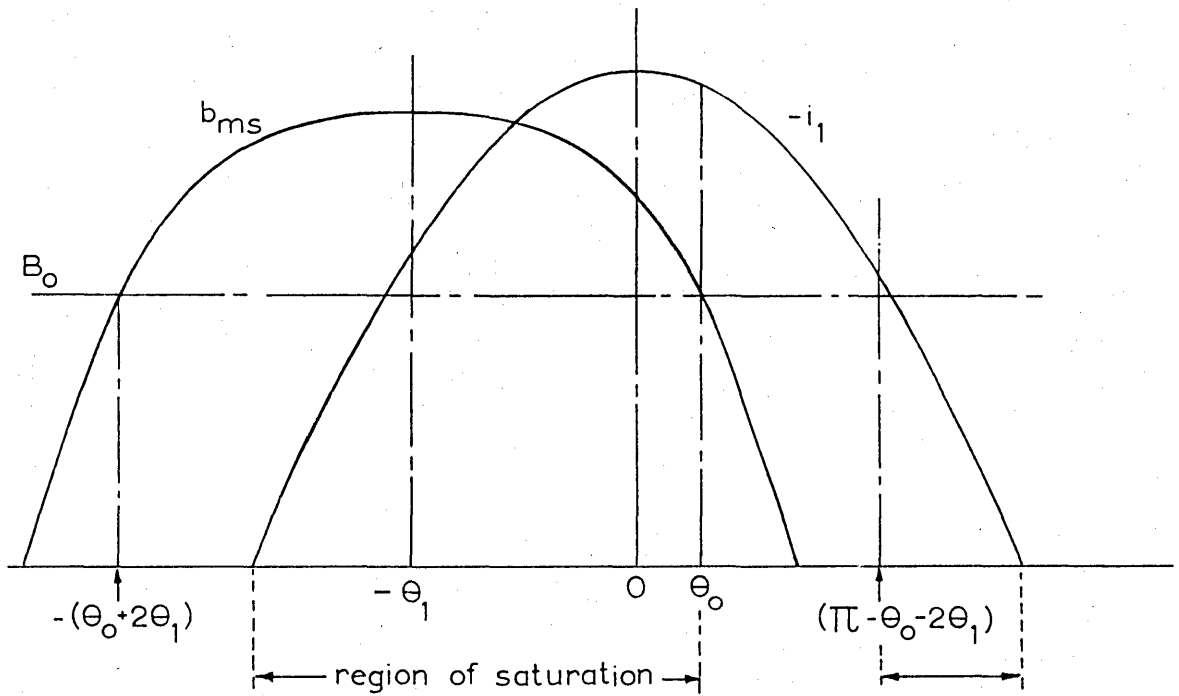


fig.42.a. Main flux saturation when  $\theta_1 > \pi/4 - \theta_0/2$

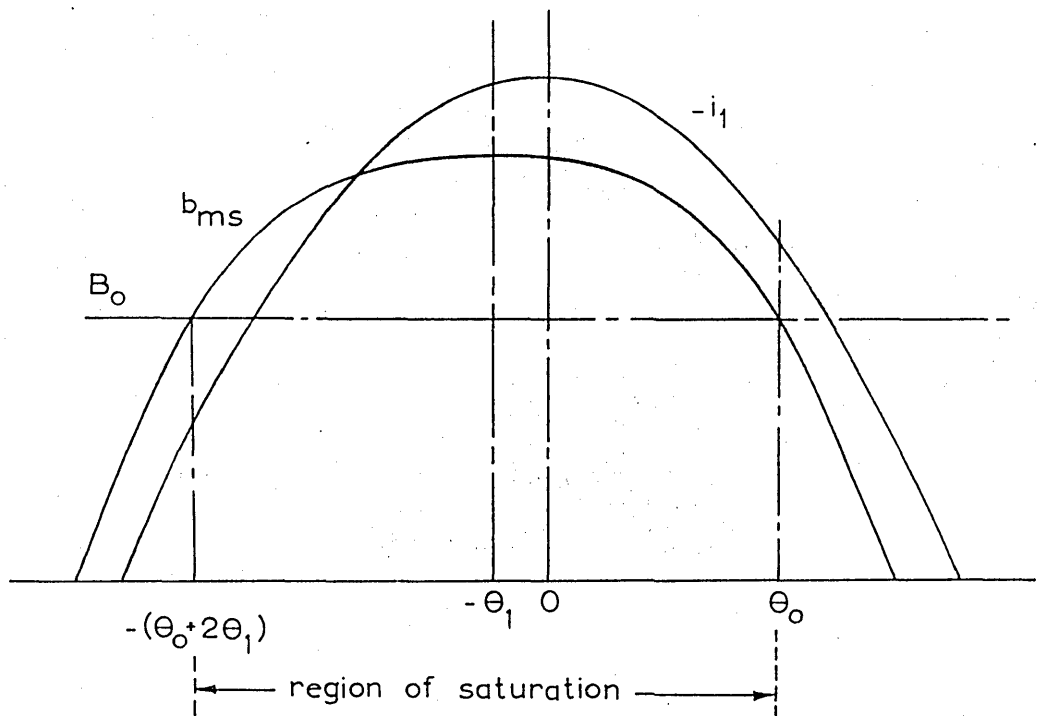


fig.42.b. Main flux saturation when  $\theta_1 < \pi/4 - \theta_0/2$

$$\begin{aligned}
k_{s1} = 1 + \frac{2}{\pi} [(a_1-1)(\theta_o + \theta_1) + \frac{(a_1-1)}{4} \cdot (\sin 2\theta_o + \sin 2(\theta_o + 2\theta_1)) + \\
+ \frac{a_2 \sin 2\theta_1}{2 \sqrt{a_3} k_3} (\tanh^{-1} \frac{\cos(\theta_o + \theta_1)}{\sqrt{a_3}} - \tanh^{-1} \frac{\sin \theta_1}{\sqrt{a_3}}) \\
- a_4 \cdot \tan^{-1} \frac{\cos \theta_1}{\sqrt{a_3-1}} - \sin^2 \theta_1 \cdot \ln \frac{1 + \cos \theta_1}{1 - \cos \theta_1}] \quad (6.90)
\end{aligned}$$

where  $a_3 = (1+3k_3)/4k_3$  and  $a_4 = \frac{2(a_3 \cos 2\theta_1 + \sin^2 \theta_1)}{\sqrt{a_3-1}}$

Case (ii). The value of  $k_s(\theta)$  is given by Eqn. 6.86 in the range  $-2\theta_1 - \theta_o < \theta < \theta_o$  and is equal to unity in the ranges  $\theta_o < \theta < \pi/2$  and  $-\pi/2 < \theta < -2\theta_1 - \theta_o$ . Thus  $k_{s1}$  is again given by an expression of the same type as shown in Eqn. 6.89, but the limits of the first two integrals must be replaced by  $(-2\theta_1 - \theta_o)$  as the lower limit and  $\theta_o$  as the upper one. The limits of the third integral must be replaced by  $(\theta_o, -\pi/2)$  and  $(\pi/2, -2\theta_1 - \theta_o)$  on the lower and upper side respectively. The final integration gives the saturation factor as:

$$\begin{aligned}
k_{s1} = 1 + \frac{2}{\pi} [(a_1-1)(\theta_o + \theta_1) + \frac{(a_1-1)}{4} (\sin 2\theta_o + \sin 2(\theta_o + 2\theta_1)) \\
- a_4 \cdot \tan^{-1} \frac{\sin(\theta_o + \theta_1)}{\sqrt{a_3-1}} - \sin^2 \theta_1 \cdot \ln \frac{1 + \sin(\theta_o + \theta_1)}{1 - \sin(\theta_o + \theta_1)}] \quad (6.91)
\end{aligned}$$

The factor  $k_{s1}$  calculated in the above section is used to increase the effective value of the air gap for the slot harmonics from  $g$  to  $k_{s1} \cdot g$  when saturation of the main magnetic flux path is present. The

formulae developed in the first 5 Sections of the present Chapter are then used with this modified air gap to compute the value of the load losses under the normal operating conditions.

P A R T   T H R E E

THE DETERMINATION OF PARAMETERS IN THE  
THEORETICAL FORMULAE

## CHAPTER 7

### THE DETERMINATION OF PARAMETERS IN THE THEORETICAL FORMULAE

Before the theoretical formulae of Chapter 6 can be used to determine the load losses of a machine, the numerical values of the quantities which appear in the formulae must be known. The existing classical methods<sup>3,35</sup> of calculating harmonic parameters and especially harmonic reactances, are grossly inaccurate since they neglect the effects of slot openings, saturation, damping etc. It is the purpose of this Chapter to calculate some of these quantities and describe the measurement of those parameters which cannot be calculated.

#### 7.1 The calculation of harmonic resistance and reactances.

There are two harmonic reactances that appear in the theoretical formulae of Chapter 6. The magnetizing harmonic reactance  $x_{mv}$  and the rotor leakage harmonic reactance  $x_{2v}$ , (e.g. see the harmonic equivalent circuit of Fig.22).

##### 7.1.1 The magnetising reactance $x_{mv}$ .

The value of  $x_{mv}$  is given by Liwshitz<sup>3</sup> as:

$$x_{mv} = \frac{x_m}{v^2} \cdot \left( \frac{k_{dpv}}{k_{dp1}} \right)^2 \quad (7.1)$$

for the  $v^{\text{th}}$  stator field harmonic; where  $x_m$  is the magnetising reactance of the fundamental.

This value of  $x_{mv}$  applies to all phase belt harmonics but not to the slot harmonics. It was shown in Section 6.1 that the orders of the slot harmonics are such that their magnitudes are modified by the stator slot permeance variations, and that this effect could approximately be taken into consideration by increasing the magnetising reactance of these harmonics by a mean factor  $(1 + \frac{\Lambda_s}{2\Lambda_o})$ . Thus the magnetising reactance of the slot harmonics is given by:

$$x_{mv} = \frac{x_m}{v^2} \left( 1 + \frac{\Lambda_s}{2\Lambda_o} \right) \quad (7.2)$$

for  $v = r \frac{S_1}{p} + 1$ ;  $r = \pm 1, \pm 2, \pm 3 \dots$

It should be remembered that for the stator slot harmonics  $k_{dpv} = k_{dp1}$ .

Eqns. 7.1 and 7.2 apply only when the machine is not saturated.

It was shown in Section 6.7, that when the main magnetic flux paths are saturated by the fundamental flux, the effective value of the air gap is increased by a factor  $k_{s1}$  given by Eqns. 6.90 and 6.91. Since

$x_m$  is inversely proportional to the air gap,  $x_{mv}$  is effectively decreased by the factor  $(1/k_{s1})$ . The value of  $k_{s1}$  in Section 6.7 was calculated only for the slot harmonics. The saturation factors for the phase-belt harmonics are slightly higher than  $k_{s1}$  but, because of the relative unimportance of these harmonics, negligible error is introduced by the use of the same saturation factor.

An apparently similar, but in fact quite different effect occurs when the fundamental leakage flux paths are saturated by the harmonic fluxes themselves. Angst<sup>32</sup> has derived saturation factors by which the zig-zag leakage reactance, (which under the present nomenclature would be called the sum of the slot harmonic magnetizing reactances), is reduced due to the saturation caused by the load currents. Angst's method of calculating the saturation factors involves an iteration process between the saturation factor formulae (with an assumed stator current) and the usual equivalent circuit to determine the value of the stator current to be used in the next iteration. Thus the saturation factors obtained by this process take into consideration the fact that magnetic saturation reduces the slot harmonics according to a law which is somewhere between a constant harmonic flux law and a constant harmonic mmf

law. These saturation factors, ( $k_{s2}$ , say) are therefore applied to reduce the value of  $x_{mv}$  when the fundamental leakage flux paths are saturated.

Thus the harmonic magnetising reactances can be calculated, under all possible conditions that can exist in a machine, from Eqns. 7.3 and 7.4.

$$x_{mv} = \frac{x_m}{v^2} \left( \frac{k_{dpv}}{k_{dp1}} \right)^2 \cdot \frac{k_{s2}}{k_{s1}} \quad (7.3)$$

for the phase-belt harmonics,

$$\text{and } x_{mv} = \frac{x_m}{v^2} \left( 1 + \frac{\Lambda_s}{2\Lambda_o} \right) \cdot \frac{k_{s2}}{k_{s1}} \quad (7.4)$$

for the slot harmonics.

It should be noted that because of the difference in the ways that the two saturation factors are defined,  $k_{s1} \gg 1$  and  $k_{s2} \ll 1$ , so that  $k_{s2}/k_{s1}$  is always less than unity.

#### 7.1.2 The rotor differential harmonic leakage reactance, ( $x_{2dv}$ ) and skew leakage reactance, ( $x_{skv}$ ).

The rotor differential harmonic leakage reactance is given by Richter<sup>35</sup> as:

$$x_{2dv} = \frac{x_m}{v^2} \cdot \left( \frac{k_{dpv}}{k_{dp1}} \right)^2 \cdot \tau'_{2dv} \cdot \frac{1}{k_{skv}^2} \quad (7.5)$$



$$\text{where: } \tau'_{2dv} = \left[ \frac{\frac{\pi p v}{S_2}}{\sin \frac{\pi p v}{S_2}} \right]^2 - 1 \quad (7.6)$$

It is well known, however, that the value of the differential leakage reactance calculated from Eqn. 7.5 is too high and the calculated harmonic torques correspondingly too low.<sup>36,37,38</sup>

In Section 6.4 it was shown that the eddy currents induced on the rotor surface damp the differential leakage flux pulsations and reduce the value of the leakage reactance by the factor  $k_{d\ell v}$  shown in Fig. 35.

Taegen<sup>38</sup> has shown that when the rotor slots are open the differential leakage reactance is modified by the slot opening, and the value of  $\tau'_{2dv}$  in Eqn. 7.6 then becomes:

$$\tau_{2dv} = \left[ \frac{\frac{\pi p v}{S_2} \cdot k_v}{\sin \frac{\pi p v}{S_2} \cdot k_v} \right]^2 - 1 \quad (7.7)$$

where  $k_v = 1 - w_{2o} / \lambda_2$ ;  $w_{2o}$  being the effective width of the slot opening, (including the very heavily saturated tooth tip) and  $\lambda_2$  the rotor slot pitch.

However, there is a further and more important influence of the rotor slot openings. By influencing the air gap permeance, the rotor slot openings affect the differential leakage fluxes to a far greater extent

than they affect the fundamental fields (e.g. they reduce the differential leakage flux much more than Carter's coefficient would indicate). This influence has not been fully realised in the past and accounts for the consistently high values that are obtained for the differential leakage reactance by using the classical methods of calculation. In Appendix V it is shown that  $x_{2dv}$  must be multiplied by a factor  $k_{ov}$  to account for this effect; and this factor is calculated in that Appendix.

Thus the rotor differential harmonic leakage reactance under unsaturated conditions is given by:

$$x_{2dv} = \frac{x_m}{\sqrt{2}} \left( \frac{k_{dpv}}{k_{dp1}} \right)^2 \cdot \tau_{2dv} \cdot \frac{k_{d\ell v} \cdot k_{ov}}{k_{skv}^2} \quad (7.8)$$

The influence of saturation on the differential harmonic leakage reactances is assumed to be the same as the influence on the magnetising reactances. Hence saturation factors of  $k_{s1}$  and  $k_{s2}$  are applied to Eqn. 7.8 to take into consideration the saturation of the main and leakage flux paths respectively.

Therefore  $x_{2dv}$  is quite generally given by:

$$x_{2dv} = \frac{x_m}{\sqrt{2}} \left( \frac{k_{dpv}}{k_{dp1}} \right)^2 \cdot \tau_{2dv} \cdot \frac{k_{d\ell v} \cdot k_{ov} \cdot k_{s2}}{k_{s1} \cdot k_{skv}^2} \quad (7.9)$$

The skew leakage reactance is given<sup>35</sup> as:

$$x_{skv} = x_{mv} \cdot \left( \frac{1 - k_{skvo}^2}{k_{skvo}^2} \right) \quad (7.10)$$

where  $k_{skvo}$  is the skew factor with respect to the harmonic in question and is given by:

$$k_{skvo} = \left( \frac{\sin \frac{\alpha_v \ell}{2}}{\frac{\alpha_v \ell}{2}} \right) \quad (7.11)$$

If the width of the squirrel cage bar is neglected, the actual skew is the geometrical skew of the rotor bars. If, however, the bar width is taken into consideration the actual skew is reduced by the factor  $\xi_v$  as shown in Section 7.3. The skew factor then becomes:

$$k_{skv} = \left( \frac{\sin \frac{\alpha_v \xi_v \ell}{2}}{\frac{\alpha_v \xi_v \ell}{2}} \right) \quad (7.12)$$

and the skew leakage reactance is given by:

$$x_{skv} = x_{mv} \cdot \left( \frac{1 - k_{skv}^2}{k_{skv}^2} \right) \quad (7.13)$$

If the saturation factors for the skew leakage reactance are assumed to be the same as the saturation factors for the harmonic magnetising reactance  $x_{mv}$ , then

Eqn. 7.13 applies to both saturated and unsaturated conditions depending on whether the value of  $x_{mv}$  in the equation is the saturated value or not.

### 7.1.3 The rotor slot leakage reactance and bar resistance.

The rotor slot leakage reactance ( $x_{2sl}$ ) and bar resistance ( $r_2$ ) can be calculated at low frequencies from the slot dimensions. At high frequencies, however, eddy currents flowing in the bar conductor reduce the slot leakage flux and increase the  $I^2R$  loss in the bar.

Thus correction factors  $k_x$  and  $k_r$  must be applied to the d.c. values of the slot reactance and resistance in order to account for the deep bar effects. It should be noted that although deep bar effects may be completely negligible as far as the fundamental is concerned, they are far from negligible for the harmonics especially for the ones of high order, e.g. the slot harmonics.

The factors  $k_x$  and  $k_r$  used in the calculations were obtained by approximating the rotor slots to an open rectangular shape, and using well known formulae.<sup>39</sup>

The factor  $k_x$  was later checked experimentally by actual measurements of the variation of slot leakage reactance with frequency. The measurements were performed on rotor

No.1(a) after, of course, the end rings were turned off. (See Section 7.2). The comparison between the calculated and measured factors is shown in Fig.43.

When the leakage flux paths are saturated, the slot leakage reactance is reduced even further by a saturation factor  $k_{s3}$  calculated by Angst.<sup>32</sup>

Thus  $x_{2s\ell}$  and  $r_2$  are given by:

$$x_{2s\ell} = x_{2os\ell} \cdot k_x \cdot k_{s3} \quad 7.14(a)$$

$$\text{and} \quad r_2 = r_{2o} \cdot k_r \quad 7.14(b)$$

#### 7.1.4 The total impedance of a rotor bar.

The resistance and reactances calculated in the last three sub-sections are referred to the stator side and apply to a unit length of rotor stack. (See Nomenclature). These quantities can be transferred back to the rotor, with respect to one rotor bar, by multiplying by the transfer factor

$$f_s^r = \frac{S_2}{3Z_1^2} \cdot \left( \frac{k_{skv}}{k_{dpv}} \right)^2 \quad (7.15)$$

Thus the total bar impedance - per unit length of rotor stack - and referred to the  $v^{\text{th}}$  stator field harmonic is:

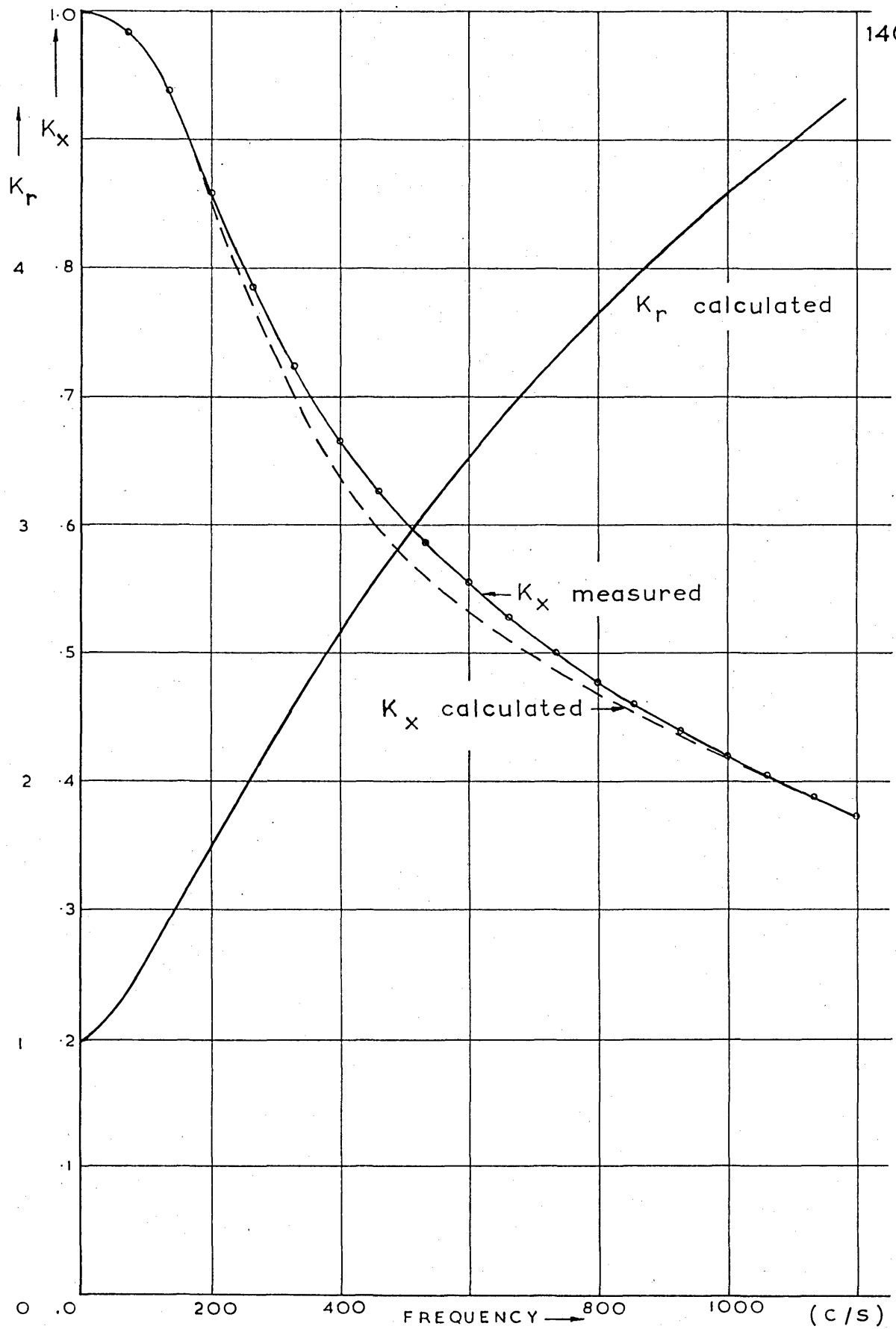


fig.43. Variation of bar resistance and reactance with frequency.  
(rotor N°1)

$$z_{bv} = f_s^r \cdot r_2 + j f_s^r \cdot (x_{mv} + x_{2dv} + x_{slv} + x_{2sl}) \quad (7.16)$$

which using Eqns. 7.3, 7.4, 7.9, 7.13, 7.14(a) and 7.14(b) gives:

$$z_{bv} = r_{bv} + j(x_{bm v} + x_{bd v} + x_{bsl}) \quad (7.17)$$

where:  $r_{bv}$  is the resistance of a unit length of a rotor bar,

$x_{bsl}$  is the slot leakage reactance of a unit length of rotor slot,

$$x_{bm v} = \frac{2\mu_o Y S_2 f_v}{g k_{c1} \cdot k_{c2} \cdot p \pi v^2} \cdot \frac{k_{s2}}{k_{s1}} \quad (7.18)$$

for the phase-belt harmonics

$$\text{and } x_{bm v} = \frac{2\mu_o Y S_2 f_v}{g k_{c1} k_{c2} p \pi v^2} \cdot \left(1 + \frac{\Lambda_s}{2\Lambda_o}\right) \cdot \frac{k_{s2}}{k_{s1}} \quad (7.19)$$

for the slot harmonics.

$$x_{bd v} = \frac{2\mu_o Y S_2 f_v}{g k_{c1} k_{c2} p \pi v^2} \cdot (k_{dlv} \cdot k_{ov}) \cdot \tau_{2dv} \cdot \frac{k_{s2}}{k_{s1}} \quad (7.20)$$

The quantities  $x_{bm v}$  and  $x_{bd v}$  are the magnetising and differential leakage harmonic reactances of a unit length of a rotor bar.

Thus it is seen from Eqns. 7.17 to 7.20 that the actual value of the total bar impedance, (not the referred

value), is unaffected by the skew of the squirrel cage.

## 7.2 Measurement of interbar resistance.

In order to calculate the losses caused by the cross currents the value of the interbar resistance must be known. Hence, after completing all other tests on rotors No.1, 8 and 10(b), their end rings were turned off and resistance measurements between all 45 pairs of adjacent rotor bars were made. The turning off of the end rings was done slowly and carefully so that the bars were not broken loose from the rotor iron in which case the contact resistance would change.

Measurements of interbar impedance were made using the circuit of Fig.44, and the results for rotor No.1(a) are shown in Fig.45. The fact that the impedance between bars is resistive even at high frequencies is shown by oscillograms 1 and 2.

Out of a total of 45 pairs of consecutive rotor bars, 41 exhibited a characteristic of type "A" (Fig. 45) and 4 a characteristic of type "B". For reasons explained later on, curves A and B of Fig.45 show values of  $4R_{bi}$ , where  $R_{bi}$  is the resistance between one particular bar and the rotor iron, deduced from the measurements.



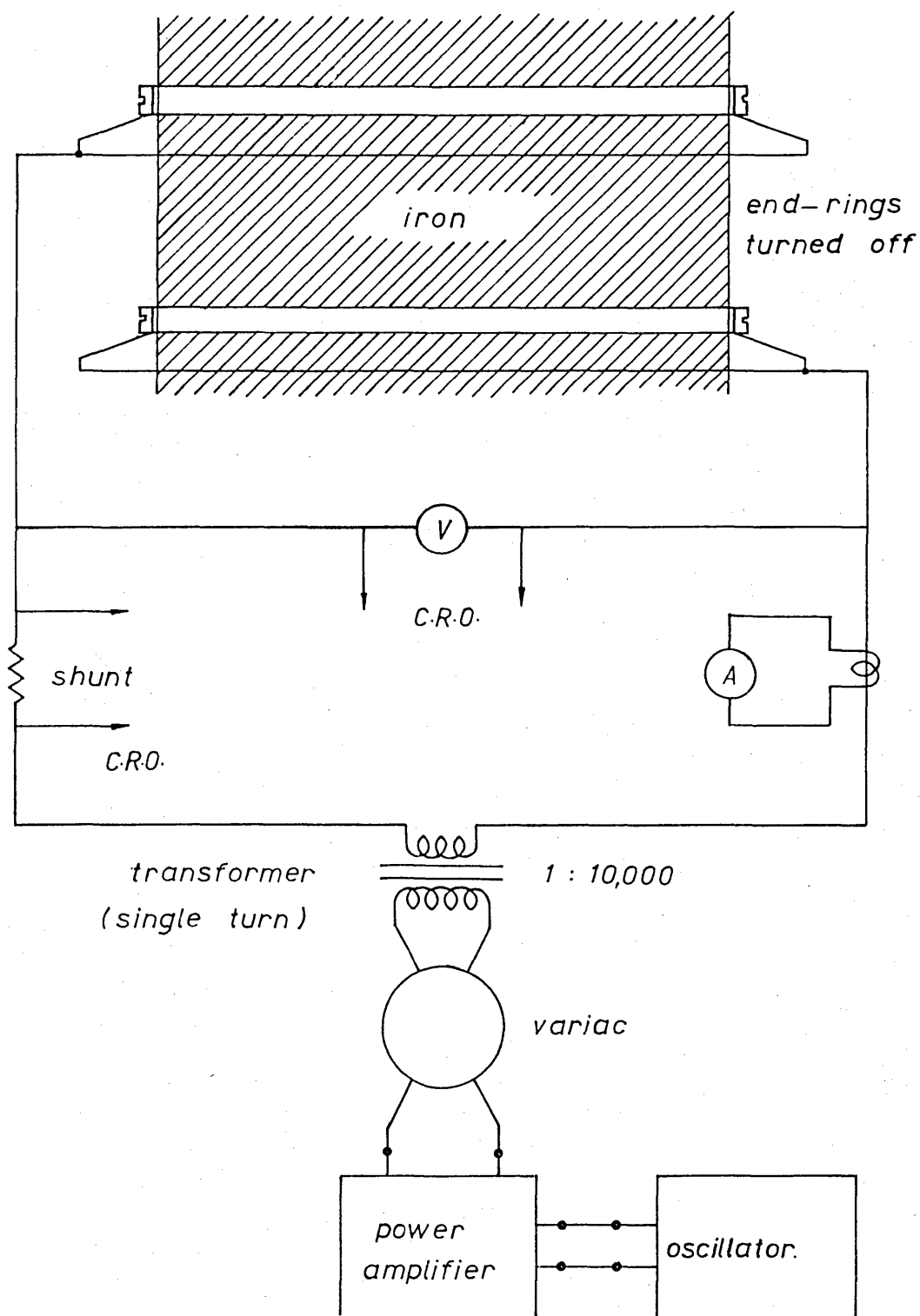


fig.44. Measurement of interbar impedance.

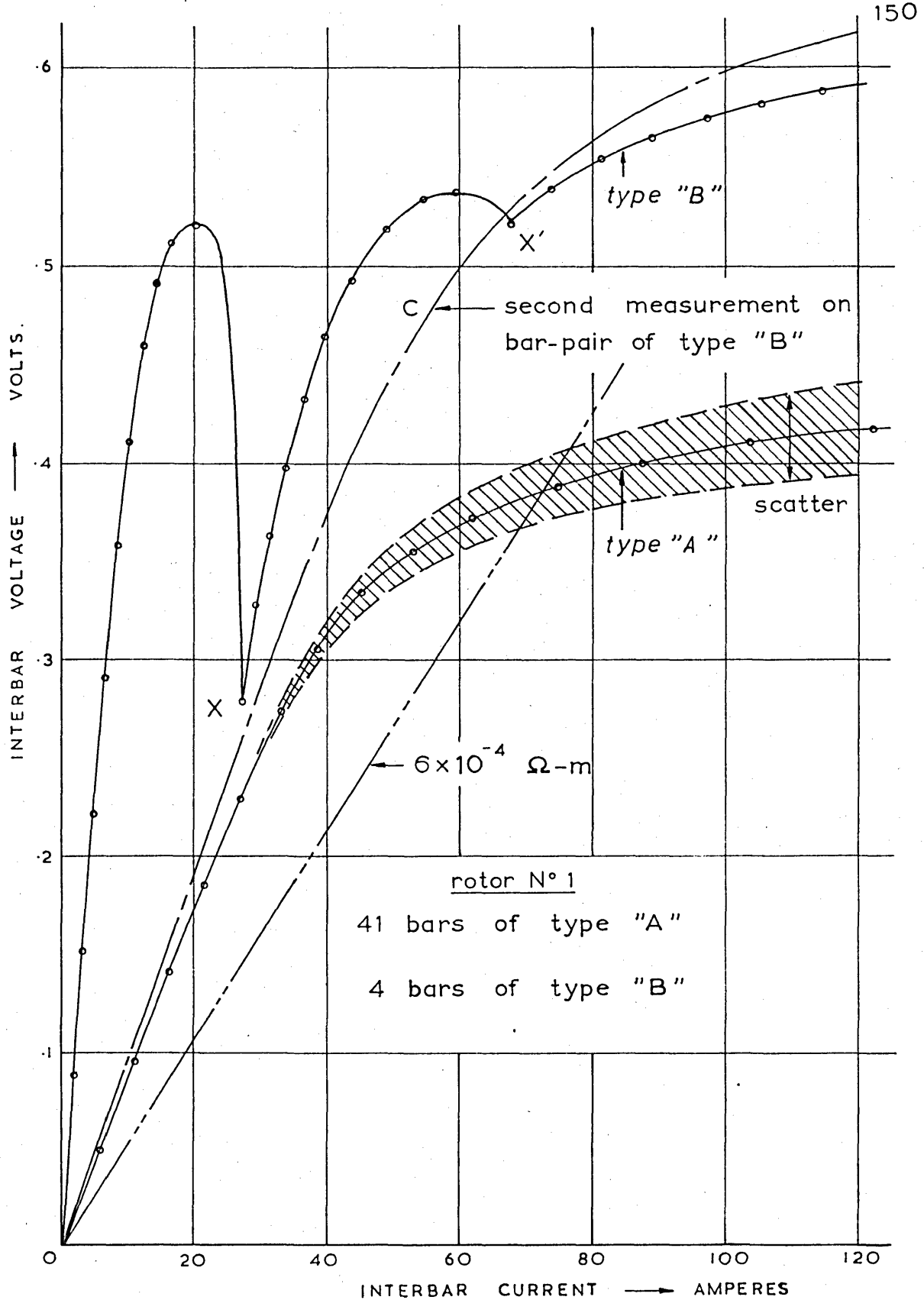
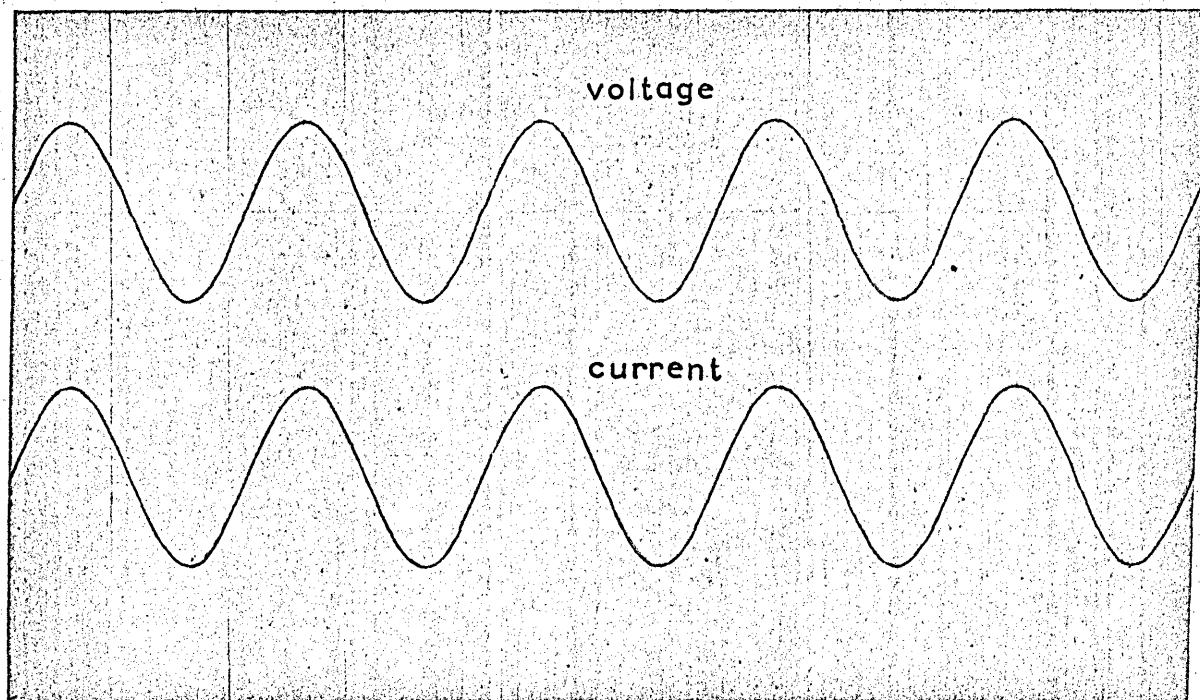
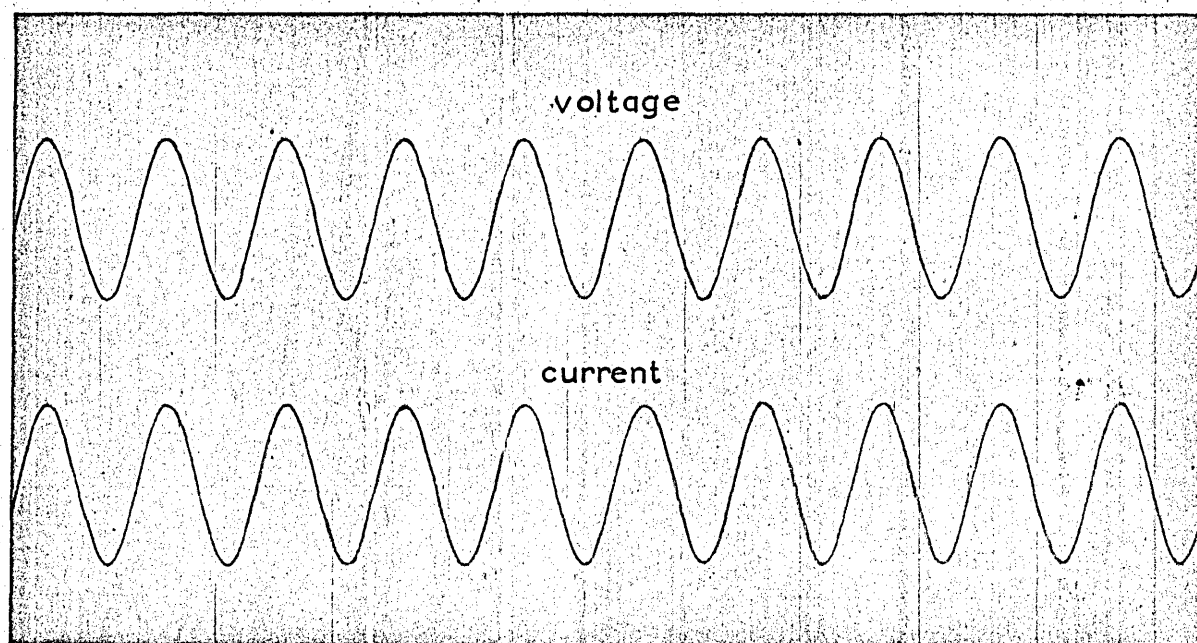


fig.45. Resistance between adjacent bars. (50 c/s)



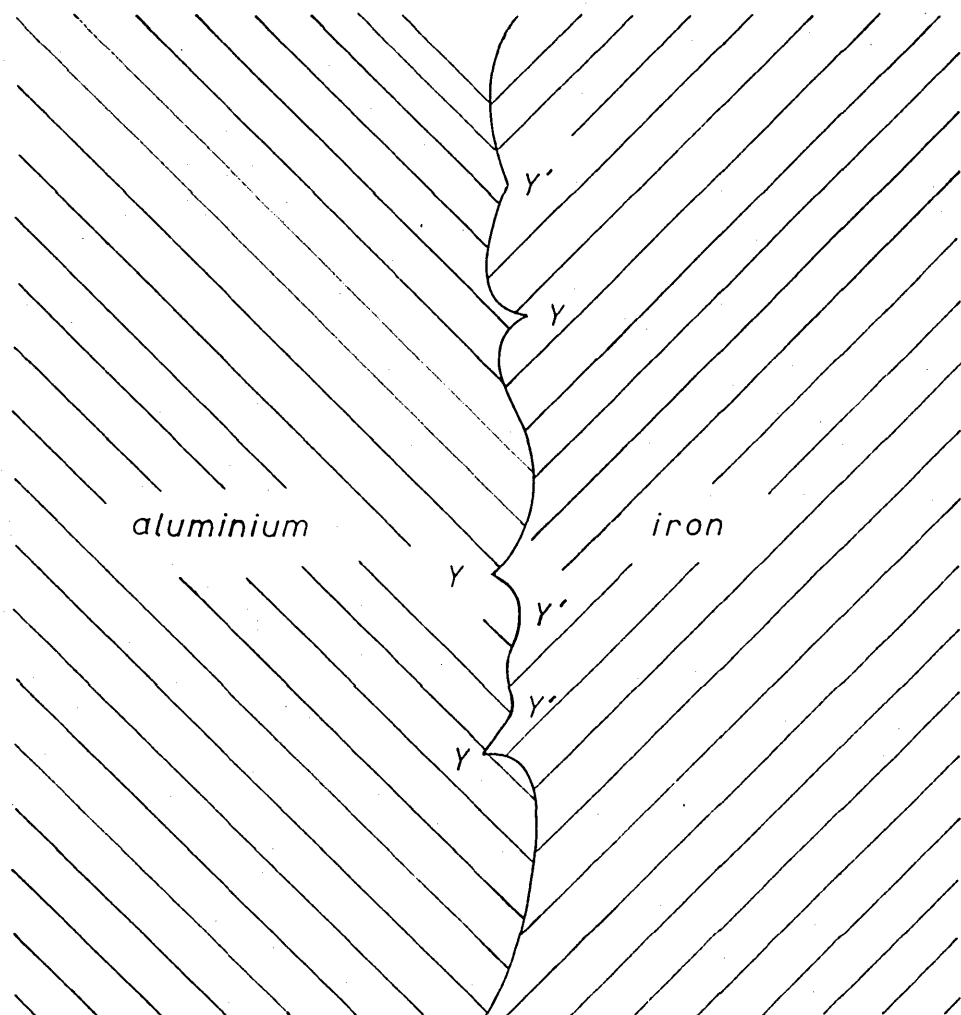
Osc.1. Waveforms from fig.44 at 50 c/s.



Osc.2. Waveforms from fig.44 at 250 c/s.

A characteristic of type "A" is what one would expect from a contact joint. The resistance decreases as the current through the contact increases. A characteristic of type "B" is, however, entirely different in nature.

This curve shows a very marked break-down effect. The initial slope of the curve corresponds to a resistance five times as large as that of curve A, indicating that the bars exhibiting this type of characteristic are much better insulated. As the voltage increases to about 500 mV a breakdown occurs of the thin insulating film between the aluminium and the iron, and there is a corresponding reduction in the contact resistance. This first breakdown of the aluminium oxide insulating film is, however, not complete. As the voltage is again increased to a value just above the value at which the first breakdown occurred, a second breakdown takes place as marked by point 'X' in Fig.45. This is probably due to the fact that the sharp points where the contact between the aluminium and the iron is most intimate, (points marked Y in Fig.46), break down first because of the higher electric field intensity around these points; whereas points marked 'Y' in the same figure break down later with a slightly higher applied voltage.



points marked  $\gamma$  cause main breakdown. (see fig. )  
 " "  $\gamma'$  " secondary " "

fig.46. The bar-iron interface.

If the test on one of the pairs of bars having a characteristic of type "B" is repeated, the dotted curve C in Fig.45 is obtained. Thus, once the insulating film breaks down, the characteristic of a bar changes permanently from that of type "B" to one of type "A". This means that the other 41 bars may have also been well insulated after manufacture, but their insulation was damaged during operation, probably because their breakdown voltage was less than that of the remaining four bars.

Although it has already been stated that the inter-bar impedance is purely resistive, the value of this resistance may change with frequency (Odok<sup>18</sup>) due to eddy currents - flowing on either side of the interface - forcing the cross currents to flow through the top layers only. Fig.47 shows the variation of  $r_{bb}$  with frequency up to 6 kc/s. From this figure it is seen that a change of only 9% occurs between d.c. and 1 kc/s. Since this is the range of frequencies induced in the rotor by the stator harmonic fields, it was assumed in the calculations that  $r_{bb}$  was independent of frequency and its value at 50 cycles per second was used throughout.

Fig.48 shows the cross voltage distribution along the bar calculated by the use of Eqn.6.48 in Section

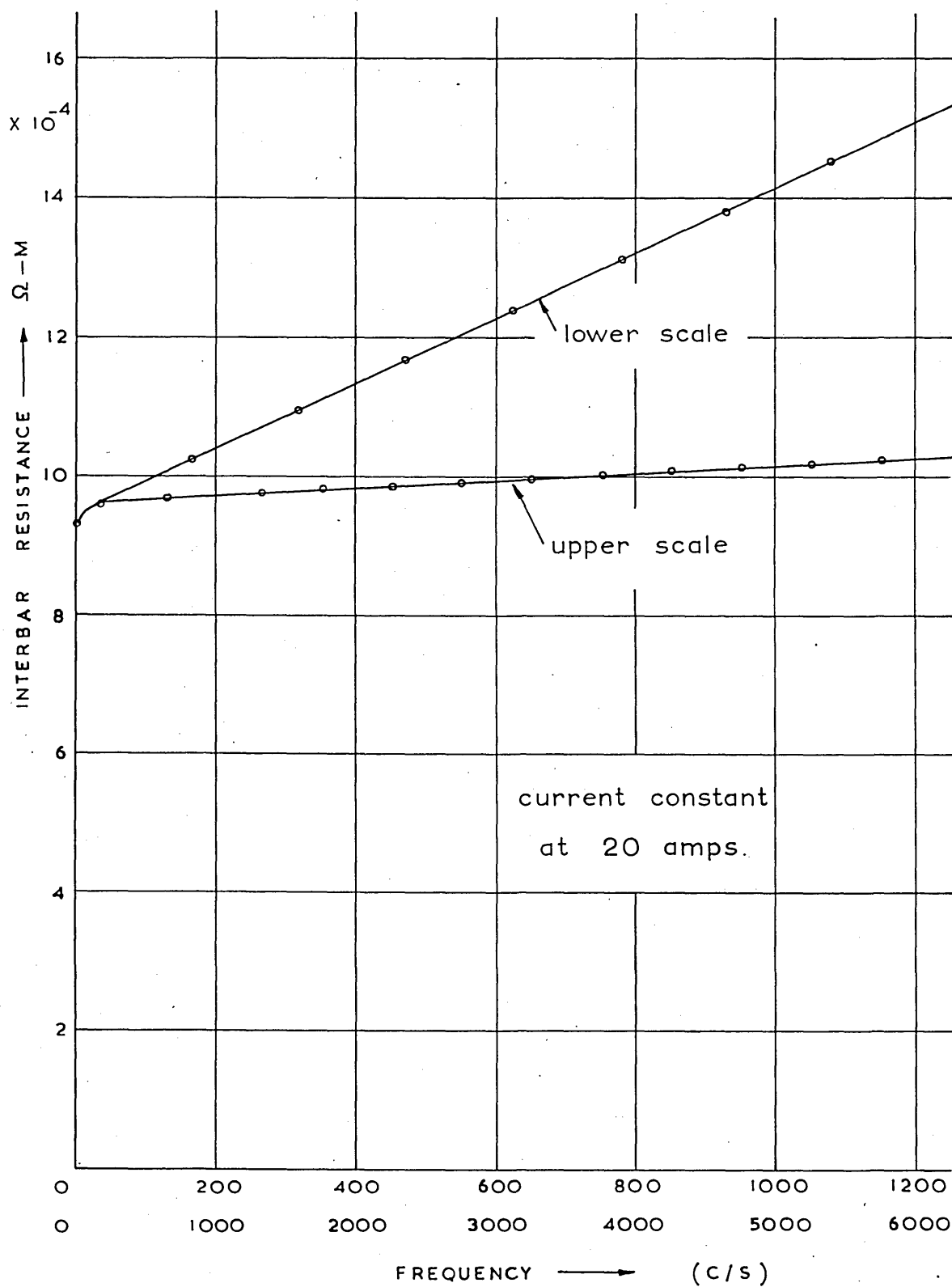


fig.47. Variation of  $r_{bb}$  with frequency.(rotor N°1)

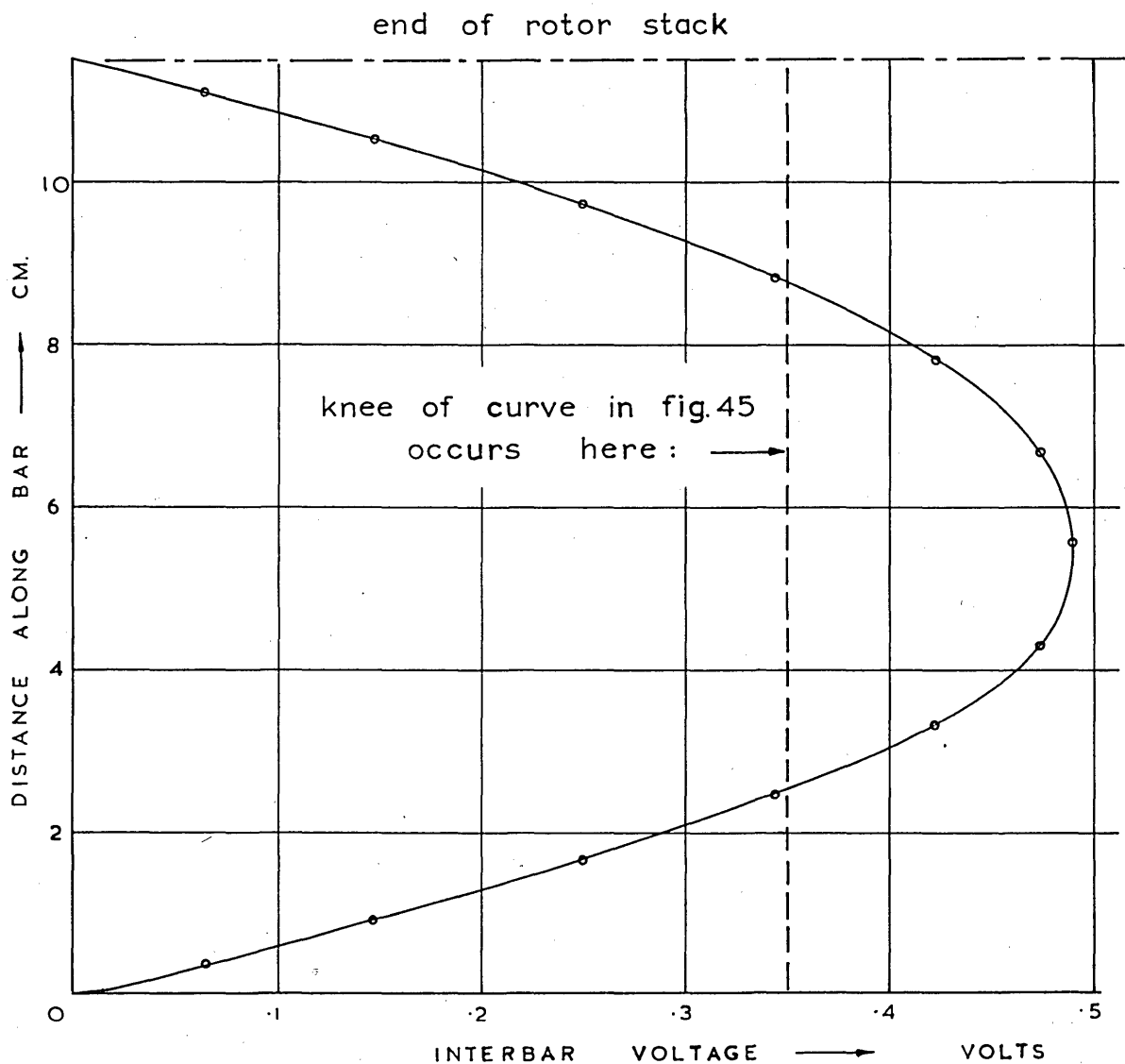


fig48. Variation of the interbar voltage along the length of the bar. (at  $s=1.5$ )

The figure shows the sum of the amplitudes for all harmonics i.e. the maximum possible value of the cross-voltage with time.



6.3. From this figure and Fig.45 the "best" possible constant value of  $r_{bb}$  can be chosen for rotor No.1(a), as shown by the straight line of Fig.45. It should be noted here that during normal operation the cross current flows through the half bar-iron contact surface of one bar, then through the tooth iron, and finally through the half contact surface of the next bar. Thus  $r_{bb}$  should be the resistance of those two half surfaces in series; neglecting the iron tooth impedance which was calculated to be small.  $r_{bb}$  is therefore given by  $4R_{bi}$  where  $R_{bi}$  is the resistance between a typical bar and the rotor iron. Since the curves A, B and C in Fig.45 show the quantity  $4R_{bi}$ , the straight line also shown in this figure is directly comparable with these curves.

Fig.49, compares the interbar resistances of rotors No.1(a), 8 and 10(b). It should be noted that this figure is plotted on a logarithmic basis and therefore it is the levels of the curves, and not their slopes, that indicate the extent to which these rotors are insulated. Thus, rotor No.8 has an interbar resistance 5 times lower, and rotor No.10(b) almost 200 times higher than that of rotor No.1(a).

In Table 2 (Chapter 2) the "best" possible constant values of  $r_{bb}$  are tabulated for all the experimental rotors. However, apart from the above mentioned three

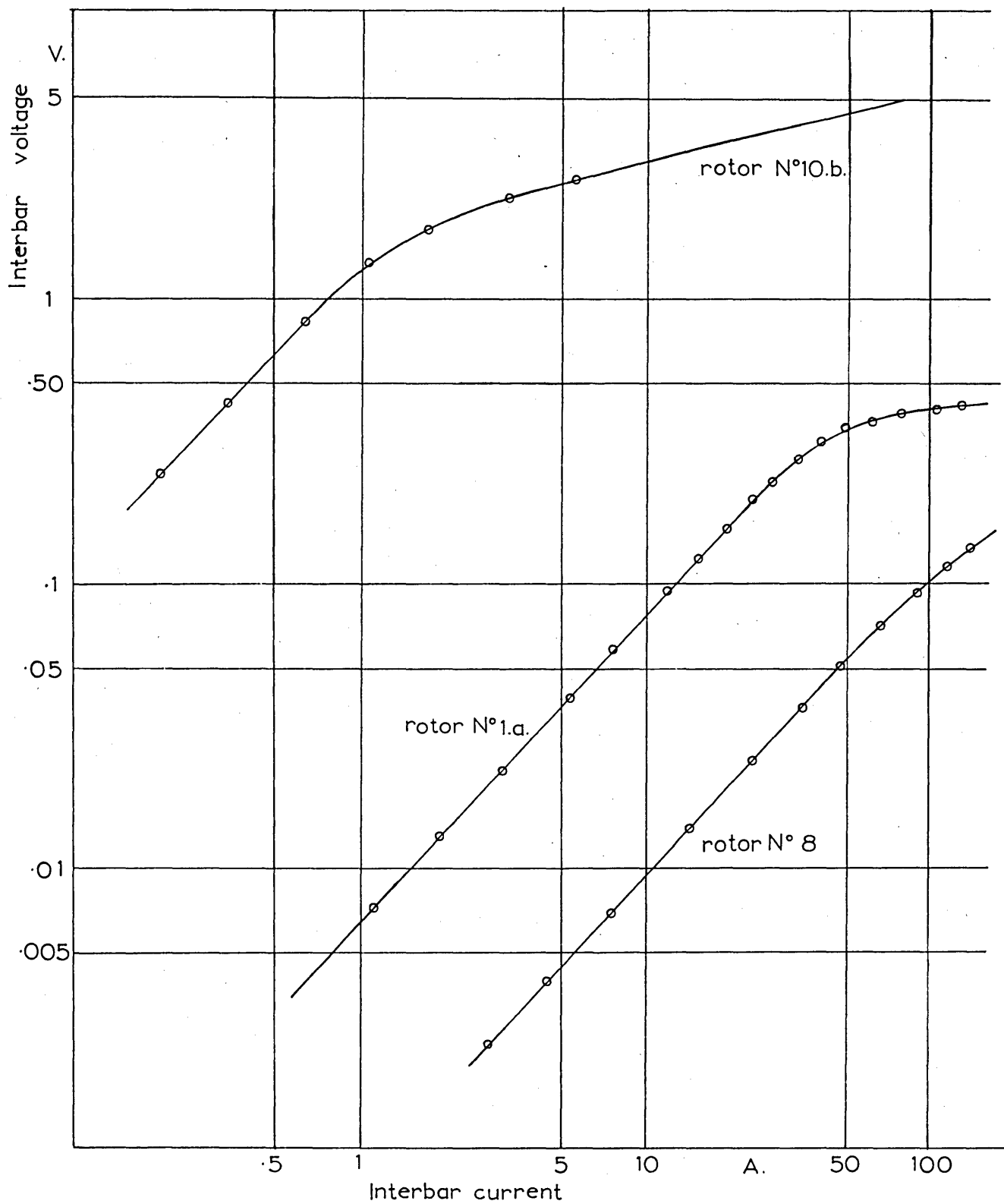


fig. 49. Interbar resistance of different rotors.

rotors which had their end rings turned off and the interbar resistances measured at current levels comparable to the ones existing under normal operation, the interbar resistances for the remaining rotors were estimated from low-current measurements. These measurements were performed by passing a current in the squirrel cage end rings and collecting it from the rotor shaft. If the resistance of the rotor bars and the iron parts of the circuit is neglected then the measured voltage drop is due to the bar-iron interfaces of all bars connected in parallel.<sup>18</sup> The interbar resistances obtained from these measurements are corrected, (using the exact results of rotors No.1(a), 8 and 10(b)), to give a good estimate of  $r_{bb}$  under normal operating conditions. It is seen from Table 2 that rotors with supposedly identical insulation do in fact have very similar values of  $r_{bb}$ . It is also seen from Fig.45 that the scatter of the measured interbar resistance characteristics for different pairs of bars, is quite small.

### 7.3 The effective skew.

Since the flux density in the air gap of a machine does not vary in the axial direction, the currents induced in the rotor would flow axially if allowed to do so. If the bars of a squirrel cage are skewed, however,

the bar currents cannot flow axially. In this case the currents will not flow parallel to the centre line of the bar, but in a direction more nearly axial.

If the resistivity of the bar material was zero all the bar current would flow from tip to tip as shown in Fig.50(a). In that case the actual skew would be:

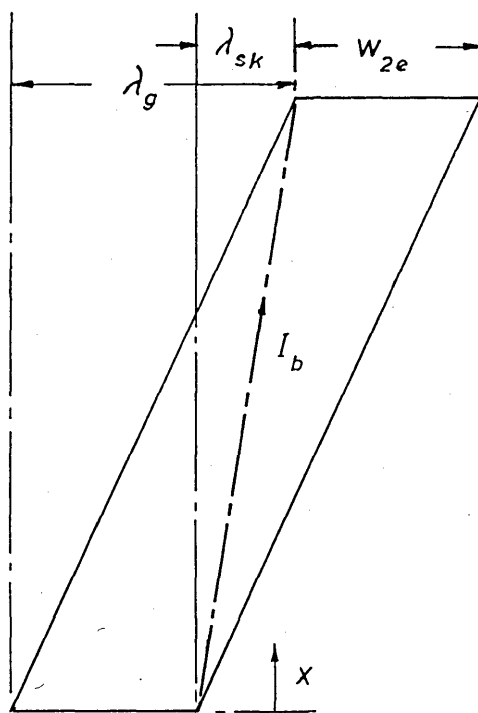
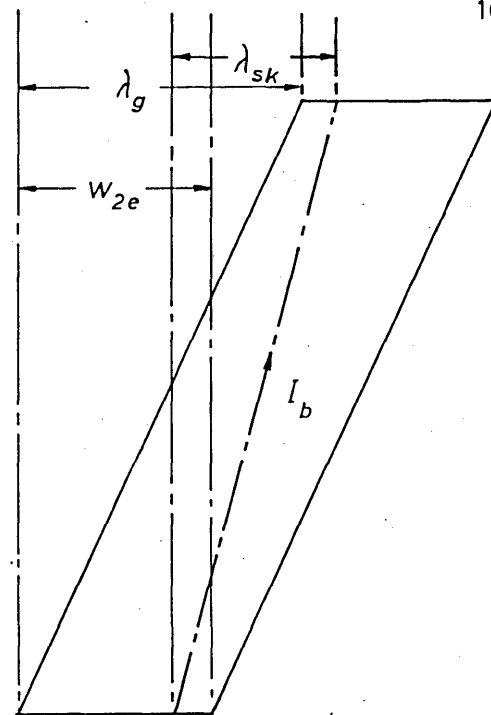
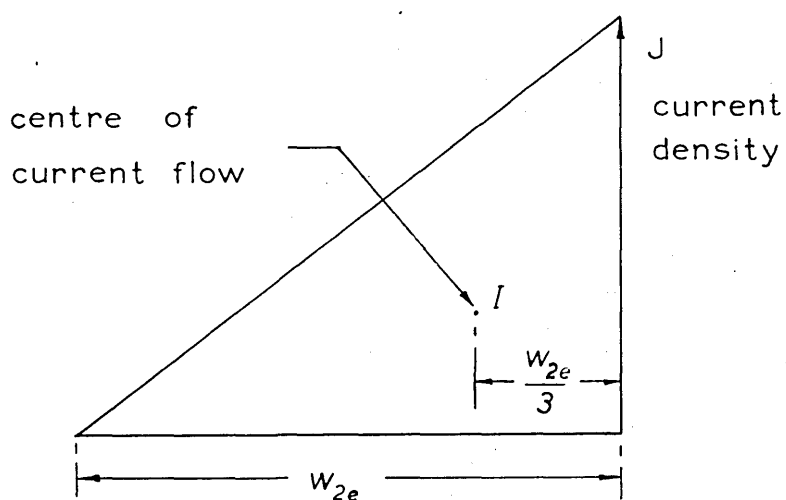
$$\lambda'_{sk} = \lambda_g - w_{2e} \quad (7.21)$$

where  $\lambda_g$  is the geometrical skew (in metres) and  $w_{2e}$  the effective bar width. (see later on).

Since the resistivity of the bar material, however, is not zero the current will distribute itself in the bar and the net current flow will then be in a direction which is a compromise between that of minimum resistance and that which deviates least from the axial direction as shown in Fig.50(b).

The current density at  $x=0$  would be much higher at the extreme right-hand corner (Fig.50(b)) than at the left-hand tip. The current density at the left-hand corner is therefore assumed to be zero and the density distribution across the bar arbitrarily taken to be linear as shown in Fig.50(c).

The actual flow of current along the bar is shown in the 3-dimensional picture of Fig.51, where the contours represent equidensity lines and the height of the surface above plane P represents the magnitude of the

fig.50a Effective skew ( $p=0$ )fig.50b Effective skew ( $p \neq 0$ )fig.50c Assumed current distribution across bar at  $x=0$

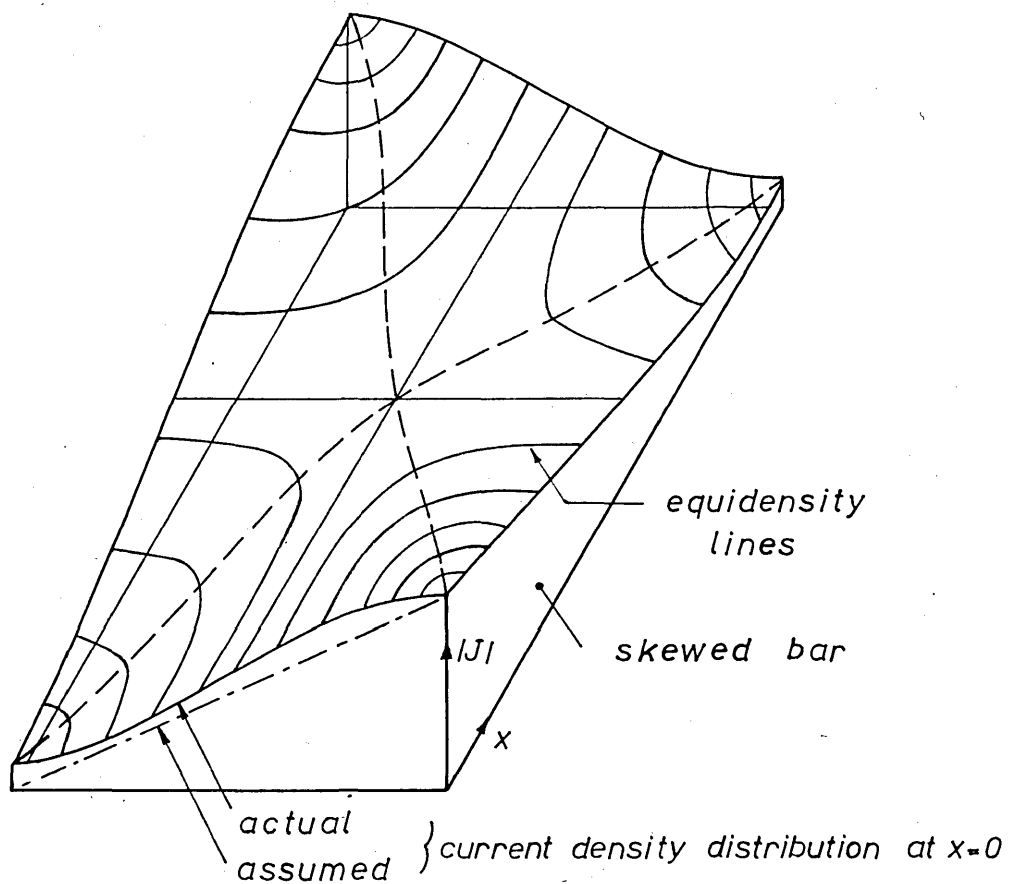


fig.51. Three dimensional current distribution in a bar.

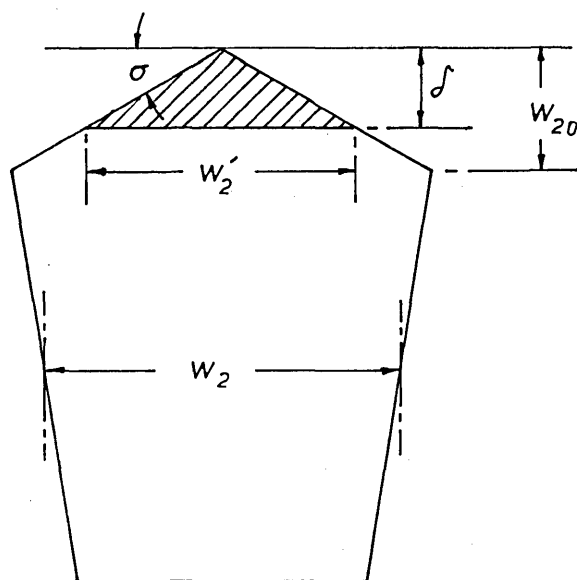


fig.52. Variation of effective skew with frequency.

current density at the point in question.

With the assumption of a linear current density distribution made above, the effective skew is given by:

$$\lambda_{sk} = \lambda_g - \frac{1}{3} w_{2e} \quad (7.22)$$

Thus knowing  $\lambda_g$  it remains to determine the effective bar width  $w_{2e}$  in order to calculate the effective skew  $\lambda_{sk}$ .

If the bar section is rectangular  $w_{2e}$  is, of course, the width of the rectangle. If the section is coffin shaped, however,  $w_{2e}$  can be taken as the mean bar width  $w_2$  shown in Fig.52 provided that the skin effect is not pronounced and the whole depth of the bar is effectively used. If the skin effect is pronounced then practically all the current is carried by the shaded area of Fig.52 and  $w_{2e}$  should be replaced by  $w'_2$ .

Thus in the numerical computations the width of the squirrel cage bar at a depth equal to the depth of penetration was used for the effective bar width  $w_{2e}$  in Eqn. 7.22. The effective skew can thus be obtained by multiplying the geometrical skew by:

$$\xi_v = \left(1 - \frac{w'_2}{3\lambda_g}\right) \quad (7.23)$$

as is done in Section 7.1.2.

P A R T   F O U R

COMPARISON OF RESULTS



## CHAPTER 8

### COMPARISON OF RESULTS

This Chapter compares the results of the tests described in Chapters 3, 4 and 5 with the results of the calculations set out in Chapter 6 using values of the parameters as calculated or measured in Chapter 7. All numerical computations were performed either on the London University Atlas computer using the Algol 60 programming language, or on the Imperial College IBM 7090 computer using Fortran IV.

#### 8.1 Speed-torque curves at low currents.

Rotor No.1(a). Fig.53 shows the torque-speed characteristics of rotor No.1(a) measured at 100 volts with a 50 c/s supply. From this figure the effects of the stator slot harmonics - 17<sup>th</sup> and 19<sup>th</sup> for the particular stator used - are clearly visible near their synchronous speeds of -88, and +79 rpm respectively. The dip due to the 7<sup>th</sup> harmonic field, though less marked can also be seen, but the 5<sup>th</sup> harmonic is virtually non existent due to the choice of the stator winding pitch. (7/9<sup>ths</sup>). These very sharp dips near the synchronous speeds of the harmonics are primarily controlled by the harmonic bar current losses. At small harmonic slips, the other two

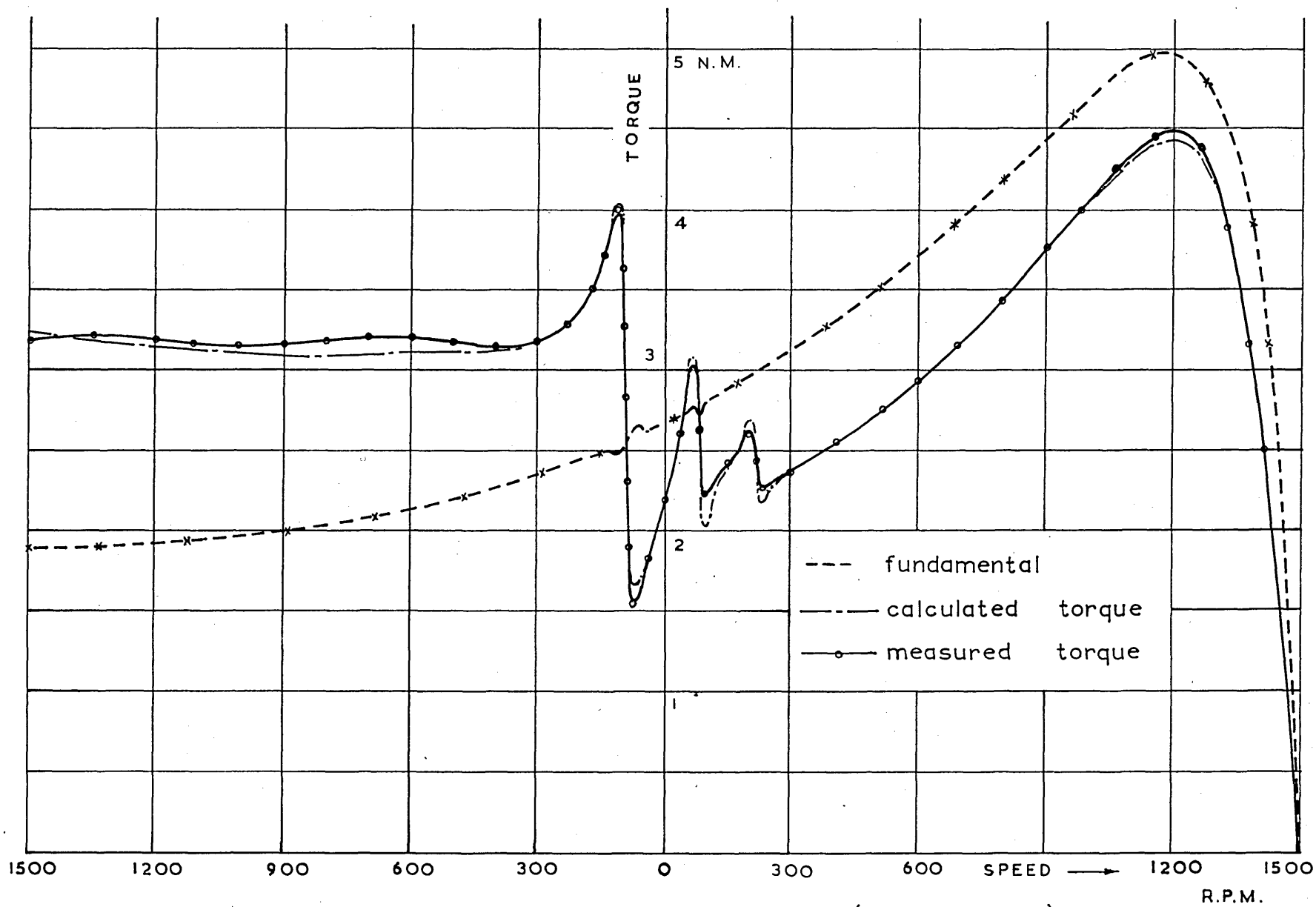


fig.53. Torque slip curves of rotor N° 1. (100 V. 50 c/s)

components of load loss (the cross current and the iron losses) are very small and therefore do not affect this part of the curve a great deal. Away from these points, of course, all three types of load loss and their associated torques become significant.

The full-line curve of Fig.53 shows the measured total electromagnetic torque, and the dotted curve the measured torque produced by the fundamental. (see Chapter 3). The chain-dotted curve is the total electromagnetic torque computed from the theoretical formulae of Chapter 6 and shows an excellent agreement with the measurements throughout the speed range. The calculated fundamental torque is to all practical purposes coincident with the measured fundamental torque.

Figs. 54 and 55, show the torque-speed characteristics of the same rotor but with frequencies of supply of  $33\frac{1}{3}$  and  $16\frac{2}{3}$  c/s respectively. These curves provide further experimental results with which the theoretically predicted curves can be compared. The agreement between the computations and the measurements is again seen to be very good.

Having established the applicability of the theoretical formulae at least as far as rotor No.1(a) is concerned, these formulae can now be used to separate

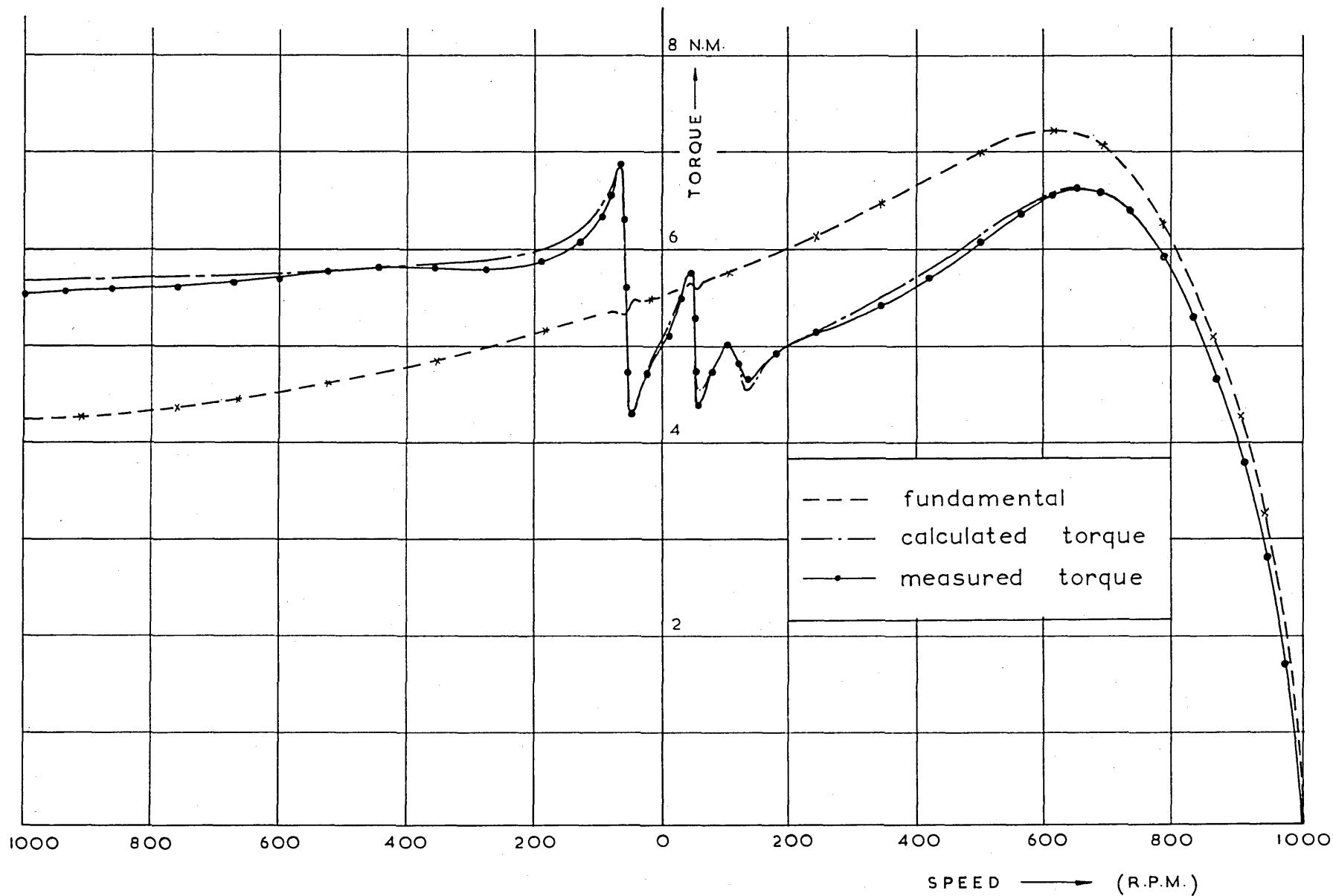


fig.54 Torque slip curves of rotor N°1 (75 volts  $33\frac{1}{3}$  c/s)

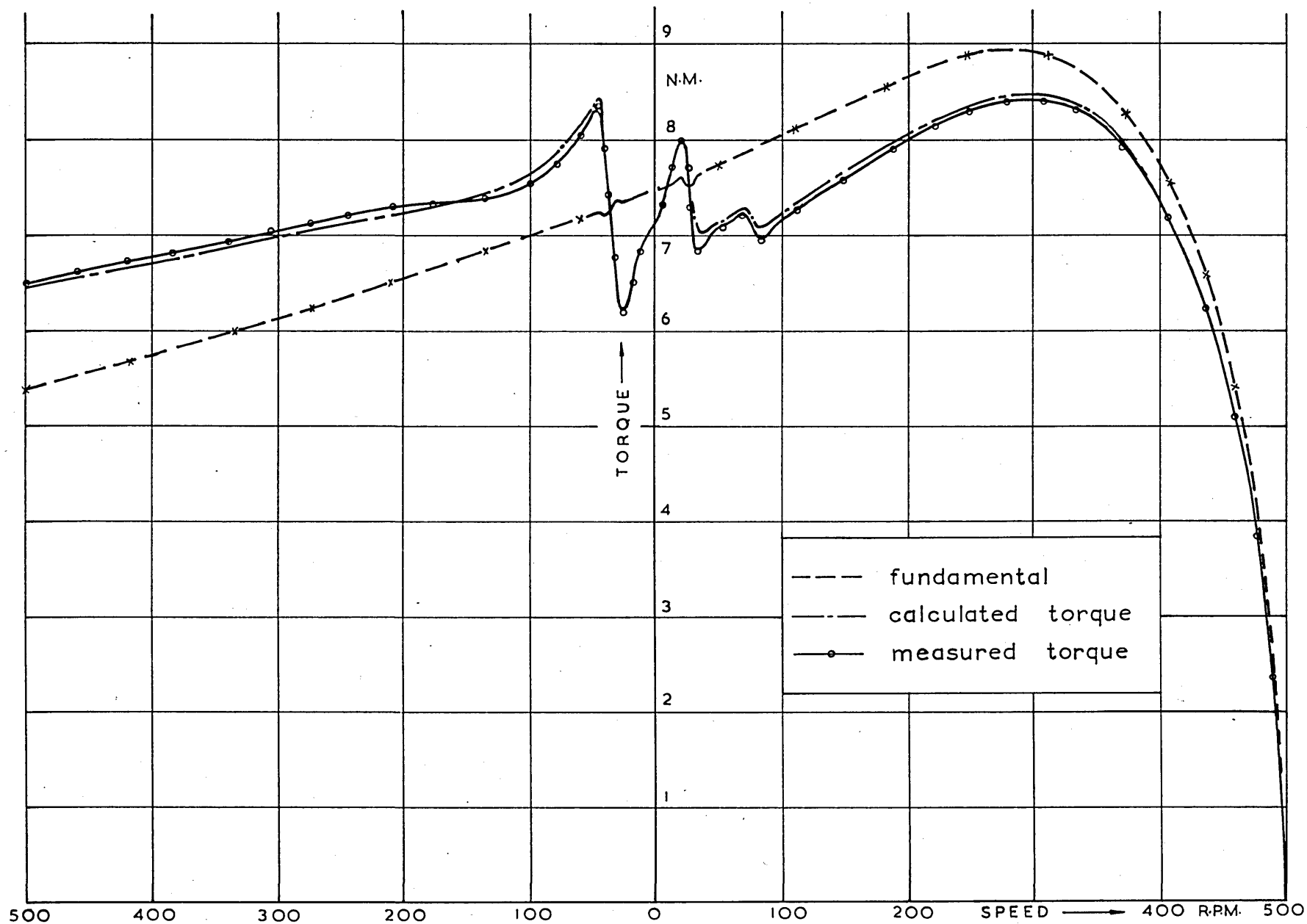


fig.55 Torque slip curves of rotor N°1 (50 volts  $16\frac{2}{3}$  c/s.)

out each component of load loss at any given value of slip. Considering the normal operating point ( $s=.05$ ) the following division is calculated.

harmonic bar current losses	:	20% of total
cross current losses	:	50% of total
iron losses	:	30% of total.

It should be noted that the iron losses include both stator and rotor surface and tooth-body losses. However numerical calculations show that the stator iron losses with this rotor are small, (mainly due to the large number of rotor slots), although it will be seen later on that this is not always the case. Of the rotor iron losses it was found that the losses in the tooth bodies contribute the largest part, and that the surface losses are relatively not so important.

Rotor No.2. Fig.56 shows the torque-slip characteristics of rotor No.2. The dips in the torque due to the stator slot harmonics near their synchronous speeds are now much more pronounced due to the increase in the harmonic bar current losses caused by the absence of skew. The rest of the curve, however, is similar in magnitude to that for rotor No.1. Again the theoretical curve shown chain-dotted is in very good agreement with the experimental speed torque curve throughout the speed range.

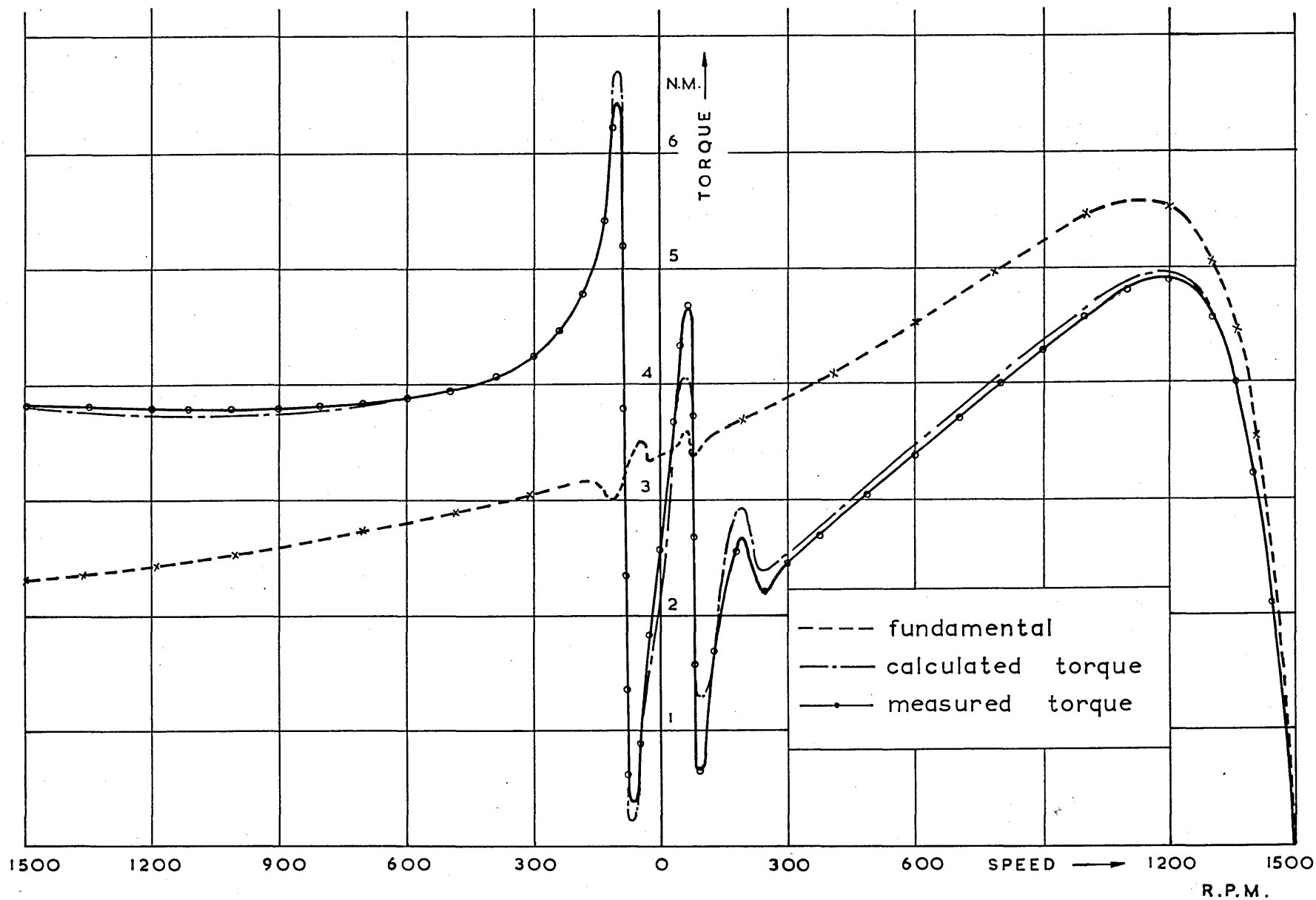


fig.56 Torque slip curves of rotor N° 2. (100 V. 50 c/s)

Considering the normal operating point ( $s=.05$ ) a once more the following subdivision of the total load loss between the three types of loss can be calculated:

harmonic bar current losses	:	80% of total
cross current losses	:	0
iron losses	:	20% of total.

With zero skew no cross currents flow irrespective of whether the squirrel cage bars are insulated or not; the cross current losses of this rotor are therefore zero. The rotor iron losses are also reduced below the value they had for rotor No.1 due to the fact that the circulating currents in the squirrel cage oppose the flux penetration into the rotor teeth. (see Section 6.5). The stator iron losses, are practically the same as for rotor No.1 and are still not very significant.

Rotor No.3. Fig.57 shows the torque-speed characteristics of rotor No.3. The dips in the torque curve due to the stator slot harmonics near their synchronous speeds have now almost disappeared, since with a skew of almost one stator slot pitch, the overall harmonic voltages and currents induced in a bar by the stator slot harmonics are practically zero, and the harmonic bar current losses are therefore negligible. It is interesting to notice that the 7<sup>th</sup> harmonic is also appreciably reduced by the skew.



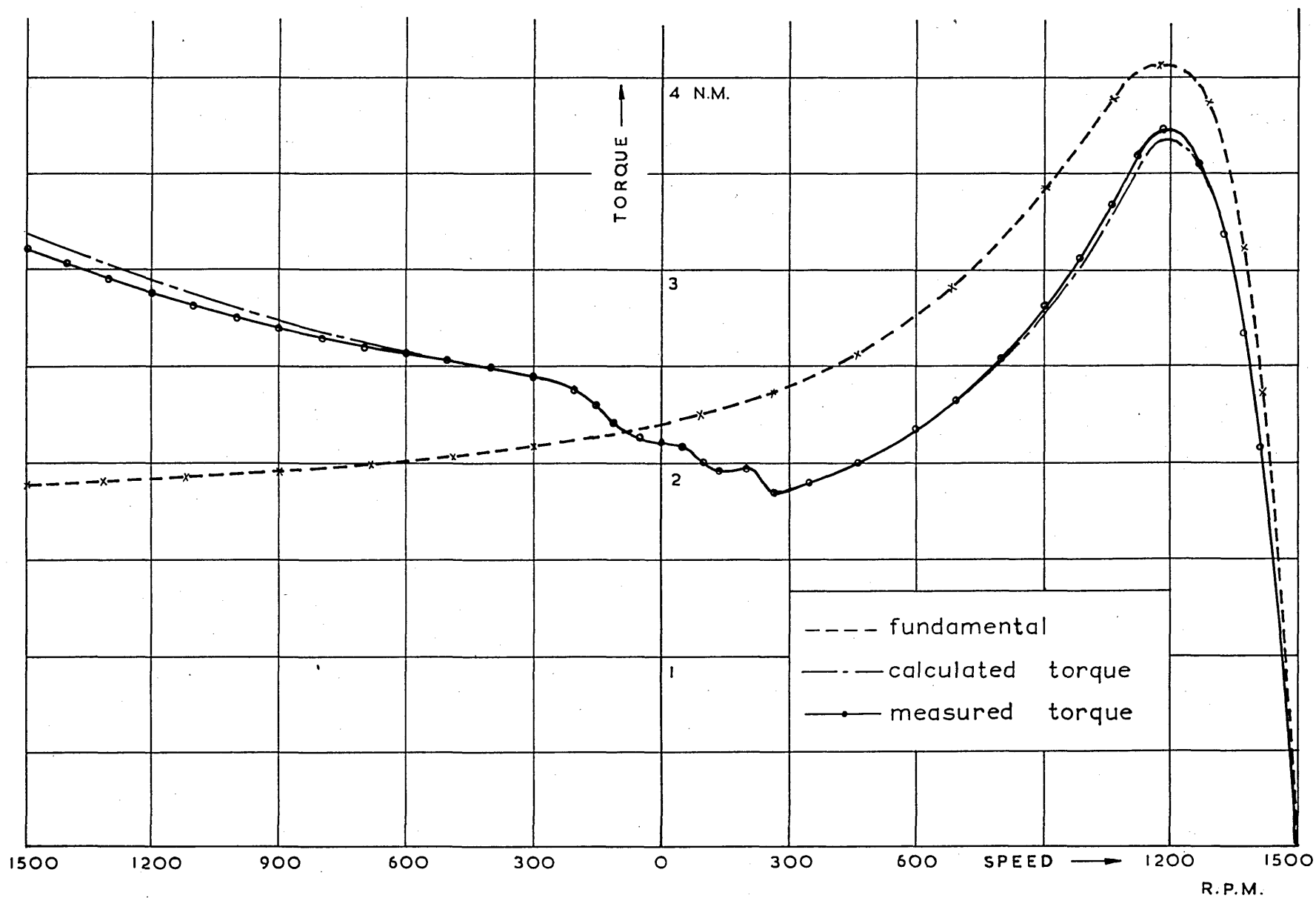


fig. 57. Torque slip curves of rotor N° 3. (100 V 50 c/s )

The computed torque speed curve shown chain-dotted is once more in close agreement with the test results.

The following subdivision of the total load losses between the three types of loss is now calculated at the full load operating conditions:

harmonic bar current loss	:	0
cross current loss	:	10% of total
iron losses	:	90% of total.

It is shown in Chapter 10 that the cross current load losses are reduced if the skew is increased and the cross path resistance  $r_{bb}$  is high. (The opposite is true if  $r_{bb}$  is low.) The value of  $r_{bb}$  corresponding to rotors Nos. 1 to 7 and rotors Nos. 10(a) and 10(b) are on the high side. Thus the value of the cross current load losses for the present rotor is reduced below the value they had for rotor No.1. The rotor iron losses on the other hand are now increased since the harmonic fluxes can penetrate the rotor teeth unopposed due to the absence of any circulating currents in the squirrel cage.

Rotor No.4. The torque-slip characteristics of this rotor are exactly the same as those of rotor No.1, thus verifying that the iron oxide scale forms an effective interlaminar insulation and that the interlaminar currents and their associated losses can be assumed to be zero.

Rotor No.5. The torque-speed characteristics of rotor No.5 are shown in Fig.58. It is seen that the total load loss for this rotor, (which is proportional to the difference between the total electromagnetic and the fundamental torques), is higher than the total load loss for rotor No.1 which has a smaller number of rotor bars. More is said about the effect of the slot numbers in Chapter 11. The agreement between the experimental and the theoretical results is seen to be good.

Rotors No.6 and 7. The torque-slip characteristics of these rotors are shown in Figs. 59 and 60 respectively. Although both of these rotors have fewer numbers of slots than rotor No.1; it is seen that whereas rotor No.6 has much lower total load losses than rotor No.1, the difference in the load losses of rotors No.7 and No.1 is not so great. It should be noted that the theory given in Chapter 6 predicts this phenomenon and it is explained further in Chapter 11.

The iron losses in the stator teeth due to the rotor slot harmonic fields are no longer negligible, (due to the small number of rotor slots) and can account for up to 15% of the total load loss.

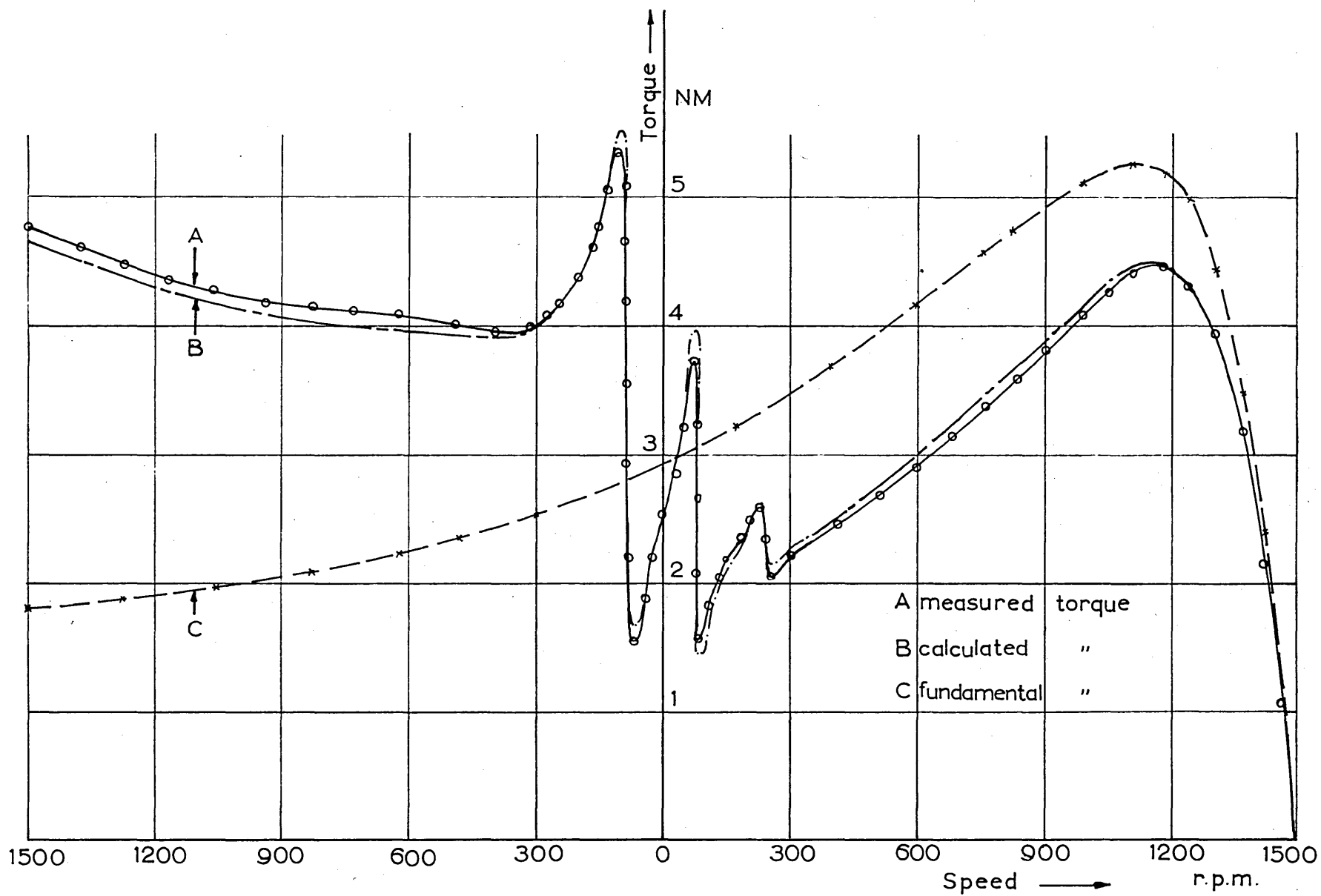


fig.58. Torque speed characteristic of rotor N° 5. (100v. 50 c/s)

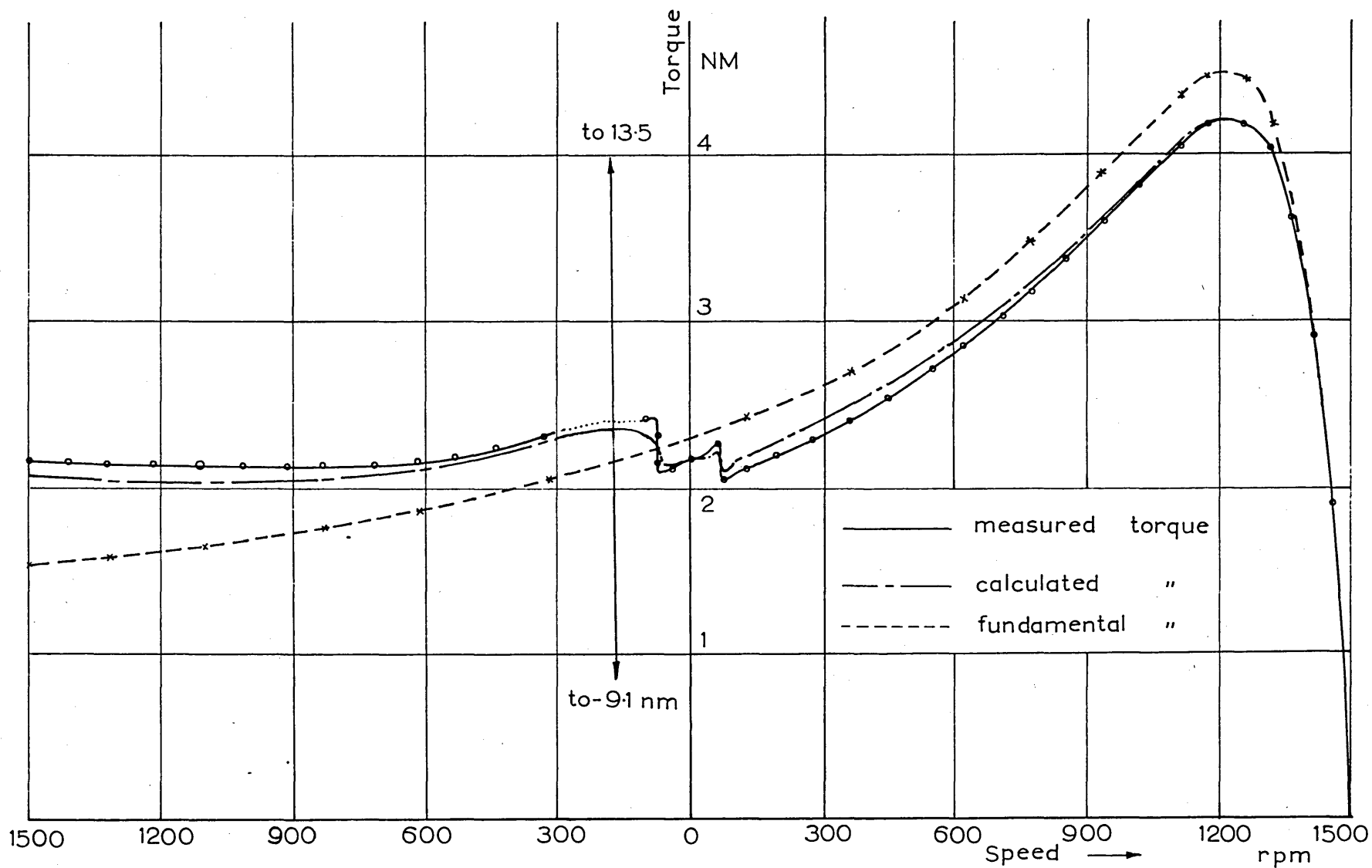


fig.59 Torque slip curves of rotor N° 6 (100v 50 c/s)

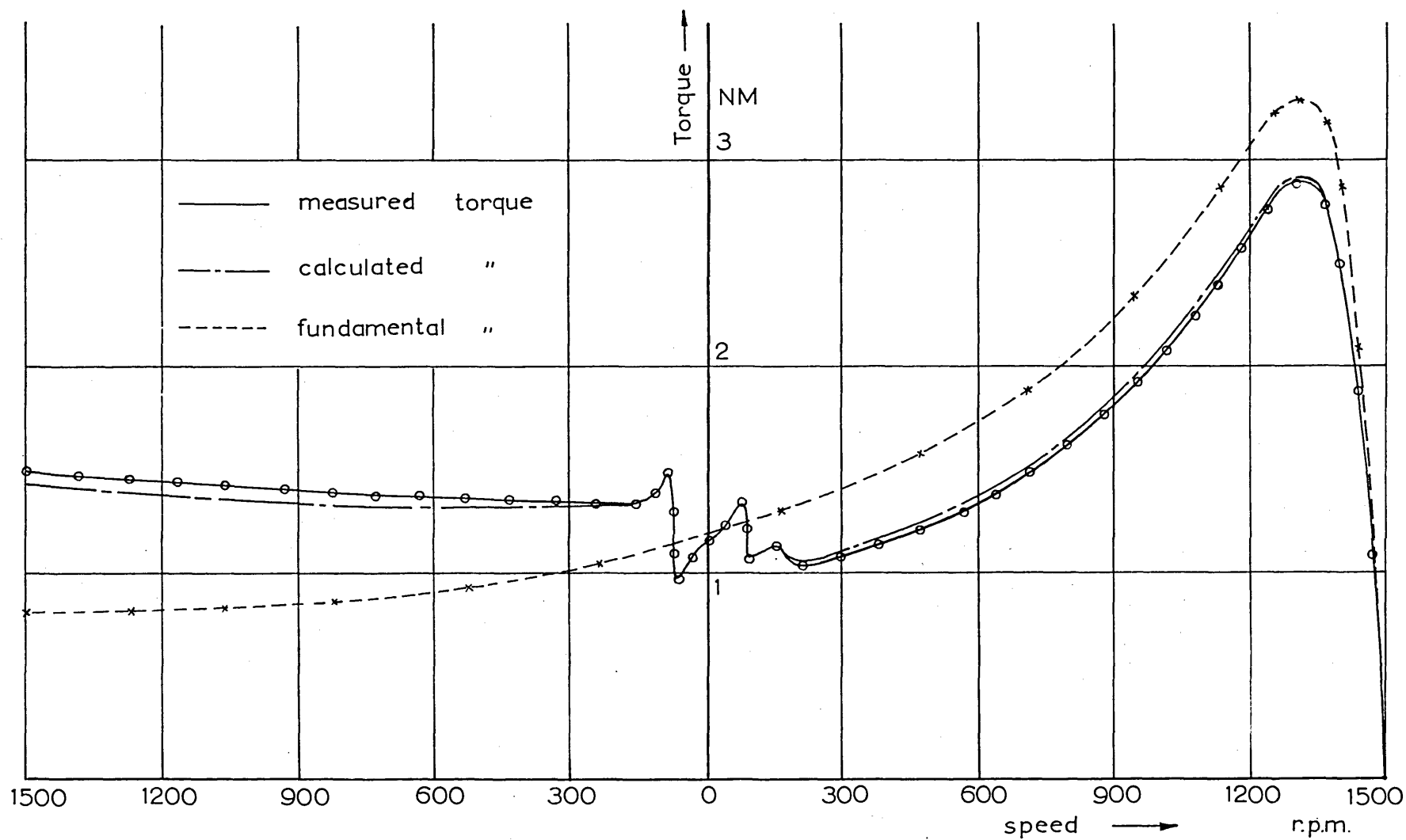


fig.60. Torque speed curves of rotor N° 7 . (100 v 50 c/s)

It can be seen from Fig.59 that rotor No.6 exhibits a very large synchronous cusp in the torque-speed curve at a reverse speed of -187.5 rpm. This synchronous torque does not affect the normal operation of the machine, but it prevents the machine from reversing when plugged, due to the fact that the torque extends well into the negative region. By an analysis of the harmonic content of the squirrel cage winding; similar to that shown by Table 5 in Chapter 6; it is found that the synchronous torque is due to the interaction of the -17<sup>th</sup> stator field harmonic with the 17<sup>th</sup> rotor field harmonic. Since these harmonics are the first slot harmonics of both the stator and the rotor - and are therefore the largest harmonics in existence - the resulting synchronous torque has the largest possible magnitude.

Rotors No.8 and 9. The torque-speed curves of rotors No.8 and 9 are shown in Figs. 61 and 62 respectively. The cross current losses for these rotors are greatly increased due to the good conduction between the squirrel cage bars and the rotor iron. The theoretical formulae are seen to predict this increase in the load losses with good accuracy and the computed curves (shown chain-dotted) are in good agreement with the measured results for both rotors. It should be noted from these figures

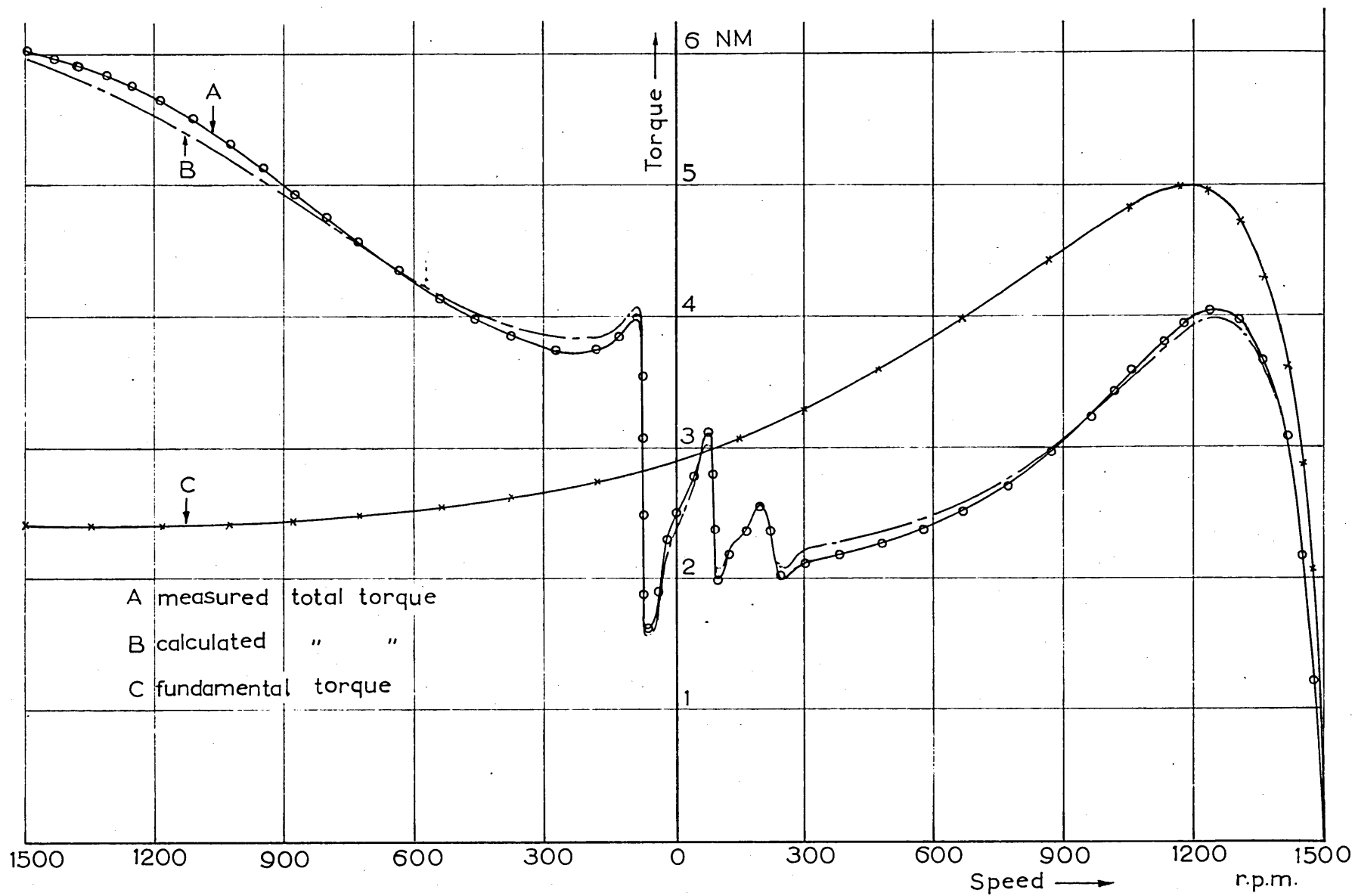


fig.61. Torque speed characteristic of rotor N° 8. (100 v. 50 c/s)



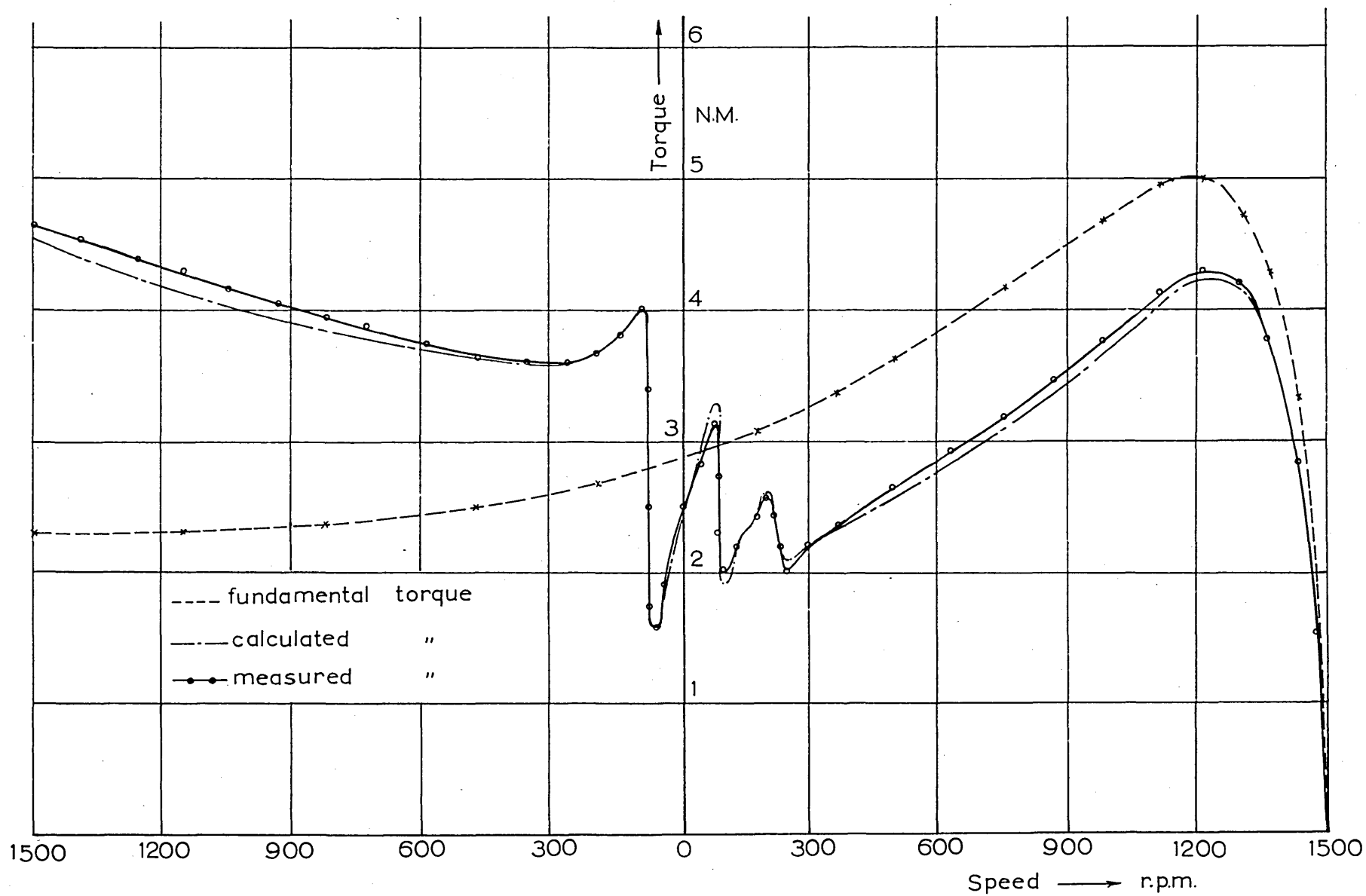


fig.62. Torque speed curves of rotor N° 9 . (100 V, 50 c/s)

that the fundamental torque is also slightly higher than its value for rotor No.1. With such a high degree of conduction between the squirrel cage bars and the rotor iron, the interbar voltages at fundamental slip frequency, are also large enough to produce fundamental cross-currents with a corresponding increase in the fundamental torque. It can be shown theoretically however that the increase in the harmonic torques due to the cross currents is always larger than the increase in the fundamental torque due to the same reason, no matter how good the conduction is. This indicates that bad squirrel cage insulation always results in greater load losses and a worse torque-slip characteristic.

Rotors No.10(a) and 10(b). Fig.63 shows the torque speed characteristics of rotor No.10(b). The dips in the torque curve due to the stator slot harmonics near their synchronous speeds are the same as those of rotor No.1 since, as has already <sup>been</sup> mentioned, these dips are primarily due to the circulating harmonic bar currents which remain unchanged. Away from these points, however, the load losses and associated torques are reduced due to the absence of the cross currents caused by the almost perfect insulation of these rotors. The iron load losses are the same as those of rotor No.1

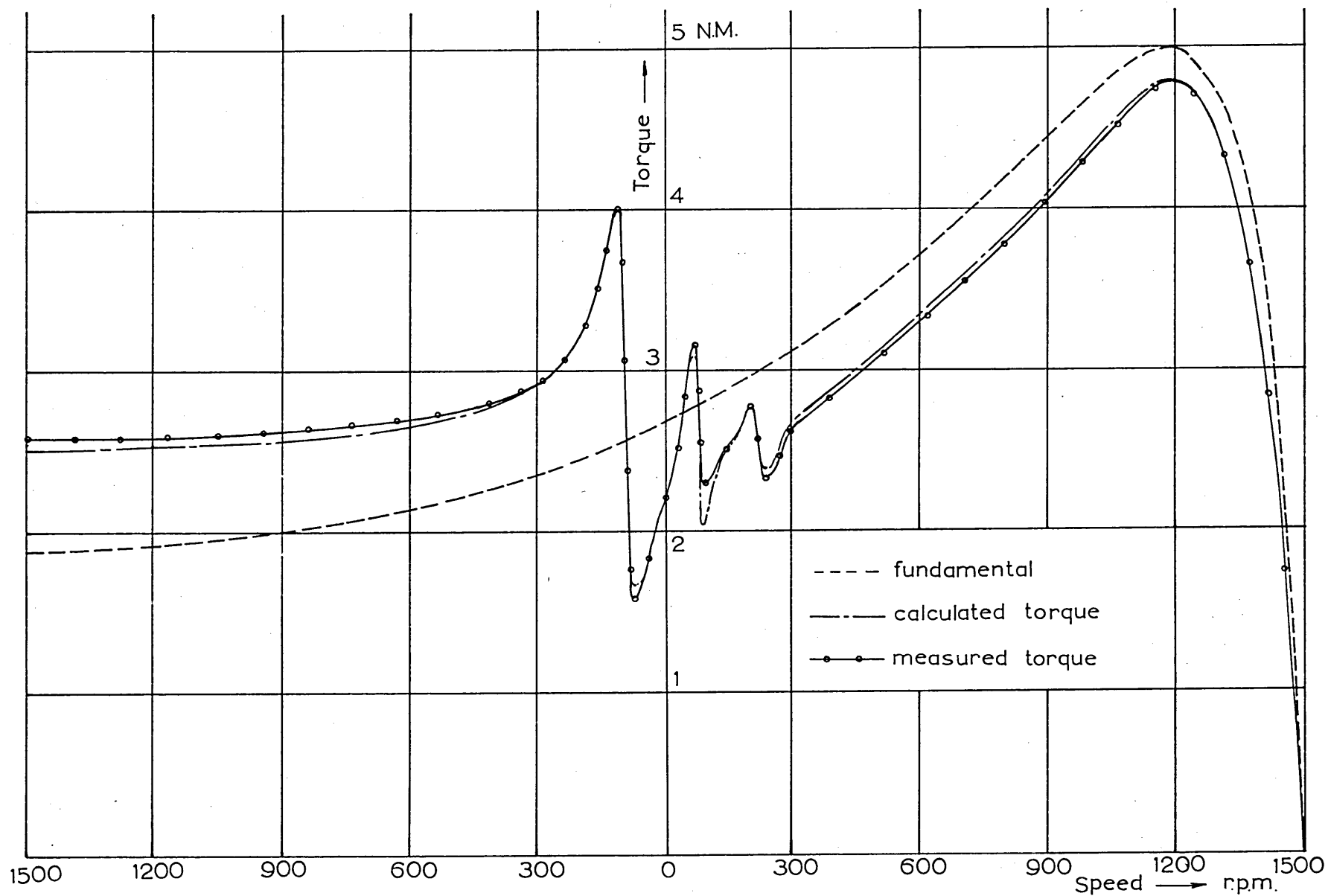


fig. 63 Torque speed curves of rotor N°10.b. (100 V., 50 c/s)

at the same value of load current.

It is seen from Fig. 63 that the calculated curve is again in good agreement with the measured one although slightly lower. This slight difference may be due to the fact that at the ends of the rotor core the squirrel cage bars were not completely insulated due to breaking - caused by the pressure applied to the core ends during casting - of the very brittle glass-silicate material used for the bar insulation. A few laminations were removed from the ends of the core when making the cross-path resistance measurements of Section 7.2.

It is worth while to comment now on the general shape of all the curves given in Figs. 53 to 63. It is seen from these figures that there is generally a loss of accelerating torque in the region  $0 < s < 1$  and a gain of braking torque in the region  $1 < s < 2$ . Since the higher harmonics, and particularly the slot harmonics, have their synchronous speeds near the standstill point, the "harmonic machines" formed by each stator and rotor field harmonic, act as generators in the accelerating range of the induction motor, and so absorb part of its torque. In the braking range on the other hand the "harmonic machines" act as motors adding to the fundamental torque of the induction motor.

Another general point of interest about these graphs is that the difference between the total and fundamental torques near standstill is comparatively small. At standstill it should be remembered that the slot harmonics, and indeed any other pair of consecutive stator or rotor harmonics; oppose each other and the net harmonic torque produced is therefore small. In this case the lower stator slot harmonic, (the 17<sup>th</sup> for the present stator), is acting as a generator with  $s_v = -1$ , whilst the other stator slot harmonic (19<sup>th</sup>) is acting as a motor with  $s_v = +1$ . Since the magnitude of the 17<sup>th</sup> harmonic is larger than that of the 19<sup>th</sup>, the net result is a small but always negative harmonic torque. Thus, this explains why the measured total torque at standstill is always slightly less than the fundamental standstill torque for all the rotors, as can be seen from Figs. 53 to 63.

### 8.2 Speed-torque curves at high currents.

The torque-slip characteristics of rotors No.1(a), 2, 3, 5, 6, 7, 8, 9, and 10(b) taken at full voltage, (400 v), are shown in Figs. 64, 65, 66, 67, 68, 69, 70, 71 and 72 respectively. The theoretically predicted curves are shown chain dotted in all figures. It is seen that the theory given in Chapter 6, with the parameters modified to include saturation as explained

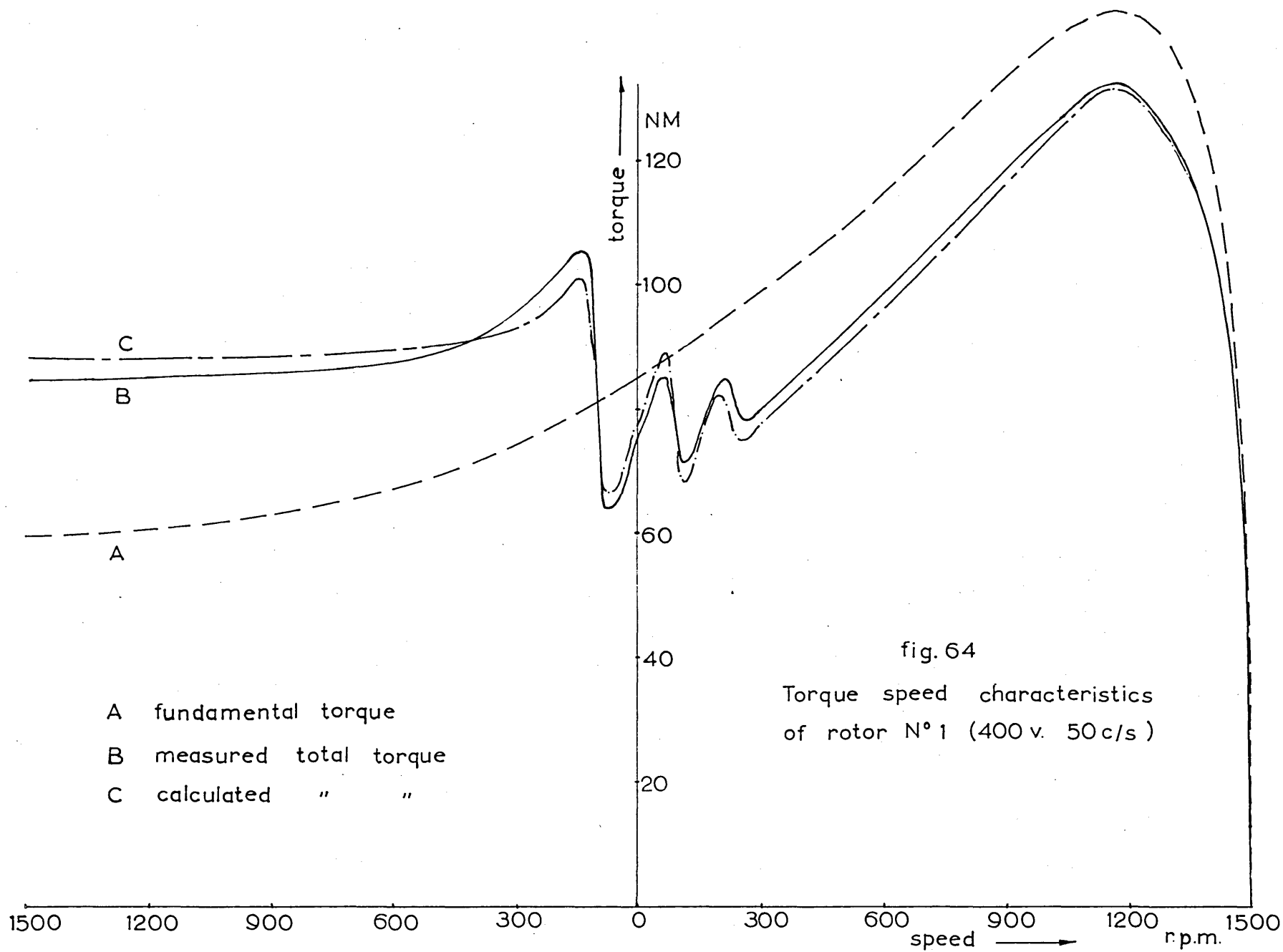


fig. 64  
Torque speed characteristics  
of rotor N°1 (400 v. 50 c/s)

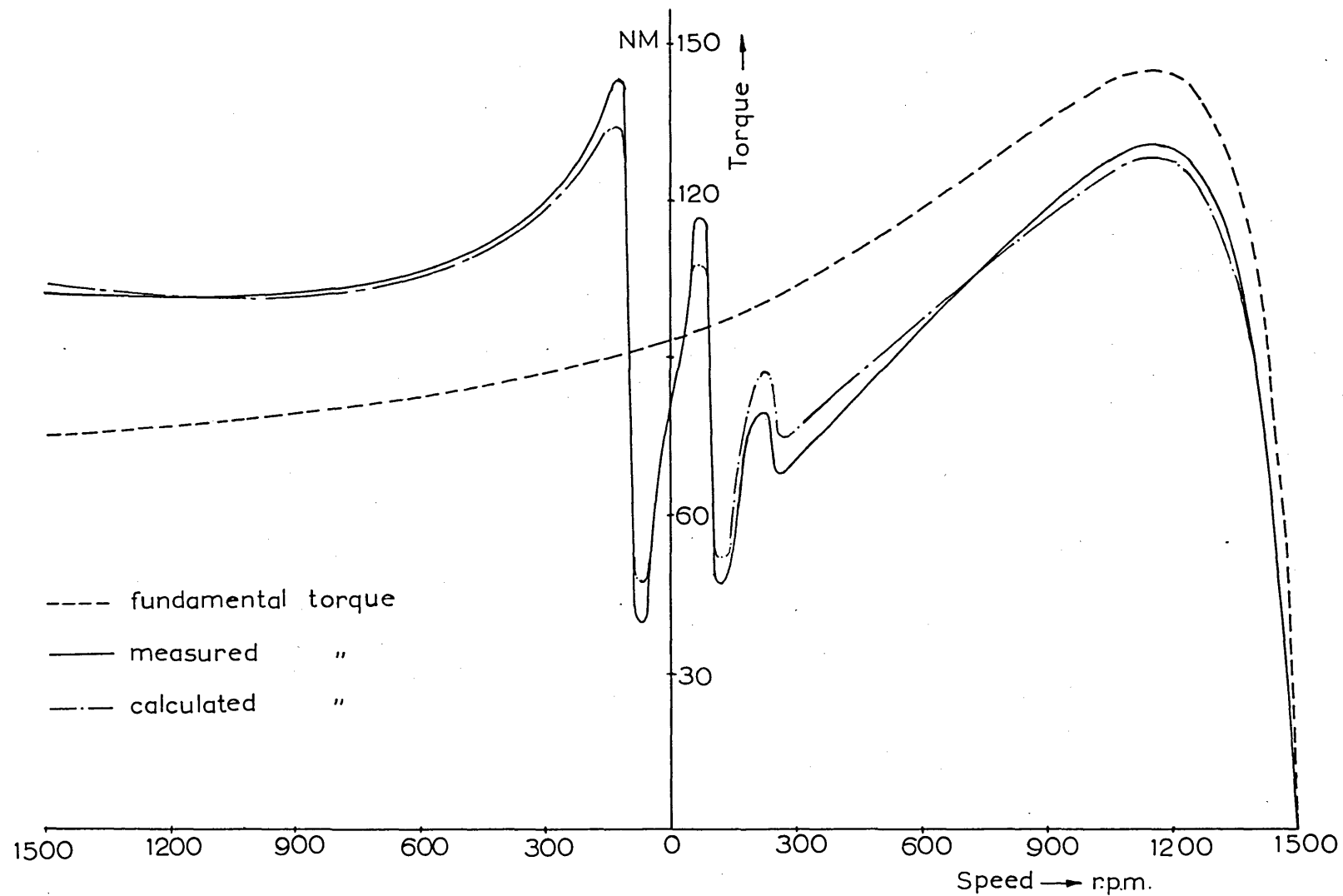


fig.65. Torque speed curves of rotor N° 2. (400 V. 50 c/s)

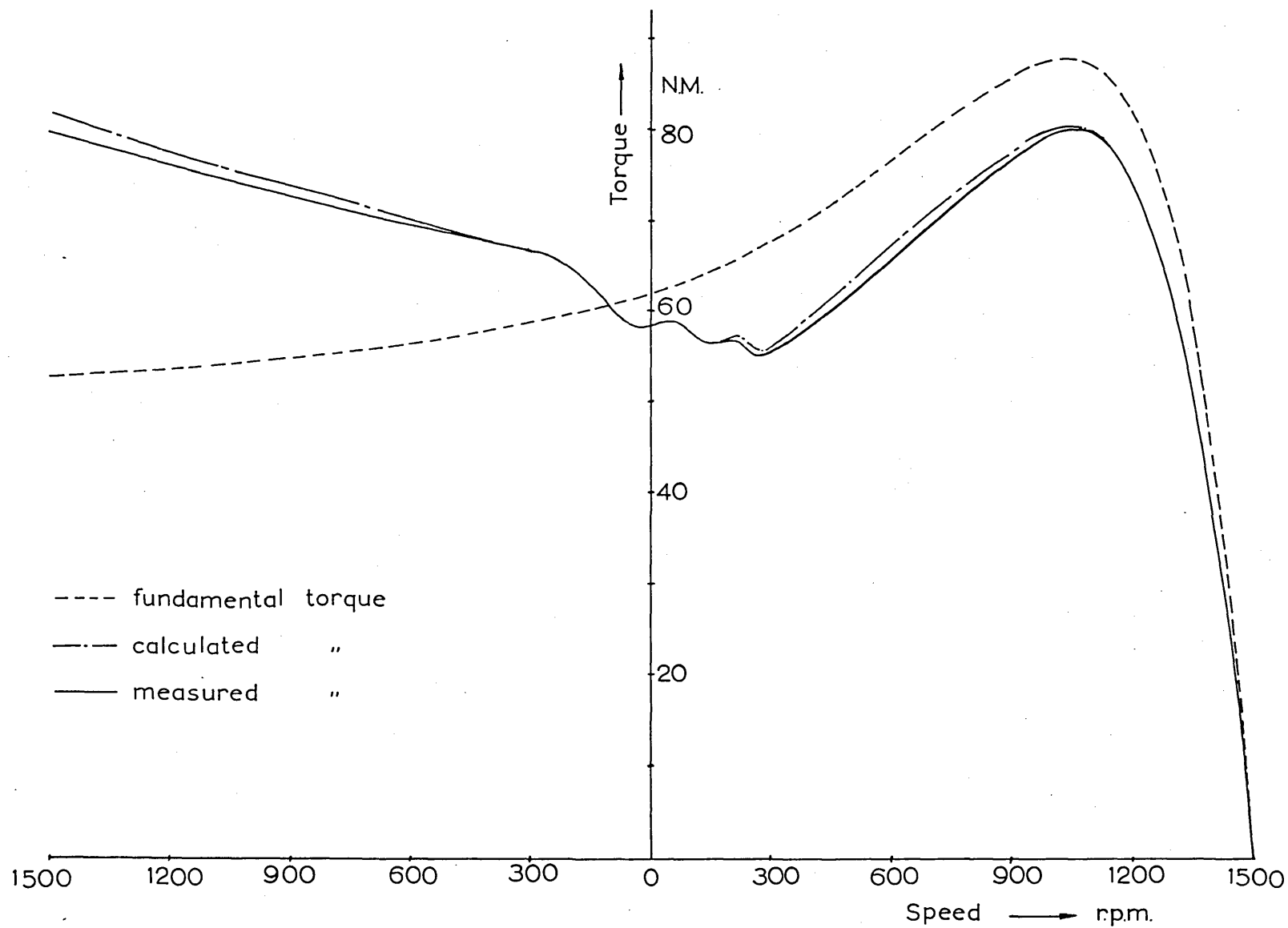


fig. 66. Torque speed curves of rotor N° 3 . (400 V, 50 c/s )



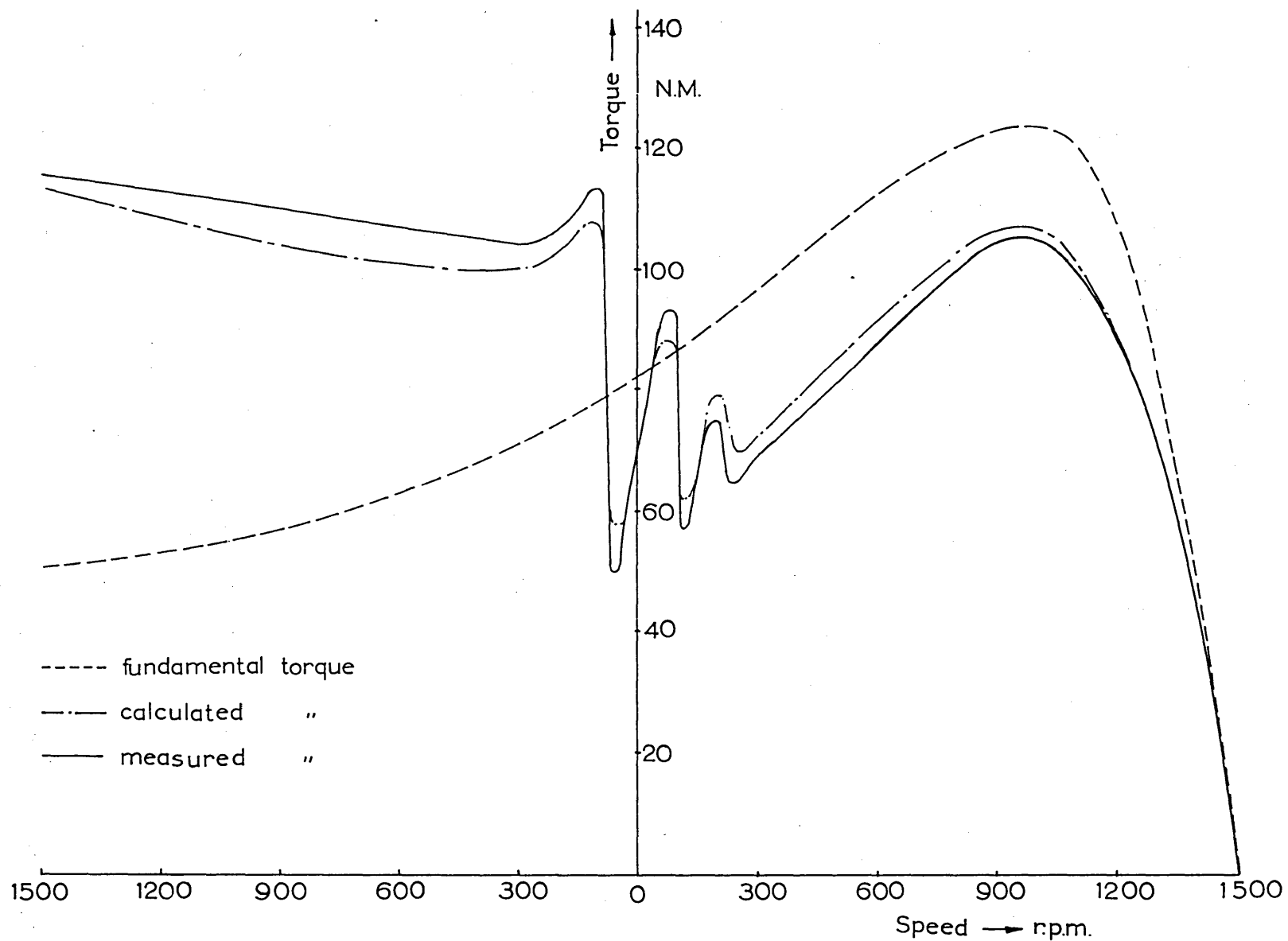


fig.67. Torque speed curves of rotor N° 5. (400 V, 50 c/s)

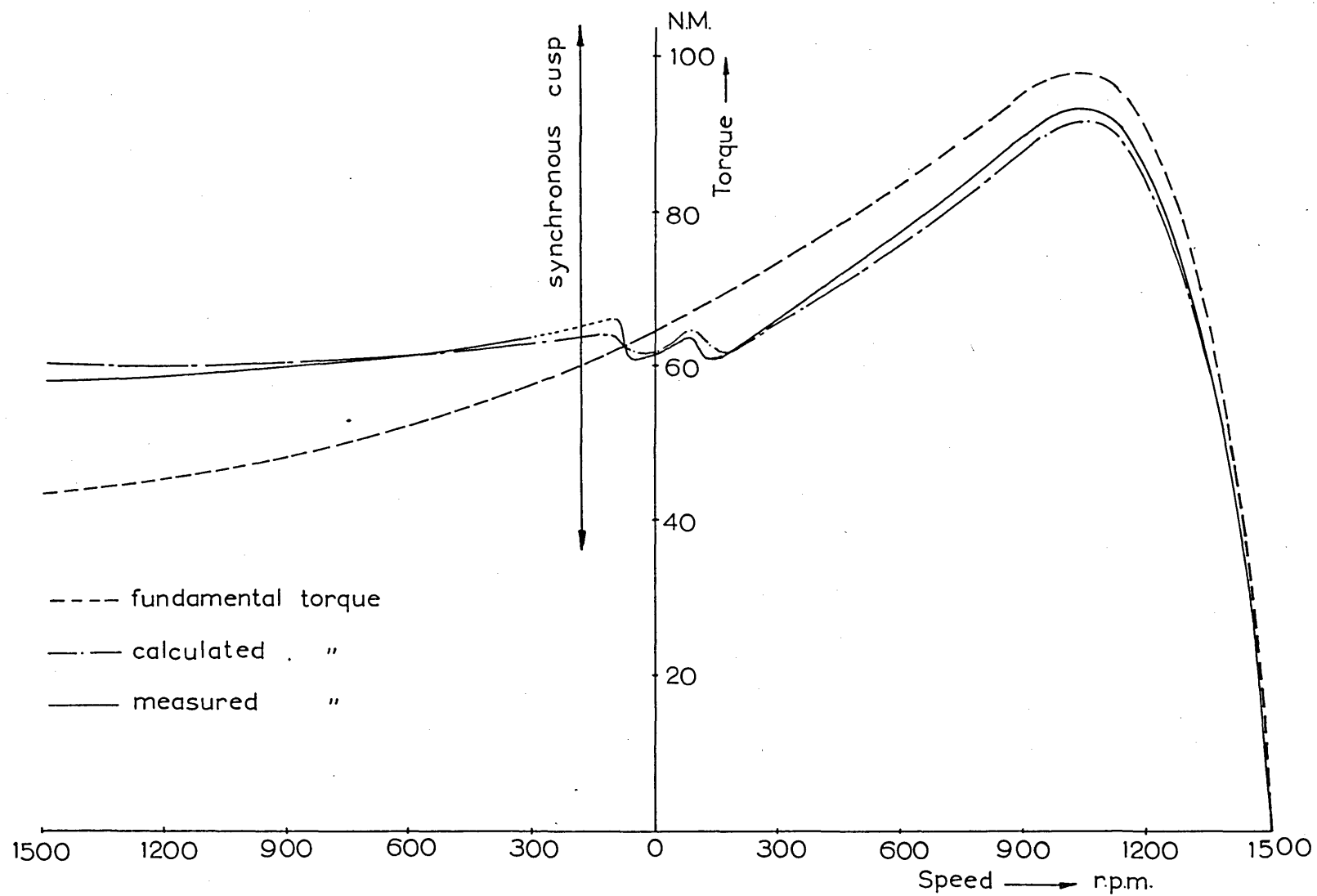


fig.68. Torque speed curves of rotor N° 6. (400 V, 50 c/s )

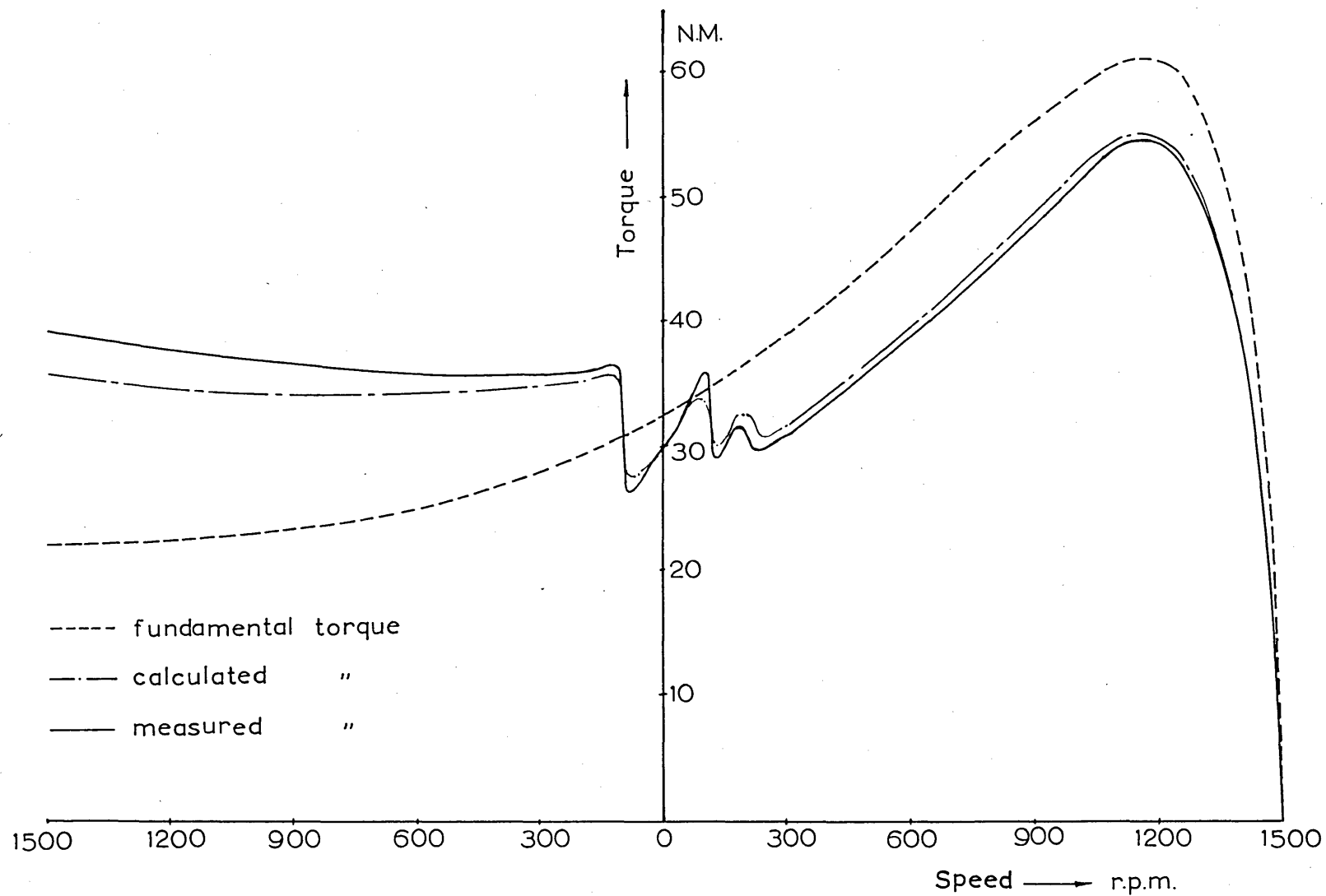


fig.69. Torque speed curves of rotor N°7. (400V, 50 c/s)

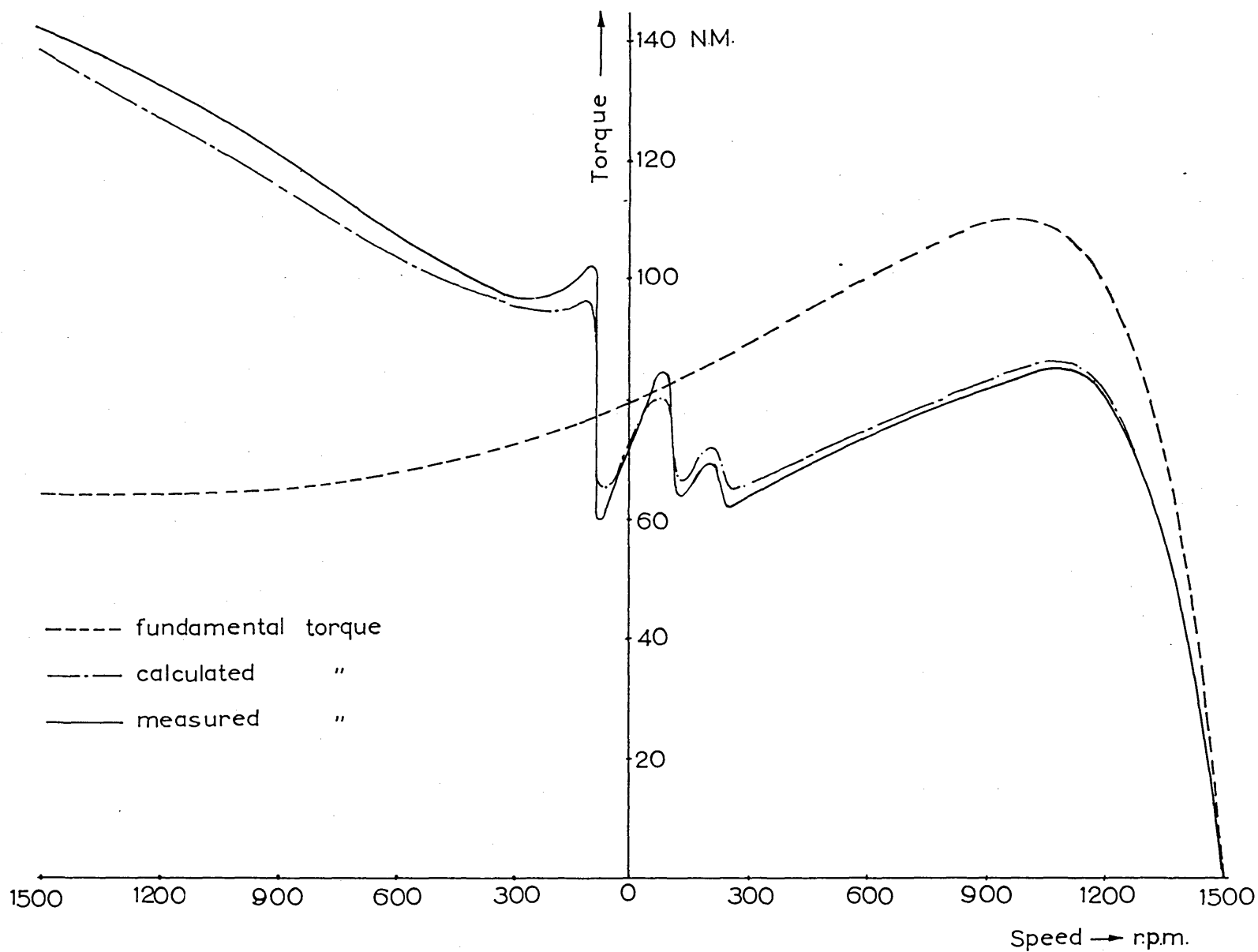


fig. 70. Torque speed curves of rotor N° 8. (400 V, 50 c/s)

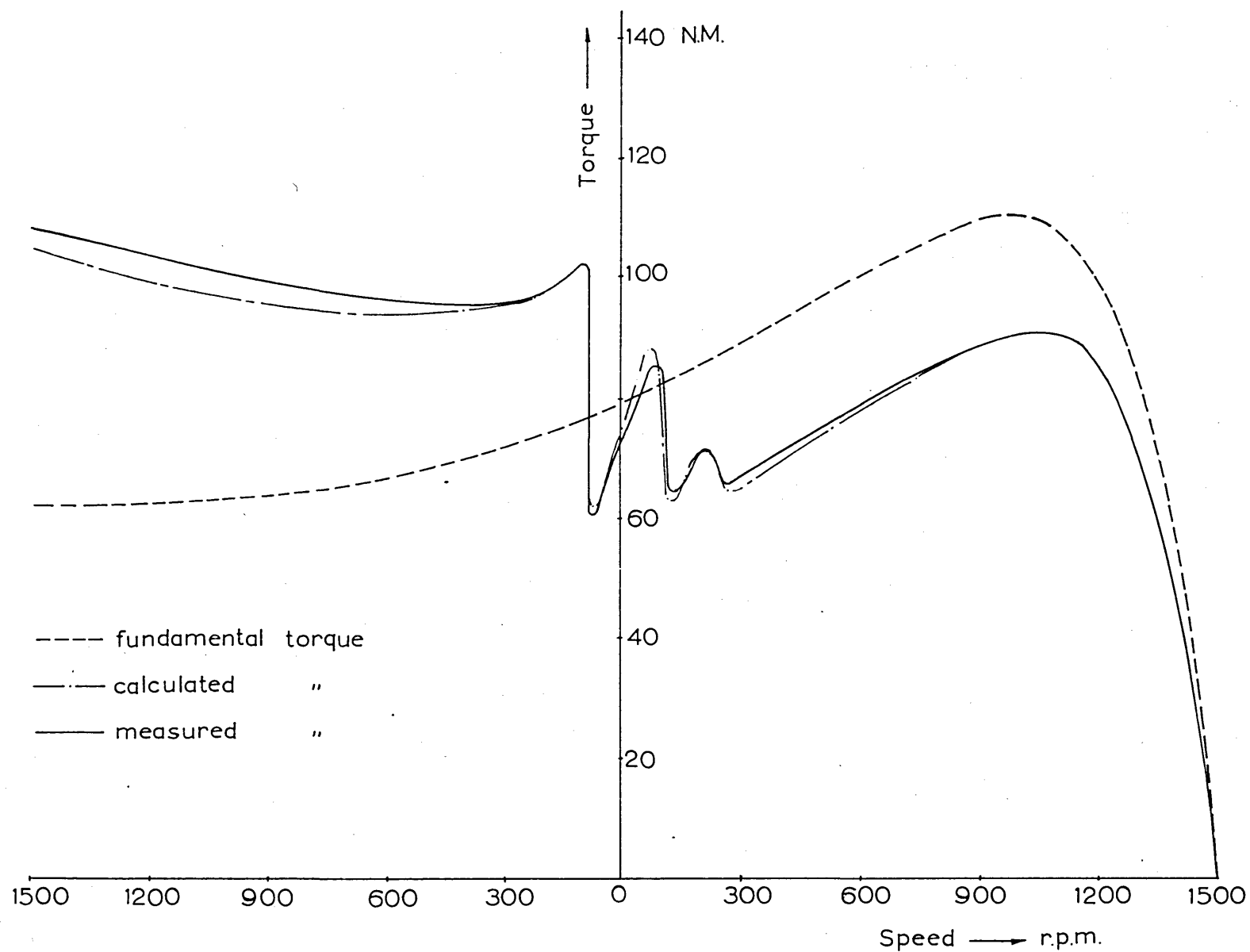
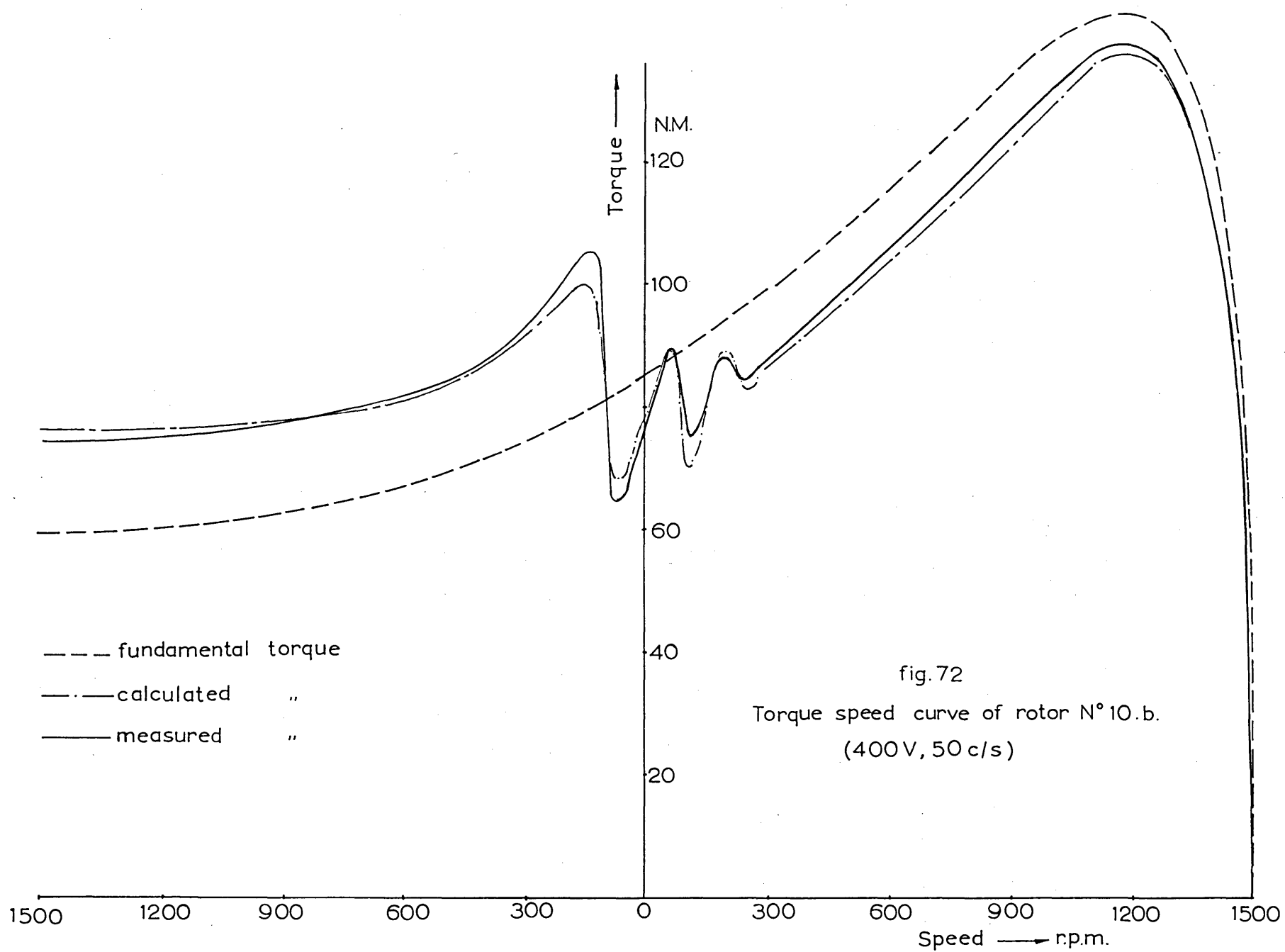


fig.71. Torque speed curves of rotor N°9. (400V, 50 c/s )



in Chapter 7, gives results which are in reasonably good agreement with the experimental ones, although the predicted curves are not as close to the measured ones as in the case of no saturation. This greater discrepancy is due to the difficulty in calculating accurate values for the saturation factors.

It should be noted that with saturation present, the total electromagnetic torque at any speed, is not proportional to the square of the voltage, nor is it exactly proportional to the square of the load current as the ordinary equivalent circuit would suggest. The fundamental torque is very nearly proportional to  $I_2^2$ . However, the harmonic torques (and hence the load losses) vary in a very complex but less rapid fashion with  $I_2$  and therefore these torques are a smaller proportion of the fundamental torque than under unsaturated conditions, because of the saturation of the leakage flux paths.

Thus the total electromagnetic torque in the motor-ing region at full voltage, is slightly higher than the torque at reduced voltage proportioned as the square of the current. This is in agreement with the experimental results obtained by other investigators.<sup>40</sup>

### 8.3 The load losses at normal load.

In Fig.73 the crosses show values of load losses for rotor No.1(a) measured under normal operating conditions by the back-to-back test at rated voltage. (400 v.). The circles in the same figure show values of the load losses of the same rotor measured at 100 v. The points shown by the triangles were measured from a reverse-rotation test, and are seen to be higher than the results of the back-to-back test.

The load losses predicted theoretically are shown by curves A and B of Fig.73 corresponding to supply voltages of 400 and 100 volts respectively. The theoretical computations are seen to agree reasonably well with the experimental results.

Table 6 compares the values of the load losses for rotors 1(a) and 10(b) as measured by the back-to-back test and also gives computed values of these losses. The values of the load losses for all rotors, as listed in the above table, are compatible with the load losses as measured from the torque-speed curves. For example, the relative values of the load losses of the different rotors measured at the reverse rotation point ( $s=2$ ) of the torque-slip characteristics of the last two Sections, are approximately the same as the relative values of the load losses obtained from the back-to-back test. Thus



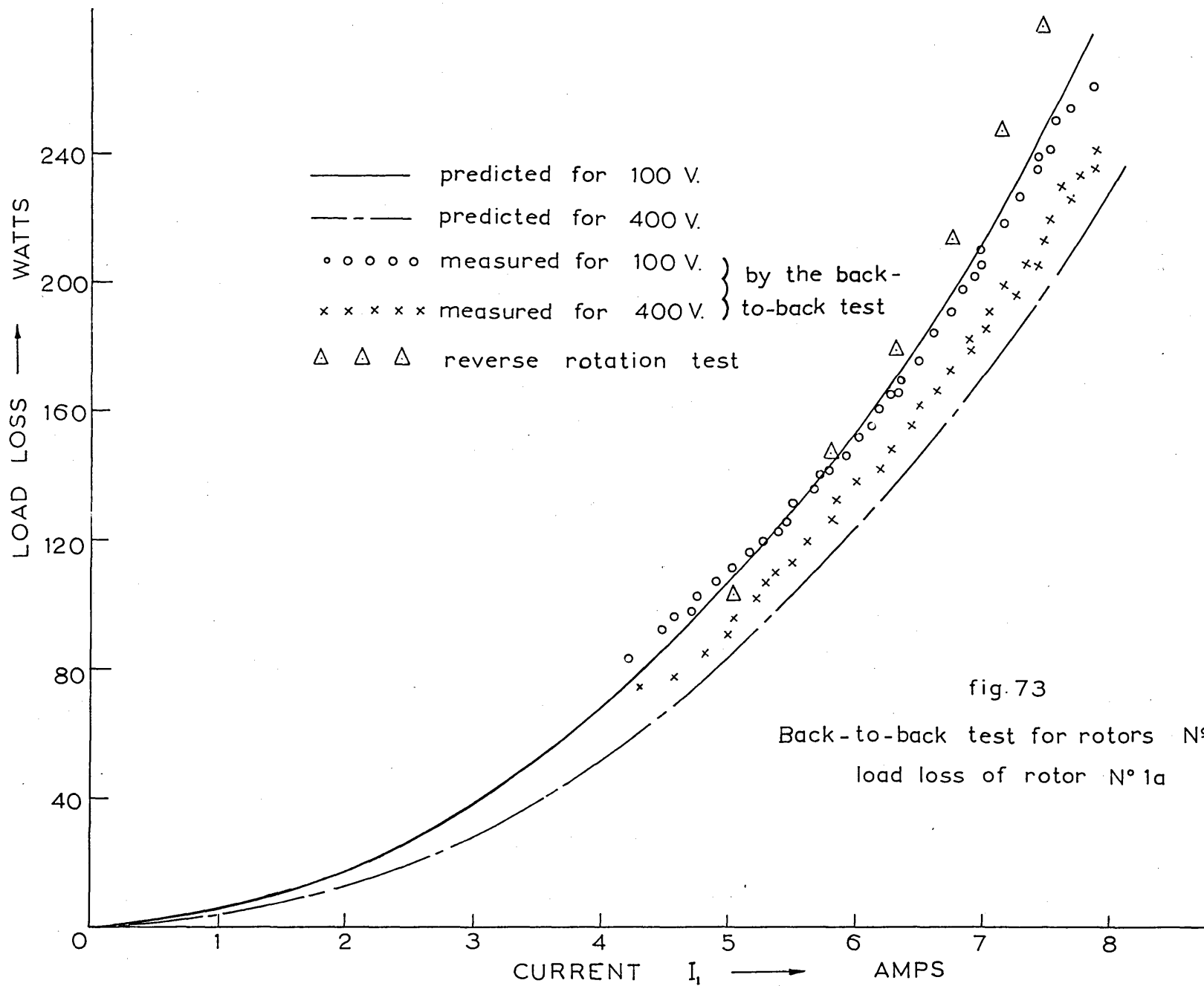


Table 6.

Comparison of load losses for different rotors measured  
by the back-to-back test.

Rotor No.	200 v. Full load current		400 v. Full load current		
	Measured	Calculated	Measured	Calculated	% of output
1(a)	186	190	171	164	3.05
2	185	180	170	152	3.04
3	179	190	158	151	2.82
4	190	195	173	163	3.09
5	352	339	320	295	5.71
6	109	93	92	76	1.64
7	241	244	215	211	3.84
8	502	461	451	407	8.07
9	305	279	277	242	4.95
10(a)	104	94	86	79	1.53
10(b)	100	94	85	79	1.52

although there may be some doubt<sup>44,45</sup> as to the absolute value of the load losses obtained by the reverse rotation test, the test gives an approximately correct value for the ratio of the load losses of two different machines and this in itself is useful.

By comparing the results of rotors No.1, 5, 6 and 7, in Table 6, the variation of load losses with slot combination can be experimentally derived and is shown by points in Fig.73(a). The curve in the same figure shows the predicted variation. A theoretical investigation of the variation of each component of the load losses with slot combination is carried out in Chapter 11.

Comparing the results of rotors No.1, 8, 9, 10(a) and 10(b) shows that the interbar resistance plays a vital role in determining the magnitude of the load losses. Thus rotor No.8 with  $\frac{1}{5}$ th of the interbar resistance of rotor No.1 has more than  $2\frac{1}{2}$  times as much load losses, whilst rotor No. 10(b) with 200 times the interbar resistance of rotor No.1 has about half the load losses of this last rotor. The values of  $r_{bb}$  for rotors No.10(a) and 10(b) are large enough to make the component of load loss due to interbar currents zero in both cases. The variation of interbar current loss with  $r_{bb}$  is discussed in greater detail in Chapter 9.

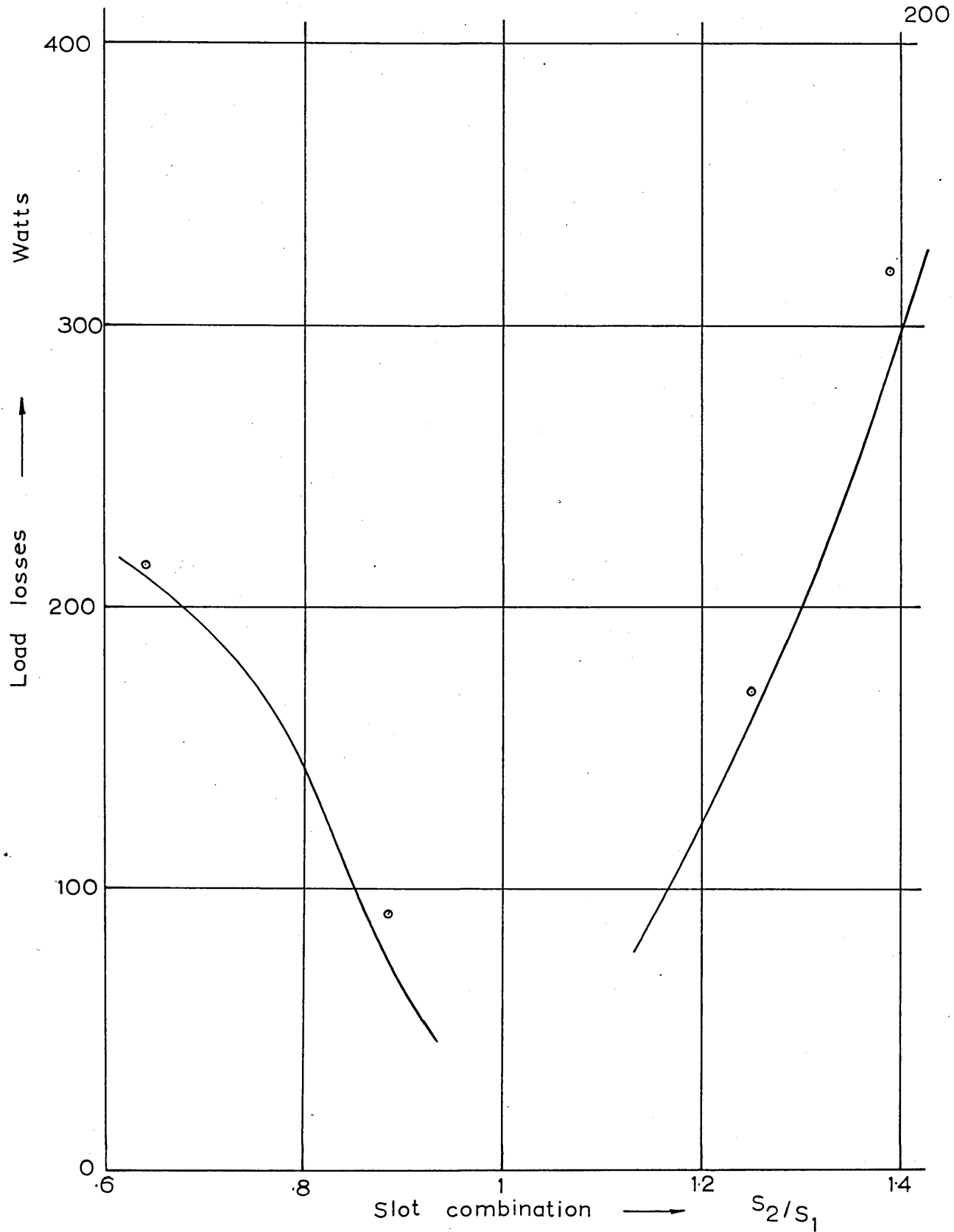


fig.73(a). Variation of total load losses with slot numbers

— theoretical curve  
○ ○ ○ experimental points

In Fig.74 curve A shows the measured values of the load losses of the slip ring machine described in Chapter 2. The results are based on a carefully conducted input-output test at rated voltage, performed by Mr. S.N.Ghani at the Imperial College Laboratories. Curve B of the same figure is the predicted value of the load losses of this machine using the theoretical formulae of Chapters 6 and 7. Since the slip ring machine is quite different in construction from the squirrel cage induction motors dealt with previously, the agreement between curves A and B in Fig.74 is important in establishing the validity of the theoretical formulae, and their applicability to any kind of induction machine.

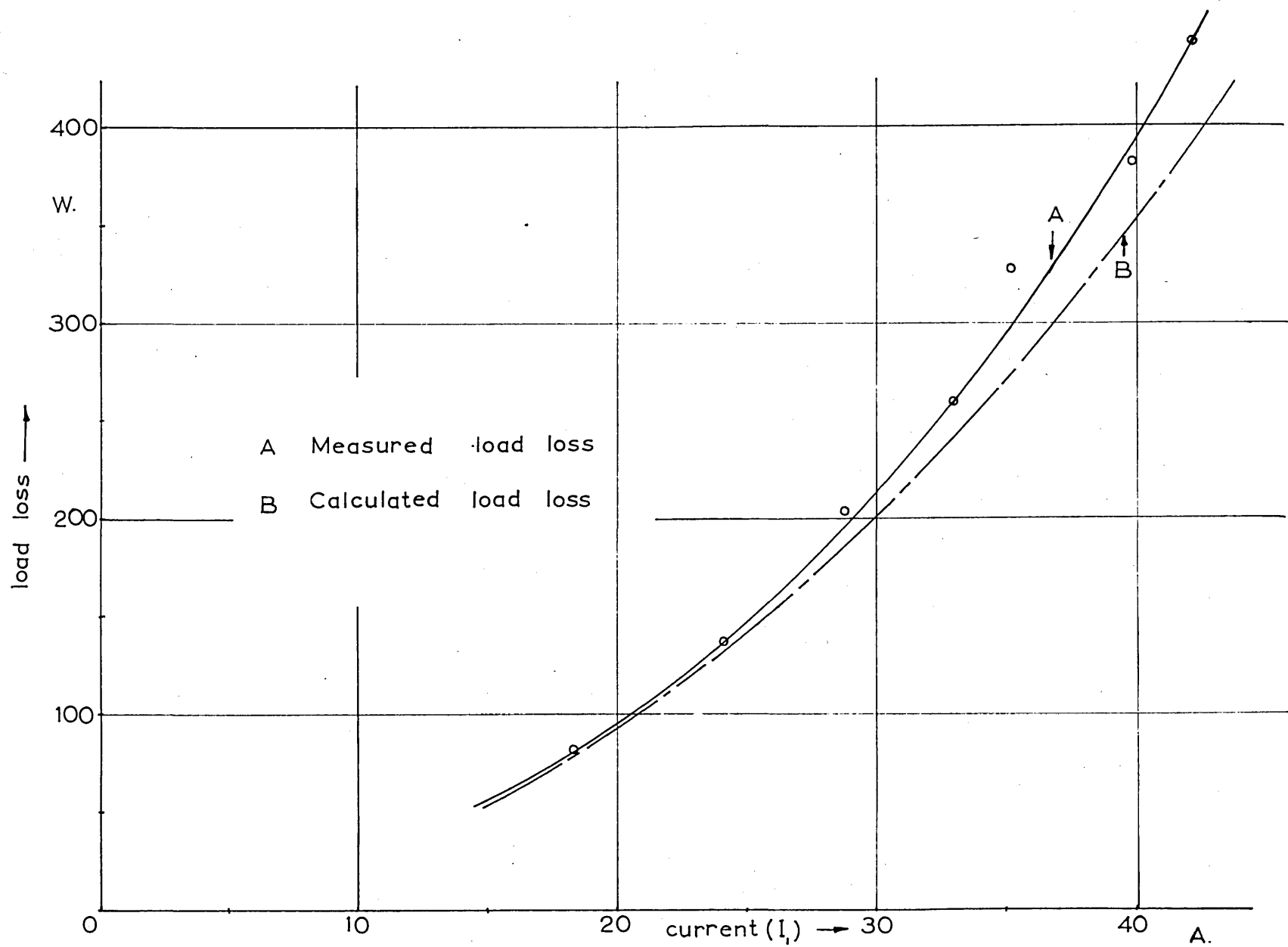


fig.74. Load losses of slip-ring machine.

P A R T   F I V E

EFFECT OF MACHINE PARAMETERS ON THE  
LOAD LOSSES

## CHAPTER 9

### THE EFFECT OF BAR INSULATION ON THE LOAD LOSSES

#### 9.1 Simplifications to cross current loss formula

Although the loss calculation (by computer) using Eqns. 6.42 or 6.43 offers no particular difficulties for a given case, a general discussion of this type of load loss with varying machine parameters is scarcely possible by its direct use.

The following two subsections deal with two special cases also dealt with by Odok.<sup>18</sup>

- (i) When the interbar resistance is low.  
and (ii) When the interbar resistance is relatively high.

##### 9.1.1 Low interbar resistance

If the interbar resistance is low enough so that:

$$\alpha_v^2 \ll \gamma_v^2$$

$$\text{i.e. } \frac{z_{bv}}{r'_{bbv}} \gg \alpha_v^2 \quad (9.1)$$

and  $\gamma_v \rightarrow \infty$  so that:

$$\sinh \gamma_v \ell \approx \cosh \gamma_v \ell \gg \cos \alpha_v \ell \quad (9.2)$$

then the loss formula of Eqn. 6.43 simplifies to:



$$P_{2v} = S_2 \cdot E_{ov}^2 \cdot R_e \left[ \frac{\ell}{z_{bv}} + \frac{2\alpha_v^2 r'_{bbv}}{\gamma_v \cdot z_{bv}^2} \right] \quad (9.3)$$

### 9.1.2 High interbar resistance

By "high interbar resistance" is meant the condition for which the following approximations hold.

$$\alpha_v^2 \gg \gamma_v^2$$

i.e.  $r'_{bbv} \gg z_{bv}$

$$\text{and } \sinh \gamma_v \ell \rightarrow \gamma_v \ell$$

$$\cosh \gamma_v \ell \rightarrow 1$$

Under these assumptions the loss formulae of Eqn. 6.43 becomes:

$$P_{2v} = S_2 \cdot E_{ov}^2 \cdot \left[ \frac{\ell}{\alpha_v^2 r'_{bbv}} + \frac{r_b \cdot \ell}{|z_{bv}|^2} \cdot \left( \frac{\sin \frac{\alpha_v \ell}{2}}{\frac{\alpha_v \ell}{2}} \right)^2 \right] \quad (9.4)$$

From Eqn. 9.4 one can now see very clearly just how much loss is due to the cross currents and how much due to the harmonic bar currents that flow in the squirrel cage. Only the first term in the square brackets contains the quantity  $r'_{bbv}$  and it indicates that the load loss due to the interbar flow decreases as  $r'_{bbv}$  increases; whereas the opposite is true for the case of low interbar resistance (Eqn. 9.3).

The second term of Eqn. 9.4 gives the loss due to the harmonic currents in the bars only. It should be noted that the term  $(\sin \frac{\alpha_v \ell}{2} / \frac{\alpha_v \ell}{2})^2$  is the skew factor. (see Sections 7.1 and 7.3).

Fig.75 shows the variation of the total losses due to the cross currents with the value of the interbar resistance  $r_{bb}$  for a constant value of skew.

## 9.2 The location of the place of dissipation of the cross current losses.

The interbar current losses due to the  $v^{\text{th}}$  stator field harmonic are given by Eqn. 6.43. If in this equation  $r_{bb}$  is set to infinity, (i.e.  $\gamma_v$  set to zero), the loss formulae becomes:

$$P_{2v\infty} = S_2 \cdot E_{ov}^2 \cdot \frac{r_b}{|z_{bv}|^2} \cdot \frac{l^2}{skv} \quad (9.5)$$

which represents only the losses produced by the harmonic currents flowing in the squirrel cage bars.

One might therefore tend to conclude that the difference between  $P_{2v}$  as given by Eqn.6.43 and  $P_{2v\infty}$  as given by Eqn. 9.5 is the power loss in the interbar region. Certainly the difference  $(P_{2v} - P_{2v\infty})$  is caused by the interbar currents; its place of dissipation, however, is not solely the interbar region. This

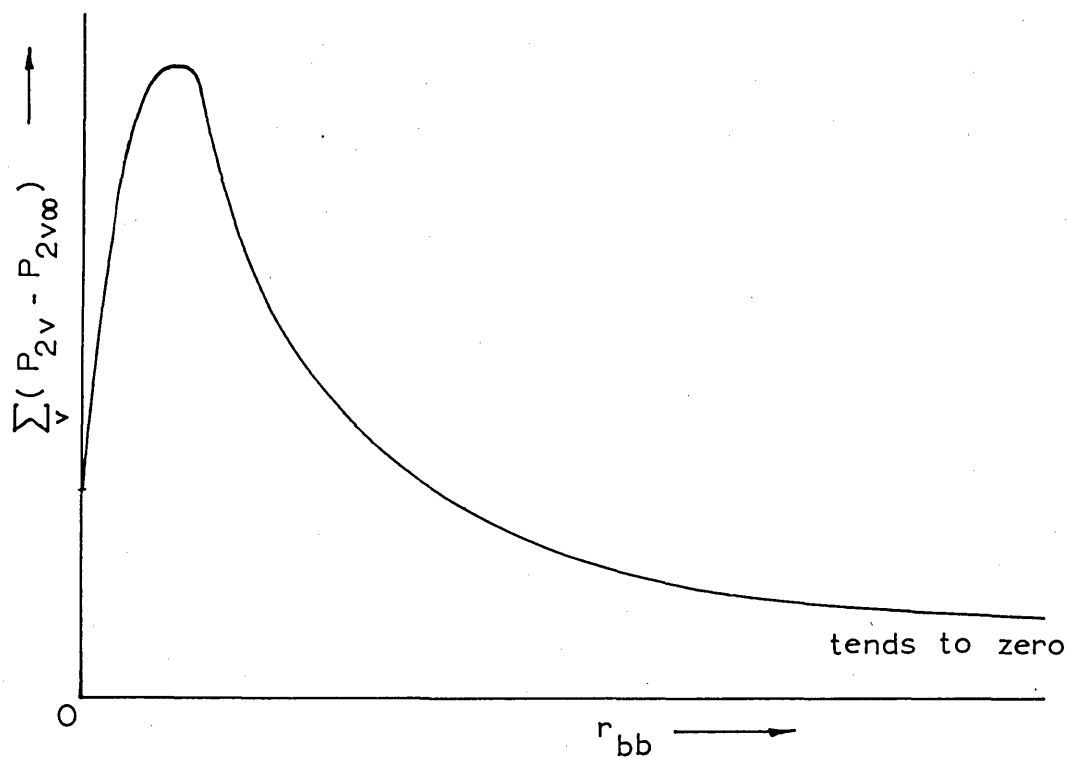


fig.75. Variation of the total loss due to the cross currents with interbar resistance.

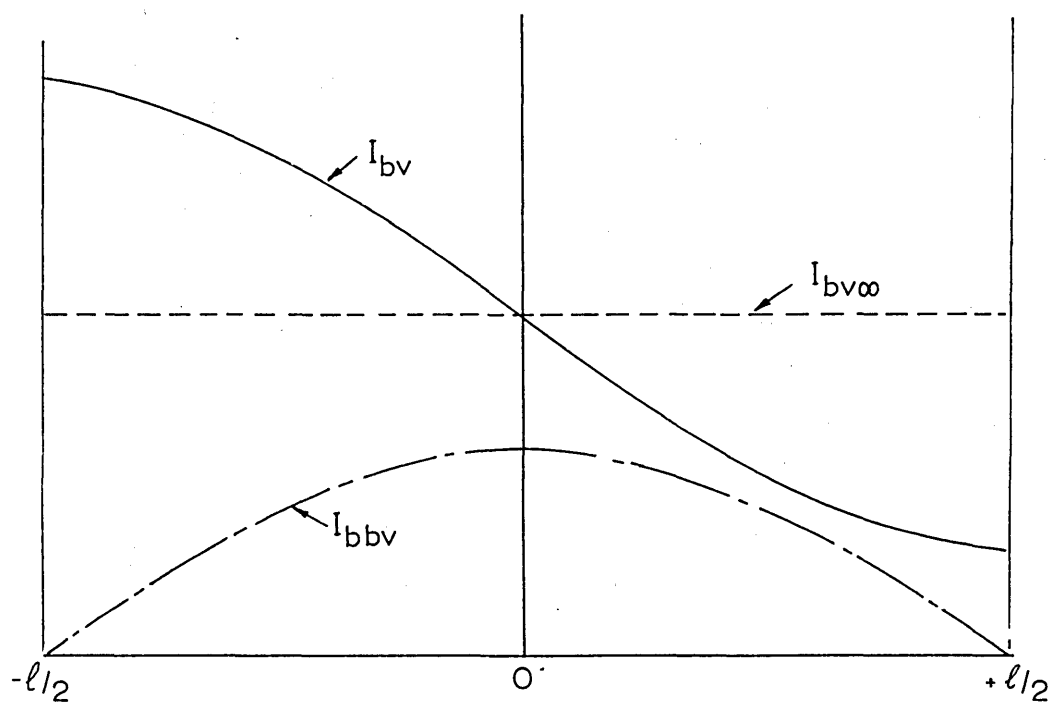


fig.76. Current distributions along a bar.

can be seen very clearly from Eqn. 6.38 which gives the value of the bar current  $I_{bv}$  at any distance  $x$  from the centre of the bar. This distribution is shown in Fig. 76. Since the current  $I_{bv}$  flowing along the bar varies along the length of the bar, the loss:

$$\int_{-\ell/2}^{\ell/2} |I_{bv}|^2 \cdot r_b \, dx$$

is in general different from what it would have been with no interbar currents flowing. In the latter case  $I_{bv}$  would have a constant value given by

$$I_{bv\infty} \equiv \left[ I_{bv} \right]_{r_{bb}=\infty} = \frac{E_{ov}}{Z_{bv}} \cdot k_{skv}$$

Thus in general the effect of the cross currents is twofold:

- (i) It increases the  $I^2R$  losses in the squirrel cage bars themselves by the amount:

$$\begin{aligned} P'_{2v} &= S_2 \cdot \left[ \int_{-\ell/2}^{\ell/2} I_{bv}^2 \cdot r_b \cdot dx - I_{bv\infty}^2 \cdot r_b \cdot \ell \right] \\ &= S_2 \cdot \int_{-\ell/2}^{\ell/2} |I_{bv}|^2 \cdot r_b \cdot dx - P_{2v\infty} \quad (9.6) \end{aligned}$$

and (ii) It causes losses in the interbar region given by:

$$P''_{2v} = S_2 \cdot \int_{-\ell/2}^{\ell/2} |I_{bbv}|^2 \cdot r_{bb} \cdot dx \quad (9.7)$$

The overall loss caused by currents in the bars and the interbar region is therefore:

$$P_{2v} = P_{2v\infty} + P'_{2v} + P''_{2v} \quad (9.8)$$

where  $(P_{2v\infty} + P'_{2v})$  is the loss in the bars and  $P''_{2v}$  the loss in the interbar region.

As an example consider the case of zero cross path resistance. Letting  $r'_{bbv} = 0$  in Eqn. 6.43 gives:

$$P_{2v} = S_2 E_{ov}^2 \cdot \ell \cdot \frac{r_b}{|z_{bv}|^2} \quad (9.9)$$

The losses  $P_{2v\infty}$  are given by Eqn. 9.5, and the losses  $P''_{2v}$  in the interbar region are obviously zero since  $r_{bb} = 0$ .

Hence from Eqn. 9.8 one obtains:

$$P'_{2v} = S_2 \cdot E_{ov}^2 \cdot \ell \cdot \frac{r_b}{|z_{bv}|^2} \cdot (1 - k_{skv}^2) \quad (9.10)$$

which is the extra loss dissipated in the bars due to the interbar currents.

It is interesting to note, from Eqn. 9.9 that a skewed and completely uninsulated squirrel cage winding behaves in exactly the same manner as a winding with no skew.

### 9.3 The modified harmonic equivalent circuit.

The loss formula of Eqn. 6.43 can be re-written in the form:

$$P_{2v} = S_2 E_{ov}^2 \ell^2 k_{skv}^2 \cdot \text{Re} \left[ \frac{1}{r'_{bbv} \cdot \ell \cdot k_{skv}^2 (\alpha_v^2 + \gamma_v^2)} + \frac{2\alpha_v^2}{r'_{bbv} \cdot \ell^2 \cdot k_{skv}^2 (\alpha_v^2 + \gamma_v^2)^2} \cdot \frac{\cosh \gamma_v \ell - \cos \alpha_v \ell}{\gamma_v \sinh \gamma_v \ell} \right] \quad (9.11)$$

and the loss formula for  $P_{2v\infty}$  (Eqn. 9.5) as:

$$P_{2v\infty} = S_2 \cdot E_{ov}^2 \cdot \ell^2 k_{skv}^2 \cdot \text{Re} \left[ \frac{1}{Z_{tbv}} \right] \quad (9.12)$$

where  $Z_{tbv} = \ell \cdot z_{bv}$  is the total impedance of one rotor bar.

The losses  $P_{2v\infty}$  can also be calculated from the harmonic equivalent circuit of Fig.77(a); where

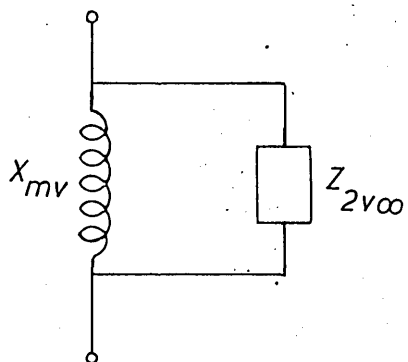
$$Z_{tbv} = jX_{mv} + Z_{2v\infty} \quad (9.13)$$

From the similarity of Eqns. 9.11 and 9.12 therefore, the losses  $P_{2v}$  can be calculated<sup>41</sup> from the equivalent circuit of Fig.77(b) where:

$$\frac{1}{Z_{tv}} \equiv \frac{1}{jX_{mv} + Z_{2v}} \quad (9.14)(a)$$

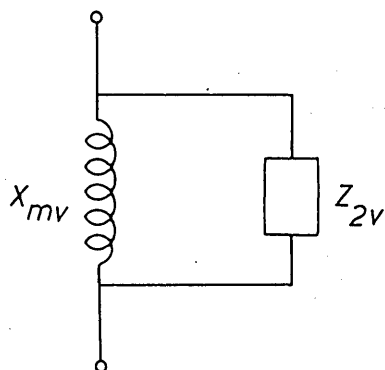
$$= \frac{1}{r'_{bbv} \ell k_{skv}^2 (\alpha_v^2 + \gamma_v^2)} + \frac{2\alpha_v^2}{r'_{bbv} \ell^2 k_{skv}^2 (\alpha_v^2 + \gamma_v^2)^2} \left[ \frac{\cosh \gamma_v \ell - \cos \alpha_v \ell}{\gamma_v \sinh \gamma_v \ell} \right] \quad (9.14)(b)$$

$$r_{bb} = \infty$$



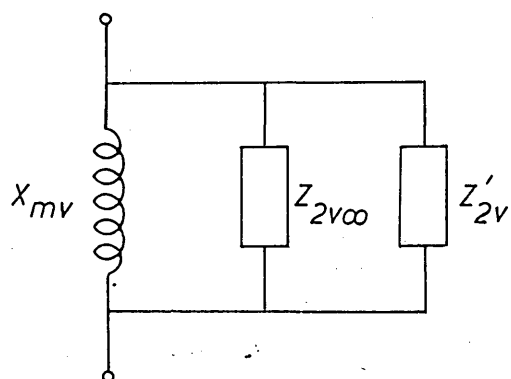
(a)

$$r_{bb} \neq \infty$$



(b)

equivalent to  
(b) above



(c)

fig. 77. Harmonic equivalent circuit including cross current effects.

$$\text{and hence } Z_{2v} = Z_{tv} - jX_{mv} \quad (9.14)(c)$$

$Z_{tv}$  is the "total generalised impedance" of the rotor, including the effects of bar and interbar currents, and  $Z_{2v}$  is the "total generalised rotor leakage impedance".

The impedance  $Z_{2v}$  can be considered as the parallel combination of two impedances:  $Z_{2v\infty}$  and  $Z'_{2v}$ , where  $Z'_{2v}$  represents the effect of the cross currents only. The resulting circuit is shown in Fig.77 (c) where:

$$\frac{1}{Z'_{2v}} = \frac{1}{Z_{2v}} - \frac{1}{Z_{2v\infty}} \quad (9.15)$$

Substituting the values of  $Z_{2v}$  and  $Z_{2v\infty}$  from Eqns. 9.14(c) and 9.13 into Eqn. 9.15 gives:

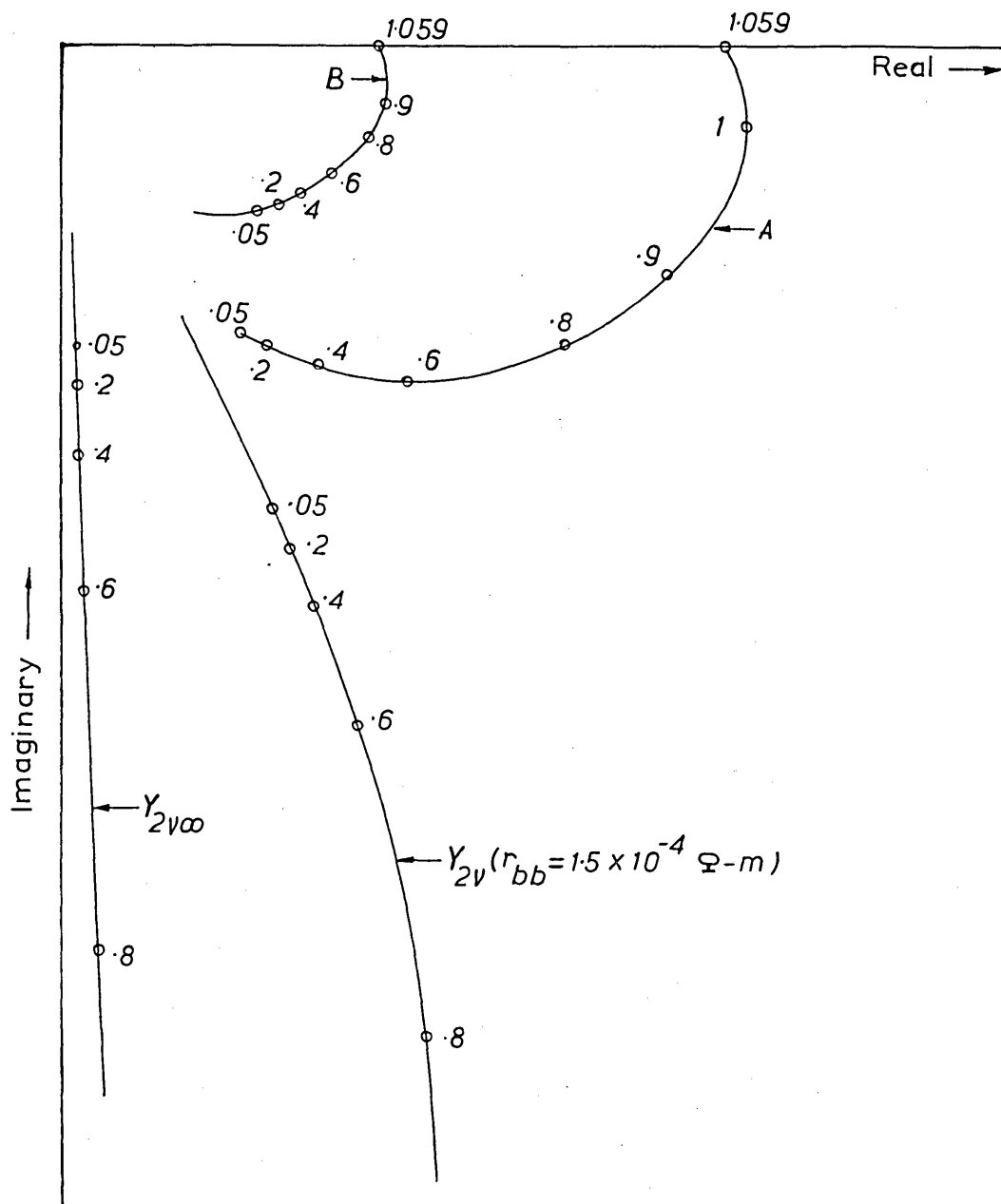
$$Z'_{2v} = \left[ \frac{Z_{tv} \cdot Z_{tbv} - X_m^2}{Z_{tbv} - Z_{tv}} \right] + jX_m \left[ \frac{Z_{tbv} + Z_{tv}}{Z_{tbv} - Z_{tv}} \right] \quad (9.16)$$

Thus if each harmonic branch of the equivalent circuit of Fig.25, representing the interaction between the  $v^{\text{th}}$  stator harmonic field and the rotor circuits, is shunted by the impedance  $Z'_{2v}$  given by Eqn. 9.16, the circuit of Fig.25 will correctly represent the effects of both bar and interbar currents. It should be noted, however, that the impedance  $Z'_{2v}$  is not composed from a constant resistance and inductance but is a complex function of frequency which is not physically realisable.



The frequency response locus of  $Y'_{2v} \equiv 1/Z'_{2v}$  is shown in Fig.78 for the first slot harmonic ( $17^{\text{th}}$ ). This figure is calculated from Eqns. 9.16 and 9.14 (b) using the parameters of rotor No.1 and curves are shown for two values of interbar resistance  $r_{bb}$ . The markings on the curves correspond to the values of the fundamental slip at each point. A slip of 0.05 is the normal full load condition.

It is possible to normalise the curves of  $Y'_{2v}$  with respect to any machine parameter, in which case the modified equivalent circuit of Fig.77 (c) can be solved (or consulted) for each harmonic without the use of a computer. This may be useful at the designing stage of a machine.



A: Admittance  $Y'_{2v} = Y_{2v} - Y_{2v\infty}$  ( $r_{bb} = 7 \times 10^{-5} \Omega\text{-m}$ )

B: " " " ( $r_{bb} = 1.5 \times 10^{-4} \Omega\text{-m}$ )

fig.78. Admittance loci of first slot harmonic. (17<sup>th</sup>)

## CHAPTER 10

### THE EFFECT OF SKEW ON THE LOAD LOSSES.

It is the intention of this Chapter to simplify the theoretical formulae of Chapters 6 and 7 in a way that will make obvious the variation of each component of load loss with skew. In this Chapter and the ones that follow, by load loss is meant the load loss of the induction machine under normal conditions of operation. Due to the simplifications introduced, the final results arrived in Sections 10.1, 10.2 and 10.3 are only of a qualitative nature.

#### 10.1 Harmonic bar current load losses.

The load losses due to the harmonic currents induced in the squirrel cage by the  $v^{\text{th}}$  stator harmonic field are given by Eqn. 9.5 as:

$$P_{2v\infty} = G_{1v} \cdot k_{skv}^2 \quad (10.1)$$

$$\text{where } G_{1v} = S_2 E_{ov}^2 r_b / |z_{bv}|^2 \quad (10.2)$$

The factor  $G_{1v}$  is a constant independent of skew, and  $k_{skv}$  is the skew factor given by Eqn. 7.12.

The total harmonic bar current losses are therefore given by:

$$P_{2\infty} = \sum_{v \neq 1} G_{1v} \cdot k_{skv}^2 \quad (10.3)$$

A numerical calculation of  $G_{1v}$  indicates that its values for the phase belt harmonics, are very much smaller than those for the slot harmonics, primarily due to the reduction of the former by the stator winding factor  $k_{dpv}$ . Thus in most practical cases the sum of Eqn. 10.3 need only extend over the slot harmonics, and in particular over the first stator slot harmonic pair of orders  $(\pm \frac{S_1}{p} + 1)$ .

The number of stator slots per pole pair is always much greater than unity, and hence  $(\pm \frac{S_1}{p} + 1)$  is very nearly equal to  $\pm \frac{S_1}{p}$ . The skew factors  $k_{skv}$  for the two slot harmonics are practically equal and have a mean value  $k_{sk}$ .

The total harmonic bar current losses given by Eqn. 10.3 therefore become:

$$P_{2\infty} = k_{sk}^2 \cdot \sum_{v=(1 \pm \frac{S_1}{p})} G_{1v} \quad (10.4)$$

Hence the variation of this component of load loss with skew depends on the factor  $k_{sk}^2$  which is shown plotted in Fig.79. The abscissa of this figure is marked in terms of the effective skew, which makes the figure quite general.

## 10.2 Cross current load losses.

The variation of losses due to interbar currents with

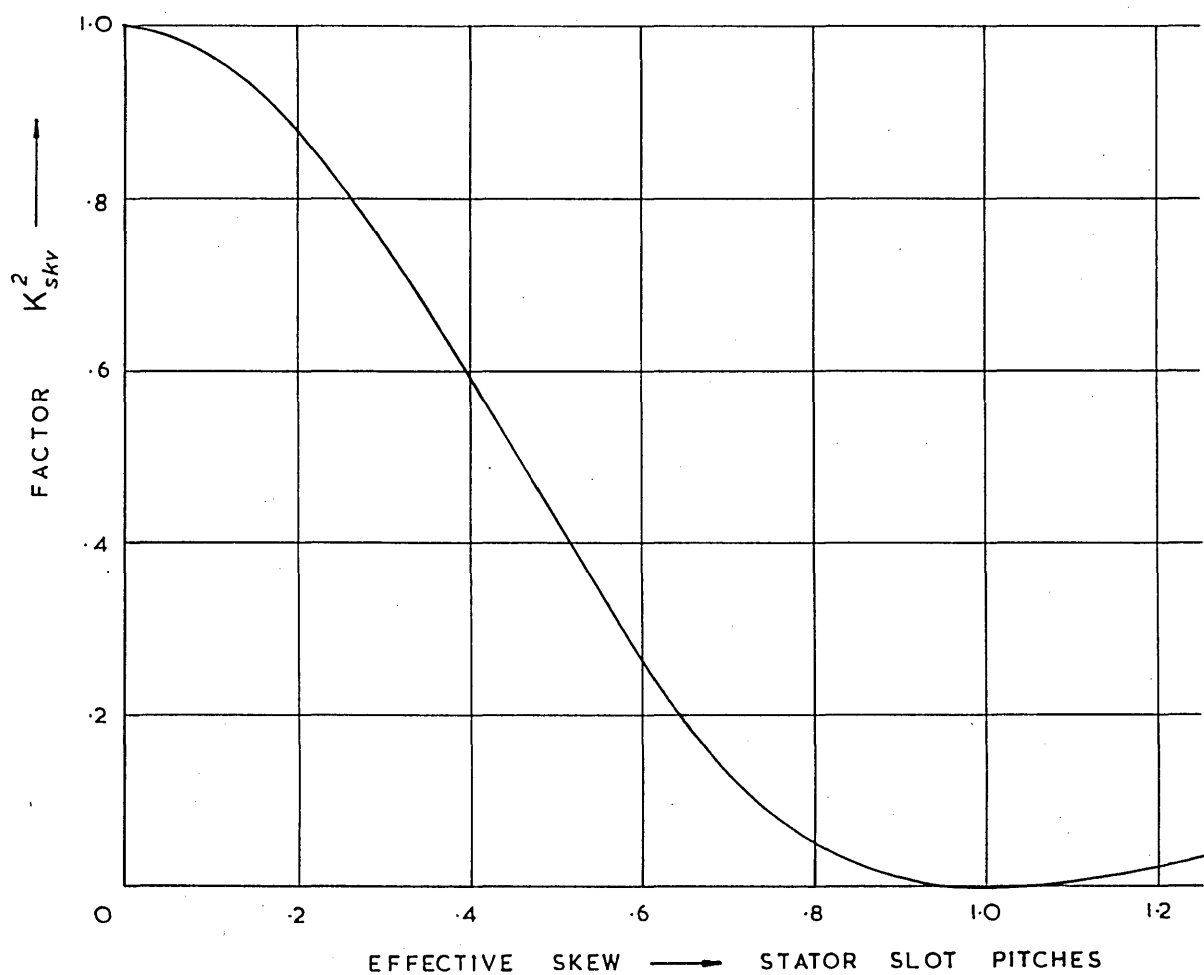


fig.79. Variation of loss factor  $K_{skv}^2$  with skew.

Losses due to harmonic currents in bars are approximately given as:  $G_{lv} K_{skv}^2$  where  $G_{lv}$  is a constant.

skew is very strongly dependent on the value of the interbar resistance, as can easily be seen by inspection of Eqns. 9.3 and 9.4. From these equations it follows that, for a relatively well insulated machine (Eqn. 9.4), the losses in the interbar region decrease as the skew increases, but that the opposite is true if the insulation is very poor. (Eqn. 9.3). The losses are, of course, zero if the skew is zero (and the end ring impedance negligible) irrespective of whether the rotor is insulated or not.

Fig.80 shows the variation of the cross-current load losses with skew, for different degrees of insulation of the squirrel cage. The curves were calculated from the exact loss formula given by Eqn. 6.43 after subtracting from it the losses due to the harmonic currents flowing in the squirrel cage bars. The calculation summed the losses of all harmonics with orders up to 100, and it was again noted that the slot harmonics were the main contributors to the total cross current load loss.

### 10.3 Iron load losses in the stator and the rotor.

The iron load losses in both the stator and the rotor, consist of the surface losses produced by the harmonic flux that closes itself in the tooth crowns,

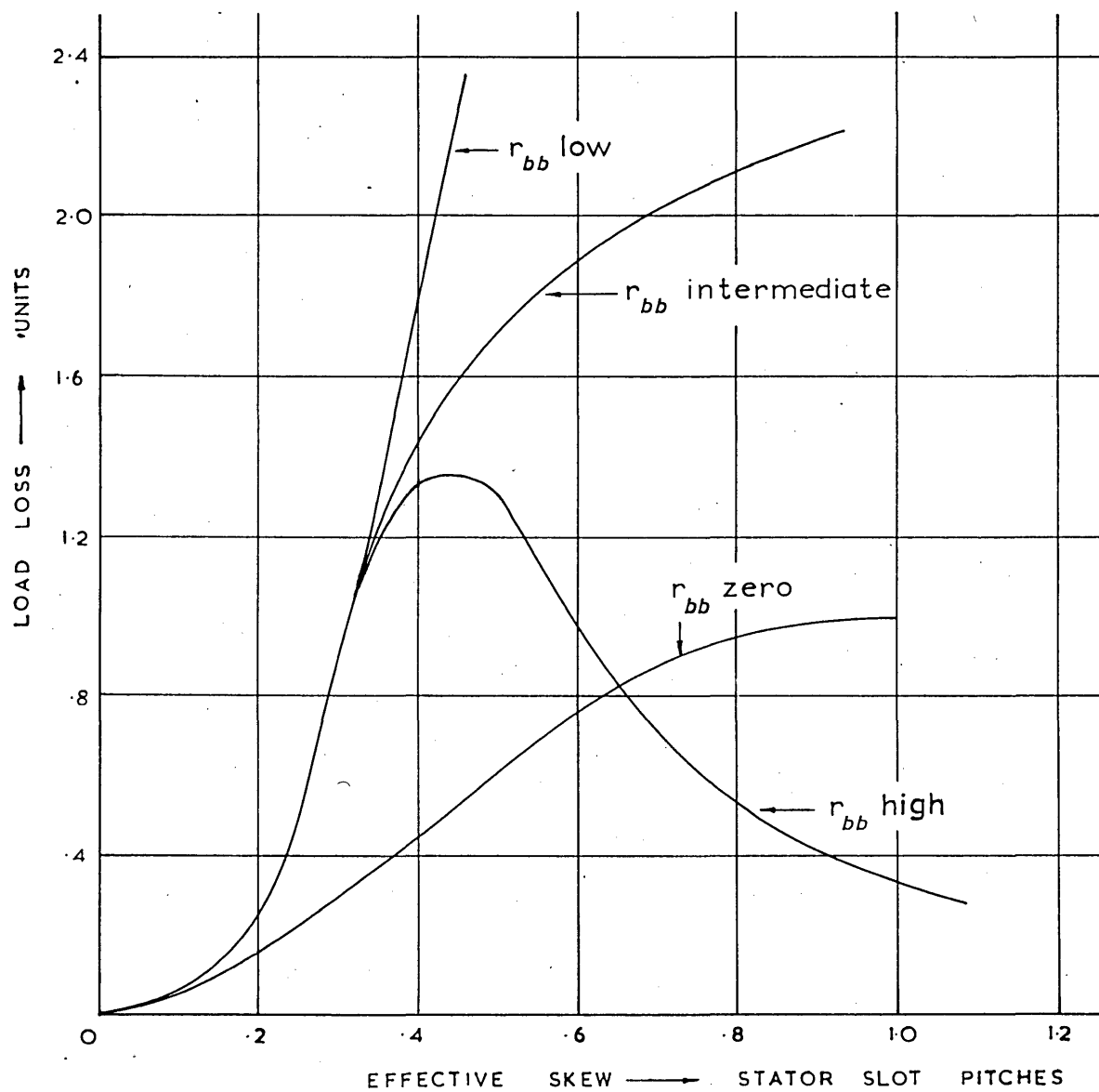


fig.80. Variation of cross-current load-losses with skew.

and the tooth body losses produced by the flux that penetrates deep into the teeth, as explained in Chapter 6. The stator and rotor surface losses and the stator tooth body losses, are practically independent of the rotor skew and need not therefore be discussed further here.

The losses in the rotor tooth bodies, are given by Eqn. 6.70. Substituting the value of  $B_{tv}''$  from Eqn. 6.68 into Eqn. 6.70 gives the losses as:

$$P_t'' = \sum_{v \neq 1} (k_{tv}'')^2 \cdot B_{1v}^2 \cdot \left(\frac{\lambda}{w_t''}\right)^2 \cdot \left(\frac{\sin \beta_v''}{\beta_v''}\right)^2 \cdot [\sigma_h f_v + \sigma_e f_v^2] W_t'' \cdot S_2 \quad (10.5)$$

Thus the rotor tooth iron losses of each harmonic are proportional to the square of the damping factor  $k_{tv}$  of that harmonic which is a function of the skew factor  $k_{skv}$  as seen by Eqn. 6.67. If only the first pair of stator slot harmonics is considered once more, the same arguments put forward in Section 10.1 apply and the losses  $P_t''$  become proportional to  $(k_t'')^2$ , where:

$$k_t'' = 1 - \frac{\bar{x}_{mv} + \bar{x}_{2dv}}{\left[ \frac{\bar{x}_{mv}}{k_{sk}^2} + \bar{x}_{2dv} + \bar{x}_{2sl} \right]} \quad (10.6)$$

$k_{sk}$  is again the mean value of the skew factor for the two slot harmonics, and the quantities with the bar



on top represent mean values of the reactances of these two harmonics.

Fig.81 shows the variation of  $(k_t'')^2$  with the effective bar skew. The figure was calculated using a value of  $\bar{x}_{mv}$  corresponding to the experimental stators, and values of  $\bar{x}_{2dv}$  and  $\bar{x}_{2sl}$  corresponding to the slot dimensions of rotor No.1. This, however, is only by the way of an illustration, and curves similar to that in Fig.81 apply to all squirrel cage induction motors.

#### 10.4 The total load loss.

Although the final results of the last three sections are only approximate, they nevertheless indicate clearly how each component of load loss varies with the skewing of the squirrel cage bars. By combining the results of those Sections the variation of the total load loss with skew can be estimated.

Fig.79 shows that the harmonic bar current losses are maximum at zero skew and minimum at full skew, whereas Fig.81 shows that the iron load losses are maximum at full skew and minimum at zero skew. For  $r_{bb}$  high Fig.80 shows that the cross current losses show a maximum at an intermediate skew. Thus for a relatively well insulated machine, the three types of loss will combine to form a total loss, which does not vary a great deal with the skewing of the squirrel cage bars.

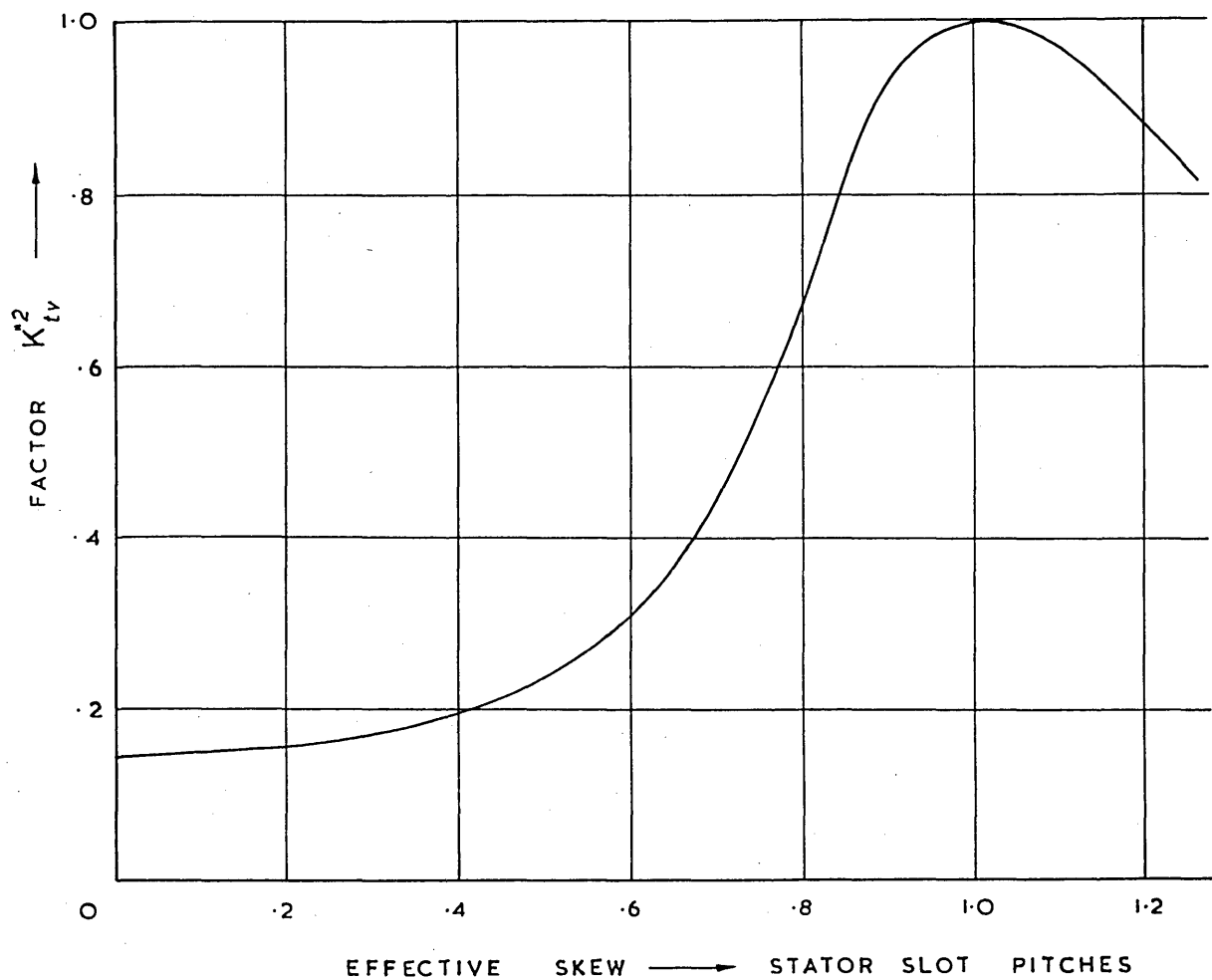


fig.81. Variation of loss factor  $K_{tv}^2$  with skew.

Iron losses in rotor teeth are approximately given as:

$$G \cdot K_{tv}^2 \quad \text{where } G \text{ is a constant.}$$

On the other hand, for a machine with poor insulation ( $r_{bb}$  low) Fig.80 shows that the cross current losses increase very rapidly indeed with increasing skew, with the result that the total losses also increase.

The above conclusions are portrayed in Fig.82 which shows the variation of the total load losses with skew.

It should be noted here that it does not necessarily follow that the smaller the value of the load loss the better is the performance of the machine. For a rotor without skew for example, (rotor No.2), the dips in the torque-speed curve near the synchronous speeds of the stator slot harmonics are very pronounced and may interfere with the starting of the motor. On the other hand a rotor with full skew, (rotor No.3) might have too high a leakage reactance, with the result that the fundamental torque is reduced. These objections are borne out by the experimental results of rotors No.1, 2 and 3 shown in Figs. 53, 56 and 57 respectively.

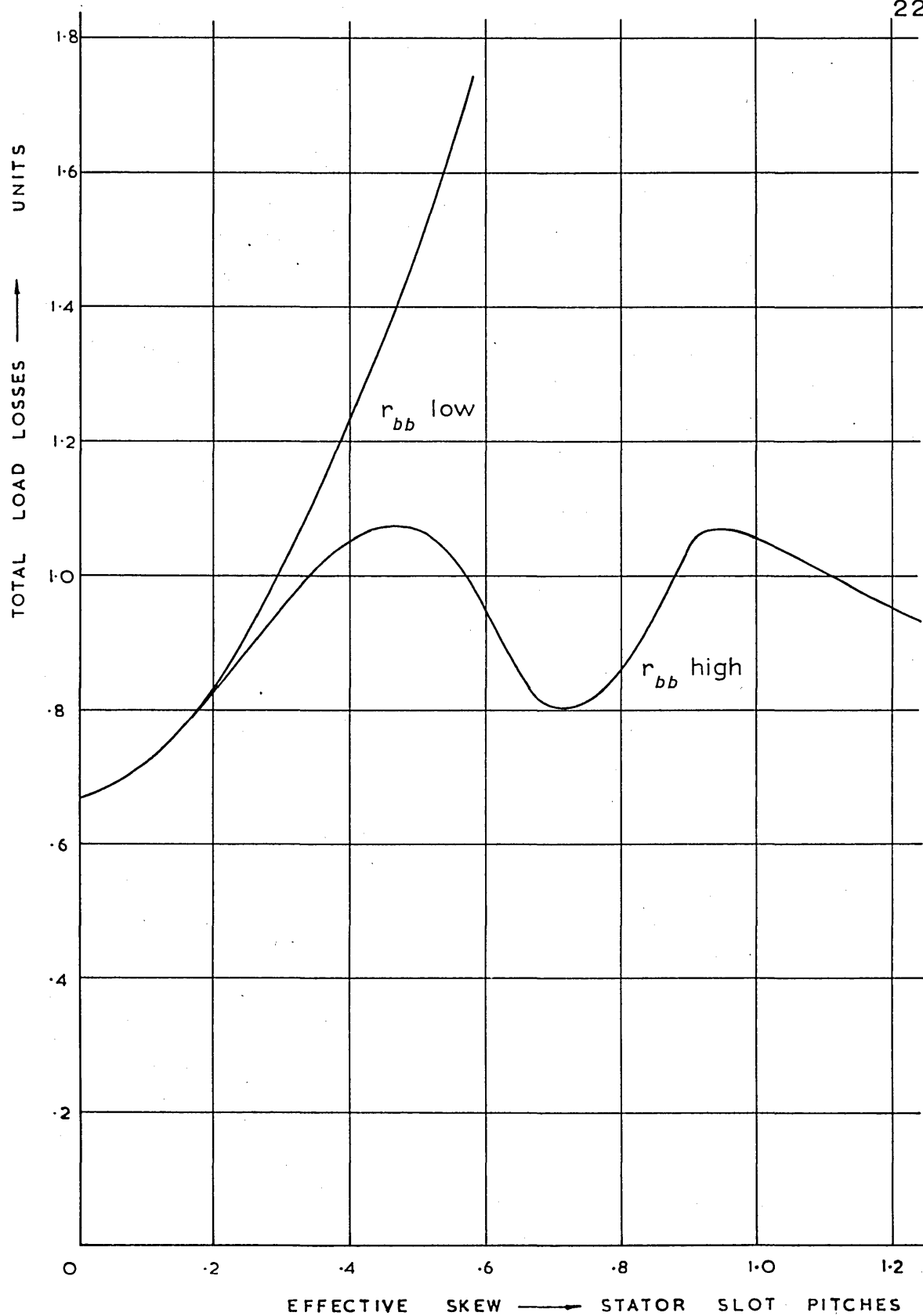


fig.82. Variation of total load losses with skew at constant current.

## CHAPTER 11

### THE EFFECT OF SLOT COMBINATION ON THE LOAD LOSSES

This Chapter shows how each component of load loss is influenced by the number of stator and rotor teeth and indicates a very effective method of reducing load losses by a proper choice of slot combination.

#### 11.1 Harmonic bar current load losses.

The harmonic bar current losses are given by  $P_{2v}$  in Eqn. 9.5. If the number of rotor slots is increased, the bar section must be decreased proportionally so that the total rotor iron area carrying the main magnetic flux remains unchanged. The value of the bar resistance ( $r_b$ ), therefore, increases in proportion to the number of rotor slots.

The bar impedance  $z_{bv}$  is given by Eqn. 7.17 as:

$$z_{bv} = r_{bv} + j(x_{bm_v} + x_{bd_v} + x_{bs\ell}) \quad (11.1)$$

At the normal operating point the harmonic frequencies are so high that the bar resistance  $r_{bv}$  in the above equation becomes totally negligible compared with the reactance term in brackets. The components of the bar reactance due to the main harmonic flux, the differential leakage flux, and the slot leakage flux were calculated in detail in Chapter 7, where the effects of permeance variations, saturation of the main and leakage flux paths, damping, etc. were considered. In the present discussion, however, these corrections

are not the main consideration and therefore the theoretical formulae are used without them, since this greatly facilitates the interpretation of the final results.

The total bar impedance, per unit length of rotor stack, is therefore given by:

$$z_{bv} \approx j(x_{bmv} + x_{bdv} + x_{bs\ell}) \quad (11.2)$$

which after substitution of the value of  $x_{bdv}$  from Eqn. 7.20 (with all the correction factors omitted) gives:

$$\begin{aligned} z_{bv} &= jx_{bmv} \left( \frac{\frac{\theta_v}{2}}{\sin \frac{\theta_v}{2}} \right)^2 + jx_{bs\ell} \\ &= jx_{bmv} \left[ \eta_v + \left( \frac{\frac{\theta_v}{2}}{\sin \frac{\theta_v}{2}} \right)^2 \right] \end{aligned} \quad (11.3)$$

$$\text{where } \theta_v = 2\pi p_v / S_2 \text{ and } \eta_v = \left( \frac{x_{bs\ell}}{x_{bmv}} \right) \quad (11.4)$$

Substituting the value of  $z_{bv}$  from Eqn. 11.3 into Eqn. 9.5 and also introducing the value of  $E_{ov}$  from Eqn. 6.35, gives after some simplification:

$$P_{2v\infty} = G_{2v} \cdot \left[ \frac{1}{\eta_v + \left( \frac{\frac{\theta_v}{2}}{\sin \frac{\theta_v}{2}} \right)^2} \right]^2 \quad (11.5)$$

where  $G_{2v}$  is a constant independent of the number of rotor slots.

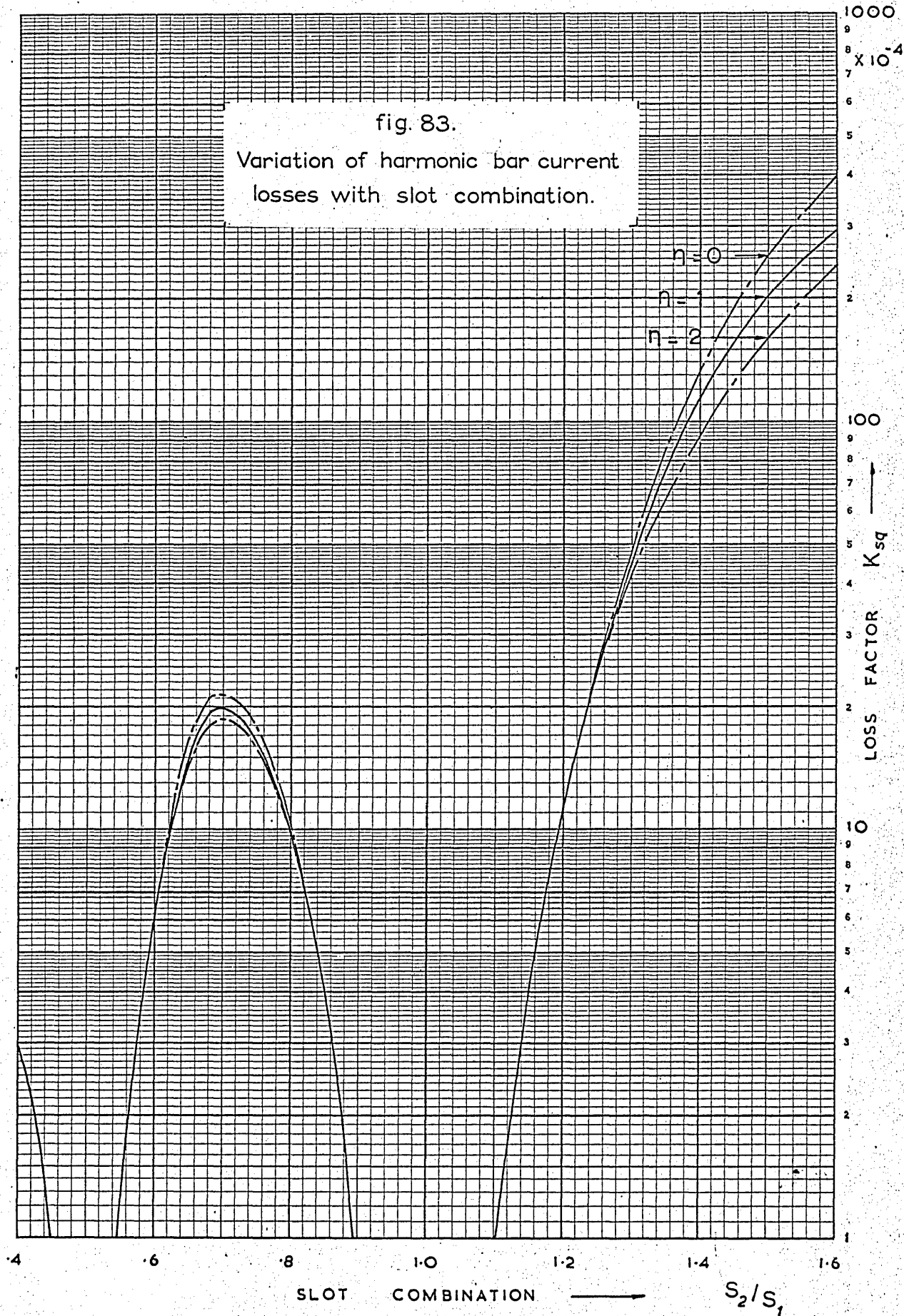
Eqn. 11.5 applies to each harmonic individually. If, once more, only the first two stator slot harmonics are considered and their orders taken to be equal to  $\pm \frac{S_1}{p}$ , (see Section 10.1), then the load loss becomes proportional to the factor:

$$k_{sq}^2 = \left[ \frac{1}{\eta_v + \left( \frac{\frac{\pi S_1}{S_2}}{\sin \frac{\pi S_1}{S_2}} \right)^2} \right]^2 \quad (11.6)$$

The variation of this loss factor with slot combination for different values of  $\eta_v$  is shown in Fig. 83. The value of  $\eta_v$  for the 45 slot rotors under investigation for example was calculated to be about .75 at the normal operating condition.

Quite part from the load losses, the no-load losses caused by the permeance variations at the air gap, vary (with slot combination) in a manner very similar to that described by Eqn. 11.6 as shown by Alger<sup>42</sup> and Baumann.<sup>43</sup> Alger also calculates the variation of this component of load loss (due to the harmonic bar currents) with the number of slots for the case where  $\eta_v = 0$ .

fig. 83.  
Variation of harmonic bar current losses with slot combination.





## 11.2 Cross current load losses.

The variation of load losses, produced by the cross currents, with slot combination is discussed in this Section separately for the cases of low and high interbar resistances. Once more only the stator slot harmonics are considered.

### (i) Low interbar resistance.

From Eqn. 9.3 it can be seen that only the second term in the square brackets contains the interbar resistance  $r'_{bbv}$  and therefore this term taken by itself gives the losses in the cross paths as:

$$P_{2v} = 2\alpha_v^2 r'_{bbv} \cdot S_2 E_{ov}^2 \cdot \text{Re} \left[ \frac{1}{\gamma_v z_{bv}^2} \right]$$

$$\text{or } P_{2v} = 2\alpha_v^2 \cdot (r'_{bbv})^{3/2} \cdot S_2 \cdot E_{ov}^2 \cdot \text{Re} \left[ z_{bv}^{-5/2} \right] \quad (11.7)$$

where  $r'_{bbv}$  is given by Eqn. 6.37 as

$$r'_{bbv} = \frac{r_{bb}}{4 \sin^2 \frac{\pi p v}{S_2}}$$

and is therefore a function of the number of rotor slots.

Substituting the expressions for  $E_{ov}$ ,  $r'_{bbv}$ , and  $z_{bv}$  into Eqn. 11.7 gives:

$$P_{2v} \approx G_{3v} \cdot \left( \frac{\pi S_1}{S_2} \right)^3 \cdot \frac{S_1 \cdot \left( \frac{\pi S_1}{S_2} \right)^{-3/2}}{\left[ \eta_v + \left( \frac{\pi S_1}{S_2} \right)^2 \right]^{5/2}} \quad (11.8)$$

where  $G_{3v}$  is a constant independent of the number of slots.

If the number of stator slots is considered fixed and the number of rotor slots varying, and if  $\eta_v$  is set equal to zero, Eqn. 11.8 becomes:

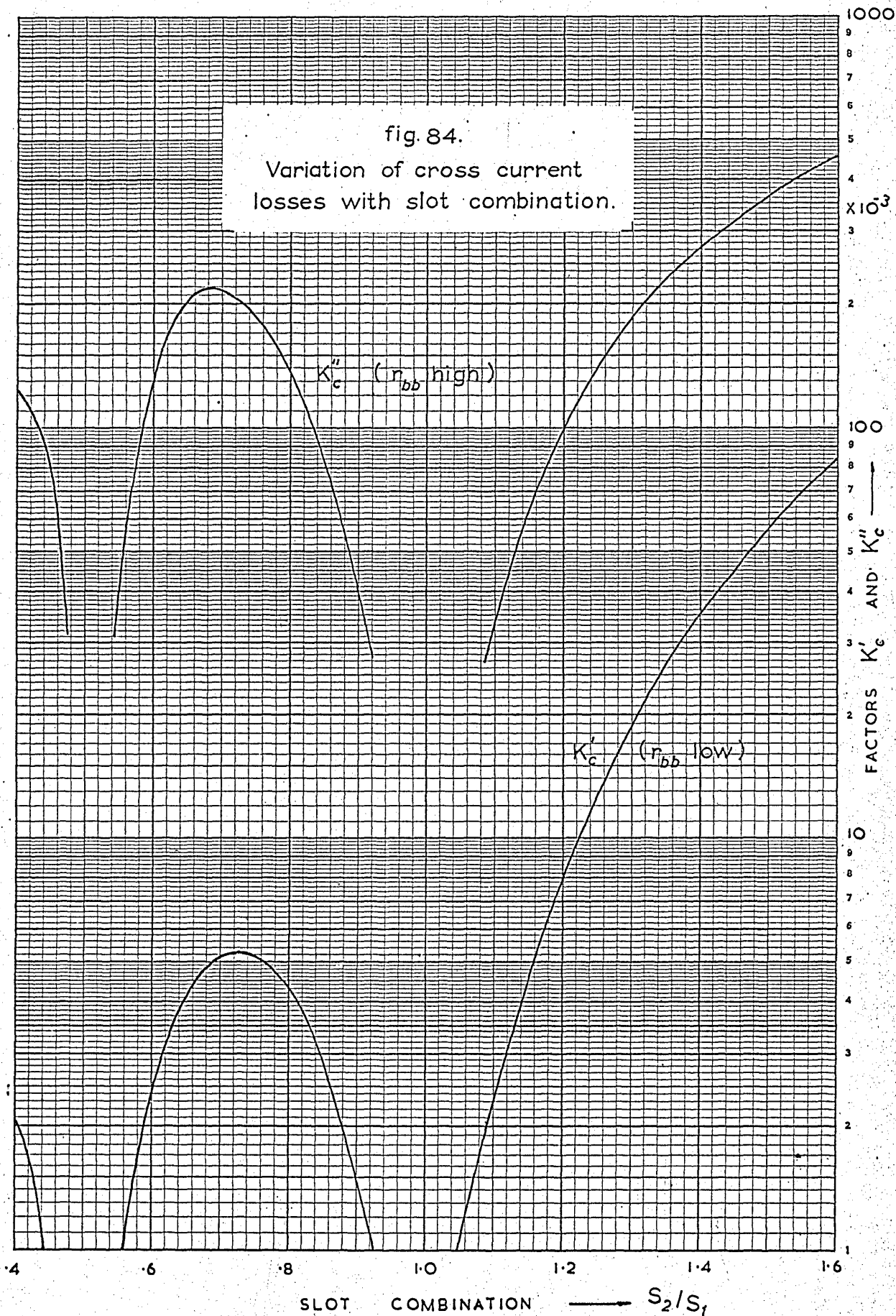
$$\begin{aligned} P_{2v} &= G_{3v} \cdot S_1 \left( \frac{\sin \frac{\pi S_1}{S_2}}{\frac{\pi S_1}{S_2}} \right)^2 \cdot \left( \frac{\pi S_1}{S_2} \right)^{-3/2} \quad (11.9) \\ &= G_{3v} \cdot S_1 \cdot k'_c \end{aligned}$$

where  $k'_c$  is the factor:  $\left( \frac{\sin \frac{\pi S_1}{S_2}}{\frac{\pi S_1}{S_2}} \right)^2 \cdot \left( \frac{\pi S_1}{S_2} \right)^{-3/2}$

The variation of  $k'_c$  with slot combination is shown in Fig.84.

(ii) High interbar resistance.

If the cross path resistance is high, the losses



produced by the cross currents are given by the first term of Eqn. 9.4 as:

$$P_{2v} = S_2 \cdot E_{ov}^2 \ell \cdot \frac{1}{\alpha_v^2 \cdot r'_{bbv}}$$

which, after substitution for  $E_{ov}$  and  $r'_{bbv}$ , becomes:

$$\begin{aligned} P_{2v} &\approx G_{4v} \cdot \frac{1}{S_1^3} \cdot \left[ \frac{\sin^2 \frac{\pi S_1}{S_2}}{\frac{\pi S_1}{S_2}} \right] \\ &= G_{4v} \cdot \frac{1}{S_1^3} \cdot k_c'' \end{aligned} \quad (11.10)$$

where  $G_{4v}$  is a constant and

$$k_c'' = \frac{\sin^2 \frac{\pi S_1}{S_2}}{\frac{\pi S_1}{S_2}}$$

The variation of  $k_c''$  with slot combination is shown in Fig.84 together with  $k_c'$ .

### 11.3 Iron load losses in the stator and rotor teeth.

#### (i) Losses in the rotor teeth.

These losses are given by Eqn. 6.70. If the expression for the tooth flux density is substituted from Eqn. 6.68 into Eqn. 6.70, the iron losses then become:

$$P_{tv}'' = G_{5v} \cdot (k_{tv}'')^2 \cdot \left[ \frac{\sin \frac{\pi S_1}{S_2}}{\frac{\pi S_1}{S_2}} \right]^2 \cdot \left( \sigma_e + p \cdot \frac{\sigma_h}{S_1} \right)$$

where  $G_{5v}$  is a constant.

The factor  $k_{tv}''$  is given by Eqn. 6.67 and it now simplifies to:

$$k_{tv}'' = 1 - \frac{\left[ \frac{\frac{\pi S_1}{S_2}}{\sin \frac{\pi S_1}{S_2}} \right]^2}{\left\{ \left[ \frac{\frac{\pi S_1}{S_2}}{\sin \frac{\pi S_1}{S_2}} \right]^2 + \frac{1}{k_{skv}^2} + \eta_v - 1 \right\}} \quad (11.11)$$

From Eqn. 11.11 it is seen that the effects of skew and slot combination are interlocked in the expression for  $k_{tv}''$  and cannot be separated into two different factors as was possible with the expressions for the losses in the squirrel cage and the cross-path region.

Since the importance of the iron losses in the rotor teeth is maximum when the squirrel cage bars are fully skewed, (see Section 10.3) only the condition of approximately full skew is considered in the present discussion. In this case the skew factor  $k_{skv}$  for the slot harmonics is very nearly zero, and the value of  $k_{tv}''$  is very nearly unity. The iron load losses in the

rotor teeth are then given by:

$$P''_{tv} \approx G_{5v} \cdot \left( \sigma_e + \frac{\sigma_h}{S_1} \right) \cdot k''_1 \quad (11.12)$$

where  $k''_1$  is the factor

$$\left( \frac{\sin \frac{\pi S_1}{S_2}}{\frac{\pi S_1}{S_2}} \right)^2$$

The variation of  $k''_1$  with slot combination is shown in Fig.85.

(ii) Losses in the stator teeth.

These losses are given by Eqn. 6.75, which, after substitution of the value of  $B'_{t\mu 0}$  from Eqn. 6.74, gives:

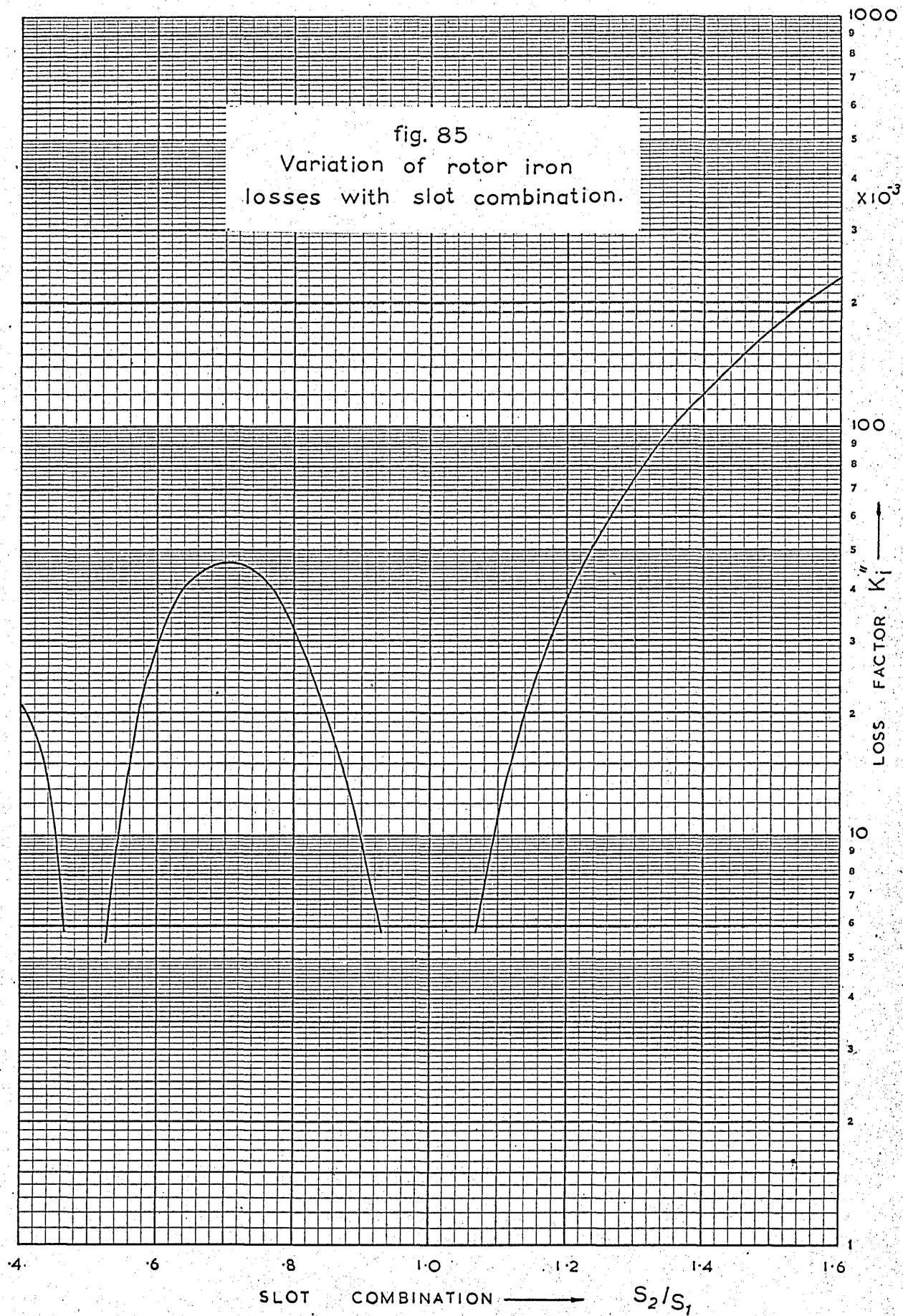
$$P'_{t\mu} \approx G_{6\mu} \cdot \left( \frac{\sin \frac{\pi S_2}{S_1}}{\frac{\pi S_2}{S_1}} \right)^2 \cdot \left( \sigma_e + p \cdot \frac{\sigma_h}{S_2} \right) \quad (11.13)$$

Since  $S_2 \gg 1$  in all practical machines, the term  $p\sigma_h/S_2$  in the last brackets of Eqn. 11.13 is small compared with  $\sigma_e$  and the above equation simplifies to:

$$P'_{t\mu} \approx G_{6\mu} \cdot \sigma_e \cdot \left( \frac{\sin \frac{\pi S_2}{S_1}}{\frac{\pi S_2}{S_1}} \right)^2 \quad (11.14)$$

The iron losses in the stator teeth induced by the rotor mmf harmonics are therefore proportional to the

fig. 85  
Variation of rotor iron  
losses with slot combination.



factor  $k'_i$ , where:

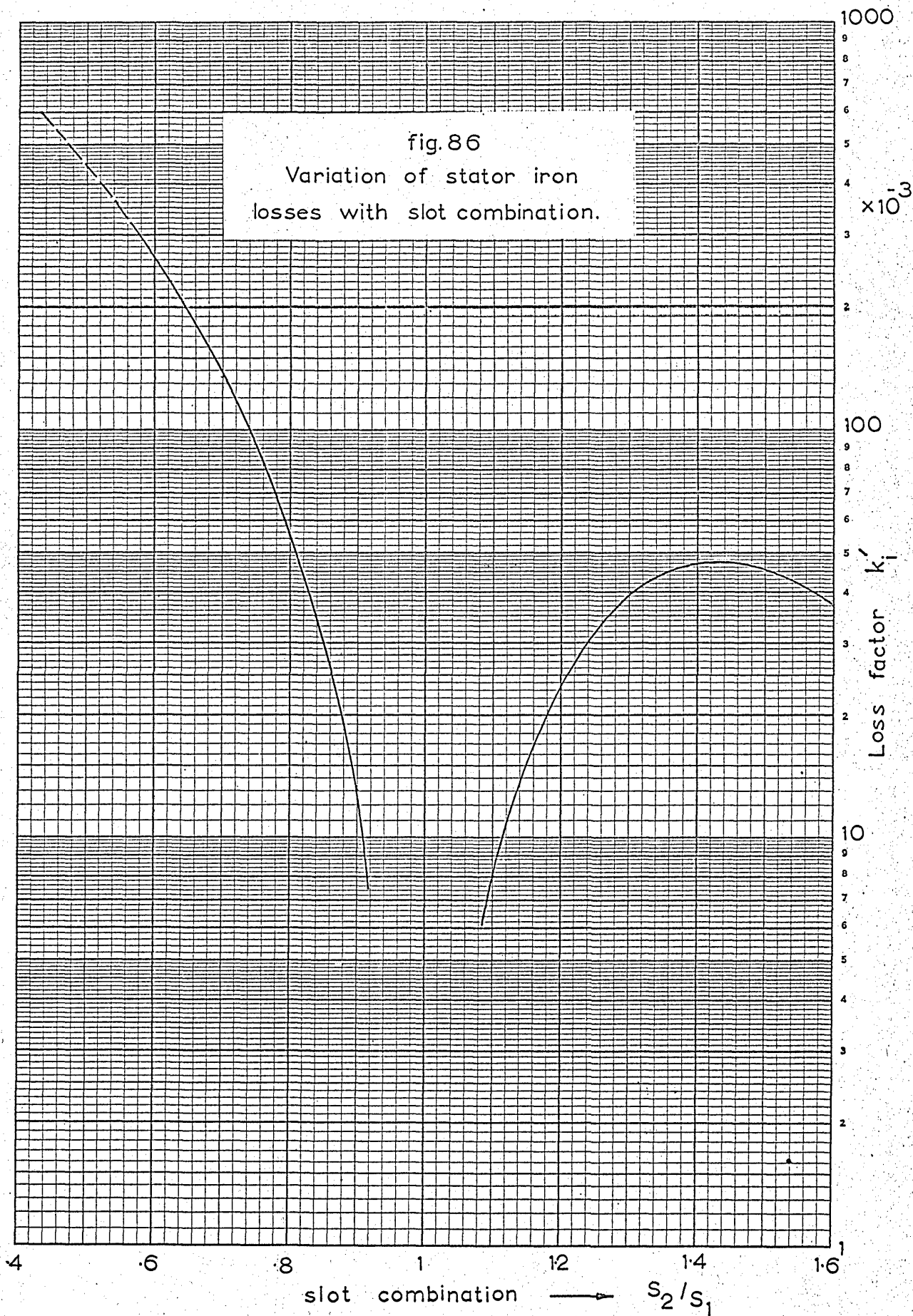
$$k'_i = \left( \frac{\sin \frac{\pi S_2}{S_1}}{\frac{\pi S_2}{S_1}} \right)^2 \quad (11.15)$$

The variation of  $k'_i$  with slot combination is shown in Fig.86.

#### 11.4 Total load loss.

Comparing Figs. 83, 84, 85 and 86, it is seen that the harmonic bar current losses, cross current losses, and rotor tooth iron losses (i.e. all components of load loss dissipated in the rotor) increase as the slot combination ( $S_2/S_1$ ) departs from the values 1,  $1/2$ ,  $1/3$ , .... etc. It is also seen that the component of load loss dissipated in the stator - i.e. the stator tooth iron loss - increases as the slot combination departs from the values 1, 2, 3 .... etc. It is therefore obvious, that the total load loss in a machine is minimised by having a number of rotor slots as nearly equal to the number of stator slots as possible i.e. keeping  $S_2/S_1 \approx 1$ . Obviously the condition  $S_1 = S_2$  must be avoided since it leads to standstill locking, and other values of slot combination near unity may produce objectionable noise<sup>47,49,50</sup> or synchronous locking torques.<sup>48,46</sup> For example, Fig.59 giving the torque-





slip characteristic of rotor No.6 (with a slot combination 36/32), shows such a locking torque in the negative speed range. The correct choice of slot combinations is therefore not an easy matter when the performance of the machine is to be optimised as a whole. However, it is seen from Figs. 83 to 86 that the variation of the load losses with slot combination is very much more pronounced than their variation with skew, (Compare Figs. 83 and 82 remembering that the first one is plotted on a semilogarithmic scale), and hence  $S_2/S_1$  should always be kept within the range  $.75 < S_2/S_1 < 1.25$ .

## CHAPTER 12

### THE EFFECT OF AIR GAP LENGTH ON THE LOAD LOSSES

#### 12.1 Harmonic bar current load losses.

These losses are given by Eqn. 9.5. If the values of  $E_{ov}$  and  $z_{bv}$  are substituted from Eqns. 6.36 (a) and 7.17, and the harmonic bar resistance neglected in comparison with the total harmonic bar reactance, then Eqn. 9.5 reduces to

$$\begin{aligned}
 P_{2v\infty} &= G_{7v} \cdot \frac{1}{\left(1 + \frac{x_{bdv}}{x_{bm v}} + \frac{x_{bs\ell}}{x_{bm v}}\right)} \\
 &= G_{7v} \cdot \frac{1}{(k_{7v} + \eta_v)} \quad (12.1)
 \end{aligned}$$

where  $G_{7v}$  and  $k_{7v}$  are constants independent of the air gap length. The bar reactance  $x_{bs\ell}$  is independent of the gap length, and the magnetising bar reactance  $x_{bm v}$  is, to the first approximation, inversely proportional to  $g$ , thus  $\eta_v = x_{bs\ell}/x_{bm v}$  is proportional to  $g$ .

Eqn. 12.1 then shows that the harmonic bar current losses decrease with increasing air gap length, but that the decrease is always less rapid than an inverse proportion.

#### 12.2 Cross current load losses.

(i) Low interbar resistance. The losses in the

cross paths with a low value of  $r_{bb}$  are given by the second term of Eqn. 9.3. With the same assumption of a negligible  $r_b$  made above, this equation becomes:

$$P_{2v} = G_{8v} \cdot \sqrt{g} \quad (12.2)$$

showing an increase in this type of loss with an increase in the air gap.

(ii) High interbar resistance. The cross current load losses with a high value of  $r_{bb}$  are given by the first term of Eqn. 9.4 which simplifies to:

$$P_{2v} = G_{9v} \cdot \frac{1}{g^2} \quad (12.3)$$

showing a decrease in this component of load loss with an increase in the air gap.

It should be noted that this decrease is very much more rapid than the increase which results when the interbar resistance is low. (Eqn. 12.2). Thus for most practical machines where  $r_{bb}$  has an intermediate value, the cross current losses generally decrease with an increase in the air gap length.

### 12.3 Iron load losses in the stator and rotor teeth.

These losses are given by Eqns. 6.70 and 6.75. Both stator and rotor iron tooth losses are seen to vary as  $1/g^2$ , since the magnitude of the stator and rotor harmonic fields vary as  $1/g$ .

#### 12.4 The total load loss.

The variation of the total load losses with air gap length can be calculated directly from the formulae of Chapters 6 and 7. It is shown (for rotor No.1) by curve A in Fig.87. This curve can be approximated quite accurately by Eqn. 12.4.

$$\frac{P_{\ell\ell g}}{P_{\ell\ell o}} \approx \frac{1}{2} \left[ \left( \frac{g_o}{g} \right) + \left( \frac{g_o}{g} \right)^2 \right] \quad (12.4)$$

where  $P_{\ell\ell g}$  and  $P_{\ell\ell o}$  are the values of the load losses at air gap values of  $g$  and  $g_o$  respectively.

Eqn. 12.4 shows that the load losses decrease with the air gap, but not as rapidly as the ratio  $\left( \frac{g_o}{g} \right)^2$  which was suggested by some investigators.<sup>35</sup> In order to verify Eqn. 12.4 experimentally the air gap of rotor No.1 was increased from .33 mm to .51 mm and its torque-slip characteristic measured at both values of air gap as shown in Fig.88. By making the necessary corrections as regards the difference in the load currents, the reduction in the load loss at .51 mm air gap as compared to its value at .33 mm air gap, is measured - at the reverse-rotation point to be 56% and calculated from Eqn. 12.4 to be 61%, a fair agreement.

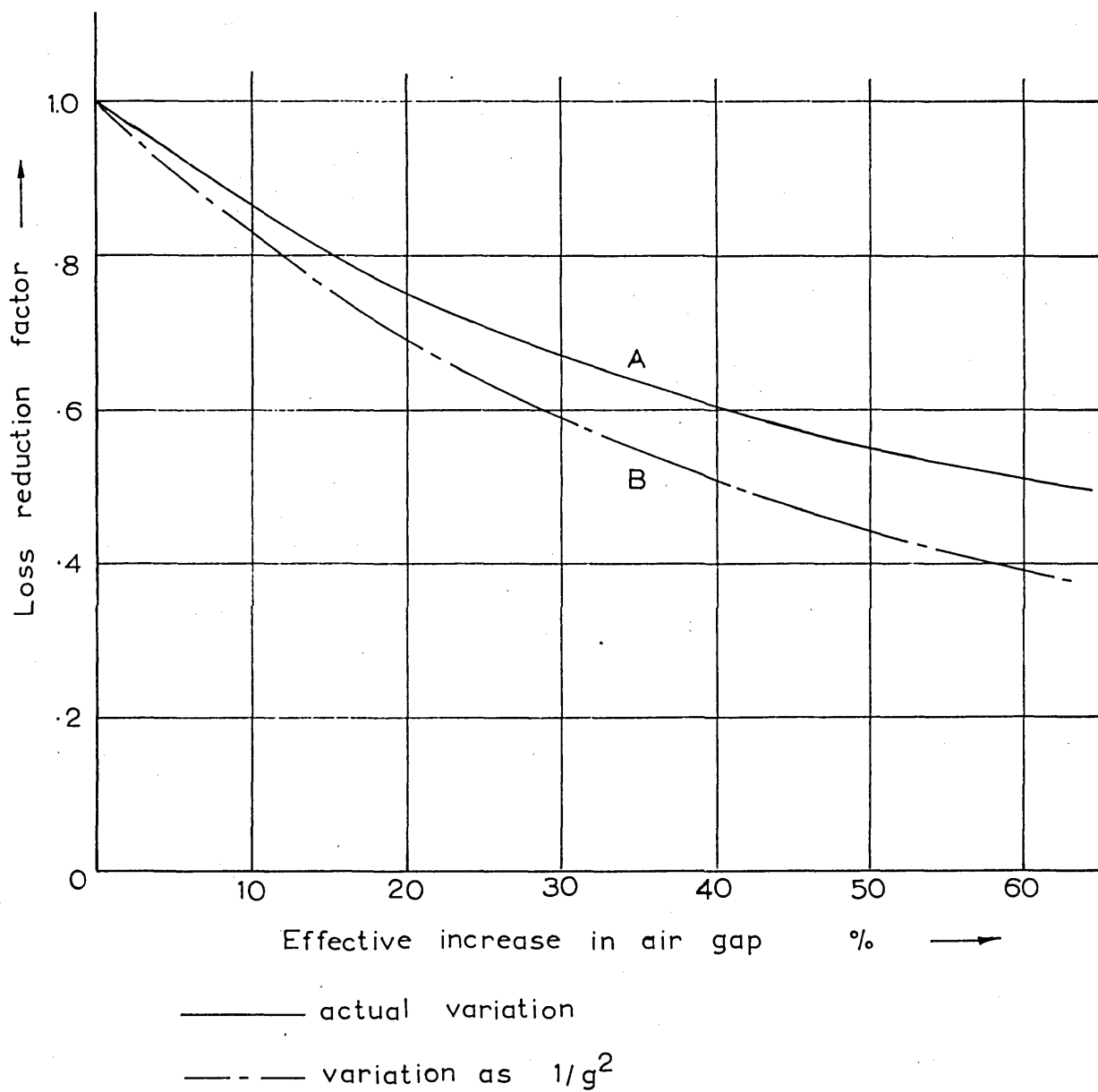


fig.87. Variation of load losses with air gap.

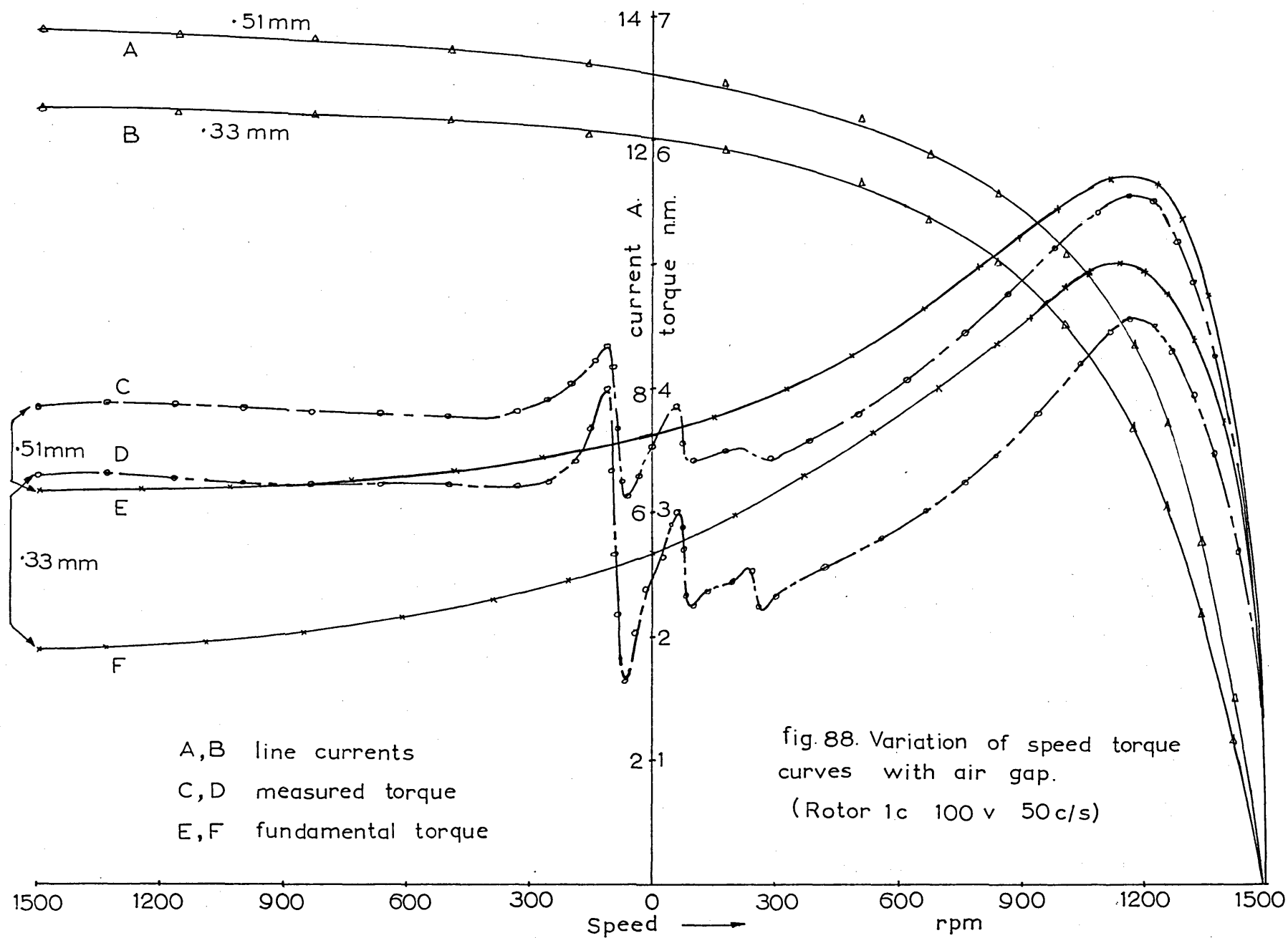


fig. 88. Variation of speed torque curves with air gap.  
(Rotor 1c 100 v 50 c/s)

## CHAPTER 13

### FURTHER VERIFICATIONS OF THE THEORY, AND "EXTRA" LOAD LOSSES CAUSED BY THE COMBINED EFFECTS OF PERMEANCE HARMONICS AND SATURATION.

#### 13.1 Measurement and prediction of the stator tooth fluxes.

In the first eight Chapters methods of calculating and measuring load losses and torques were presented and good agreement between the results was obtained. The basis of an accurate theoretical determination of the load losses, or their associated torques, is the ability to calculate correctly the magnitudes of the harmonic magnetic fields that exist in the machine and the values of the harmonic reactances due to these fields.

The harmonic fields are calculated in detail in Section 6.1, Chapter 7, and in Appendices II and V. It is therefore desirable to have a direct experimental verification of the magnitude of these fields which would serve as a very valuable intermediate check in the calculation of the load losses.

A measurement which can be done quite easily is that of the stator tooth flux. Ten turns of very fine wire were wound round each of six stator teeth;



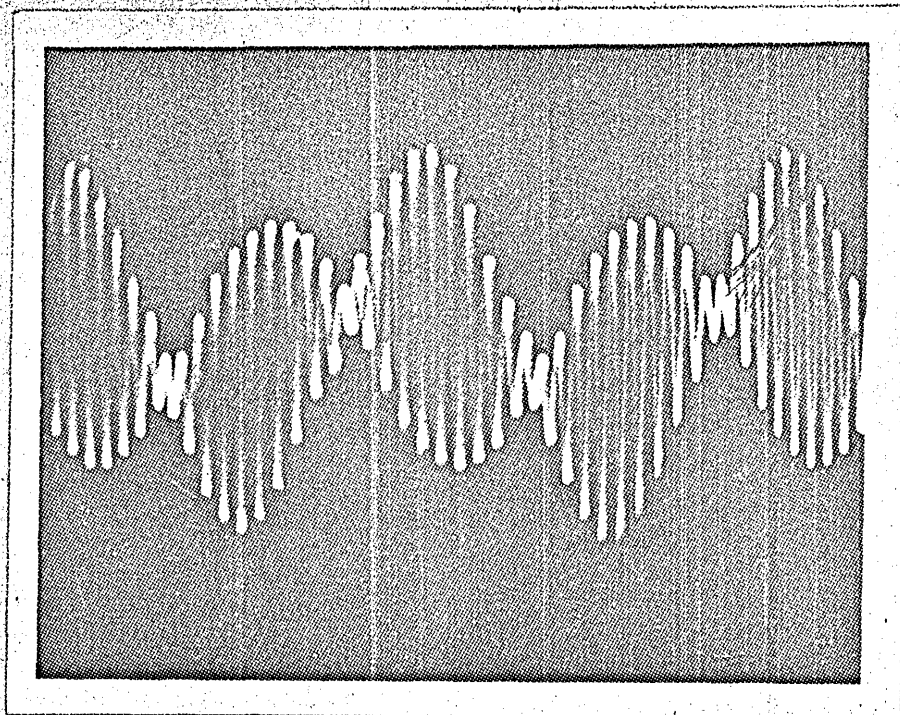
with the wire lying along the centre-line of the stator slots. The voltage generated in the search coils was then a measure of the flux that enters one stator slot pitch and almost all of this flux passes down the stator tooth. A typical oscillogram of this flux is shown in Osc.3.

The air gap flux density field due to the  $v^{\text{th}}$  stator harmonic is given by Eqn. 6.5 as  $b_{1v} = f_{1v} \cdot \Lambda$  where  $f_{1v}$  and  $\Lambda$  are given by Eqns. 6.1 and 6.4 respectively. The air gap flux density field due to the  $\mu^{\text{th}}$  rotor slot harmonic, produced by the rotor currents induced by the fundamental field, is  $b_{2\mu} = f_{2\mu} \cdot \Lambda$  where  $f_{2\mu}$  is given by Eqn. 6.21. Hence the total flux that enters the stator tooth over a stator slot pitch is:

$$\phi'_t = \int_0^{\frac{2\pi Y}{S_1}} (b_{1v} + b_{2\mu}) dx_1 \quad (13.1)$$

(It should be noted that the origin is taken at the centre of a stator slot as shown in Fig.23.)

Substituting the values of  $b_{1v}$  and  $b_{2\mu}$  and performing the integration, Eqn. 13.1 gives after some manipulation:



Osc. 3. Waveform of stator tooth flux, (with rotor N° 1)

$$\begin{aligned}
\varphi_t' &= \sum_v \varphi_{ov1} \cdot sr\left(\frac{v\pi p}{S_1}\right) \cdot \left\{ 1 - \sum_{c \text{ pos.}} \frac{\gamma_c'}{\left[1 - \left(\frac{cS_1}{vp}\right)^2\right]} \right\} \cdot \cos\left(\omega t + \theta_v - \frac{v\pi p}{S_1}\right) \\
&\quad - \sum_v \varphi_{ov1} \cdot \sum_{d=\pm 1, \pm 2, \dots} \frac{\gamma_d''}{2} sr\left[\frac{\pi p}{S_1}\left(v + \frac{dS_2}{p}\right)\right] \cdot \cos\left\{\omega_3 t + \theta_v - \left(v + \frac{dS_2}{p}\right) \frac{\pi p}{S_1}\right\} \\
&\quad + \sum_\mu \varphi_{o\mu 1} \cdot sr\left(\frac{\mu\pi p}{S_1}\right) \cdot \left\{ 1 - \sum_{c \text{ pos.}} \frac{\gamma_c'}{\left[1 - \left(\frac{cS_1}{\mu p}\right)^2\right]} \right\} \cdot \\
&\quad \cos\left[\left(1 + \frac{k_2 S_2}{p}(1-s)\right)\omega t + \theta_\mu - \frac{\mu\pi p}{S_1}\right] \\
&\quad - \sum_\mu \varphi_{o\mu 1} \cdot \sum_{d=\pm 1, \pm 2, \dots} \frac{\gamma_d''}{2} \cdot sr\left[\frac{\pi p}{S_1}\left(\mu + \frac{dS_2}{p}\right)\right] \cdot \\
&\quad \cos\left[\omega_3' t + \theta_v - \left(\mu + \frac{dS_2}{p}\right) \cdot \frac{\pi p}{S_1}\right] \quad (13.2)
\end{aligned}$$

$$\text{where: } \omega_3 = \omega - \frac{dS_2 \pi \omega_r R}{pY} \quad (13.3)$$

$$\omega_3' = \left[1 + \frac{k_2 S_2}{p}(1-s)\right]\omega - \frac{dS_2 \pi \omega_r R}{pY} \quad (13.4)$$

The function  $sr(\theta)$  is defined as:  $sr(\theta) \equiv \left(\frac{\sin \theta}{\theta}\right)$

$$\text{Also } \varphi_{ov1} = \frac{3\sqrt{2}\mu_o Z_1 k_{dpv} \cdot \bar{I}_1 Y}{\pi g k_{c1} k_{c2} \cdot v \cdot S_1} \quad (13.5)$$

$$\text{and } \varphi_{0\mu 1} = \frac{3 \sqrt{2} \mu_o Z_1 k_{dp1} \bar{I}_2 Y}{\pi g k_{c1} k_{c2} (1 + \frac{k_2 S_2}{p}) \cdot S_2 \cdot k_{sk1}} \quad (13.6)$$

In an exactly analogous way the flux that enters a rotor tooth over a rotor slot pitch is given by:

$$\varphi_t'' = \int_0^{\frac{2pY}{S_2}} (b_{1v} + b_{2v}) dx_2 \quad (13.7)$$

which after integration becomes:

$$\begin{aligned} \varphi_t'' = & \sum_v \varphi_{02v} \text{sr} \left( \frac{v\pi p}{S_2} \right) \left\{ 1 - \sum_{d \text{ pos.}} \frac{\gamma_d''}{\left[ 1 - \left( \frac{dS_2}{v p} \right)^2 \right]} \right\} \cdot \cos \left( \omega_1 t + \theta_v \frac{v\pi p}{S_2} \right) \\ & - \sum_v \varphi_{02v} \sum_{c=-1, +2, \dots} \frac{\gamma_c'}{2} \cdot \text{sr} \frac{\pi p}{S_2} \cdot \left( v + \frac{cS_1}{p} \right) \cdot \\ & \quad \cos \left( \omega_2 t + \theta_v - \left\{ v + \frac{cS_1}{p} \right\} \frac{\pi p}{S_2} \right) \\ & + \sum_{\mu} \varphi_{02\mu} \text{sr} \left( \frac{\mu\pi p}{S_2} \right) \cdot \left\{ 1 - \sum_{d \text{ pos.}} \frac{\gamma_d''}{\left[ 1 - \left( \frac{dS_2}{\mu p} \right)^2 \right]} \right\} \cdot \\ & \quad \cos \left( \omega_1 t + \theta_{\mu} - \frac{\mu\pi p}{S_2} \right) \\ & - \sum_{\mu} \varphi_{02\mu} \sum_{c=-1, +2, \dots} \frac{\gamma_c'}{2} \cdot \text{sr} \frac{\pi p}{S_2} \cdot \left( \mu + \frac{cS_1}{p} \right) \cdot \\ & \quad \cos \left[ \omega_2 t + \theta_{\mu} - \left( \mu + \frac{cS_1}{p} \right) \frac{\pi p}{S_2} \right] \quad (13.8) \end{aligned}$$

$$\text{where: } \omega_1 = \omega - \frac{v\pi\omega_r R}{Y} \quad (13.9)$$

$$\omega_2 = \omega - \frac{v\pi\omega_r R}{Y} - \frac{cS_1\pi\omega_r R}{pY} \quad (13.10)$$

$$\omega_1' = \left\{1 + \frac{k_2 S_2}{p} \cdot (1-s)\right\} \omega - \frac{\mu\pi\omega_r R}{Y} \quad (13.11)$$

$$\omega_2' = \left\{1 + \frac{k_2 S_2}{p} \cdot (1-s)\right\} \omega - \frac{\mu\pi\omega_r R}{Y} - \frac{cS_1\pi\omega_r R}{pY} \quad (13.12)$$

Also,  $\varphi_{o2v} = \varphi_{ov1} \cdot \left(\frac{S_1}{S_2}\right)$ , and  $\varphi_{o2\mu} = \varphi_{o\mu 1} \cdot \left(\frac{S_1}{S_2}\right)$ , where

$\varphi_{ov1}$  and  $\varphi_{o\mu 1}$  are given by Eqns. 13.5 and 13.5 respectively.

Eqns. 13.2 and 13.8 give exact expressions for the stator and rotor tooth fluxes. The fluxes in the stator teeth due to the stator harmonics occur at low frequencies, (line frequency), and cause negligible losses. The fluxes in the rotor teeth due to the rotor harmonics also occur at low frequencies, (fundamental slip frequency), and their associated losses are also negligible. Thus the fluxes in the teeth of a member of the machine (stator or rotor) caused by the field harmonics due to that member, can be neglected and only the fluxes caused by the field harmonics of the opposite member need be considered. This amounts to neglecting the first two terms of Eqn. 13.2, and the last two terms of Eqn. 13.8. It is interesting to note that if the effect of the slot openings on the air gap permeance is also neglected, i.e. if one assumes a uniform air gap of value  $g_{c1} \cdot k_{c2}$ , then Eqn. 13.8 reduces to Eqn. 6.51, and Eqn. 13.2 reduces to

a flux expression corresponding to the flux density given by Eqn. 6.74.

In Section 6.1 it was proved that the fundamental mmf interacts with the slot permeance variations of the air gap to produce fields of the same order and frequency as the slot harmonic fields due to the mmf harmonics. It was also shown in that Chapter that the slot harmonic fields due to both causes can be vectorially added to give a resultant slot harmonic frequency field as shown by Eqn. 6.16 in the case of the stator fields and by Eqn. 6.24 in the case of the rotor fields.

In an exactly analogous manner, the resultant slot harmonic frequency tooth fluxes can be derived and are shown by Eqns. 3.13 and 3.14 for the stator and rotor teeth respectively.

$$\left[ \varphi'_{\text{res.}} \right]_{\text{slot}} = \varphi' \cdot \frac{k_2 S_2}{\left( \frac{k_2 S_2}{p} + 1 \right)} \cdot \sqrt{1 + \frac{1}{\alpha''}} \cdot \sqrt{1 + \frac{2 \sin \theta_2}{\alpha'' + \frac{1}{\alpha''}}} \quad (13.13)$$

$$\left[ \varphi''_{\text{res.}} \right]_{\text{slot}} = \varphi'' \cdot \frac{r S_1}{\left( \frac{r S_1}{p} + 1 \right)} \cdot \sqrt{1 + \frac{1}{\alpha'}} \cdot \sqrt{1 + \frac{2 \sin \theta_1}{\alpha' + \frac{1}{\alpha'}}} \quad (13.14)$$

where:

$$\varphi' \cdot \frac{k_2 S_2}{\left( \frac{k_2 S_2}{p} + 1 \right)} = \varphi_{o\mu 1} \cdot \left( \frac{\sin \frac{\mu \pi p}{S_1}}{\frac{\mu \pi p}{S_1}} \right)$$

$$\text{where } \mu = \frac{k_2 S_2}{p} + 1 \quad k_2 = \pm 1, \pm 2, \pm 3, \dots$$

and:

$$\varphi''_{\left(\frac{rS_1}{p} + 1\right)} = \varphi_{o2v} \cdot \left( \frac{\sin \frac{v\pi p}{S_2}}{\frac{v\pi p}{S_2}} \right)$$

$$\text{where } v = \frac{rS_1}{p} + 1 \quad r = \pm 1, \pm 2, \pm 3, \dots$$

and  $\alpha'$  and  $\alpha''$  are given by Eqns. 6.16(a) and 6.25 (a) respectively.

The positive signs in the square roots of Eqns. 13.13 and 13.14 correspond to negative values of  $r$  and  $k_2$  and vice versa.

The resultant stator tooth slot harmonic flux

$\left[ \varphi_{\text{res.1}} \right]_{\text{slot}}$  occurs at the rotor slot harmonic frequency of:

$$\omega_{2\mu} = \left\{ 1 + (1-s) \frac{k_2 S_2}{p} \right\} \cdot \omega_o \quad (13.15)$$

whereas the resultant rotor tooth slot harmonic flux

$\left[ \varphi_{\text{res.2}} \right]_{\text{slot}}$  occurs at the stator slot harmonic frequency of:

$$\omega_{1v} = \{ 1 - (1-s)v \} \omega_o \quad (13.16)$$

as can easily be seen from Eqns. 13.2 and 13.8.

From Eqns. 13.13 and 13.16 the stator tooth flux and the voltages that this flux would induce in the 10-turn search coils can be calculated. A comparison of the measured coil voltages, (taken with the machine running

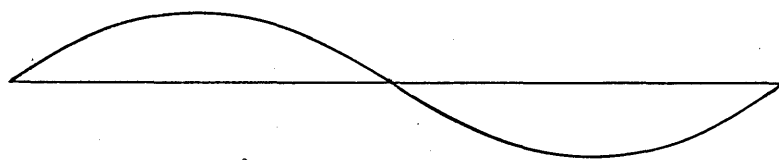
under normal operating conditions), with the calculated values of these voltages, shows an exact agreement as far as the frequency of the signals is concerned and an agreement of  $\pm 4\%$  in the magnitude of the signals for all degrees of current loading and all the rotors listed in Table 2. This agreement is the final experimental proof of the validity of the theoretical formulae of Chapters 6 and 7. In the experiments the various frequency components of the search coil voltages were separated out on a Radiometer wave analyser.

It may be interesting to comment now on the general waveform of the tooth flux oscillograms. This waveform is composed of:

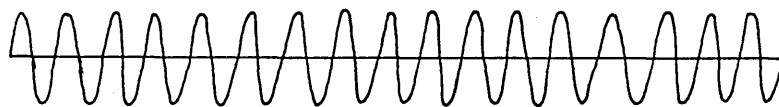
- (i) The "main" supply-frequency component due to the fundamental flux, as shown in Fig.89(a).
- (ii) A "first" rotor slot-harmonic-frequency component given by Eqns. 13.13 and 13.15 with  $k_2 = -1$ .  
The last equation shows that, during normal machine operation when  $s \ll 1$ , this component represents a field travelling in a direction opposite to that of the fundamental field and has  $(1-S_2/p)$  as many poles. (See Fig.89(b)).
- (iii) A "second" slot-harmonic-frequency component given by the same equations as before but with



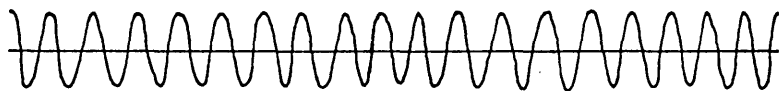
fundamental



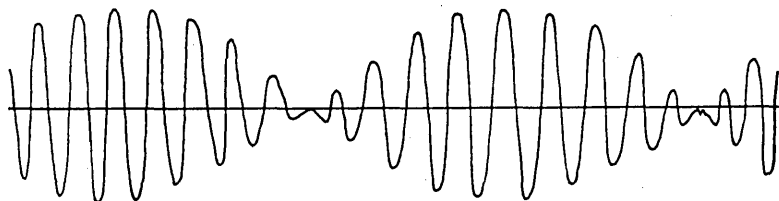
a

first slot  
harmonic

b

second slot  
harmonic

c

sum of slot  
harmonics $d = b + c$ 

total:

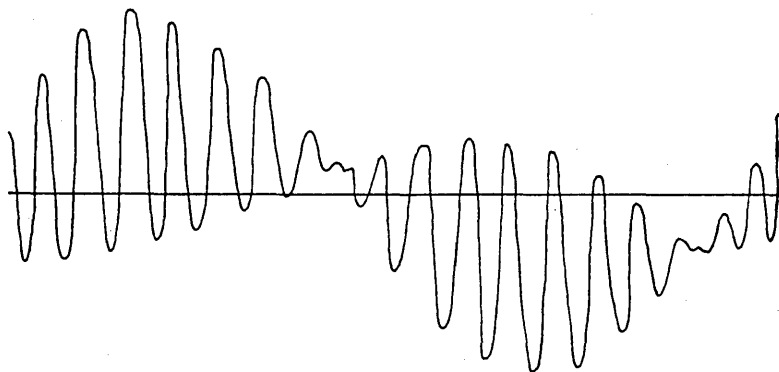
 $e = a + b + c$ 

fig. 89. Waveforms of tooth fluxes.

- $k_2 = +1$ . This represents a wave travelling in the same direction as the fundamental wave and has  $(1+S_2/p)$  as many poles. (See Fig.89(c)).
- (iv) Other slot harmonic components given by  $k_2 = \pm 2, \pm 3$  etc. These will be neglected in this qualitative explanation.

Considering the first two slot harmonics by themselves, they can be added together to form the amplitude modulated wave of Fig.89(d). When this wave is added to the fundamental, the resultant tooth flux waveform is as shown in Fig.89(e), which has the same shape as the oscillogram of the stator tooth flux. (Osc.3).

### 13.2 Load losses caused by the combined effects of permeance harmonic fields and saturation.

All the theoretical work of Chapter 6 is concerned with the magnetic fields, (and their associated losses) produced by the non sinusoidal mmf distribution. The effect of the slot openings on the magnitude of these fields has been considered, but the magnetic fields caused by the air gap permeance variations due to the slot openings themselves have been neglected, on the grounds that the losses these fields produce are part of the no load loss and as such are outside the scope of the present work. (See Section 6.1). This is true

if the saturation of the leakage reactances at the full load value of the current is negligible, as is the case with all machines with closed or semiclosed slots, but it is not true if the full load current causes appreciable saturation, as in the case of machines with completely closed slots.

On no load the current flowing in the squirrel cage winding is practically zero and the reactance of the winding is unsaturated and high. On load a current  $I_2$  flows in the squirrel cage bars, and if the rotor slots are closed by a thin magnetic bridge, this will become saturated and the bar reactance will be reduced. Thus although the magnitude of the field harmonics due to the permeance variations may be the same on load as it is on no load, the currents these harmonic fields induce in the bars - and hence the losses produced - are higher on load than on no load.<sup>52</sup>

This increase of the losses caused by the permeance harmonic fields between load and no load is therefore equivalent to and indistinguishable from an increase in the load losses caused by the fields due to the mmf harmonics.

Let the losses in the rotor caused by the field due to the stator mmf harmonic when excited by a current  $I_1$  be:

$$\mathcal{L}_{2v}(x_{2v}, \dots \text{ other machine parameters})$$

where  $\mathcal{L}_{2v}$  is a function representing the sum of the rotor load loss formulae given in Chapter 6.  $\mathcal{L}_{2v}$  is a function of all the machine parameters including the rotor leakage reactance which is separated out.

Also let the losses in the stator caused by the field due to the  $\mu^{\text{th}}$  rotor mmf harmonic when excited by a current  $I_2$  be  $\mathcal{L}_{1\mu}$ ; where  $\mathcal{L}_{1\mu}$  is a function representing the stator surface and tooth body iron loss formulae of Section 6.6.  $\mathcal{L}_{1\mu}$  is independent of either the stator or the rotor harmonic leakage reactances.

The magnitudes of the fields due to the stator slot openings are given by Eqn. 6.16(a) as a fraction  $1/\alpha'$  of the value of the corresponding (same order) slot harmonic field due to the stator mmf harmonics at full load. Similarly, the magnitudes of the fields due to the rotor slot openings are given by Eqn. 6.25(a) as a fraction  $1/\alpha''$  of the corresponding slot harmonic field due to the rotor mmf harmonics at full load.

The total harmonic losses on no load are therefore given by:

$$P_{ho} = \left| \frac{I_o}{I_1} \right|^2 \cdot \sum_{v \neq 1} \mathcal{L}_{2v}(x_{2v}, \dots) + \left( \frac{1}{\alpha'} \right)^2 \sum_{v \neq 1} \mathcal{L}_{2v}(x_{2v}, \dots) + \left( \frac{1}{\alpha''} \right)^2 \sum_{\mu \neq 1} \mathcal{L}_{1\mu} \quad (13.17)$$

where the first term of Eqn. 13.17 is the loss caused by the stator mmf harmonics on no load, and the second and third terms are the losses caused by the permeance flux harmonics also on no load. The losses in the stator due to the rotor mmf harmonics are zero, since on no load  $I_2$  is negligible and these harmonics are also negligible.

When the machine is on load the harmonic losses become:

$$\begin{aligned}
 P_{h\ell} = & \sum_{v \neq 1} \mathcal{L}_{2v}(x'_{2v}, \dots) + \sum_{\mu \neq 1} \mathcal{L}_{1\mu} \\
 & + \left(\frac{1}{\alpha'}\right)^2 \sum_{v \neq 1} \mathcal{L}_{2v}(x'_{2v}, \dots) + \left(\frac{1}{\alpha''}\right)^2 \sum_{\mu \neq 1} \mathcal{L}_{1\mu}
 \end{aligned}
 \tag{13.18}$$

where  $x'_{2v}$  is the value of the secondary harmonic leakage when saturated by the load current  $I_2$  flowing in the squirrel cage.

The measured load loss would therefore be:

$$\begin{aligned}
 P_{\ell\ell \text{ meas.}} &= P_{h\ell} - P_{ho} \\
 &= \sum_{v \neq 1} \mathcal{L}_{2v}(x'_{2v}, \dots) + \sum_{\mu \neq 1} \mathcal{L}_{1\mu} - \\
 &\quad - \left| \frac{I_o}{I_1} \right|^2 \sum_{v \neq 1} \mathcal{L}_{2v}(x'_{2v}, \dots) + \left(\frac{1}{\alpha'}\right)^2 \cdot \\
 &\quad \cdot \left[ \sum_{v \neq 1} \mathcal{L}_{2v}(x'_{2v}, \dots) - \sum_{v \neq 1} \mathcal{L}_{2v}(x_{2v}, \dots) \right]
 \end{aligned}
 \tag{13.19}$$

The third term of Eqn. 13.19 is normally small and can be neglected, whereas the last term is the "extra" load loss introduced by the combined effects of slot openings and saturation when  $x'_{2v}$  is appreciably different from  $x_{2v}$ .

It should be noted that  $x_{2v}$  is the total harmonic leakage reactance of the rotor. The differential harmonic leakage is almost always the largest component of the total and can never be saturated by the full load current.<sup>32</sup> Also of the slot leakage only the part corresponding to the tooth tip or the slot bridge will be saturated, and the rest will remain unaffected. Thus although the saturation of the slot bridge may vary between extremes from no load to full load, the value of  $x_{2v}$  varies more slowly since the largest portion of it remains constant.

It is interesting to note that when the number of rotor slots is near the number of stator slots, the differential harmonic leakage becomes very large indeed and the other leakage reactance components can be neglected in comparison. The value of  $x_{2v}$  then remains constant and the "extra" load losses are negligible. Conversely if the slot combination is far away from unity the relative importance of the reactance due to the slot bridge increases

and large variations of  $x_2$  may then result between load and no load. The "extra" load losses will then become important. Thus these losses can be minimised in the same way as the load losses produced by the fields due to the mmf harmonics, by making  $S_2/S_1 \approx 1$ .

Although none of the experimental rotors used in this investigation had slots completely closed with iron bridges, a theoretical investigation has been carried out to determine the magnitude of the "extra" load losses in rotor No.1.

The losses in the rotor produced by the harmonic fields due to the stator slot openings, can be determined from formulae analogous in every way to those of Chapter 6, by replacing the amplitudes of the fields due to the mmf harmonics by the amplitudes of the fields due to the permeance harmonics. The variation of  $x_2'$  with current  $I_2$  is determined from the magnetisation curve of the rotor iron. When these values of secondary leakage reactances are introduced into the formulae, the variation of the rotor losses produced by the harmonic fields due to the stator permeance variations, with  $I_2$  can be calculated and is shown in Fig.90.

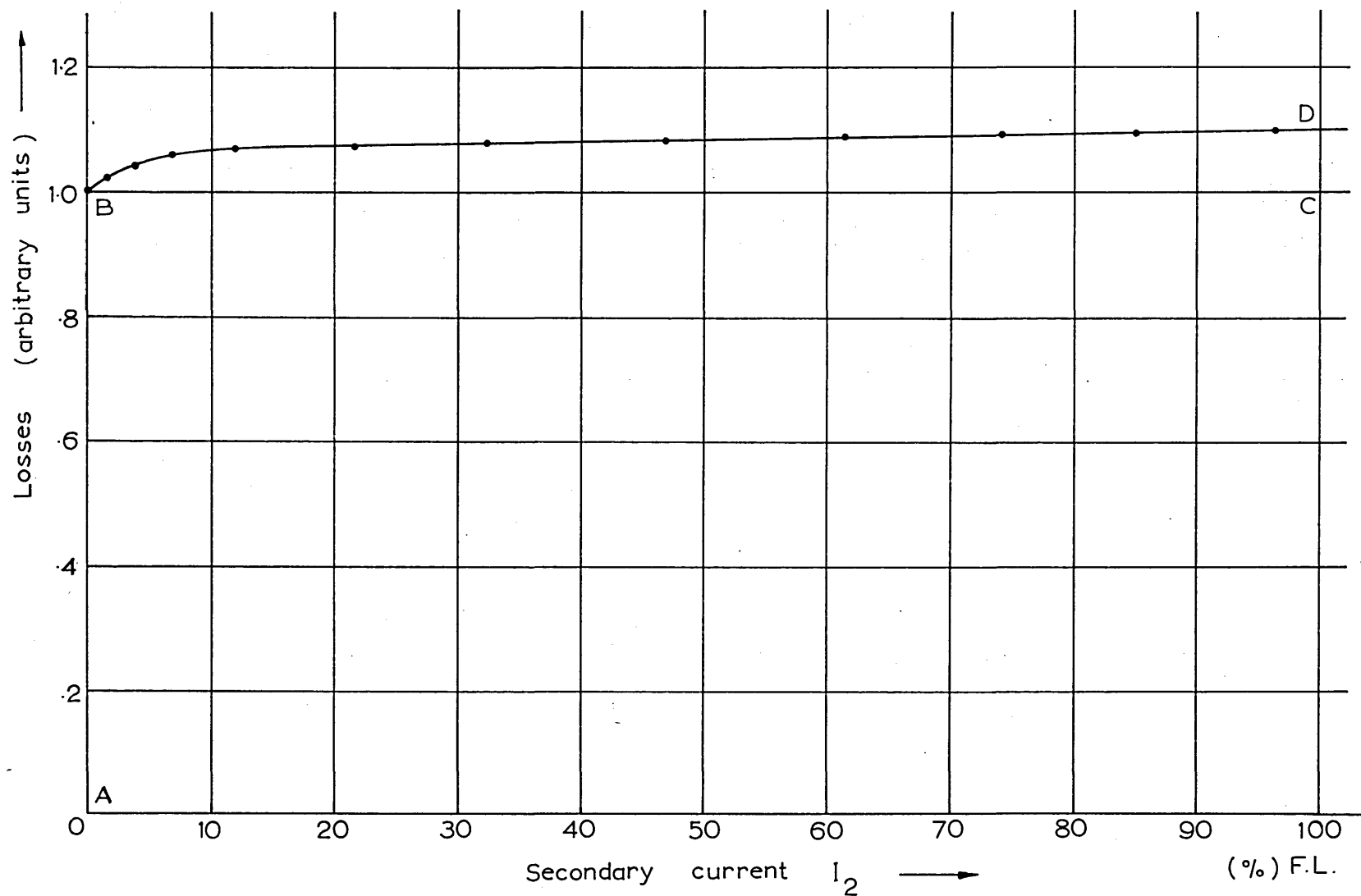


fig.90 Variation of rotor losses due to fluxes caused by stator slot permeance variations with  $I_2$ . (AB=High frequency no load loss, CD="Extra" load loss)



The ordinate of the curve in Fig.90 at a zero value of rotor current, (stator current value of  $I_0$ ) represents the high frequency - harmonic - no load loss in the rotor. It is seen from Fig.90 that the rotor losses produced by the stator slot openings (which may be a significant part of the total no load loss) increases when the machine is on full load by 10% above the no load value of these losses.

## CHAPTER 14

### CONCLUSIONS AND SUGGESTIONS FOR FURTHER WORK

Part one of the thesis describes three different methods of measuring load losses either directly or by means of the torque slip characteristics. The measurement of the torque speed curves, both with the swinging stator dynamometer, (at low values of current loading), and using a d.c. tachogenerator with a differentiator, (at high values of current loading), has been done in the past. The methods described here, however, achieve a very much better accuracy, particularly in the accelerometer test. In this last test an accuracy of 2% has been achieved by incorporating a variable element filter in the device in order to eliminate the commutator ripple noise from the tachogenerator output. Without this filter only qualitative results can be obtained from the accelerometer as was the case in the past. The direct measurement of load losses under full load conditions, using the back-to-back test arrangement, is entirely new and constitutes the most reliable and accurate test to date. The load losses can easily be obtained from this test to an accuracy of 1-2%.

Part two of the thesis calculates the losses produced by the field harmonics that are generated in the air gap of the machine due to the non-sinusoidal winding distri-

bution on the stator and rotor surfaces. The losses considered are:

- (i)  $I^2R$  losses in the squirrel cage bars due to the harmonic currents that are induced in them by the rotating field harmonics.
- (ii) Losses caused by the interbar currents that flow in the rotor when the squirrel cage is skewed but not completely insulated from the rotor iron laminations.
- and (iii) Losses in the stator and rotor iron. These losses include both those dissipated at or near the surface and those dissipated in the tooth bodies. Both eddy current and hysteresis losses were considered.

The resulting load loss formulae contain harmonic parameters (mainly reactances) which cannot be accurately determined by classical methods of calculation. It was found necessary to apply the following corrections to these parameters: (The correction factors are calculated in Sections 6.1, 6.4, 6.5 and 6.7 of Part 2 and the entire of Part 3).

- (i) The magnitudes of the slot harmonic fields are altered by the influence of the slot-openings.

- (ii) The different harmonic leakage reactances are reduced by eddy currents induced in the rotor iron surface.
- (iii) The rotor tooth flux is reduced by the damping action of the harmonic currents that flow in the squirrel cage winding.
- (iv) The magnitudes of the harmonic fields are reduced when the iron is saturated by, either the main flux, or the fundamental leakage (mainly harmonic) fluxes.
- (v) The differentail harmonic leakage reactances are reduced by the slot openings much more than Carter's coefficient would suggest.
- (vi) The effective skew of the squirrel cage winding is different from its geometrical value and is reduced by the width of the rotor bars.

It is considered to be of importance that all the correction factors are calculated in a rather rigorous manner. None of the factors or values of parameters used in this thesis are empirical and the present work has removed much of the empiricism that was considered necessary in the past.

In Part 4 the experimental results obtained in Part 1 are compared with the theoretical predictions of Part 2 using the values of parameters determined in Part 3.

The agreement between theoretical and experimental results for all the tests on all 11 squirrel cage rotors and one slip ring motor was found to be very good and far better than anything published to date.

In Part 5 there is a general discussion of the effect of machine parameters on the load losses. Section 9.3 shows how the harmonic equivalent circuit of the induction motor can be modified to include the effects to interbar currents by shunting the secondary impedance branch by an operational impedance  $Z'_{2v}$ , which was calculated. The effect of skew of the squirrel cage bars on the load losses is discussed in Chapter 10, where it was shown that for a relatively well insulated rotor, skewing does not make a great deal of difference as far as the load losses are concerned, but that for a badly insulated machine the skew should be kept to a minimum to limit these losses.

In Chapter 11 it was shown that the load losses vary with slot combination in a very much more pronounced way than they do with any other machine variable. It was pointed out that the load losses are minimised when the slot combination is near unity, and although this conclusion was known from past experience, it is the first time that a quantitative variation of the total load loss with the ratio  $S_2/S_1$  has been derived.

In Chapter 12 it was shown that the load losses decrease as the air gap is increased, but controlling the load losses in this way is not easy, because the main magnetic fields also depend a great deal on the air gap length. For example an increase in  $g$  also decreases the main magnetising reactance  $X_m$  and hence increases the no load current  $I_0$  which is an undesirable effect.

In Chapter 13 some measurements of the stator tooth fluxes are given and comparisons with theoretical results provide a further check on the theory. Measurements of the rotor tooth fluxes were not taken but this could be done by future investigators and could provide very important information on the behaviour of the squirrel cage. (For example it could give an experimental check on the damping factors  $k_{tv}$  in Section 6.5 and  $k_{d\ell v}$  in Section 6.4). These measurements could be done by either inserting search coils in the rotor and amplifying the signal by means of an amplifier rotating with the rotor before collecting it from slip rings, or by building an inverted machine which has the squirrel cage on the stationary member and the primary winding on the rotating member supplied through slip rings.<sup>54</sup> Also in Chapter 13 the "extra" load losses introduced by the

combined effects of the slot openings and saturation are investigated theoretically. Future work could include an experimental investigation on this topic by testing two rotors identical in every respect except the size of the rotor slot bridge.

Finally it should be noted that although eleven entirely different squirrel cage rotors, and one slip ring motor, have been tested and the results provide a very good check on the theoretical work, the theory has not been applied to large induction machines. It is felt that the same formulae derived in Chapter 6 apply without any modification to induction motors in general whether they are squirrel cage or slip-ring, small or large; this last type, however, should be investigated further in future work.

## APPENDIX I

### The distribution of power flow in the back-to-back test

Fig.91 shows a line diagram of the power flow in the back-to-back test.

Let  $T$  = electromagnetic torque, which is equal on the two machine sets.

$T_{fm}$ ,  $T_{fg}$  = fundamental torques, on motor and generator respectively.

$T_{lm}$ ,  $T_{lg}$  = stray torques, corresponding to the load losses.

$P_{fem}$ ,  $P_{feg}$  = stator iron losses.

From Fig.91 the electrical power input to the two induction machines is:

$$P_{ac} = P_2 - P_1 \quad (I.1)$$

The power to the induction motor is:

$$P_2 = (P_{fem} + 3I_{1m}^2 R_{1m}) + \omega_o \cdot T_{fm} \quad (I.2)$$

where:  $T_{fm} = T + T_{lm} \quad (I.3)$

The power from the generator is:

$$P_1 = \omega_o T_{fg} - (P_{feg} + 3I_{1g}^2 R_{1g}) \quad (I.4)$$

where:  $T_{fg} = T - T_{lg} \quad (I.5)$



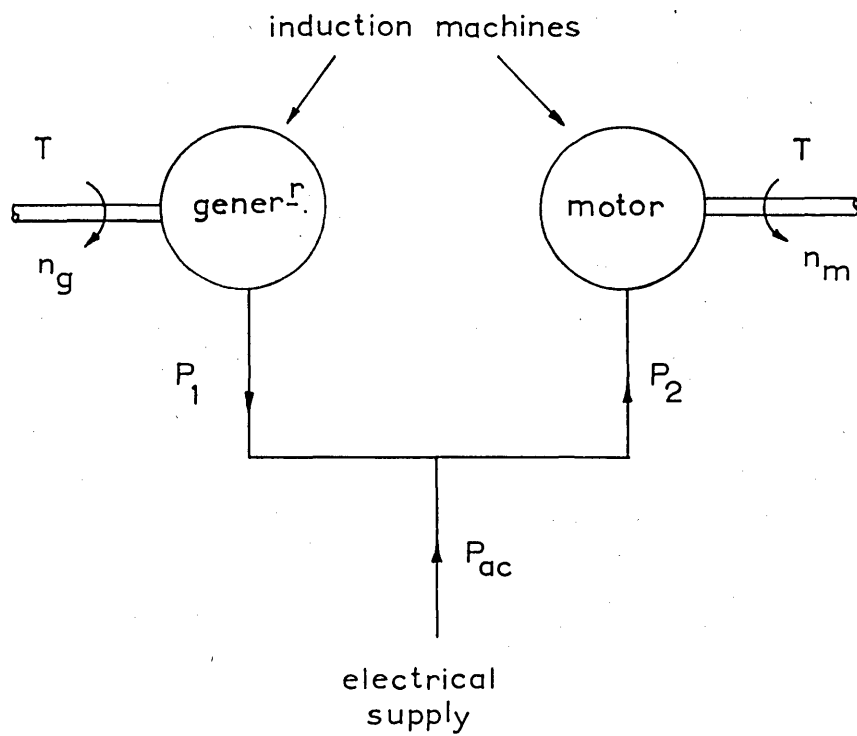


fig.91 Power flow in the back to back test

Substituting Eqns. (I.2) to (I.5) into Eqn. (I.1)

gives:

$$P_{ac} = (P_{fem} + P_{feg} + 3I_{1m}^2 R_{1m} + 3I_{1g}^2 R_{1g}) + \{T_{\ell m} \cdot 2\pi n_m + T_{\ell g} \cdot 2\pi n_g\} \\ - \left[ T_{\ell g} \cdot \frac{n_g s_g}{1+s_g} - T_{\ell m} \cdot \frac{n_m s_m}{1-s_m} \right] \quad (I.6)$$

The first term in the round brackets of Eqn. I.6 is the total stator loss of the two induction machines; the second term in the curly brackets is the load loss; and the terms in the square brackets are small because of the low value of slip during normal load. Their difference is even smaller and can be neglected.

The net mechanical power input to the two induction machines is:

$$P_{mech.} = 2\pi T(n_g - n_m) \\ = (s_g \omega_o T_{fg} + s_m \omega_o T_{fm}) + \left[ T_{\ell g} \cdot \frac{n_g s_g}{1+s_g} - T_{\ell m} \cdot \frac{n_m s_m}{1-s_m} \right] \quad (I.7)$$

The first term in the round brackets of Eqn. I.7 is the fundamental rotor conductor loss and the second term in the square brackets is the same as the last term of Eqn. I.6 and is therefore negligible.

Adding Eqn. I.7 to I.6 checks that the net power input to the induction machines,  $(P_{ac} + P_{mech})$  is the total electrical power loss in these machines.

## APPENDIX II

### The mmf distribution produced by a three-phase winding

In order to avoid unnecessary complications that are introduced by unsymmetrical windings, and because the machines under investigation have two-layer lap windings, only this type of winding is considered here. However, it can be quite easily shown that the conclusions drawn in this Appendix are quite general and apply to all types of machine windings.

Fig.92 shows a two-layer lap winding with a pitch of  $w$ . Although the actual winding goes from A to A', B to B' etc., in the mathematical analysis the winding can be considered to be made up of two full pitch windings in two layers, as shown by A to A'', B to B'', etc.

#### (a) TOP LAYER

Taking the origin as the centre of a slot, the mmf of phase I can be written as:

$$f_{vI} = \sum_{c=0}^{q-1} \bar{A}_v \cdot \sin v \left( \frac{\pi x}{Y} - \frac{c\pi\lambda_1}{Y} \right) \cdot \sin \omega t$$

where  $\bar{A}_v$  is the amplitude of the  $v^{\text{th}}$  mmf harmonic.

If the winding of Fig.92 has a total of  $m_1$  phases the mmf of the  $(n-1)^{\text{st}}$  phase is given by:

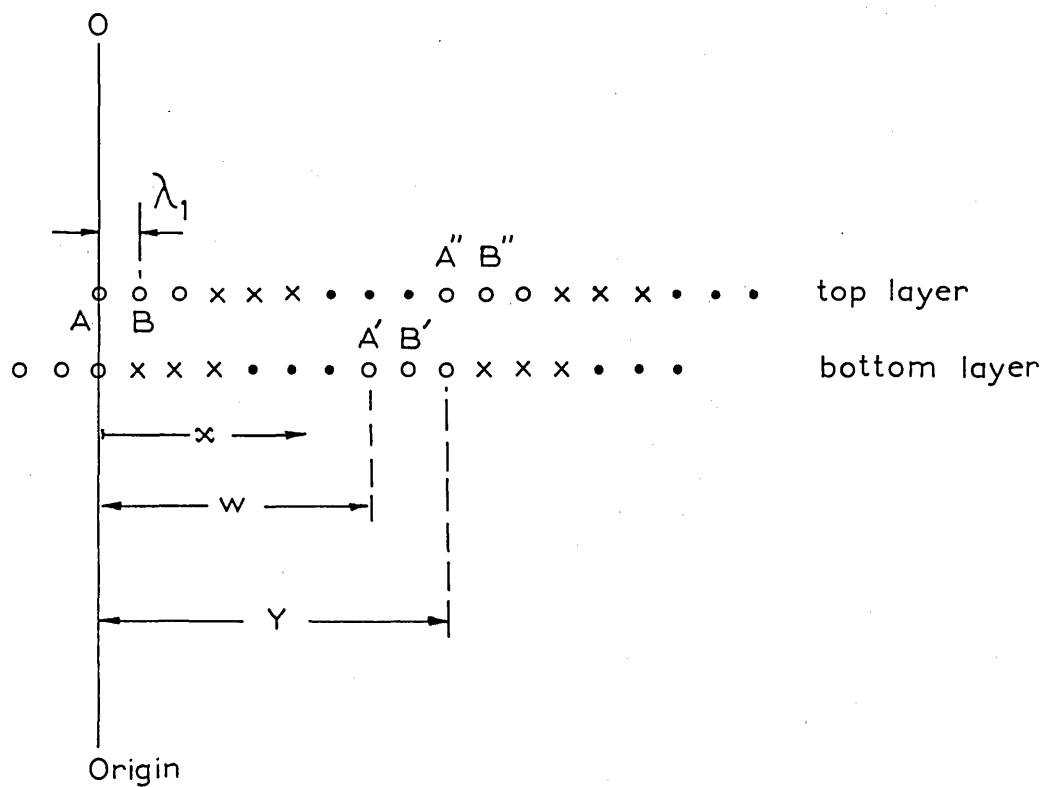


fig.92 Two layer lap winding with:

$$q=3, \quad m_1=3, \quad w/Y = 7/9.$$

$$f_{vn} = \sum_{c=0}^{q-1} \bar{A}_v \cdot \sin v \left( \frac{\pi x}{Y} - \frac{c \pi \lambda_1}{Y} - \frac{n\pi}{m_1} \right) \cdot \sin \left( \omega t - \frac{n\pi}{m_1} \right)$$

and the total  $v^{\text{th}}$  harmonic mmf due to the top layer is therefore

$$f_{v\text{top}} = \sum_{n=0}^{m_1-1} \sum_{c=0}^{q-1} \bar{A}_v \cdot \sin \left( \omega t - \frac{n\pi}{m_1} \right) \cdot \sin v \left( \frac{\pi x}{Y} - \frac{c \pi \lambda_1}{Y} - \frac{n\pi}{m_1} \right) \quad (\text{II.1})$$

(b) BOTTOM LAYER

The time phase angle of the bottom layer is the same as for the top one but the space phase angle is less by:  $v(1-w/Y)\pi$  radians.

Thus the total  $v^{\text{th}}$  harmonic mmf due to the bottom layer is:

$$f_{v\text{bottom}} = \sum_{n=0}^{m_1-1} \sum_{c=0}^{q-1} \bar{A}_v \cdot \sin \left( \omega t - \frac{n\pi}{m_1} \right) \cdot \sin v \left( \frac{\pi x}{Y} - \frac{c \pi \lambda_1}{Y} - \frac{n\pi}{m_1} + \pi \left( 1 - \frac{w}{Y} \right) \right) \quad (\text{II.2})$$

(c) TOTAL

From Eqns. II.1 and II.2 the total  $v^{\text{th}}$  harmonic mmf for the whole winding is:

$$f_v = \sum_{n=0}^{m_1-1} \sum_{c=0}^{q-1} \bar{A}_v \sin(\omega t - \frac{n\pi}{m_1}) \cdot 2 \sin \frac{v\pi}{2Y} x$$

$$x \sin \left\{ \frac{v\pi x}{Y} - \frac{v\pi \lambda_1}{Y} - \frac{v\pi n}{m_1} + \frac{v\pi}{2} \left(1 - \frac{v}{Y}\right) \right\} \quad (\text{II.3})$$

Performing the summation with respect to  $c$  one obtains after some simplification:

$$f_v = \bar{A}_v \cdot 2q \cdot k_{dv} \cdot k_{pv} \cdot \sum_{n=0}^{m_1-1} \sin v\pi \left\{ \frac{x}{Y} + \frac{1}{2} \left(1 - \frac{v}{Y}\right) - \frac{\lambda_1(q-1)}{2Y} - \frac{n}{m_1} \right\} x$$

$$x \sin \left( \omega t - \frac{r\pi}{m_1} \right) \quad (\text{II.4})$$

If  $v$  is allowed to have both positive and negative values, then Eqn. II.4 can be condensed to:

$$f_v = \bar{A}_v \cdot k_{dpv} \cdot q \cdot \sum_{n=0}^{m_1-1} \cos \left\{ \omega t + \frac{n\pi}{m_1}(v-1) - \frac{v\pi x}{Y} - \frac{v\pi}{2} + \frac{v\pi \lambda_1}{2Y}(q-1) \right\}$$

$$(\text{II.5})$$

Performing the summation with respect to  $n$  one finally obtains:

$$f_v = \bar{F}_v \cdot \cos \left( \omega t - \frac{v\pi x}{Y} + \theta_v \right) \quad (\text{II.6})$$

where

$$\bar{F}_v = \bar{A}_v \cdot m_1 q k_{dpv} \cdot \left( \frac{\sin(v-1) \frac{\pi}{2}}{m \sin(v-1) \frac{\pi}{2m}} \right) \quad (\text{II.7})$$

$$\text{and } \theta_v = \left(\frac{m-1}{2}\right) \cdot \frac{(v-1)\pi}{m_1} + (q-1) \frac{v\pi\lambda}{2Y} - v\left(1 - \frac{w}{Y}\right) \frac{\pi}{2} \quad (\text{II.8})$$

It can be easily shown from Eqn. II.8 that the angles  $\theta_v$  for the fundamental ( $v=1$ ) and for the slot harmonics of the winding ( $v = r \frac{S_1}{p} + 1$ ) differ only by an integer number of  $2\pi$  radians.



### APPENDIX III

#### The calculation of the constants A and B in Eqn. 6.38

It is stated in Section 6.3 that the constants A and B in Eqn. 6.38 can be found from the two conditions

$$\left[ \frac{\partial I_{bv}}{\partial x} \right]_{atx=\pm \ell/2} = 0$$

From Eqn. 6.38

$$I_{bv} = A \cosh \gamma_v x + B \sinh \gamma_v x + \frac{E_{ov} e^{j\alpha_v x}}{r'_{bbv} (\alpha_v^2 + \gamma_v^2)}$$

$$\text{hence } \frac{\partial I_{bv}}{\partial x} = A \gamma_v \sinh \gamma_v x + B \gamma_v \cosh \gamma_v x + \frac{j\alpha_v E_{ov} e^{j\alpha_v x}}{r'_{bbv} (\alpha_v^2 + \gamma_v^2)}$$

Putting  $x = +\ell/2$  and  $x = -\ell/2$  in the above equation gives:

$$A \gamma_v \sinh \frac{\gamma_v \ell}{2} + B \gamma_v \cosh \frac{\gamma_v \ell}{2} + \frac{j\alpha_v E_{ov} e^{j\frac{\alpha_v \ell}{2}}}{r'_{bbv} (\alpha_v^2 + \gamma_v^2)} = 0 \quad (\text{III.1})$$

$$\text{and } -A \gamma_v \sinh \frac{\gamma_v \ell}{2} + B \gamma_v \cosh \frac{\gamma_v \ell}{2} + \frac{j\alpha_v E_{ov} e^{-j\frac{\alpha_v \ell}{2}}}{r'_{bbv} (\alpha_v^2 + \gamma_v^2)} = 0$$

(III.2)

Subtracting (III.2) from (III.1) gives:

$$A = \frac{\alpha_v \cdot E_{ov}}{r'_{bbv} (\alpha_v^2 + \gamma_v^2)} \cdot \left( \frac{\sin \frac{\alpha_v \ell}{2}}{\gamma_v \sinh \frac{\alpha_v \ell}{2}} \right) \quad (\text{III.3})$$

Adding (III.2) to (III.1) gives:

$$B = \frac{-j\alpha_v E_{ov}}{r'_{bbv} (\alpha_v^2 + \gamma_v^2)} \cdot \left( \frac{\cos \frac{\alpha_v \ell}{2}}{\gamma_v \cosh \frac{\alpha_v \ell}{2}} \right) \quad (\text{III.4})$$

# APPENDIX IV

## The penetration of a travelling magnetic field into a lamination

Consider an mmf wave of the form:

$$f_v = \bar{F}_v \cdot e^{j(\omega_v t + \frac{v\pi y}{Y})} \quad (\text{IV.1})$$

to travel on the two sides of a lamination of thickness  $h$  as shown in Fig.33, where  $\bar{F}_v$  is the phasor value of the mmf.

If the displacement current in the iron is neglected in comparison with the conduction current, Maxwell's equations for the field vectors inside the lamination become :

$$\text{curl } \underline{H} = \underline{J} \quad (\text{IV.2})(a)$$

$$\text{curl } \underline{E} = - \frac{\partial \underline{B}}{\partial t} \quad (\text{IV.2})(b)$$

$$\underline{E} = \rho \underline{J}$$

$$\text{and } \underline{B} = \mu \mu_o \underline{H}$$

where  $\mu$  will be taken as a constant.

From Eqns. IV.2(a) and IV.2(b) one obtains:

$$\text{curl curl } \underline{H} = \text{curl } \underline{J}$$

$$\text{or: } \text{curl curl } \underline{B} = \frac{-\mu \mu_o}{\rho} \cdot \frac{\partial \underline{B}}{\partial t}$$

which becomes:  $\text{grad div } \underline{B} - \nabla^2 \underline{B} = \frac{-\mu\mu_o}{\rho} \frac{\partial \underline{B}}{\partial t}$

and since  $\text{div } \underline{B} = 0$  everywhere:

$$\nabla^2 \underline{B} = \mu\mu_o \frac{\partial \underline{B}}{\partial t} \quad (\text{IV.3})$$

Since  $\underline{B}$  has only one component;  $B_y$ , (see Fig.33)

Eqn. IV.3 becomes:

$$\frac{\partial^2 B_y}{\partial x^2} + \frac{\partial^2 B_y}{\partial y^2} = \frac{\mu\mu_o}{\rho} \cdot \frac{\partial B_y}{\partial t} \quad (\text{IV.4})$$

Now obviously since the applied mmf on the surfaces of the lamination has the form of Eqn. IV.1, the y-component of the phasor magnetic field inside the iron will be given by an expression of the form:

$$B_y = B_1 \cdot e^{j(\omega_v t + \frac{v\pi y}{Y})}$$

where  $B_1$  is a function of  $x$  in Fig.33.

Thus the operator  $\frac{\partial}{\partial t}$  in Eqn. IV.4 can be replaced by  $j$  and the operator  $\frac{\partial^2}{\partial y^2}$  by:  $-(\frac{v\pi}{Y})^2$ .

Eqn. IV.4 therefore becomes:

$$\frac{\partial^2 B_y}{\partial x^2} - \left[ \frac{j \omega_v \mu\mu_o}{\rho} + \left(\frac{v\pi}{Y}\right)^2 \right] \cdot B_y = 0$$

and if  $k^2$  is substituted for the expression in square brackets then:

$$\frac{\partial^2 B_y}{\partial x^2} - k^2 B_y = 0 \quad (\text{IV.5})$$

# APPENDIX V

## The reduction of the differential leakage reactance by the slot openings.

Eqn. 6.23 gives the rotor fields in the air gap of an induction motor. If only the influence of the rotor slot openings on these fields is considered, (and the stator slot openings neglected), this equation can be rewritten as:

$$b_{\left(\frac{k_2 S_2}{p} + 1\right)} = \bar{B}_{\left(\frac{k_2 S_2}{p} + 1\right)} \cdot \left[ \cos \rho(k_2) - \sum_{d=\pm 1, \pm 2, \dots} \frac{\gamma_d''}{2} \cos \rho(k_2 - d) \right] \quad (V.1)$$

where the function  $\rho(k_2)$  is given by:

$$\rho(k_2) \equiv \left[ 1 + (1-s) \frac{k_2 S_2}{p} \right] \omega t - \frac{\pi x_1}{Y} \left( \frac{k_2 S_2}{p} + 1 \right) + \theta_\mu \quad (V.2)$$

Eqn. (V.1) can be expanded for different values of  $k_2$  to give:

$k_2 = 0$  (fundamental field)

$$b_1 = \bar{B}_1 \cdot \cos \rho(0) - \bar{B}_1 \sum_{d=\pm 1, \pm 2, \dots} \frac{\gamma_d''}{2} \cdot \cos \rho(-d) \quad (V.3)$$

$k_2 = -1$  (backward rotating, rotor first slot harmonic)

$$b_{\left(1 - \frac{S_2}{p}\right)} = \bar{B}_{\left(1 - \frac{S_2}{p}\right)} \cdot \cos \rho(-1) - \bar{B}_{\left(1 - \frac{S_2}{p}\right)} \sum_{d=\pm 1, \pm 2, \dots} \frac{\gamma_d''}{2} \cdot \cos \rho(-1 - d) \quad (V.4)$$

$k_2 = +1$  (forward rotating, rotor first slot harmonic)

$$b_{\left(\frac{S_2}{p} + 1\right)} = \bar{B}_{\left(\frac{S_2}{p} + 1\right)} \cdot \cos p(1) - \bar{B}_{\left(\frac{S_2}{p} + 1\right)} \cdot \sum_d \frac{\gamma_d''}{2} \cdot \cos p(1-d) \quad (V.5)$$

$k_2 = -2$  (backward rotating, rotor second slot harmonic)

$$b_{\left(1 - \frac{2S_2}{p}\right)} = \bar{B}_{\left(1 - \frac{2S_2}{p}\right)} \cdot \cos p(-2) - \bar{B}_{\left(1 - \frac{2S_2}{p}\right)} \cdot \sum_d \frac{\gamma_d''}{2} \cdot \cos p(-2-d) \quad (V.6)$$

$k_2 = +2$  (forward rotating, rotor second slot harmonic)

$$b_{\left(1 + \frac{2S_2}{p}\right)} = \bar{B}_{\left(1 + \frac{2S_2}{p}\right)} \cdot \cos p(2) - \bar{B}_{\left(1 + \frac{2S_2}{p}\right)} \cdot \sum_d \frac{\gamma_d''}{2} \cdot \cos p(2-d) \quad (V.7)$$

etc. ...

Fields of the same order can be added or subtracted from each other to produce a resultant field. Fields of the same order occur when the value of  $(k_2 - d)$  for a certain  $k_2$  and  $d$ , is the same as another value of  $k_2$ . (See Eqn. V.1). For example when  $d = +1$  the second term of Eqn. (V.4) and the first term of Eqn. (V.6) can be added together.

Considering only the first two harmonics produced by the air gap permeance variations, ( $d = \pm 1$  and  $\pm 2$ ) the total airgap rotor field can be calculated from Eqns.

(V.3) to (V.7) as:

$$\begin{aligned}
 b_g'' = & \left[ \bar{B}_1 - \frac{\gamma_1''}{2} \left\{ \bar{B}_{(1-\frac{S_2}{p})} + \bar{B}_{(1+\frac{S_2}{p})} \right\} - \frac{\gamma_2''}{2} \left\{ \bar{B}_{(1-\frac{2S_2}{p})} + \bar{B}_{(1+\frac{2S_2}{p})} \right\} \right] \cos p(0) \\
 & + \left[ \bar{B}_{(1-\frac{S_2}{p})} - \frac{\gamma_1''}{2} \left\{ \bar{B}_1 + \bar{B}_{(1-\frac{2S_2}{p})} \right\} - \frac{\gamma_2''}{2} \cdot \bar{B}_{(1+\frac{S_2}{p})} \right] \cdot \cos p(-1) \\
 & + \left[ \bar{B}_{(1+\frac{S_2}{p})} - \frac{\gamma_1''}{2} \cdot \left\{ \bar{B}_1 + \bar{B}_{(1+\frac{2S_2}{p})} \right\} - \frac{\gamma_2''}{2} \cdot \bar{B}_{(1-\frac{S_2}{p})} \right] \cdot \cos p(1) \\
 & + \left[ \bar{B}_{(1-\frac{2S_2}{p})} - \frac{\gamma_1''}{2} \cdot \bar{B}_{(1-\frac{S_2}{p})} - \frac{\gamma_2''}{2} \cdot \bar{B}_1 \right] \cdot \cos p(-2) \\
 & + \left[ \bar{B}_{(1+\frac{2S_2}{p})} - \frac{\gamma_1''}{2} \cdot \bar{B}_{(1+\frac{S_2}{p})} - \frac{\gamma_2''}{2} \bar{B}_1 \right] \cdot \cos p(2) \\
 & \dots \dots \text{etc.} \quad (V.8)
 \end{aligned}$$

The first term of Eqn. (V.8) is the fundamental field produced by the rotor. The quantities in the curly brackets of this term are totally negligible.

The second and third terms of Eqn. V.8 represent the first rotor slot harmonic pair, and the fourth and fifth terms the second rotor slot harmonic pair. These last four terms of Eqn. V.8 contain terms involving  $\bar{B}_1$ , the

fundamental field. In Section 6.1 it is shown how these fields can be separated out and considered to produce only no load losses provided that the remaining fields due to the mmf harmonics are multiplied by a certain factor. This will not be discussed further in this Appendix and the quantities, (in the last four terms of Eqn. V.8) involving  $\bar{B}_1$  will be left out.

Thus the first slot harmonic pair of the rotor field becomes:

$$\left[ \bar{B}_{(1 \pm \frac{S_2}{p})} - \frac{\gamma_1''}{2} \cdot \bar{B}_{(1 \pm \frac{2S_2}{p})} - \frac{\gamma_2''}{2} \cdot \bar{B}_{(1 \pm \frac{S_2}{p})} \right] \cdot \cos p(\pm 1) \quad (V.9)$$

and the second slot harmonic pair of the rotor field becomes:

$$\left[ \bar{B}_{(1 \pm \frac{2S_2}{p})} - \frac{\gamma_1''}{2} \bar{B}_{(1 \pm \frac{S_2}{p})} \right] \cdot \cos p(\pm 2) \quad (V.10)$$

Expressions (V.9) and (V.10) show that the rotor slot openings reduce the rotor slot harmonic fields.

Reference 3 shows that the reactance corresponding to a sinusoidal magnetic field of magnitude B and order n is proportional to B/n. Thus the reactances of the first harmonic pair are: (From expression V.9 and Eqn.V.2)



$$x_{(1 \pm \frac{S_2}{p})} = K \cdot \left[ \bar{B}_{(1 \pm \frac{S_2}{2})} - \frac{\gamma_1''}{2} \bar{B}_{(1 \pm \frac{2S_2}{p})} - \frac{\gamma_2''}{2} \bar{B}_{(1 \pm \frac{S_2}{p})} \right] \cdot \frac{1}{(1 \pm \frac{S_2}{p})} \quad (V.11)$$

and of the second harmonic pair: (From expression V.10 and Eqn. V.2)

$$x_{(1 \pm \frac{2S_2}{p})} = K \cdot \left[ \bar{B}_{(1 \pm \frac{2S_2}{p})} - \frac{\gamma_1''}{2} \bar{B}_{(1 \pm \frac{S_2}{p})} \right] \cdot \frac{1}{(1 \pm \frac{2S_2}{p})} \quad (V.12)$$

The differential leakage reactance of the rotor (with respect to the fundamental field) is defined by:<sup>35</sup>

$$x_{2d1} = \sum_{m \neq 0} x_{(1 \pm \frac{mS_2}{p})} \quad (V.13)$$

and if only the first two rotor slot harmonic pairs are considered:

$$x_{2d1} \approx x_{(1 + \frac{S_2}{p})} + x_{(1 - \frac{S_2}{p})} + x_{(1 + \frac{2S_2}{p})} + x_{(1 - \frac{2S_2}{p})}$$

which using Eqns. (V.11) and (V.12) becomes:

$$\begin{aligned}
x_{2d1} \approx K \cdot & \left[ \left\{ \bar{B} \frac{1}{(1+\frac{S_2}{p})} - \frac{\gamma_1''}{2} \cdot \bar{B} \frac{1}{(1+\frac{2S_2}{p})} - \frac{\gamma_2''}{2} \cdot \bar{B} \frac{1}{(1-\frac{S_2}{p})} \right\} \cdot \frac{1}{(1+\frac{S_2}{p})} \right. \\
& + \left\{ \bar{B} \frac{1}{(1-\frac{S_2}{p})} - \frac{\gamma_1''}{2} \cdot \bar{B} \frac{1}{(1-\frac{2S_2}{p})} - \frac{\gamma_2''}{2} \cdot \bar{B} \frac{1}{(1+\frac{S_2}{p})} \right\} \cdot \frac{1}{(1-\frac{S_2}{p})} \\
& + \left\{ \bar{B} \frac{1}{(1+\frac{2S_2}{p})} - \frac{\gamma_1''}{2} \cdot \bar{B} \frac{1}{(1+\frac{S_2}{p})} \right\} \cdot \frac{1}{(1+\frac{2S_2}{p})} + \\
& \left. + \left\{ \bar{B} \frac{1}{(1-\frac{2S_2}{p})} - \frac{\gamma_1''}{2} \cdot \bar{B} \frac{1}{(1-\frac{S_2}{p})} \right\} \cdot \frac{1}{(1-\frac{2S_2}{p})} \right] \\
& \qquad \qquad \qquad (V.14)
\end{aligned}$$

If the rotor slot openings are neglected

( $\gamma_1'' = \gamma_2'' = 0$ ) the differential leakage reactance becomes:

$$\begin{aligned}
x_{2d10} = K \left[ \frac{\bar{B} \frac{1}{(1+\frac{S_2}{p})}}{(1+\frac{S_2}{p})} + \frac{\bar{B} \frac{1}{(1-\frac{S_2}{p})}}{(1-\frac{S_2}{p})} + \frac{\bar{B} \frac{1}{(1+\frac{2S_2}{p})}}{(1+\frac{2S_2}{p})} + \frac{\bar{B} \frac{1}{(1-\frac{2S_2}{p})}}{(1-\frac{2S_2}{p})} \right] \\
\qquad \qquad \qquad (V.15)
\end{aligned}$$

Therefore the rotor slot openings reduce the differential leakage reactance with respect to the fundamental field by the factor:

$$k_{o1} \equiv \frac{x_{2d1}}{x_{2d1o}} \quad (V.16)$$

or:

$$k_{o1} = \frac{A_1}{C_1} \quad (V.17)$$

where  $A_1$  and  $C_1$  are given by the right hand sides of Eqns. (V.14) and (V.15) respectively. The values of the rotor flux densities in these two expressions are given by Eqn. (6.24) and the values of  $\gamma_1''$  and  $\gamma_2''$  are given in Ref.16.

Although only the reduction of the differential leakage reactance of the fundamental wave has been derived here, it can be easily shown that the differential leakage reactance of the  $v^{\text{th}}$  field harmonic is reduced by a factor:

$$\begin{aligned} k_{ov} &\equiv \frac{x_{2dv}}{x_{2dvo}} \\ &= \frac{A_v}{C_v} \end{aligned} \quad (V.18)$$

where  $A_v$  and  $C_v$  are given by expressions exactly analogous to the right hand sides of Eqn. (V.14) and (V.15), but referred to the  $v^{\text{th}}$  harmonic.

Numerical computations for rotor No.1 for example gave values of  $k_{o1}$  (by which the differential leakage

reactance of the fundamental is reduced) of 0.89, and of  $k_{ov}$  (by which the differential leakage reactance of the stator slot harmonic fields is reduced) of 0.66.

REFERENCES

1. American Standard Test Code for polyphase induction motors and generators. (American Standards Association, 1954).
2. "Methods of declaring efficiency of electrical machinery". British Standards Rule 269-1927, with Amendment 4, Aug.1961.
3. Liwschitz, M.: "Electric Machinery" Vol.II (Van Nostrand, 1961), 2nd ed.
4. Alger, P.L.: "The nature of polyphase induction machines" (Wiley, 1961), 2nd ed.
5. Thompson, W.G. and Ledbetter, J.: "Precision dynamometry in testing electrical machines". G.E.C. Journal, Vol.32, No.1, 1965.
6. Emmerling, A.A.: "Modern equipment for the precise testing of motors". G.E.Review, Vol.37, 1934.
7. Leader, C.C. and Phillips, F.D.: "Efficiency tests of induction machines." Trans. A.I.E.E. Vol.53, 1934, p.1628.
8. Meunier, P.: "Note sur L'Essai Des Moteurs Asynchrones". L'Eclairage Electrique, Vol.34, 1903, p.228.
9. Bird, B.M.: "Measurement of stray load losses in squirrel cage induction motors." Proc. I.E.E., Vol. III, 1964, p.1697.

10. Morgan, T.H. and Seigfried, V.: "Stray load loss tests on induction machines". Trans. A.I.E.E., Vol. 55, 1936, p.493.
11. Morgan, T.H. and Narbutovskih, P.M.: "Stray load loss tests on induction machines." Trans. A.I.E.E. Vol.53, 1934, p.286.
12. Christofides, N. "Origins of load losses in induction motors with cast aluminium rotors". Machines report No.57, Imperial College.
13. Barton, T.H. and Ahmad, V.: "The measurement of induction motor stray loss and its effect on performance." Proc. I.E.E., Pt.C, Monograph No.255U, 1957.
14. Barton, T.H. and Ahmad, V.: "The measurement and prediction of induction motor stray loss at large slips." Proc. I.E.E., Pt.C, Monograph No.219 U, 1957.
15. Freeman, E.: "Calculation of harmonics due to slotting". Proc. I.E.E., Monograph No.523 U, 1962.
16. Oberretl, K.: "New facts about parasitic torques in induction motors". Bulletin Oerlikon, No.348, 1962.
17. Rossmailer, V.: Calculation of the stray load losses in induction machines caused by uninsulated bars". E.u.M., Vienna, Vol.57, 1937, p.249.
18. Odok, A.: "Stray load losses and stray torques in induction machines". Trans. A.I.E.E., Vol.77, 1958, p.43.

19. Pipes, L.: Applied mathematics for engineers and physicists". McGraw-Hill, (book).
20. Dreyfus, L.: "Theorie der Zusatzlichen Eisenverluste in Drehstromasynchronmotoren". A.f.E. Vol.20, 1928, pp.37-87, 188-210, 273-298.
21. Carter, G.W.: "A note on the surface loss in a laminated pole face." Proc. I.E.E., Vol.102C, 1955, p.217.
22. Carter, G.W.: "The electromagnetic field in its engineering aspects". (book), Longmans, 1954.
23. Ball, J.D.: "The unsymmetrical hysteresis loop ". Trans. A.I.E.E. Vol.34, 1915, p.2693.
24. Spooner, T.: "Tooth pulsations in rotating machines". Trans. A.I.E.E., Vol.43, 1924, p.260.
25. Spooner, T. and Kinnard, I.F.: "Surface iron losses with reference to laminated materials". Trans. A.I.E.E., Vol.43, 1924, p.262.
26. Richter, R.: "Elektrische Maschinen". (Book), Vol.1, Springer, 1954.
27. Baumann, F.: "An elementary analysis of load loss." G.E. unpublished report No.28190, 1938.
28. Steel Company of Wales. "Electrical sheet steels", 1960, Publication.

29. Read, J.C.: "Investigations on core loss and saturation." B.T.H. Eng. Report No.1754, 1924 (unpublished).
30. Spooner, T.: "Permeability", Trans. A.I.E.E., Vol.42, 1923, p.340.
31. Smith, W.: "Effect of a superimposed constant field upon the a.c. permeability and energy loss in iron". Physical Review, 1921, p.416.
32. Angst, G.: "Saturation factors for the leakage reactance of induction motors with skewed rotors". Trans. A.I.E.E., Vol.82.
33. Chapman, F.T.: "A study of the induction motor.". (book) 1930, Chapman and Hall.
34. Lee, C.H.: "Saturation harmonics of polyphase induction motors". Trans. A.I.E.E. Vol.80, 1961, p.957.
35. Richter, R.: "Elektrische Maschinen". (book), Vol.4, Springer, 1954.
36. Taegen, F.: "Uber die Oberfeldmomente von Drehstrom-Asynchronmotoren mit Kafiglaufern". Dr. Ing. thesis; T.H. Hannover; 1961.
37. Agarwal, P.D.: "Equivalent circuits and performance calculations of canned motors". Trans. A.I.E.E., Vo.79 1960, p.635.



38. Taegen, F.: Die Bedeutung der Läufer<sup>"</sup>nutschlitze für die Theorie der Asynchronmaschine mit Käfig<sup>"</sup>läufer." A.f.E., Vol.48, 1964, p.373.
39. Field A.B.: Eddy currents in slot wound conductors", Trans. A.I.E.E. Vol.24, p.659, 1905.
40. Summers, E.R.: "Effects of stray load loss on the torque characteristics of polyphase induction motors". G.E. unpublished report 63654 - Oct. 1944.
41. Nicolaide, A.: "Pierderi suplimentare in rotorele in colirie ale masinilor asincrone si sincrone." Electrotehnica, Vol.12, 1964.
42. Alger, P.L.: "Induced high frequency currents in squirrel cage windings". Trans. A.I.E.E., Vol.76, 1957, p.724.
43. Baumann, F.: Tooth flux pulsations due to reluctance variations in induction motors." G.E. unpublished report 28190, 1938.
44. Chalmers, B.J. and Williamson, A.C.: "Stray losses in squirrel cage induction motors - Validity of reverse rotation test." Proc. I.E.E., Vol.110, 1963, p.1773.
45. Schwarz, K.K.: "A survey of basic stray losses in squirrel cage induction motors". Proc. I.E.E., Vol. 111, 1964, p.1565.

46. Dreese, E.: "Synchronous motor effects in induction machines." Trans. A.I.E.E., Vol.49, 1930, p.1033.
47. Fritze, H.: "Noise created by electrical machinery", A.f.E., Vol.10, 1921, p.73.
48. Kron, G.: "Induction motor slot combinations" Trans. A.I.E.E. Vol.50, 1931, p.757.
49. Pestarini, J.: "Central forces in asynchronous motors". Revue generale de l'electricite, Vo.24, 1928, p.517.
50. Appleman, W.R.: "The cause and elimination of noise in small motors". Trans. A.I.E.E., Vol.56, 1937, p.1359.
51. Arnold, E.: "Die Wechselstromtechnik", (book), Springer, 1910, Vols. 1 and V.1.
52. Alger, P.L.: Private Communication. Dec. 1965 and Jan.1966.
53. Christofides, N.: Reply to the discussion on the paper: "The origins of load losses in squirrel cage induction motors with cast aluminium rotors". Proc. I.E.E.
54. Chalmers, B.J.; Davis, E.J.; Alger, P.L.:  
Contributions to the discussion of paper in Ref.53.